



Development of a finite element strategy for the modeling of nano-reinforced materials

Dang Phong Bach

► To cite this version:

Dang Phong Bach. Development of a finite element strategy for the modeling of nano-reinforced materials. Mechanical engineering [physics.class-ph]. Université de Technologie de Compiègne, 2020. English. NNT : 2020COMP2550 . tel-03177046

HAL Id: tel-03177046

<https://theses.hal.science/tel-03177046v1>

Submitted on 22 Mar 2021

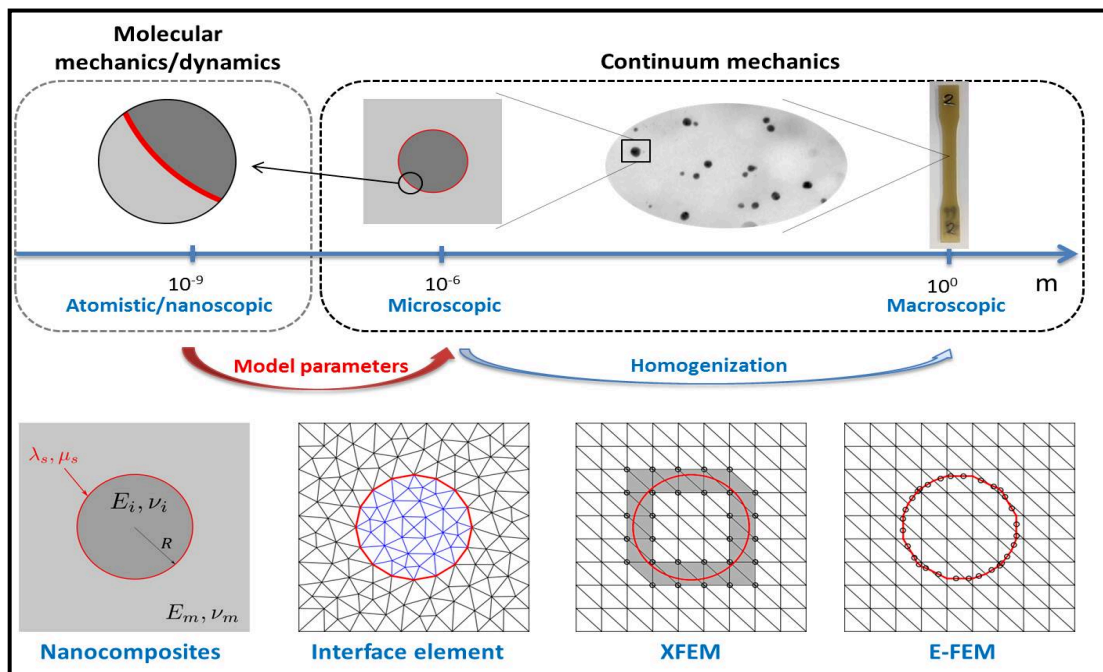
HAL is a multi-disciplinary open access archive for the deposit and dissemination of scientific research documents, whether they are published or not. The documents may come from teaching and research institutions in France or abroad, or from public or private research centers.

L'archive ouverte pluridisciplinaire **HAL**, est destinée au dépôt et à la diffusion de documents scientifiques de niveau recherche, publiés ou non, émanant des établissements d'enseignement et de recherche français ou étrangers, des laboratoires publics ou privés.

Par **Dang Phong BACH**

Development of a finite element strategy for the modeling of nano-reinforced materials

Thèse présentée
pour l'obtention du grade
de Docteur de l'UTC



Soutenue le 9 mars 2020

Spécialité: Mécanique Avancée : Unité de recherche en Mécanique - Laboratoire Roberval (FRE UTC - CNRS 2012)

D2550



Université de Technologie de Compiègne
Laboratoire Roberval UMR CNRS 7337

Development of a finite element strategy for the modeling of nano-reinforced materials

par

Dang Phong BACH

Thèse de doctorat

En vue de l'obtention du grade de
Docteur de l'Université de Technologie de Compiègne

Spécialité : Mécanique Avancée

Soutenue le 09 Mars 2020

Jury de Soutenance

Djimédo KONDO
Julien YVONNET
Bostjan BRANK
Nadège BRUSSELLE-DUPEND
Bedoui FAHMI
Delphine BRANCHERIE
Ludovic CAUVIN

Université Pierre et Marie-Curie
Université Gustave Eiffel
University of Ljubljana
IFP Energies nouvelles
Université de Technologie de Compiègne
Université de Technologie de Compiègne
Université de Technologie de Compiègne

Président
Rapporteur
Rapporteur
Examinatrice
Examineur
Directrice
Directeur

Acknowledgements

Firstly, I would like to express my most sincere appreciation to my supervisors Prof. Delphine Brancherie and Dr. Ludovic Cauvin for giving me the opportunity to carry out my doctoral research, and for providing continuous support of my PhD study and research. They are so patient, motivated, enthusiastic and knowledgeable. It has been an honor to be their PhD student. I appreciate all their contributions of time, ideas to make my PhD experience productive and stimulating. I learned a lot from them: hard-working spirit, serious attitude towards research, etc.

Besides my supervisors, I would like to thank the rest of my thesis committees: Prof. Julien Yvonnet and Prof. Bostjan Brank who had the difficult task to make a report on my manuscript, Prof. Djimédo Kondo and Mme. Nadège Brusselle-Dupend and Dr. Fahmi Bédoui who made me the honor to examine my work.

Special gratitude is extended to Prof. Pierre Villon, Prof. Alain Rassineux and Dr. Fahmi Bédoui for their invaluable insights and suggestions during my PhD work. I am grateful to all staff of Roberval laboratory for all their assistance.

I am also grateful to my friends in Roberval laboratory who gave me their help, encouragement, and comfort at the coffee room as well as at the sports hall: Khalil, Alan, Céline, Solène, Elisa, Benoît, David, Guillaume, Thibault, Xavier, Corentin, Youcef, Ivan, Tea, Cong Cuong, Xuan Nam, Tuan Anh, Cong Uy ... I really treasure the time we have spent together during the past three years. Especially, I owe my sincere gratitude to my friend, Sitou, who helped me a lot not only in the scientific aspect but also in daily life at Compiègne.

To my family, especially dear my parents, who follow every step I walk with their wholehearted support, I simply cannot thank them enough. Their encouragement gave me the driving force to finish this journey.

Last but not least, I would like to give my special thanks to my love, Huyen, for her understanding, sacrifice, and unconditional love.

Abstract: The modelization of nano-reinforced material requires to take into account the size effect caused by the local phenomena at the interface between the nano-inclusion and the matrix. This size effect is interpreted through an increase in the ratio interface/volume and can be taken into account by introducing a surface elasticity at the interface. Whereas a lot of works have been developed from the analytical point of view, few contributions are related to numerical description and implementation of such surface elasticity in Finite Element Method (FEM).

Our studies aim to develop efficient numerical tools based on FEM for the modeling of nanocomposites. Firstly, we evaluate the two existent numerical strategies namely the XFEM approach and the Interface element approach in reproducing the size effect in the homogenization process. Secondly, based on a performance test on the three types of formulations of E-FEM for the case of weak discontinuity, we propose an enhanced SKON formulation allowing to incorporate the effect of a coherent interface. Finally, the numerical modeling on the nonlinear behavior of nanocomposites is investigated. In the first step, a von Mises type elastoplastic law with linear isotropic hardening is considered for the bulk while the interface is considered as linear elastic.

Keywords: *finite element method, XFEM, E-FEM, homogenization, nanocomposite, surface elasticity, size effect, plasticity.*

Résumé: La modélisation des matériaux nano-renforcés nécessite de prendre en compte l'effet de taille induit par les phénomènes locaux à l'interface entre la nano-inclusion et la matrice. Cet effet de taille est interprété par une augmentation du rapport interface/volume et peut être pris en compte en introduisant une élasticité surfacique à l'interface. Alors que de nombreux travaux ont été développés du point de vue analytique, peu de contributions ont trait à la description numérique et à la mise en œuvre de cette élasticité surfacique dans la méthode des éléments finis (FEM).

Nos études visent à développer des outils numériques efficaces basés sur la FEM pour la modélisation de nanocomposites. Dans un premier temps, nous évaluons les deux stratégies numériques existantes, à savoir l'approche XFEM et l'approche des éléments d'interface, dans la reproduction de l'effet de taille dans le processus d'homogénéisation. Deuxièmement, sur la base d'un test de performance des trois types de formulations d'E-FEM dans le cas de discontinuités faibles, nous proposons une formulation améliorée de SKON permettant d'intégrer l'effet d'une interface cohérente. Enfin, la modélisation numérique du comportement non linéaire des nanocomposites est étudiée. Lors de la première étape, une loi élastoplastique de type von Mises avec durcissement linéaire isotrope est considérée pour le volume, tandis que l'interface est considérée comme élastique linéaire.

Mots-clés : *méthode éléments finis, XFEM, E-FEM, homogénéisation, nanocomposites, élasticité surfacique, effet de taille, plasticité.*

Contents

1	General introduction	1
1.1	Background and motivations	1
1.2	Outline	3
1.3	Notations	4
2	Size effect in nanocomposite materials: state of the art	7
2.1	Introduction	8
2.1.1	Nanocomposite and its size effect	8
2.1.2	Size effect: Experimental evidence	11
2.2	Interphase or interface?	13
2.3	Molecular dynamics simulations	16
2.4	Analytical models	18
2.4.1	Eshelby's problem with interface effect	19
2.4.2	Generalized Mori-Tanaka model and Generalized self-consistent method for spherical inclusion	20
2.4.3	Composite cylinder assemblages model and Generalized self- consistent model for cylindrical inclusion	21
2.4.4	Generalized Voigt and Reuss bounds	22
2.4.5	Generalized Hashin-Shtrikman lower bound	23
2.4.6	Comparison and conclusions on analytical models	24
2.5	Numerical models based on FEM	25
2.5.1	Surface/interface element in standard FEM	26
2.5.2	XFEM/level set approach	28
2.5.3	Other promising methods: Cut-FEM, Embedded-FEM	30
2.5.4	Conclusion on numerical approaches	31
2.6	Homogenization problem with coherent interface model	31
2.6.1	Basic elements of differential geometry for surface	32
2.6.1.1	Projection operators	32
2.6.1.2	Superficial (surface) fields	32
2.6.1.3	Surface gradient, surface divergence	33
2.6.2	Problem of composite material with coherent interface	34
2.6.2.1	Equilibrium equations and boundary conditions	35
2.6.2.2	Constitutive equations for the bulk and the interface	36

2.7	Conclusion	37
3	FEM with surface/interface element and eXtended-FEM for modeling size effect of nanocomposites: a comparative study.	39
3.1	Introduction	40
3.2	Governing equations	41
3.3	Finite element implementation	43
3.3.1	Standard FEM with surface/interface element	44
3.3.2	XFEM/level-set approach for modeling size effect	46
3.4	Numerical results	49
3.4.1	Eshelby's problem with coherent interface	50
3.4.1.1	Convergence analysis	50
3.4.1.2	Investigation of local field	51
3.4.1.3	Size effect indicator	53
3.4.2	Size dependence of effective properties of two-phases nanocomposites	54
3.4.3	Effective properties of a nanoporous material and influence of the boundary conditions	56
3.4.4	Spherical void (axisymmetric model)	59
3.4.5	Nanoporous material with random microstructure	60
3.5	Conclusion	65
4	Embedded-FEM approach for modeling the size effect in nanocomposite	67
4.1	Introduction	68
4.2	E-FEM formulations to handle weak discontinuities	70
4.2.1	Hu-Washizu three-field variational formulation	70
4.2.2	Enhanced assumed strain method	71
4.2.3	E-FEM discretization	73
4.2.4	Resolution strategy	77
4.3	Performance of the three E-FEM formulations: SOS, KOS and SKON	78
4.4	E-FEM approaches for two phases material with strong contrast of properties	81
4.5	E-FEM with coherent interface model	88
4.5.1	Surface strain enhancement	88
4.5.2	Variational formulation with coherent interface model	89
4.5.3	Enhanced surface strain interpolation	91
4.6	Numerical examples using E-FEM with interface effect	94
4.6.1	Eshelby problem with coherent interface	94
4.6.2	Two phases nanocomposite	96
4.6.3	Nanocomposites with random micro-structures	99

4.7	Conclusion	101
5	Modeling nonlinear behavior with surface elasticity by numerical approaches	103
5.1	Introduction	104
5.2	Plasticity model	104
5.2.1	Plasticity model with von Mises plasticity criterion	105
5.2.2	Numerical integration	108
5.3	Finite element implementation	113
5.3.1	Interface element approach	113
5.3.2	XFEM approach	114
5.3.3	E-FEM approach	115
5.4	Nonlinear results	117
5.4.1	Interface element approach	117
5.4.2	XFEM and E-FEM	120
5.5	Conclusion	123
6	General conclusion and perspectives	125
6.1	General conclusion	125
6.2	Perspectives	128
A	E-FEM with numerical evaluation of curvature	131
A.1	Numerical evaluation of curvature	131
A.2	Influence of the numerical evaluation of the curvature on the results	132
	Bibliographie	133

List of Figures

2.1	Different reinforcement morphologies of nanocomposites [Fu et al., 2019].	9
2.2	Range of length and time scales of the multi-scale methods for nanocomposite materials [Gates et al., 2005].	9
2.3	– Surface area as a function of particle size [Jesson and Watts, 2012].	10
2.4	Evolution of Young’s modulus versus volume fraction for different particle sizes in (a) [Douce et al., 2004] and (b) [Mishra et al., 2005].	11
2.5	Particle size effect on alumina nanoparticles composites in [Cho et al., 2006]	12

2.6	Particle size effect on PMMA/silica nanocomposites Young's modulus in (a) [Blivi et al., 2016] and (b) [Blivi, 2018].	12
2.7	Interphase and interface models.	14
2.8	Periodic box of different neat and nanocomposites model used for molecular dynamic simulation in [Adnan et al., 2007] with non-deformable spherical inclusion.	17
2.9	First Eshelby problem with coherent interface.	19
2.10	Mori-tanaka model and Generalized self-consistent method with coherent interface.	21
2.11	Size effect on effective bulk modulus of a spherical inclusion nanocomposite- Estimation by different models in the literature - $\kappa_m = 20$ GPa, $\kappa_i = 35$ GPa, $\mu_m = 15$, $f = 0.2$	25
2.12	Surface element in standard FEM and its result from [Wei et al., 2006].	27
2.13	Summary of the effective response of the RVE versus size for different stiffness ratios and different types of interfaces. The graphs show the component xx of the macroscopic Piola stress versus the normalized RVE size by a physical dimension at the microstructure denoted d [Javili et al., 2017].	27
2.14	An XFEM/level set mesh with an interface, showing fully enriched elements, partially enriched elements and unenriched (standard) elements. Also shown is the boundary Γ_{blend} where the enrichment vanishes [Chessa and Belytschko, 2003].	28
2.15	Normalized effective bulk modulus versus pore radius [Yvonnet et al., 2008]	29
2.16	Spherical inclusion problem with the spring-layer interface [Zhu et al., 2011] (β_1 is a relative elastic stiffness of the imperfect interface). . . .	29
2.17	Problem of two phases material with an imperfect interface.	35
3.1	Problem of two phases material with coherent interface.	41
3.2	An example of XFEM mesh and Interface element mesh.	43
3.3	Interface element and bulk neighbor elements.	45
3.4	Enrichment function ψ for a circle interface in XFEM.	47
3.5	Element cut by the interface Γ , approximated interface and integration points in XFEM.	47
3.6	Problems with coherent interface are treated in the plane strain context: (a) Eshelby problem ; (b) Two-phases material; (c) XFEM mesh; (d) Interface element mesh.	49
3.7	Convergence analysis for the extended Eshelby problem ($\beta = 1$) with a coherent interface.	51
3.8	Geometry for local strain field investigation	51
3.9	Mesheres for local strain field investigation.	52

3.10 ϵ_{xx} along the line A-B for different values of α (XFEM vs Interface element).	52
3.11 Size effect indicator versus inclusion radius for the extended Eshelby problem ($\beta = 1$).	53
3.12 Size dependence of effective plane strain bulk modulus of two-phases materials for $\alpha = 0.2$ and $\alpha = -0.2$ for different values of the stiffness contrast β	55
3.13 Size dependence of effective plane strain shear modulus of two-phases materials for $\alpha = 0.2$	56
3.14 Three types of boundary conditions.	57
3.15 Size effect in effective plane-strain bulk modulus for different type of boundary conditions.	57
3.16 Size-dependent effective plane-strain shear modulus for different type of boundary conditions.	58
3.17 Spherical void with coherent interface is treated with axisymmetric model.	59
3.18 Size-dependent effective bulk modulus with a spherical nanovoid for different type of boundary condition (IE: Interface element; MT: Mori-Tanaka).	60
3.19 Size-dependent effective shear modulus with a spherical nanovoid for different types of boundary condition (MT: Mori-Tanaka).	60
3.20 Conforming meshes of RVEs with randomly distributed nano-voids.	61
3.21 Statistical convergence on the normalized effective bulk modulus for different RVEs by the Interface element approach ($f = 0.3$, $E = 70$ GPa, $\nu = 0.32$, $\lambda_s = 6.842$ N/m, $\mu_s = -0.375$ N/m).	61
3.22 Deformation under hydro-static load $\bar{\epsilon}_{11} = \bar{\epsilon}_{22} = 0.5$, ($f = 0.3$, $E = 70$ GPa, $\nu = 0.32$, $\lambda_s = 6.842$ N/m, $\mu_s = -0.375$ N/m)	62
3.23 Two different samples for a 30 randomly distributed nano-voids RVE.	63
3.24 Normalized effective plane-strain bulk modulus for nanoporous material with randomly distributed nano-voids ($f = 0.3$, $E = 70$ GPa, $\nu = 0.32$, $\lambda_s = 6.842$ N/m, $\mu_s = -0.375$ N/m).	63
3.25 Convergence test on number of standard d.o.f.	64
4.1 Problem of two phases material with a perfect interface (classical composite).	70
4.2 Shape function $\mathbf{M}(\mathbf{x})$ in a discontinuous element	75
4.3 Classical first Eshelby problem and two-phase material problem ($R = 1nm$, $f = 0.2$).	78
4.4 Convergence analysis of the three formulations of E-FEM in treating the First Eshelby problem and the two phase material problem.	79
4.5 ϵ_{xx} along the line A-B for the classical first Eshelby problem.	80
4.6 ϵ_{xx} and σ_{xx} along the line A-B for the classical two phases problem.	81

4.7	ϵ_{xx} along the line A-B for different E-FEM formulations with $\beta = 100$ and $\beta = 1000$	82
4.8	Traction test of a two phases bar using SKON formulation in the case of stiffness coefficients $\beta = 10$ and $\beta = 10^6$ ($E_{matrix} = 70$ GPa, $\nu_{matrix} = \nu_{inclusion} = 0$).	83
4.9	Traction test of a three phases bar using SKON formulation in the case of stiffness coefficients $\beta = 10$ and $\beta = 10^6$	84
4.10	Two phases composite problem is treated by SKON with special mesh	85
4.11	$\beta = 10$ with special mesh.	85
4.12	$\beta = 100$ with special mesh.	86
4.13	$\beta = 1000$ with special mesh.	86
4.14	$\beta = 10^6$ with special mesh.	86
4.15	Problem definition: two phases material with imperfect interface. . .	88
4.16	Discontinuous element	88
4.17	Element cut by the interface Γ , approximated interface and integration points in E-FEM.	93
4.18	Convergence analysis for the Eshelby problem with and without surface elasticity for the three methods: E-FEM, XFEM and Interface element.	94
4.19	Convergence analysis of E-FEM for the extended Eshelby problem with different values of α , compared to XFEM results ($\beta = 1$).	95
4.20	ϵ_{xx} along the line A-B for different values of α (E-FEM vs XFEM). .	96
4.21	Size effect in effective plane-strain bulk modulus for circular inclusion ($f = 0.2$, $E_m = 70$ GPa, $E_i = 0.1E_m$, $\nu_m = \nu_i = 0.32$).	97
4.22	Size effect in effective plane-strain bulk modulus for ellipse inclusion ($f = 0.2$, $E_m = 70$ GPa, $E_i = 0.1E_m$, $\nu_m = \nu_i = 0.32$).	97
4.23	Arbitrary shapes	98
4.24	Size effect and shape dependence in normalized effective bulk modulus. $E_m = 10E_i$, $\nu_m = \nu_i = 0.32$, $f = 0.2$	99
4.25	Several samples for 30 randomly distributed nano-inclusions.	99
4.26	Size effect for effective plane-strain bulk modulus with randomly distributed nano-inclusions ($f = 0.3$, $E_m = 70$ GPa, $E_i = 0.1E_m$, $\nu_m = \nu_i = 0.32$; $\lambda_s = 6.842$ N/m, $\mu_s = -0.375$ N/m, corresponding to $k_s = 6.092$ N/m).	100
5.1	Resolution algorithm for standard plasticity model	109
5.2	Computation of final stress from the elastic trial state by radial return mapping algorithm, where total deformation is kept fixed [Ibrahimbegovic, 2009].	111
5.3	Resolution algorithm with E-FEM approach	116

5.4	Deviatoric stress $(\mathbf{dev} \boldsymbol{\sigma})_{II}$ on deformed mesh for different interface parameters under a simple traction test.	118
5.5	Hardening variable ξ for different interface parameters under a simple traction test.	119
5.6	Homogenized elastoplastic effective behavior under a simple traction test.	119
5.7	Integration points turned into plastic phase for different time steps with XFEM and E-FEM for interface set A.	120
5.8	Homogenized elastoplastic behavior for three different radius of nano-inclusion using XFEM, E-FEM or Interface element approach.	121
5.9	Homogenized elastoplastic behavior for different shapes of inclusion.	123
6.1	Contributions of this PhD work	126
6.2	Convergence analysis for the Eshelby problem with a coherent interface and different values of α (XFEM using Eq. (6.1) vs standard XFEM).	128
A.1	Convergence analysis for the Eshelby problem with a circular inclusion	133
A.2	Size effect in effective plane-strain bulk modulus for ellipsoidal inclusion ($a = 2b$, $f = 0, 2$, $E_m = 70$ GPa, $E_i = 0, 1E_m$, $\nu_m = \nu_i = 0, 32$, $\lambda_s = 6.842$ N/m, $\mu_s = -0.375$ N/m).	133

List of Tables

3.1	Results for different size of RVEs treated by the Interface element approach ($f = 0.3$, $E = 70$ GPa, $\nu = 0.32$, $\lambda_s = 6.842$ N/m, $\mu_s = -0.375$ N/m).	62
3.2	Comparison of computational cost (XFEM vs IE).	64
4.1	Comparison of computational cost (XFEM vs E-FEM vs IE).	100
5.1	State and associated variables.	105
5.2	Comparison of computational cost in the case of elastoplastic behavior (XFEM vs E-FEM vs IE).	122

Chapter 1

General introduction

Contents

1.1 Background and motivations	1
1.2 Outline	3
1.3 Notations	4

1.1 Background and motivations

Due to their remarkable mechanical behavior for low reinforcement mass fraction (less than 5%) [Cauvin et al., 2010], nano-reinforced polymers are increasingly used as structural materials. This interest has induced considerable worldwide research on nanocomposites mechanical behavior. Most of these studies focused mainly on experimental processing and characterization or analytical modeling.

One of the main features of nanocomposites compared to conventional composites is the so-called size effect they exhibit: for a given volume fraction of nano-fillers, the (macro) homogenized behavior depends on the size of the fillers. Since standard experimental setups are not able to access the local phenomena arising at the nano or even sub-nano scales, Molecular Dynamic (MD) simulations [Shenoy, 2005, Mi et al., 2008] are often employed to "identify" the model parameters to be used in continuum mechanics based modelization.

One of the biggest challenges for the modeling of these materials lies in taking into account the size effect induced by the nano-fillers on the macroscopic behavior of the material as suggested by several experimental studies (for instance [Reynaud et al., 2001, Cho et al., 2006, Blivi et al., 2016]). This size effect, commonly attributed to local phenomena at the atomic scale, can be interpreted through an increase in the ratio (interface matrix-inclusions)/(volume fraction of inclusions). The influence of the local phenomena on the overall properties of the material can be modeled in the framework of continuum mechanics by an interphase or an imperfect interface

whose properties can be characterized by MD simulation. By adding imperfect interface models or interphase between matrix and inclusion into the homogenization methods, the behavior and effective properties of nanocomposites can be estimated. From the analytical point of view, two different types of approaches are considered: either an interface model with surface elasticity ([Sharma et al., 2003, Duan et al., 2005b, Chen et al., 2007, Quang and He, 2009, Brisard et al., 2010a, Monchiet and Kondo, 2013, Dormieux and Kondo, 2013, Nazarenko et al., 2017]) or an interphase model is taken into account ([Boutaleb et al., 2009, Paliwal et al., 2012, Benveniste, 2013]). The main limitation of all these studies based on analytical developments remains in their restriction to quite simple shapes of inclusions (spheres, cylinders, ...). Moreover, the extension of these developments to non-linear behaviors is not straight forward (very recent nonlinear studies are proposed in [Brach et al., 2017a, Brach et al., 2017b]). The development of dedicated numerical approaches is, therefore, necessary to circumvent all these limitations. However, very few contributions are related to numerical description and implementation of such interface/interphase models in Finite Element codes. These developments are based mainly on the standard Finite element method with the surface-type element as in [Wei et al., 2006] or the eXtended Finite element method (XFEM) in [Yvonnet et al., 2008]. In addition, the evaluation of the efficiency of these two numerical approaches as well as the numerical modelization for nonlinear behavior in the case of nanocomposite are not available.

As mentioned, the weak discontinuities induced by the presence of inclusions can be numerically modeled by XFEM. Nevertheless, another choice can be to consider Embedded Finite Element Method (E-FEM), widely used for the description of strong discontinuities. Even if this approach has the potential to handle the weak discontinuity, its application in the numerical homogenization is quite limited. We can found several works that couple weak and strong discontinuities in the E-FEM framework as in [Hautefeuille et al., 2009, Benkemoun et al., 2010, Roubin et al., 2015, Idelsohn et al., 2017]. However, the evaluation of the performance as well as the level of accuracy of this method in handling weak discontinuities (in the context of the homogenization of the macroscopic properties) has never been performed.

To the best of our knowledge, XFEM and E-FEM are two of the most efficient tools for handling discontinuities on structured meshes (unfitted meshes). Compared to the global kinematic enrichment of XFEM, the local enhancement of E-FEM separately handles the local equilibrium of the interface and the global equilibrium. As in the coherent interface model, the interface equilibrium is locally governed by the Young-Laplace equation, E-FEM seems well adapt in this context. Keeping this idea in mind, an E-FEM strategy seems very promising for modeling homogenized behavior of nanocomposites including nanoreinforcement size effect.

From these motivations, the objectives of this PhD work are summarized as

follows:

- Compare the efficiency of the two existent numerical approaches numerical approaches found in the literature namely XFEM and Interface element;
- Evaluate the E-FEM formulations for numerical homogenization;
- Develop a numerical approach in the context of E-FEM to take into account the interface effect on homogenized properties in the case of nanoreinforced materials;
- Extend the numerical approaches to handle nonlinear behaviors of the nanocomposites constituents.

1.2 Outline

The outline of this thesis is as follows:

In chapter 2, we firstly give a general introduction about nanocomposite material as well as the interesting size effect they exhibit. The experimental evidence and the explanation of this effect from the atomistic/molecular point of view are then presented. Before reporting on the state of the art in this domain, the notion of interphase and interface which are needed for the vast majority of models and simulations are defined. Next, we present different types of studies that deal with the size effect observed in nanocomposites. They are ranging from the very fine-scales (atom, nano) with Molecular Dynamic simulation to the continuum mechanical scales (micro, macro) with the analytical and numerical micromechanical models. To end the chapter, the principal hypothesis and the main equations needed for the problem in hand are presented.

In chapter 3, we present a comparative study of the performance of the Interface element approach and XFEM/level set approach in modeling the size effect. For a fair comparison, these two approaches are implemented in the same framework, considering the same element topology. After validation of the implemented strategies, we investigate, in particular, the influence of the homogenization hypothesis in terms of boundary conditions and random microstructure on the computed effective mechanical properties. The comparison of the convergence analysis and the computation of effective mechanical properties give an evaluation of the two studied approaches and provides a good basis to elaborate a new numerical computation method.

In chapter 4, a new numerical approach based on the Embedded Finite Element Method (E-FEM) is elaborated in order to model size effect of nanocomposites. For this purpose, a performance comparison of three formulations of E-FEM in the case of weak discontinuity is performed. Based on its good performance, the E-FEM standard Statically and Kinematically Optimal Nonsymmetric (SKON) formulation

is chosen to incorporate a surface elasticity at the interface between the matrix and the inclusions. The results obtained with the proposed approach for a couple of problems are confronted to those obtained with analytical solutions and with the Interface element approach.

In chapter 5, the numerical models presented in the previous chapters are used in the context of non-linear behavior. A von Mises type elastoplastic law with linear isotropic hardening is considered for the bulk while the interface is considered as linear elastic. The implicit backward Euler integration scheme and the return mapping algorithm have been used. Results on the homogeneous nonlinear behavior on the deviatoric part of the stress and strain obtained from the three different numerical approaches are then presented and compared.

Finally, conclusions and perspectives are drawn in chapter 6.

1.3 Notations

- Tensors and vectors

a	Scalar	\mathbf{a}	Vector
\mathbf{A}	Second order tensor	\mathbb{A}	Fourth order tensor
\mathbf{I}	Second order identity tensor	\mathbb{I}	Fourth order identity tensor
\mathbf{n}	Normal vector	\mathbf{P}	Projector operator onto interface
$\mathbf{a} \cdot \mathbf{b} = a_i b_i$		$\mathbf{A} : \mathbf{B} = A_{ik} B_{ki}$	
$\mathbf{A} \cdot \mathbf{b} = A_{ij} b_j$		$\mathbb{A} : \mathbf{B} = A_{ijkl} B_{lk}$	
$\mathbf{A} \cdot \mathbf{B} = A_{ik} B_{kj}$		$\mathbf{a} \otimes \mathbf{b} = a_i b_j$	

- Mathematical symbols

$\llbracket \{\bullet\} \rrbracket$	Jump of a quantity $\{\bullet\}$ over the interface.
∇	Gradient operator
∇^s	Symmetric gradient operator
∇_s	Surface gradient operator
∇_s^s	Symmetric surface gradient operator
div	Divergence operator
div_s	Surface divergence operator
dev	Deviatoric part
\mathcal{K}	Curvature tensor
$\{\dot{\bullet}\}$	Derivative with respect to the time of a quantity $\{\bullet\}$

- Mechanical symbols

λ, μ	Lame's constants of the bulk
λ_s, μ_s	Lame's constants of the interface

\mathbf{u}	Displacement field in the bulk
\mathbf{a}	Additional degree of freedom vector
ψ	Enrichment function in XFEM
\mathbf{u}_s	Displacement field on the interface
$\boldsymbol{\epsilon}$	Infinitesimal strain tensor in the bulk
$\boldsymbol{\epsilon}_s$	Infinitesimal strain tensor on the interface
$\boldsymbol{\gamma}$	Enhanced strain tensor in the bulk
$\boldsymbol{\gamma}_s$	Enhanced strain tensor on the interface
\mathbf{M}	Enhanced shape function in E-FEM
$\boldsymbol{\sigma}, \boldsymbol{\sigma}_s$	Cauchy stress tensor in the bulk and on the interface
\mathbb{C}	Fourth order elastic tensor
\mathbb{C}^s	Fourth order surface/interface elastic tensor
\mathbb{C}^{ep}	Consistence elastoplastic tangent tensor
K	Hardening modulus
ξ	Hardening variable
f	Yield function
σ_y	Elastic limit stress
q	Stress-like variable associated to the hardening variable
\mathcal{D}	Plasticity dissipation
γ	Lagrange plastic multiplier
$\boldsymbol{\zeta}$	Plastic flow direction
$\{\bullet\}^{trial}$	Trial values of variable $\{\bullet\}$
$\Delta \mathbf{u}$	Incremental displacement

- Abbreviations

FEM	Finite Element Method
MD	Molecular Dynamics
RVE	Representative Volume Element
MTM	Mori-Tanaka Model
GSCM	Generalized Self-Consistence Method
CCA	Composite Cylinder Assemblages
HS	Hashin-Shtrickman bounds
IE	Interface Element approach
XFEM	eXtended Finite Element method
E-FEM	Embedded Finite Element method
KUBC	Kinematic Uniform Boundary Condition
SUBC	Stress Uniform Boundary Condition
PBC	Periodic Boundary Condition
EAS	Enhanced Assumed Strain
SOS	Statically Optimal Symmetric

KOS	Kinematically Optimal Sysmetric
SKON	Statically and Kinematically Optimal Non-symmetric
d.o.f	Degree of freedom

Chapter 2

Size effect in nanocomposite materials: state of the art

In this chapter, we first give a general introduction about nanocomposite material as well as its interesting size effect. The experimental evidence and the original explanation of this effect from the atomistic/molecular point of view are then presented. Before a brief review of the studies and the results obtained in this domain, the notion of interphase and interface needed for the vast majority of models and simulations is defined. Next, we present different types of studies that deal with the size effect of nanocomposites. They are ranging from the very fine-scales (atom, nano) with Molecular Dynamic simulation to the continuum mechanical scales (at the micro and the macro scales) with the analytical and numerical micromechanical models. In order to account for the size effect in nanocomposites, the problem we consider in this Ph.D. thesis with its principal assumptions and main equations is introduced.

Contents

2.1	Introduction	8
2.1.1	Nanocomposite and its size effect	8
2.1.2	Size effect: Experimental evidence	11
2.2	Interphase or interface?	13
2.3	Molecular dynamics simulations	16
2.4	Analytical models	18
2.4.1	Eshelby's problem with interface effect	19

2.4.2	Generalized Mori-Tanaka model and Generalized self-consistent method for spherical inclusion	20
2.4.3	Composite cylinder assemblages model and Generalized self-consistent model for cylindrical inclusion	21
2.4.4	Generalized Voigt and Reuss bounds	22
2.4.5	Generalized Hashin-Shtrikman lower bound	23
2.4.6	Comparison and conclusions on analytical models	24
2.5	Numerical models based on FEM	25
2.5.1	Surface/interface element in standard FEM	26
2.5.2	XFEM/level set approach	28
2.5.3	Other promising methods: Cut-FEM, Embedded-FEM	30
2.5.4	Conclusion on numerical approaches	31
2.6	Homogenization problem with coherent interface model	31
2.6.1	Basic elements of differential geometry for surface	32
2.6.1.1	Projection operators	32
2.6.1.2	Superficial (surface) fields	32
2.6.1.3	Surface gradient, surface divergence	33
2.6.2	Problem of composite material with coherent interface	34
2.6.2.1	Equilibrium equations and boundary conditions	35
2.6.2.2	Constitutive equations for the bulk and the interface	36
2.7	Conclusion	37

2.1 Introduction

2.1.1 Nanocomposite and its size effect

A nanocomposite is a composite material whose particularity is to be composed of at least one constituent with one or more nanoscopic dimensions (less than 100 nm). The nanoscopic scale lies between the usual microscopic scale and that of the molecules. Nanocomposites can be classified according to the type of reinforcements, namely particles (spherical), fiber and platelets (see Figure 2.1).

The challenge with the nanocomposites stands in accounting for the specificities of their microstructure or even "nanostructure" on their macroscopic behavior in order to express their constitutive laws. Because of the nanometric size of their reinforcements, multi-scale modeling approaches have to be adapted in order to predict the nanocomposite behavior integrating the phenomena occurring at nano

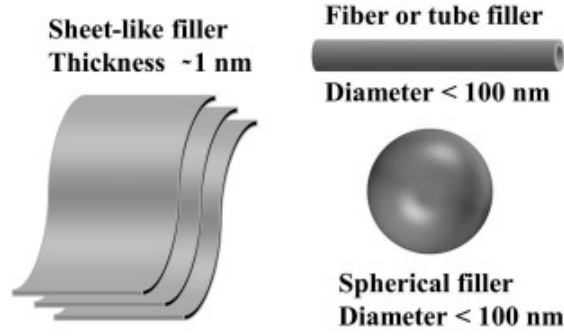


Figure 2.1: Different reinforcement morphologies of nanocomposites [Fu et al., 2019].

or sub-nano scales. As illustrated in Figure 2.2, the smallest scale that can be considered the multiscale model stands in a quantum description of materials based on molecular mechanics or molecular dynamics.

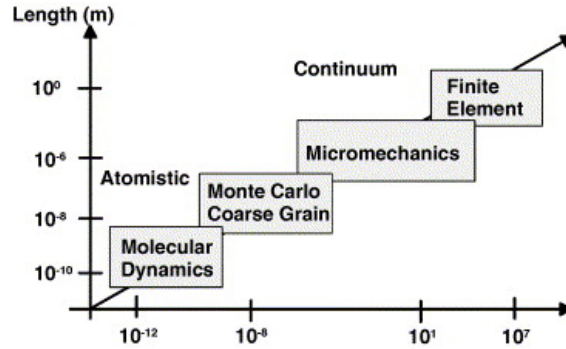


Figure 2.2: Range of length and time scales of the multi-scale methods for nanocomposite materials [Gates et al., 2005].

Nanocomposite materials are increasingly used in industry due to the improvements they offer compared to conventional composites. They are widely used in the aerospace and automotive industries [Bogue, 2011, Gu et al., 2016, Kausar et al., 2017, Naskar et al., 2016] where improving the performance of structures combined with their lightness are daily challenges. Nanocomposites require less fillers (less than 10 % by weight) and offer higher performance than conventional composites [Blivi, 2018]. Besides their mechanical properties improvement, other interesting properties such as thermal, electrical, optical, fire resistance, gas barrier, etc are also enhanced. In the scope of this thesis, we focus on the mechanical properties of the material.

The size effect observed on those materials at least on the mechanical behavior is one of the most attractive characteristics of this kind of materials: for a given volume fraction of inclusions, the physical (mechanical) properties depend on the size of the inclusions. This size effect, commonly attributed to local phenomena at the atomic scale, can be interpreted through an increase in the ratio (interface/surface matrix-inclusions) / (volume).

Streitz et al [Streitz et al., 1994] showed, by molecular dynamics simulations, that the stresses present at the surface of a material or at the interface between two bodies can cause a displacement of the equilibrium position of the atoms present in this zone compared to those further away from the borders or the interfaces. This modification in interatomic distances affects the elastic properties of objects of nanoscopic dimensions. Indeed, the atoms on the surface or the interface of solid bodies are, in an environment different from those located in the volume of the material and their equilibrium position and their energy are in general different from those of the atoms located far from interfaces, the properties of a solid being related to the position and energy of the constituent atoms.

In a body in which the number of surface atoms is relatively small to the total number of atoms, the properties of the surface atoms (different from those of the other atoms) will not significantly modify the overall properties of the body and can be neglected. This is the case with classical composites. However, compared to conventional composites, nanocomposites have a high interfacial surface ($10^8 \text{m}^2/\text{m}^3$, [Marceau, 2003]). As shown in Figure 2.3, the matrix/inclusion interface area is approximately 1000 times greater for nanocomposites than for conventional composites and therefore, the phenomena taking place at the interface zones (causing size effect) are no longer negligible.

Number of particles (N)	Radius/ nm (single object)	Total Surface Area/ m^2	Specific Surface m^2/g
1	47.7×10^6	2.9×10^{-2}	2.9×10^{-5}
10^1	22.1×10^6	6.2×10^{-2}	6.2×10^{-5}
10^2	10.3×10^6	1.3×10^{-1}	1.3×10^{-4}
10^3	4.77×10^6	2.9×10^{-1}	2.9×10^{-4}
10^{12}	4.77×10^3	2.9×10^2	2.9×10^{-1}
10^{21}	4.77	2.9×10^5	2.9×10^2
Assumptions: i) each particle is spherical ($V = [4\pi r^3]/3$); ii) 1 kg silica; iii) ($\rho = 2.2 \text{ g/cm}^3$) Hence: the mass of single particle can be found by dividing 1 kg by N. The surface area of a particle can be determined ($A_p = 4\pi r^2$) and the total surface area of the volume (A_v) is then $N \cdot A_p$. The specific surface area is then $A_v/1000$, to give an area in m^2/g . 290 m^2 is several times the floor area of an average house, for example.			

Figure 2.3: – Surface area as a function of particle size [Jesson and Watts, 2012].

The smaller the inclusion size, the greater the surface area of interface matrix/inclusion and the impact of the interface effect becomes more obvious. As a consequence, the macroscopic mechanical properties depend not only on the volume fraction but also on the size of the inclusions. To illustrate this dependence, exper-

imental evidence of the size effect in nanocomposites will be presented in the next subsection.

2.1.2 Size effect: Experimental evidence

In the experimental point of view, the effect of the size of the inclusions in nanocomposite has been shown in several studies [Douce et al., 2004], [Mishra et al., 2005], [Cho et al., 2006], [Blivi et al., 2016], [Blivi, 2018].

In their work, Douce et al [Douce et al., 2004] and Mishra et al [Mishra et al., 2005] measured the Young modulus of a Polysiloxane reinforced by silica nanoparticles and of a Polypropylene reinforced by calcium carbonate (CaCO_3) nanoparticles, respectively, for different sizes and volume fractions of inclusions. As shown in Figure 2.4, for a given volume fraction of reinforcements, an increase of the Young modulus is observed when the particles size decrease.

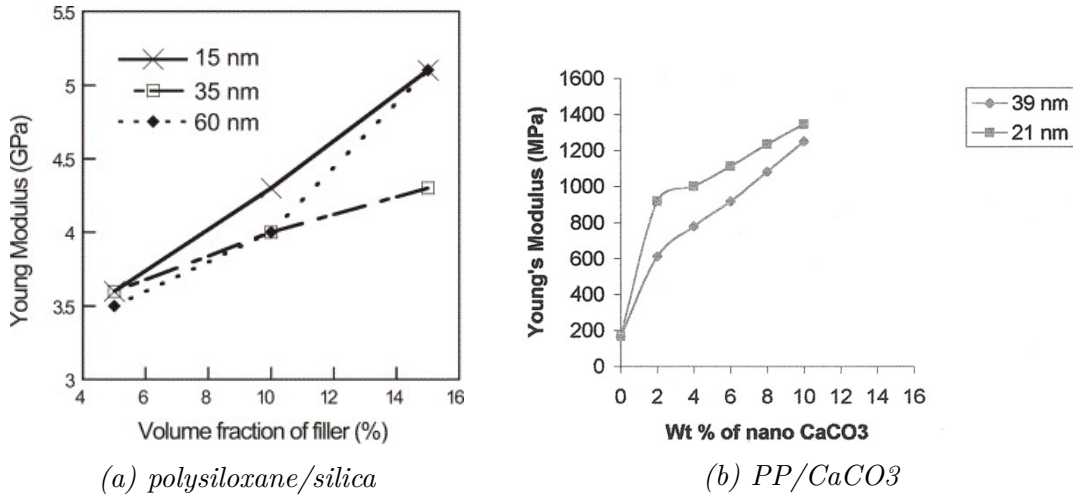


Figure 2.4: Evolution of Young's modulus versus volume fraction for different particle sizes in (a) [Douce et al., 2004] and (b) [Mishra et al., 2005].

To highlight this size effect of the reinforcements, Cho et al [Cho et al., 2006] performed a more complete study of a nanocomposite made of vinyl ester resin reinforced by alumina nanoparticles. For fixed volume fraction (1% and 3%) of nanoreinforcements, different sizes of particles varied from macro (0.5 mm) to nano (15 nm) scale were considered. As can be emphasized in Figure 2.5a, a size effect is clearly observed with the particles are smaller than $1 \mu\text{m}$, the Young's modulus of the material increasing with a decrease of the particle sizes, while the Young's modulus is not affected by the size of the particle, when they are bigger than $1 \mu\text{m}$. In addition to its elastic behavior, Cho et al studied the material response during tensile tests and, as shown in Figure 2.5b, the behavior is clearly impacted by the size of the particle.

More recently, the experimental works of Blivi et al [Blivi et al., 2016], [Blivi, 2018] focused on the study of the size effect of PMMA/silica nanocomposites. As

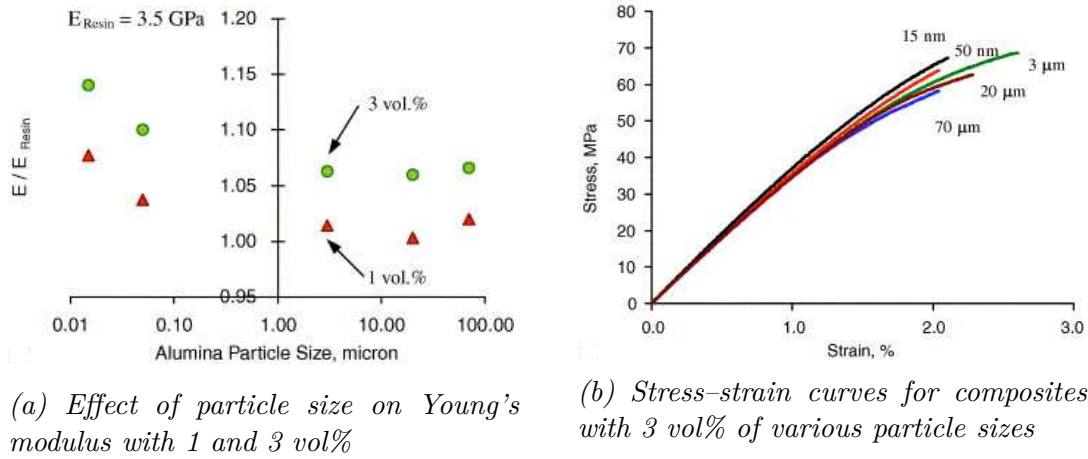


Figure 2.5: Particle size effect on alumina nanoparticles composites in [Choi et al., 2006]

presented in Figure 2.6, with constant volume fractions on inclusions, fixed at 4% and 8%, Young's modulus increase when particle diameter decrease. In their study, they observed a similar effect of the particle size on the viscoelastic mechanical properties (glass transition and degradation temperatures).

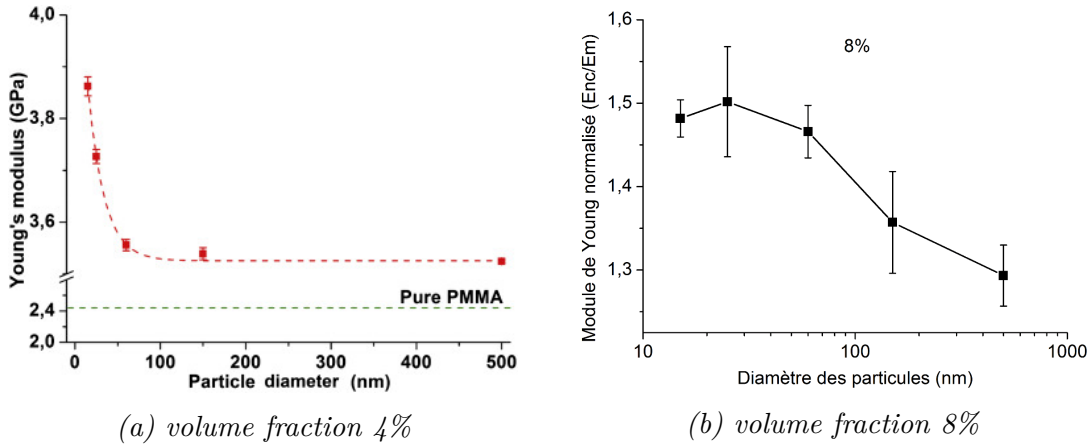


Figure 2.6: Particle size effect on PMMA/silica nanocomposites Young's modulus in (a) [Blivi et al., 2016] and (b) [Blivi, 2018].

Even experimental based research seems to be the best way to observe the size effect and ideally determine the relationships between micro/nano-structure and properties of nanocomposites, the development of models and theories that interpret and predict the observed behavior under the corresponding conditions is still essential in the material research process. In order to further study the size effect and to report from a theoretical point of view (from the point of view of modeling), different tools and strategies on different scales can be considered. These tools and strategies range from the fine scales (atom, nano) with Molecular Dynamics Simulation to bigger scales (micro, meso, and macro) where the continuum mechan-

ics is applicable. Before getting into these methods, the notions of interphase and interface should be clarified, they are introduced in the next subsection.

2.2 Interphase or interface?

An interface, in a simple way, is the point (line, curve, surface) at which the matrix ends and the reinforcement begins. Thus, in the Finite Element Method (FEM) or micro-mechanical models, an interface is typically modeled with at least one zero-dimensional terms. More specifically, the interface can be described as the boundary between two different chemical and/or microstructure layers. However, such boundaries rarely have no chemical or atomic interaction, and therefore a region, called interphase, can be defined as the volume of material affected by the interaction at the interface. A three-dimensional interphase will lead to a gradation of properties from one phase to another rather than the abrupt change necessitated by the acceptance of a two-dimensional interface. In [Drzal et al., 1983], the author offered the following definition of the interphase:

"The interfacial region (i.e. the interphase) is the region beginning at the point in the fiber at which the properties differ from those of the bulk filler and ending at the point in the matrix at which the properties become equal to those of the bulk matrix. The chemistry, polymer chain mobility, degree of cure and crystallinity are likely to be altered in that region. . . "

In order to model the size effect in the nanocomposite, the different properties (or energy of atoms as presented previously) in the interaction zone needs to be taken into account via an interface or interphase. In the context of nanocomposites and in the point of view of modelization, the use of the interphase requires a very fine scale to be able to capture the gradient of the fields in the direction of thickness, which is only a few nanometers or even a few angstroms. Hence, the interphase concept is appropriate for the simulation methods at the atomistic scale like the Molecular Dynamics simulation. On the other hand, the interface concept is often used for the continuum mechanical scale (micromechanical models, FEM) where the effects of the interaction zone on the mechanical fields are described via an imperfect interface. The interface models have the advantage to avoid the mathematical and mechanical complexity due to the size of interphase. Depending on the different impact on the mechanical fields, the imperfect interface models are divided into three main categories (see Figure 2.7): cohesive interface, coherent interface and general interface. These interface models describe the discontinuity induced by the interaction zone on the displacement field or the stress field or both of them.

Among these models, the most widely used are the coherent interface model and the spring-layer model. These two models were derived by using the asymptotic approach on a very thin region (interphase) [Bövik, 1994, Benveniste, 2006]. According

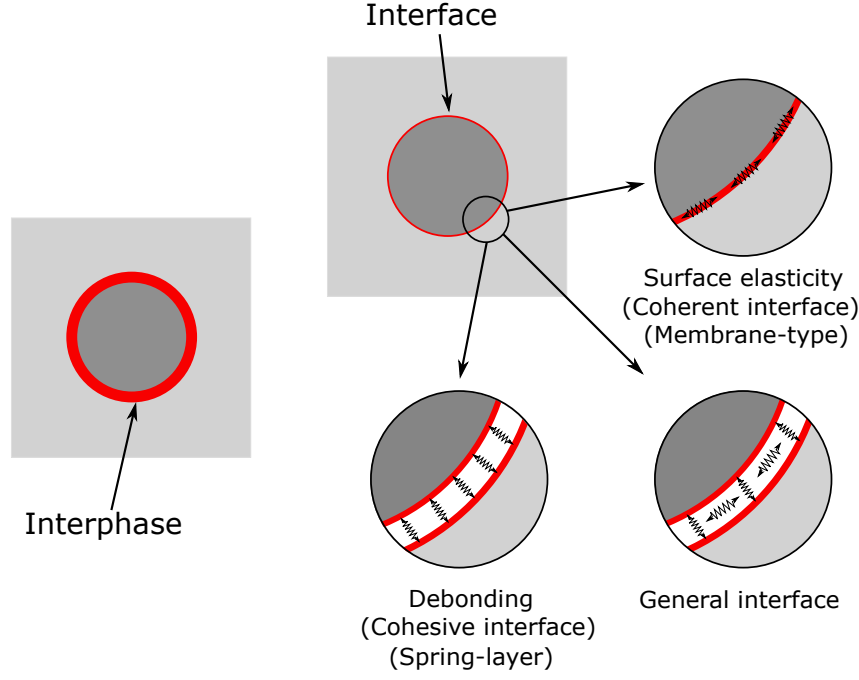


Figure 2.7: Interphase and interface models.

to the linear spring-layer model, the traction vector is continuous across an interface while the displacement vector across the interface suffers a jump related to the traction vector (debonding). This model is derived for interphases much softer than the bulk phases and is often used to describe the decohesion of matrix/inclusion. On the contrary, the coherent interface model prescribes that the displacement vector is continuous while the traction vector is discontinuous across the interface. In this context, the Hadamard relation [Hill, 1961] (see Eqs. (2.49)) implies that the gradient of displacement suffers a jump along the direction normal to the interface but is continuous in the plane tangent to the interface. Besides, the traction vector jump and the surface stress are related by the generalized Young-Laplace equation [Povstenko, 1993, Chen et al., 2006] (see Eq. (2.1)), which describes the static equilibrium of the interface. Another ingredient of the coherent interface model is that the surface stress and surface strain tensors obey a two-dimensional surface linear elasticity law (see Eq. (2.7)).

- Generalized Young-Laplace equation

$$[[\boldsymbol{\sigma}]] \cdot \mathbf{n} + \mathbf{div}_s \boldsymbol{\sigma}_s = \mathbf{0} , \quad (2.1)$$

where $\boldsymbol{\sigma}_s$ is the surface stress tensor, $\boldsymbol{\sigma}$ denotes the bulk Cauchy stress and \mathbf{n} is the normal vector to the interface.

The surface divergence \mathbf{div}_s is defined as:

$$\mathbf{div}_s \{\bullet\} = \nabla \{\bullet\} : \mathbf{P} \quad (2.2)$$

with

$$\mathbf{P} = \mathbf{I} - \mathbf{n} \otimes \mathbf{n} , \quad (2.3)$$

where \mathbf{P} is the projection operator and \mathbf{I} is the second order identity tensor.

- Principle of the surface elasticity

Historically, the notion of surface or interface stress in solid bodies has been introduced by Gibbs [Gibbs, 1906] and its development continued during the last century. We can cite in particular the works of [Shuttleworth, 1950], [Eyring, 1954], [Orowan, 1970], [Camarata, 1994], [Fried and Gurtin, 2007], [Gu, 2008] and [Hamilton and Wolfer, 2009]. The surface stresses can be defined in different ways. Gurtin et al. [Gurtin et al., 1998] bind them to tangential deformations in the solids, these deformations being different in the two solids located at the interface. From a physical point of view, the stress on the surface of the inclusion $\boldsymbol{\sigma}_s$ is related to the residual stress τ_0 present on the surface and to the surface energy γ existing on the interface matrix/inclusion. This surface stress $\boldsymbol{\sigma}_s$ can be defined through Shuttleworth's equation [Shuttleworth, 1950]:

$$\boldsymbol{\sigma}_s = \tau_0 + \frac{\partial \gamma(\boldsymbol{\epsilon}_s)}{\partial \boldsymbol{\epsilon}_s} , \quad (2.4)$$

where $\gamma(\boldsymbol{\epsilon}_s)$ is the surface-strain energy, and $\boldsymbol{\epsilon}_s$ is the surface strain, defined as (see Gurtin and Murdoch [Gurtin and Ian Murdoch, 1975]):

$$\boldsymbol{\epsilon}_s = \mathbf{P} \cdot \boldsymbol{\epsilon} \cdot \mathbf{P} , \quad (2.5)$$

In the case of isotropic surface, Eq. (2.4) can be written as:

$$\boldsymbol{\sigma}_s = \tau_o \mathbf{I} + 2(\mu_s - \tau_o) \boldsymbol{\epsilon}_s + (\lambda_s + \tau_o) \text{tr}(\boldsymbol{\epsilon}_s) \mathbf{I} , \quad (2.6)$$

where μ_s and λ_s are Lamé's constants characterizing the interface Γ .

In the absence of τ_o , Bottomley and Ogino [Bottomley and Ogino, 2001] proposed a linear relation between the surface stress tensor $\boldsymbol{\sigma}_s$ and the surface strain tensor $\boldsymbol{\epsilon}_s$:

$$\boldsymbol{\sigma}_s = \mathbb{C}^s : \boldsymbol{\epsilon}_s , \quad (2.7)$$

where \mathbb{C}^s is the surface elastic stiffness tensor.

For the isotropic surface and in absence of τ_o , Eq. (2.6) becomes:

$$\boldsymbol{\sigma}_s = 2\mu_s \boldsymbol{\epsilon}_s + \lambda_s \text{tr}(\boldsymbol{\epsilon}_s) \mathbf{I} , \quad (2.8)$$

This surface elasticity represents the mechanical behavior of the interface and can be considered as the constitutive law of the material at the interface. By considering this surface elasticity, the energy of the surface can be taken into account to provide

the contribution of the interface to the effective properties of the material.

The interphase and interface concepts have been widely used in the context of solid and fluid mechanics. In this Ph.D. thesis work, we focus on the use of these concepts to model the size effect of nanocomposites. In the following of this chapter, we will present the different methods which allow accounting for the size effect. Let's start from the finest scale with the Molecular Dynamic Simulation.

2.3 Molecular dynamics simulations

Molecular dynamics (MD) is a computer simulation method for studying the physical movements of atoms and molecules. It allows simulating the behavior of materials at the atomic scale by providing information on the structure and mobility of the system made of atoms or molecules. On the other hand, the size of the studied systems is quickly restricted by their complexity. In the framework of nanocomposites, MD simulation makes it possible to account for the behavior of inclusions/matrix assemblies at the atomic scale and, thus, to better understand the particle/matrix interaction. More generally, MD is a predictive tool for the behavior of materials at the atomic structure scale. The studied system is represented by the atoms or the molecules that constitute it, as well as by all the interactions between these different atoms or molecules and the forces applied to the system.

The molecular dynamics simulation requires the definition of interaction forces between matrix and inclusions. These interaction forces have never been measured and are considered as deriving from an empirical potential (classical molecular dynamics) or calculated from the first principles of quantum mechanics (*ab initio*). Besides, one of the main features of MD simulation is that the number of atoms being simulated needs to be big enough to capture the mechanical fields of interest at the macro scale of continuum mechanics and therefore intensively arise the computational cost of the simulation.

To reduce the expensive cost, in the DM studies on nanoparticles, the nanoparticle are generally considered as a hard-sphere (non-deformable) [Brown et al., 2003], [Adnan et al., 2007] (see Figure 2.8). This kind of assumptions is very efficient from the point of view of the gain in computational time but lacks the mechanical contribution of the inclusion. Another way for dealing with the cost of MD is to cooperate with the micromechanical modeling. In that case, MD is used to provide the information of the interaction zone (interphase, interface, surface) where continuum mechanics is not valid. The information related to mechanical properties or dimensions of the interaction zone is then updated to the micromechanical approaches at bigger scales (micro, macro). At the boundary between Molecular Dynamics and micromechanical modeling, we can note the work of Odegard et al. [Odegard et al., 2005] on the simulation of polyamides matrix with silica nanoparticles. The

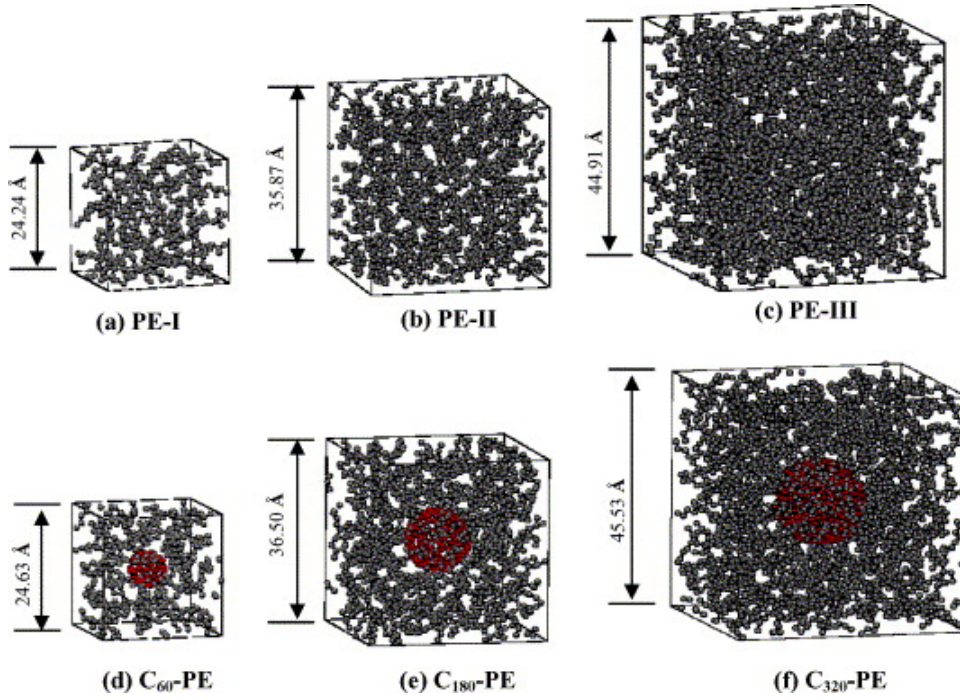


Figure 2.8: Periodic box of different neat and nanocomposites model used for molecular dynamic simulation in [Adnan et al., 2007] with non-deformable spherical inclusion.

micromechanics model includes an effective interface between the polyamides and nanoparticle with properties and dimensions that are determined using the results of molecular dynamics simulations. Similarly, from the perspective of the micromechanical models, it is possible to account for the local phenomena via the interface or interphase model, and the parameters of these interfaces/interphases can be obtained from MD simulations. For example, Shenoy [Shenoy, 2005] and Mi et al [Mi et al., 2008] used MD to calculate the surface elastic constants (surface stress and surface stiffness) needed for the surface elasticity theory [Gurtin and Ian Murdoch, 1975] (presented in the previous section). These surface elastic constants are widely used in the analytical and numerical approaches in which the coherent interface model with the surface elasticity is employed.

As discussed in the previous section, since the scale of interest for MD simulation is very fine (atomic scale), the interphase concept is often chosen to represent the interaction zone [Brown et al., 2003], [Brown et al., 2008], [Paliwal et al., 2012]. The thickness and mechanical properties of the interphase could be determined by coupling the MD simulation and a (semi-)analytical homogenization schemes. For example, with the introduction of constant thickness interphase between matrix and inclusion, Marcadon et al [Marcadon et al., 2013] presented a confrontation between MD simulations and the improved dilute coated inclusion (IDCI) model [Marcadon et al., 2007] to investigate particle size effects of polymer nanocomposites. In this study, the MD simulation allows to observe and determine the thickness of the

interphase. The moduli obtained from MD simulation are then fitted to the IDCI model to deduce the mechanical properties of the interphase.

Beside cooperating to a micromechanical model, several MD studies consider the elastic properties of the interface/interphase as stochastic variables [Yu et al., 2009], [Vu-Bac et al., 2014], [Le et al., 2016]. For instance, Le et al [Le et al., 2016] proposed to build, based on results arising from MD simulations, a random field model for the elastic properties of the interphase region surrounding the silica nanoscopic inclusion. However, the use of stochastic models is often accompanied by Monte Carlo simulations resulting in large computational costs.

The MD simulation plays a very important role in multiscale methods. It is the main tool for investigating the local phenomena at the atomic/nanoscale level and to calculate the properties of the interface/interphases needed in the approaches at bigger scales (homogenization schemes, FE simulations,...). In the next section, several micromechanical models are presented. These models investigate the size effect by taking into account the imperfect interface between matrix and inclusions.

2.4 Analytical models

In terms of analytical works, several forms of micromechanical models (homogenization) have been extended to take into account the size effect in the nanocomposites through the introduction of an imperfect interface between the matrix and the inclusions. Except for a few studies [Marcadon, 2005], [Marcadon et al., 2007], the interphase concept is rarely used in the analytical studies due to the ratio between the size of the inclusions and the size of the interphase. Indeed, inclusions and interphase sizes are on the same scale (nanoscopic), and the overall mechanical properties depend not only on the size of the inclusion but also on the size and the mechanical properties of the interphase. Instead of using the interphase concept with all the complexity related to its characterization, homogenization schemes with interface effect offers a particularly interesting alternative. Indeed, the results obtained from the use of the interface concept involve only the shape of the reinforcements, their dimensions, and constitutive laws at their interface with the matrix.

Interface effects affect the effective properties of composite materials by modifying average stresses (and strain) in the inclusions and the matrix. The effective modulus of a composite with consideration of interface effects can be estimated using micromechanical models, provided that appropriate modifications are made to take into account the jumps of displacement (spring-layer model) and/or stress (coherent interface model) at the interfaces. As already mentioned, this Ph.D. work focuses on the prediction of the mechanical behavior of nanocomposite including the size effect due to the nanoscopic inclusions. In that case, we need to implement the imperfect interface models presented previously into the micromechanical model.

With the introduction of the surface stress and the surface elasticity, the coherent interface model turns out to be suitable for the micromechanical approaches to investigate the interface effect as well as the size effect in nanocomposites. There exists today an extensive literature on the generalized form of the micromechanical approaches in which the coherent interface model is incorporated in order to account for the interface effect. Few of them, are presented in this section: Eshelby's problem with interface effect, Generalized Mori-Tanaka model, Generalized self-consistent method, Generalized Voigt and Reuss bounds and Generalized Hashin-Shtrikman bounds.

2.4.1 Eshelby's problem with interface effect

Despite researches dating back to 1950 [Shuttleworth, 1950, Gurtin and Ian Murdoch, 1975], the concept of surface/interface stress is first considered in elastic micromechanical models in [Sharma et al., 2003, Sharma and Ganti, 2004] (the erratum of these articles is published in [Sharma and Ganti, 2005, Sharma et al., 2006]). These studies dealt with Eshelby's problem in which a surface elasticity on the interface between matrix and inclusion is introduced.

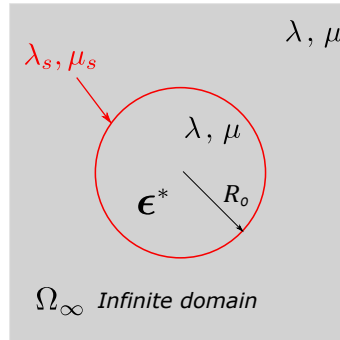


Figure 2.9: First Eshelby problem with coherent interface.

In their study, Sharma et al [Sharma and Ganti, 2004] presented the analytical solution of a cylindrical/spherical inclusion with interface effect subjected to a uniform dilatational eigenstrain in an infinite medium (see Figure 2.9). Although they did not provide the complete Eshelby tensor expression for this case, the exact deformation fields have been presented for

- Spherical inclusion (in spherical coordinates):

$$\varepsilon_{rr}(r) = \varepsilon_{\theta\theta}(r) = \varepsilon_{\phi\phi}(r) = \frac{3\kappa\varepsilon^* - 2\tau_o/R_o}{4\mu + 3\kappa + 2\kappa^s/R_o} \mid r < R_o \quad (2.9)$$

$$\varepsilon_{rr}(r) = - \left[\frac{3\kappa\varepsilon^* - 2\tau_o/R_o}{4\mu + 3\kappa^M + 2\kappa^s/R_o} \right] \frac{2R_o^3}{r^3} \mid r > R_o \quad (2.10)$$

$$\varepsilon_{\theta\theta}(r) = \varepsilon_{\phi\phi}(r) = \left[\frac{3\kappa\varepsilon^* - 2\tau_o/R_o}{4\mu + 3\kappa + 2\kappa^s/R_o} \right] \frac{R_o^3}{r^3} \mid r > R_o, \quad (2.11)$$

where R_o is the radius of the inclusion, $\kappa = \lambda + 2\mu/3$ is the bulk modulus of the medium (λ and μ are the bulk Lamé's constants), $\kappa^s = 2(\lambda^s + \mu^s)$ is the surface modulus (λ^s and μ^s are the surface Lamé's constants) and ε^* is the dilatational eigenstrain prescribed in the inclusion with $\varepsilon^* = \varepsilon_{11}^* = \varepsilon_{22}^* = \varepsilon_{33}^*$.

- Cylindrical inclusion (in cylindrical polar coordinates):

$$\varepsilon_{rr}(r) = \varepsilon_{\theta\theta}(r) = \frac{3k\varepsilon^* - \tau_o/R_o}{2\mu + 3k + \kappa_s/R_o} \mid r < R_o \quad (2.12)$$

$$\varepsilon_{rr}(r) = - \left[\frac{3k\varepsilon^* - \tau_o/R_o}{2\mu + 3k + \kappa_s/R_o} \right] \frac{R_o^2}{r^2} \mid r > R_o \quad (2.13)$$

$$\varepsilon_{\theta\theta}(r) = \left[\frac{3k\varepsilon^* - \tau_o/R_o}{2\mu + 3k + \kappa_s/R_o} \right] \frac{R_o^2}{r^2} \mid r > R_o \quad (2.14)$$

$$\varepsilon_{rr}(r) = 0, \quad (2.15)$$

where $k = 2(\lambda + \mu)/3$ is the plane strain bulk modulus, $\kappa_s = \lambda^s + 2\mu^s$ is the plane strain surface modulus, and the dilatational eigenstrain is $\varepsilon^* = \varepsilon_{11}^* = \varepsilon_{22}^*, \varepsilon_{33}^* = 0$.

In these extensions of Eshelby's problem, the stress fields in the spherical/cylindrical inclusion were found to be uniform under the considered dilatational eigenstrain and hydrostatic remote loading conditions. Duan et al [Duan et al., 2005a] derived the complete Eshelby tensor and stress concentration tensor in the inhomogeneity and showed that those tensor are, in general, not uniform. They used their results for accounting for interface effects in the Generalized Mori-Tanaka model and the Generalized self-consistent method.

2.4.2 Generalized Mori-Tanaka model and Generalized self-consistent method for spherical inclusion

Compared to the dilute scheme [Eshelby, 1957] that link average stress in the inclusion to the macroscopic stress, the basic idea of Mori-Tanaka method (MTM) [Mori and Tanaka, 1973] is to relate the average stress in the inclusion to the average stress in the matrix. Hence, in the context of spherical inclusion, in the Mori-Tanaka model, spherical inclusion with radius R_0 is embedded in an infinite matrix subjected to an imposed remote field equal to the average stress (strain) field in the matrix of the composite (see Figure 2.10a).

The generalized self-consistent method (GSCM) [Christensen and Lo, 1979] has been developed from the composite sphere assemblage model (CSA) [Hashin, 1962]. GSCM is a three-phase model in which a spherical inhomogeneity (of radius R_0) with a matrix shell (of radius R_1) is embedded in an infinite effective medium and the boundary conditions are specified at infinity (see Figure 2.10b).

Duan et al [Duan et al., 2005b] extended Mori-Tanaka model and GSCM by incorporating surface elasticity in the estimations of the effective bulk and shear

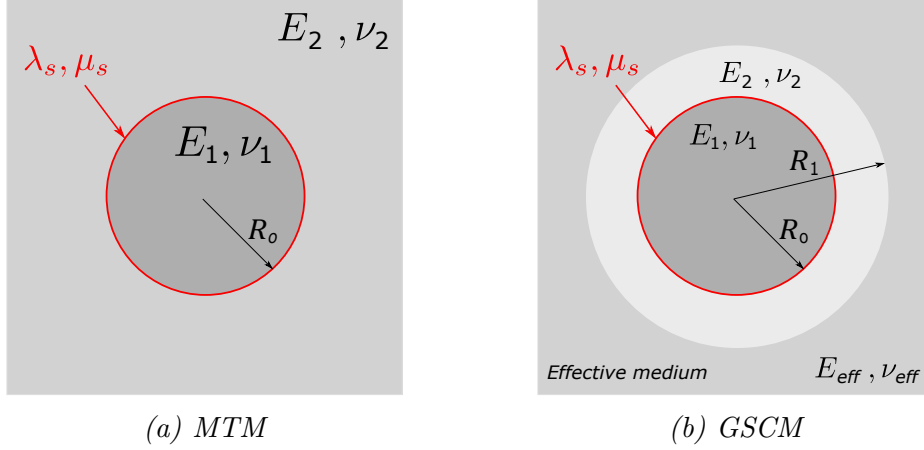


Figure 2.10: Mori-tanaka model and Generalized self-consistent method with coherent interface.

moduli of materials reinforced with spherical nano-inclusions. The results of this study showed a perfect agreement between these two models for the effective bulk modulus given by the following expression:

$$\kappa_{eff} = \frac{3\kappa_1 (3\kappa_2 + 4f\mu_2) + 2\mu_2 [4f\mu_2\kappa_s^r + 3\kappa_2 (2 - 2f + \kappa_s^r)]}{3[3(1-f)\kappa_1 + 3f\kappa_2 + 2\mu_2 (2 + \kappa_s^r - f\kappa_s^r)]}, \quad (2.16)$$

where subscript ($i = 1$) and ($i = 2$) stand, for the inclusion and the matrix, respectively, $\kappa_s^r = \kappa_s / (R_0\mu_2)$ where $\kappa_s = 2(\lambda_s + \mu_s)$ is the interface bulk modulus, R_0 is the radius of the inclusion and f is the volume fraction.

When $\kappa_s \rightarrow 0$, the expression of κ_{eff} reduces to the classical expression of Mori-Tanaka scheme and GSCM model (without interface effect). The authors also provided the solutions for finding the effective shear modulus according to the Mori-Tanaka model and GSCM although the results obtained from these two models are different at high volume fractions.

2.4.3 Composite cylinder assemblages model and Generalized self-consistent model for cylindrical inclusion

Not only the case of spherical inclusions presented previously but also the case of fibrous nanocomposite with cylindrical inclusion (circular base) have been analytically modeled. The fibrous nanocomposite referred to a columnar microstructure where the micro geometrical characteristic of the constituent phases is homogeneous along one and only one direction (the fiber direction). The first study accounting for an imperfect interface in fibrous nanocomposite was proposed by Chen et al [Chen et al., 2007]. In this study, the five effective constants characterizing the overall elastic behavior of the transversely isotropic composite (Hill's moduli [Hill, 1964]) are derived. While the effective transverse modulus, longitudinal and transverse moduli,

and axial shear modulus are calculated by using of composite cylinder assemblages model (CCA) [Hashin and Rosen, 1964], the effective transverse shear modulus is estimated through the generalized self-consistent method (GSCM) [Christensen and Lo, 1979]. The analytical estimations obtained in this study clearly show that the effective modulus of unidirectional nanofibrous composites depends on the fiber cross-section size. We present here the expression of the effective transverse (plane strain) bulk modulus:

$$k_{eff} = k_2 + \frac{f(k_1 - k_2 + \frac{k_s}{2r})(k_2 + m_2)}{k_2 + m_2 + (1 - f)(k_1 - k_2 + \frac{k_s}{2r})}, \quad (2.17)$$

where $k_s = \lambda_s + 2\mu_s$, subscripts ($i = 1$) and ($i = 2$) refer to the inclusion and the matrix, respectively, and m denotes the transverse shear modulus and k the bulk modulus.

Without surface effect ($k_s = \lambda_s = \mu_s = 0$), Eq. (2.17) provides the well-known result obtained in the case of perfect interface [Hill, 1964].

It can be emphasized that the results of [Chen et al., 2007] are obtained in the case where the interface, fiber, and matrix phases are transversely isotropic. For the more general case with cylindrically anisotropic phases, Le Quang et He [Quang and He, 2009] gave an estimate of homogenized thermoelastic modulus by using the generalized self-consistent method (GSCM) with the incorporation of a coherent thermoelastic interface model. This study is based on the extension of their previous works [Le Quang and He, 2007] for classical fibrous composites. When the phases are set to be transverse isotropic, we recover the results obtained by Chen et al [Chen et al., 2007].

Besides the estimation of the effective properties of nano-reinforced materials, studies related to bounds on the effective moduli have also been performed [Le Quang and He, 2008], [Brisard et al., 2010a], [Brisard et al., 2010b]. These bounds are useful references allowing to check the consistency of the previous approximations. In that context, generalized Voigt and Reuss bounds and generalized Hashin-Shtrikman lower bound will be briefly introduced in the next subsections.

2.4.4 Generalized Voigt and Reuss bounds

The first attempt at establishing bounds on the effective elastic moduli of nanocomposite material came from Le Quang and He [Le Quang and He, 2008]. In this study, they extended the variational principle to multiphase materials with linear coherent interfaces. The explicit first-order upper and lower bounds for the effective elastic moduli in both the case of spherical and cylindrical (with circular base) inclusions have been derived. The expression for the upper and lower bounds on the effective bulk modulus are given as follows:

- Cylindrical inclusion (effective transverse modulus)

$$\begin{cases} k_{(+)} = c_0 k_0 + \sum_{i=1}^p c_i \left(k_i + \frac{\kappa_{si} + \mu_{si}}{2r_i} \right) \\ k_{(-)} = \left[\frac{c_0}{\kappa_0} + \sum_{i=1}^p \frac{c_i}{k_i + \frac{\kappa_{si} + \mu_{si}}{2r_i}} \right]^{-1} \end{cases} \quad (2.18)$$

- Spherical inclusion

$$\begin{cases} \kappa_{(+)} = c_0 \kappa_0 + \sum_{i=1}^p c_i \left(\kappa_i + \frac{4}{3} \frac{\kappa_{si}}{r_i} \right) \\ \kappa_{(-)} = \left[\frac{c_0}{\kappa_0} + \sum_{i=1}^p \frac{c_i}{\kappa_i + \frac{4\kappa_{si}}{3r_i}} \right]^{-1} \end{cases} \quad (2.19)$$

where c_i is the volume fraction of the phase i , phase o corresponds to the matrix, κ_i and μ_i are the elastic moduli, r_i is the radius of the inclusion, κ_{si} and μ_{si} are the elastic moduli of the interface surrounding the inclusions of phase i .

These bounds coincide with the well-known classical Voigt and Reuss bounds when interface effects are omitted ($\kappa_{si} = \mu_{si} = 0$) or when the radii r_i of the inclusion is large enough.

2.4.5 Generalized Hashin-Shtrikman lower bound

In the context of nano-reinforced materials, Brisard et al [Brisard et al., 2010a] apply variational approaches to determine the lower bound of Hashin-Shtrikman type of the bulk modulus. In that development, the difficulty lies in the bidimensional nature of the interface's stiffness tensor. The establishment of this Hashin-Shtrikman type bounds requires to compare the stiffnesses of the interface (2D) with the stiffness of the reference material (3D). To overcome this difficulty, the authors introduced a thin elastic layer analogy based on the asymptotic analysis which allows deducing the 3D bulk and shear moduli of the equivalent elastic layer from their 2D counterparts. A polarization framework for the derivation of second-order bounds on the elastic moduli of composites with interface effects was then proposed. This polarization framework was firstly applied for mono-disperse spherical nano-inclusions, providing the following lower bound:

$$\kappa_{eff} = \kappa_m + f \frac{3\kappa_m + 4\mu_m}{3f\kappa_m + 4\mu_m + 3(1-f)\kappa_p} (\kappa_p - \kappa_m), \quad (2.20)$$

where $\kappa_p = \kappa_i + \frac{4\kappa_s}{3r}$, κ_i , κ_m , κ_s are the bulk modulus of the inclusion, the matrix and the interface, respectively, μ_m is the shear modulus of the matrix, r is the radius of

the inclusions and f is their volume fraction.

This lower bound improves the first-order generalized Reuss bound (Eq. (2.19)) proposed by Le Quang and He [Le Quang and He, 2008] and provides the same results from those obtained with the generalized Mori-Tanaka model (Eq. (2.16)) established by Duan et al [Duan et al., 2005b]. The polydispersity was also considered by assuming that all inclusions and interfaces share the same elastic moduli $\kappa_i, \mu_i, \kappa_s$ and μ_s while their radius can be diverse. In the same line of their study, Brisard et al proposed in [Brisard et al., 2010b] the lower bound of the shear modulus.

2.4.6 Comparison and conclusions on analytical models

We propose in this subsection to compare the result of the prediction of the effective bulk modulus of nanocomposite with spherical inclusions for the generalized models of [Duan et al., 2005b], [Le Quang and He, 2008] and [Brisard et al., 2010a]. Figure 2.11a shows the different estimations of this homogenized modulus according to the interface modulus κ_s while Figure 2.11b represents the evolution of the effective bulk modulus with respect to the radius of the inclusion. We can see the influence of the size effect on the effective bulk modulus given by different models of the literature. This comparison allows us first of all to note that a decrease in the size of the inclusions produces an increase in the absolute value of the effective elastic modulus of the composite (compared to the case without interfaces). When the interface modulus κ_s is zero (no interface effect), the estimations provide the exact result of the homogenized bulk modulus of the classical Mori-Tanaka scheme. On the other hand, for the cases of $\kappa_s > 0$, all estimations give higher values than the classical Mori-Tanaka estimate. Moreover, as expected, the lower generalized bound of Hashin-Shtrikman [Brisard et al., 2010a] coincides perfectly with the Generalized Mori-Tanaka model [Duan et al., 2005b] when accounting for interface effects.

In summary, it can be seen that a large number of publications have introduced the interface effect in micromechanical models to predict the size effect on the elastic behavior of nanocomposites. They extended the classical models by adding an imperfect interface between matrix and inclusion. These interfaces have generally been considered with simple shapes (spherical or cylindrical) of the inclusion to simplify the analytical developments. In addition, analytical research on nonlinear behavior of this kind of material is rarely found in the literature. We can mention here the two first studies [Brach et al., 2017a] and [Brach et al., 2017b] which account for the size effect for nonlinear behavior of nanoporous materials. In these studies, the matrix is assumed to be a rigid-ideal plastic material obeying to a general isotropic yield criterion. In the case of isotropic loading conditions, the authors provided the exact microscopic limit state of nanoporous materials. The size effects associated with the possible nanosize of voids have been accounted for via a coherent interface at the cavity boundary. The limitations on inclusions shape

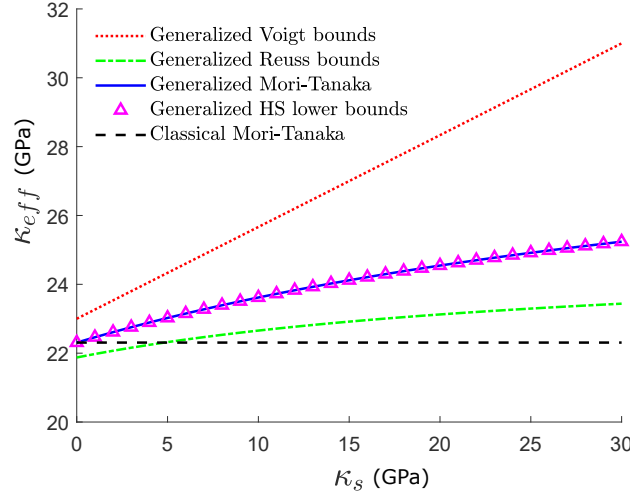
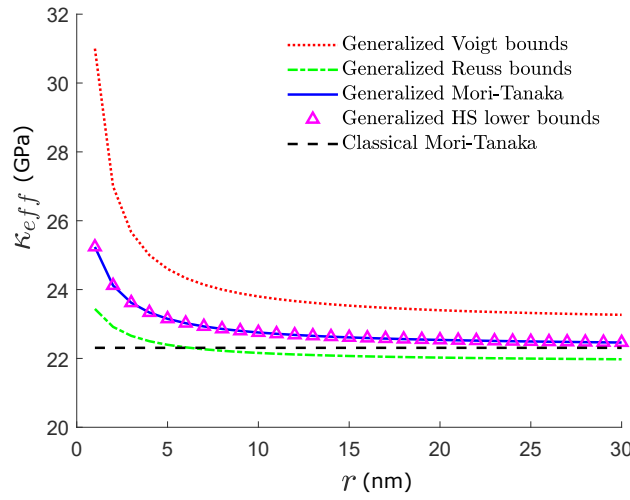
(a) in terms of κ_s , ($r = 1$ nm)(b) in terms of radius of inclusion r , ($\kappa_s = 30$ N/mm)

Figure 2.11: Size effect on effective bulk modulus of a spherical inclusion nanocomposite- Estimation by different models in the literature - $\kappa_m = 20$ GPa, $\kappa_i = 35$ GPa, $\mu_m = 15$, $f = 0.2$.

of the analytical models can be overcome by using the numerical model based on FEM, the mostly considered FEM approaches in the context of nanocomposite are presented in the next section.

2.5 Numerical models based on FEM

In order to solve the homogenization problems, the analytical models, presented in the previous section, require "simple" shapes of inclusions (spherical or circular cylindrical shapes). Therefore, numerical approaches are very necessary to break through this limitation. The continuum finite element method (FEM) lies in the framework of continuum mechanics and can be associated with imperfect interface models intro-

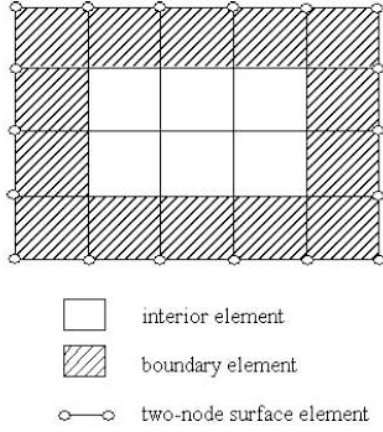
duced in section 2.2 to model the size effect. FEM approaches allow circumventing the high computational cost inherent to molecular dynamics computations while efficiently reproducing surface/interface effects, at least at a phenomenological point of view.

The numerical approaches can be divided into two main categories based on discretization techniques. The first one requires a conforming mesh (fitted FEM) in which the interface coincides with element edges. The interface is then explicitly discretized by using the element side or edges as lower-dimensional entities (surface/interface element). The second type can be performed on the regular mesh (uniform/structured mesh) and no discretization effort is needed. The interface is defined by a scalar zero level set function independent from the background mesh (unfitted FEM). The interface is implicitly discretized by the piecewise approximation of the intersections between the level set function and the mesh. On the elements which are cut by the interface, additional degrees of freedom are required to describe the interface behavior as well as the discontinuity of the mechanical fields.

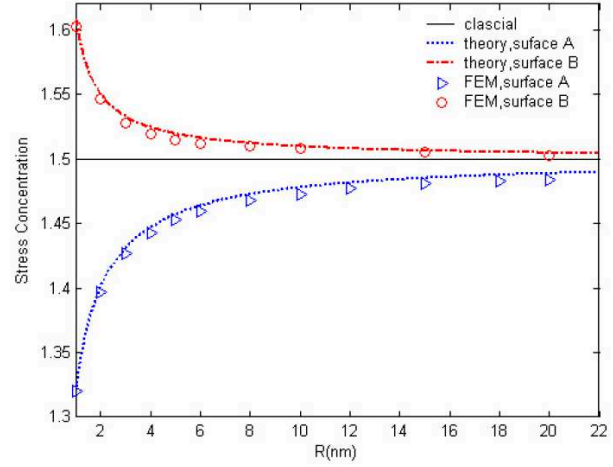
2.5.1 Surface/interface element in standard FEM

Size-dependent mechanical behavior in nanostructured materials has been first treated numerically by Wei et al [Wei et al., 2006] with the introduction of surface elements in a standard FEM framework. Due to its attachment to the volume element, these surface elements can reflect the rigidity of the surface (surface elasticity) and transmit the surface stress to the bulk of the material (see Figure 2.12a). The size effect on the stress concentration (which relates the stress in the inclusion to the applied remote stress) is then computed and compared to the analytical results from [Sharma and Ganti, 2004] (see Figure 2.12b).

While in [Wei et al., 2006], the coherent interface model has been used in the framework of infinitesimal strain, Javili et al [Javili et al., 2015] conducted a similar study within the framework of finite strains. In their studies, besides the coherent interface model, they considered different interface models. Still in the context of finite strains, Esmaili et al [Esmaili et al., 2017], employed a standard finite element implementation with interface element accounting for surface elasticity in order to predict the degradation of a non-coherent interface. More recently, Javili et al [Javili et al., 2017] studied a general imperfect interface treated by using the interface element approach. As shown in Figure 2.13, in the case of perfect interface model no size effect was observed on the macroscopic Piola-Kirchhoff stress. When the general interface model is considered, the material response is the combination of the results obtained from the cohesive (spring-layer) and elastic (coherent) interface models. While the cohesive interface introduces a less rigid behavior, the response of the elastic interface leads to a more rigid effect.



(a) Schematic diagram of mesh map of solid containing surface element



(b) Variation of stress concentration with void radius R

Figure 2.12: Surface element in standard FEM and its result from [Wei et al., 2006].

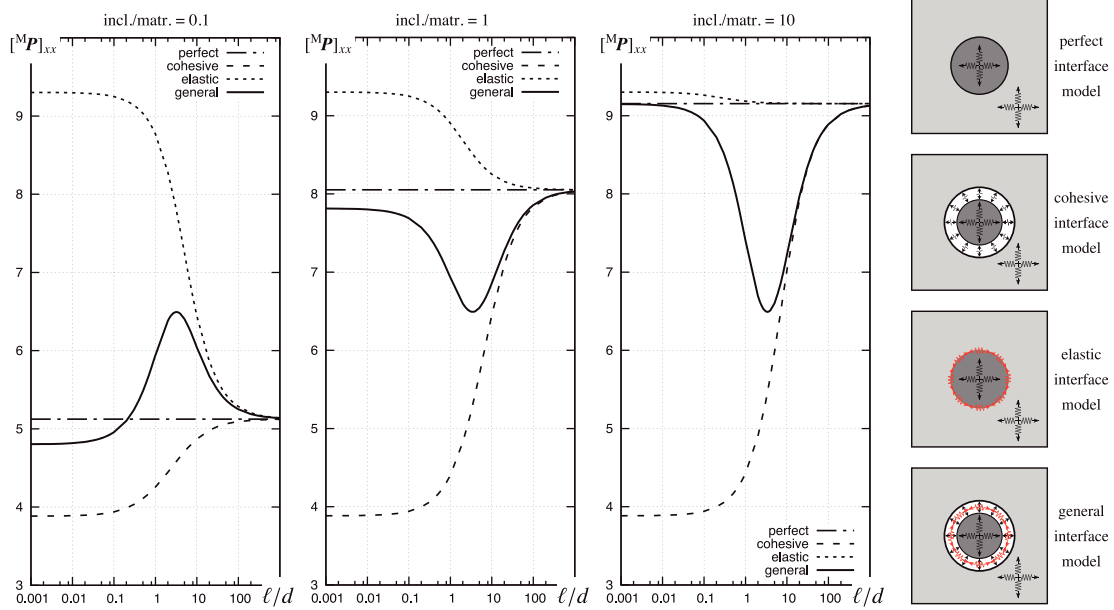


Figure 2.13: Summary of the effective response of the RVE versus size for different stiffness ratios and different types of interfaces. The graphs show the component xx of the macroscopic Piola stress versus the normalized RVE size by a physical dimension at the microstructure denoted d [Javili et al., 2017].

It should be noted that to have an efficient implementation of the finite element method, the surface/interface elements need to be chosen to be consistent with the bulk elements. Thanks to this choice, the common facet or edge of two adjacent bulk

elements can be regarded as an interface element and therefore the interface can be explicitly discretized. The standard FEM with surface/interface element is perhaps the most simple and explicit way for modeling the composite material in general and taking into account the imperfect interface in particular. However, it requires conforming meshes, which are costly to create for complex geometries or random microstructures. This approach will be studied in more detail, for comparison to the XFEM approach, in chapter 3.

2.5.2 XFEM/level set approach

In order to overcome the drawback of conforming mesh requirement and to account for singularities (discontinuities) of the mechanical fields, the concept of eXtend Finite Element Method (XFEM) was introduced in [Moës et al., 1999, Moës and Belytschko, 2002]. This approach extends or enriches the approximation space (see Figure 2.14) so that we can naturally reproduce the complex function associated with the problem of discontinuity, singularity, boundary layer, etc. In terms of numerical homogenization, Sukumar et al [Sukumar et al., 2001] has successfully modeled the problem with inclusions (and holes) with a perfect interface by the level-set method (LSM) [Osher and Fedkiw, 2001] in the framework of XFEM.

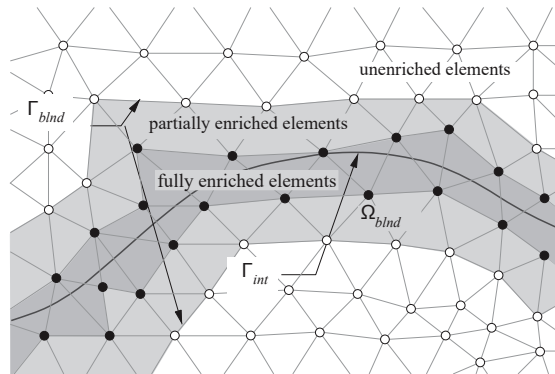


Figure 2.14: An XFEM/level set mesh with an interface, showing fully enriched elements, partially enriched elements and unenriched (standard) elements. Also shown is the boundary Γ_{bnd} where the enrichment vanishes [Chessa and Belytschko, 2003].

The surface/interface terms (surface tension) have been firstly treated in the context of fluid mechanics using XFEM by Chessa and Belytschko [Chessa and Belytschko, 2003]. In solid mechanics and especially for nanocomposites, Yvonnet et al [Yvonnet et al., 2008] evaluated the size effect for different shapes of inclusion even the arbitrary shapes and random microstructures by using a coherent interface model in the framework of XFEM/level set strategy. The relevance of their numerical method was verified by comparing the effective bulk modulus calculated by XFEM and those given by the existing analytical solutions of Le Quang and He [Quang and

He, 2009] and Duan et al [Duan et al., 2005b]. As can be seen in Figure 2.15, a good agreement between XFEM/level set and the analytical solutions has been reported for both cylindrical and spherical nanopores.

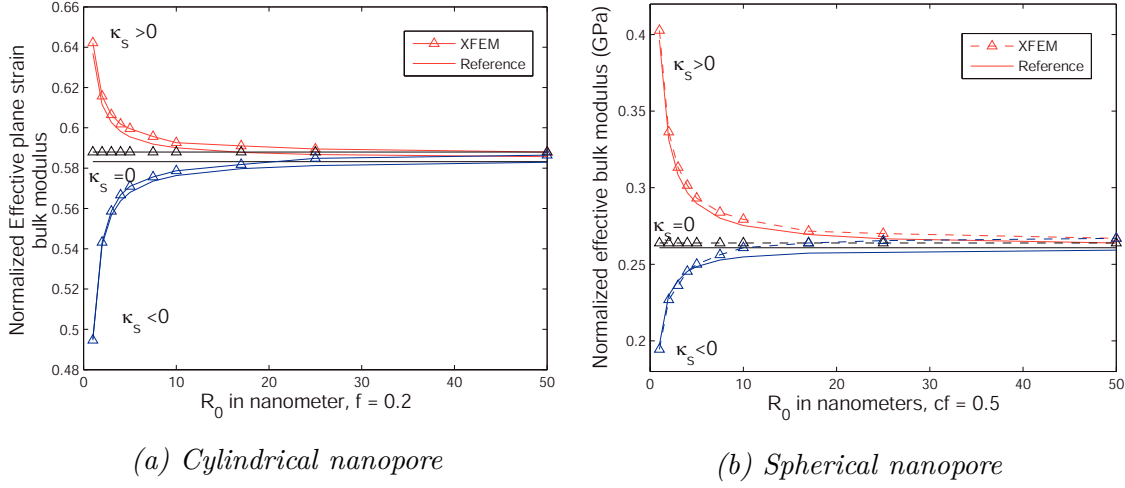


Figure 2.15: Normalized effective bulk modulus versus pore radius [Yvonnet et al., 2008]

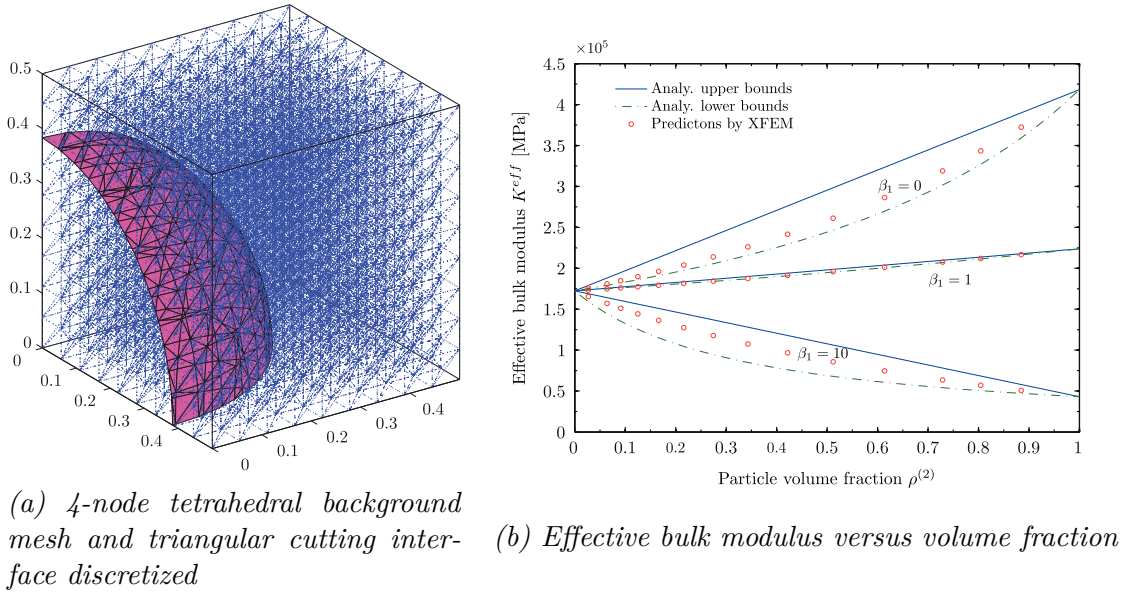


Figure 2.16: Spherical inclusion problem with the spring-layer interface [Zhu et al., 2011] (β_1 is a relative elastic stiffness of the imperfect interface).

In the same context of XFEM/level set, Farsad et al [Farsad et al., 2010] considered the same type of numerical model but added interface decohesion while Zhu et al [Zhu et al., 2011] used the XFEM approach to build composite three-dimensional problem using tetrahedron elements. In their study, Zhu et al [Zhu et al., 2011] considered the spring-layer interface model which makes the displacement vector discontinuous across the interface whereas the traction vector is continuous and is,

in the linear case, proportional to the displacement vector jump. Their results in terms of effective elastic modulus were compared with the analytical upper and lower bounds derived by Hashin [Hashin, 1992] (see Figure 2.16).

In the XFEM/level set approach, the geometry of the micro/nano structure is entirely defined by the level-set functions, which are independent of the mesh discretization. Therefore, the advantage of this approach is to handle complex geometries of inclusion and interface without discretization effort. Nevertheless, the number of degrees of freedom and integration points is raised compared to standard FEM. In addition, degradation of convergence due to the presence of surface elasticity has been also reported by Yvonnet et al [Yvonnet et al., 2008]. A more detail study of this approach will be presented, for comparison to the Interface element approach, in chapter 3.

2.5.3 Other promising methods: Cut-FEM, Embedded-FEM

Besides XFEM, in the framework of unfitted FEM, there exist other promising approaches, although they have not yet been used in the case of nano-reinforced materials.

- Cut Finite Element Method

Developed by Burman et al [Burman and Hansbo, 2010], CutFEM is a general method for dealing with complicated problems involving complex geometries of surface/interface. The basic idea of discretization in CutFEM is to embed the $(d - 1)$ -dimensional surface/interface in a d -dimensional mesh and use the basic functions of the higher dimensional mesh but integrate over the interface [Olshanskii et al., 2009]. Based on this approach, Cenanovic et al [Cenanovic et al., 2016] suggested a formulation allowing to integrate of elastic membranes in a finite element formulation. The displacement field is continuous, the membrane model used in this study is based on the surface elasticity introduced by Gurtin and Murdoch [Gurtin and Ian Murdoch, 1975]. However, no local relation between surface stress and stress in the bulk (generalized Young-Laplace equation) is imposed. It should be noted that in this work, the membrane equations are simply added to the bulk equations and the equilibrium equations of the bulk and the membrane are related to the same displacement field. The membrane, therefore, shares the same degrees of freedom as the bulk, and no additional degree of freedom is required. Although the CutFEM approach needs stabilization due to ill-conditioning of the linear system (see [Burman et al., 2015], [Burman et al., 2016] for details), once the coherent interface model is applied, this approach can completely take into account the interface energy as well as reproduce the size effect of nanocomposites.

- Embedded finite element method (E-FEM)

Embedded finite element method (Embedded FEM or embedded discontinuity approach) is based on a local enhancement on the element which contains the discon-

tinuities either in the displacement field (strong discontinuities [Simo et al., 1993]) or in the strain field (weak discontinuities [Ortiz et al., 1987]). Compared to the global kinematic enrichment of XFEM, Embedded FEM is less expensive in terms of computational cost. The comparison study of Oliver et al [Oliver et al., 2006] between E-FEM and XFEM for capturing strong discontinuity showed that there is not a big difference in the accuracy as well as the efficiency. The E-FEM approach separately handles the global and local equilibrium equations [Roubin et al., 2015] and therefore allows to conveniently impose the weak form of the generalized Young Laplace equation at the local level (interface embedded in the element). Starting from this advantage and the fact that this method has not been widely applied in numerical homogenization, we chose to extend the Embedded FEM approach to take into account the weak discontinuity and the interface behavior in order to model the interface effects present in nano-reinforced materials. These developments will be discussed in details in chapter 4.

2.5.4 Conclusion on numerical approaches

Whereas a lot of works have been developed from the analytical point of view, few contributions are related to numerical development in Finite Element codes. We only found in the literature two numerical approaches that dealt with the size effect observed in the nanocomposites. Besides, these two approaches suffer certain drawbacks such as the conforming mesh requirement of the Interface element approach or the degradation of the convergence of XFEM. Moreover, the nonlinear behavior of nanocomposite has hardly been taken into account. These restrictions motivated the initial objective of this work: the development of an efficient finite element strategy for the modeling of nano-reinforced material not only for elastic behaviors but also for nonlinear behaviors. We chose, in this Ph.D. work, to evaluate the capabilities of E-FEM in predicting homogenized properties of nano reinforced materials. The specificities of this homogenization problem are presented in the next section.

2.6 Homogenization problem with coherent interface model

In order to predict the effective behavior of nanocomposite material including the size effect due to the nanoscopic inclusions, a heterogeneous problem containing different materials (matrix and inclusions) and coherent interfaces is considered. Besides the classical equilibrium equation for the bulk, the equilibrium of the interface is described by the generalized Young-Laplace equation. Before presenting the basic problem, the elements of differential calculus in surface/interface context are presented.

2.6.1 Basic elements of differential geometry for surface

Following the theories and research on the elastic material surfaces/interfaces of [Gurtin and Ian Murdoch, 1975], [Fried and Gurtin, 2007] and [Gu, 2008], the definition of interface/surface terms related to projection operators, superficial fields, surface gradient, and surface divergence are presented in this subsection.

2.6.1.1 Projection operators

We introduce two complementary orthogonal projection operators defined at any point x of interface Γ by

$$\mathbf{P}^\perp(\mathbf{x}) = \mathbf{n}(\mathbf{x}) \otimes \mathbf{n}(\mathbf{x}) , \quad (2.21)$$

$$\mathbf{P}(\mathbf{x}) = \mathbf{I} - \mathbf{n}(\mathbf{x}) \otimes \mathbf{n}(\mathbf{x}) , \quad (2.22)$$

where \mathbf{I} is the second order identity tensor and \mathbf{n} is the normal vector of the interface Γ .

Geometrically, $\mathbf{P}(\mathbf{x})$ projects any vector $\mathbf{v} \in \mathbb{R}^k$ onto the tangent space of Γ at the \mathbf{x} position while $\mathbf{P}^\perp(\mathbf{x})$ projects \mathbf{v} , still at the \mathbf{x} position, on the normal line of Γ along $\mathbf{n}(\mathbf{x})$. So any vector $\mathbf{v} \in \mathbb{R}^k$ can uniquely be decomposed into a normal component \mathbf{v}_n and a tangential component \mathbf{v}_s :

$$\mathbf{v} = \mathbf{v}_n + \mathbf{v}_s, \quad \mathbf{v}_n = \mathbf{P}^\perp \cdot \mathbf{v}, \quad \mathbf{v}_s = \mathbf{P} \cdot \mathbf{v} . \quad (2.23)$$

Since the operators \mathbf{P} and \mathbf{P}^\perp are orthogonal projectors, they verify the following relations:

$$\begin{aligned} \mathbf{P}^2 &= \mathbf{P}, \quad (\mathbf{P}^\perp)^2 = \mathbf{P}^\perp, \quad (\mathbf{P})^T = \mathbf{P}, \\ (\mathbf{P}^\perp)^T &= \mathbf{P}^\perp, \quad \mathbf{P} \cdot \mathbf{P}^\perp = \mathbf{P}^\perp \cdot \mathbf{P} = \mathbf{0} . \end{aligned} \quad (2.24)$$

2.6.1.2 Superficial (surface) fields

A second order tensor field \mathbf{T} on Γ is a superficial field if and only if

$$\mathbf{T}(\mathbf{x}) \cdot \mathbf{n}(\mathbf{x}) = \mathbf{0} \quad \forall \mathbf{x} \in \Gamma . \quad (2.25)$$

For any second order tensor field \mathbf{H} defined on Γ , the field $\mathbf{T}(\mathbf{x}) = \mathbf{H}(\mathbf{x}) \cdot \mathbf{P}(\mathbf{x})$ is superficial, because $\mathbf{P}(\mathbf{x}) \cdot \mathbf{n}(\mathbf{x}) = \mathbf{0}$. In addition, a second order tensor field \mathbf{T} defined on Γ is superficial if and only if

$$\mathbf{T}(\mathbf{x}) \cdot \mathbf{P}(\mathbf{x}) = \mathbf{T}(\mathbf{x}) \quad \forall \mathbf{x} \in \Gamma . \quad (2.26)$$

For example, to get a precise idea of the matrix form of a surface field \mathbf{T} , if we consider the case where Γ is a plane surface whose normal vector \mathbf{n} coincides with the vector \mathbf{e}_1 of an orthonormal basis $\{\mathbf{e}_1, \mathbf{e}_2, \mathbf{e}_3\}$ in a 3D case and $\{\mathbf{e}_1, \mathbf{e}_2\}$ in a 2D case

$$\mathbf{T}_{3D} = \begin{bmatrix} 0 & T_{12} & T_{13} \\ 0 & T_{22} & T_{23} \\ 0 & T_{32} & T_{33} \end{bmatrix} \quad \text{and} \quad \mathbf{T}_{2D} = \begin{bmatrix} 0 & T_{12} \\ 0 & T_{22} \end{bmatrix} \quad (2.27)$$

A superficial field $\mathbf{T}(\mathbf{x})$ defined on Γ is said to be tangential if and only if

$$\mathbf{T}^T(\mathbf{x}) \cdot \mathbf{n}(\mathbf{x}) = \mathbf{0} . \quad (2.28)$$

It is immediate to deduce that any symmetrical superficial tensor field is necessarily tangential and \mathbf{P} is a tangential superficial tensor and if \mathbf{T} is a tangential superficial tensor, then $\mathbf{T} = \mathbf{P} \cdot \mathbf{T} \cdot \mathbf{P}$. Using the example of a planar surface normal \mathbf{e}_1 , a tangential superficial field \mathbf{T} takes the form

$$\mathbf{T}_{3D} = \begin{bmatrix} 0 & 0 & 0 \\ 0 & T_{22} & T_{23} \\ 0 & T_{32} & T_{33} \end{bmatrix} \quad \text{and} \quad \mathbf{T}_{2D} = \begin{bmatrix} 0 & 0 \\ 0 & T_{22} \end{bmatrix} \quad (2.29)$$

It can be noticed that in the 3D case, the interface is a plane surface, therefore, a tangential superficial tensor can be reduced to a 2×2 matrix. Meanwhile, in the 2D case, the interface reduces to a curve line and the tangential superficial tensor becomes a scalar that can be presented under the form $\mathbf{T} = T_{22}\mathbf{P}$.

2.6.1.3 Surface gradient, surface divergence

The surface gradient operator is the tangential derivative, defined by:

$$\nabla_s\{\bullet\} = \nabla\{\bullet\} \cdot \mathbf{P} . \quad (2.30)$$

Because of its definition, $\nabla_s\{\bullet\}$ is a superficial field, therefore, the gradient operator $\nabla\{\bullet\}$ can be decomposed into a surface and a normal terms:

$$\nabla\{\bullet\} = \nabla_s\{\bullet\} + \nabla_n\{\bullet\} \quad \text{with} \quad \nabla_n\{\bullet\} = \nabla\{\bullet\} \cdot \mathbf{P}^\perp . \quad (2.31)$$

The surface divergence is defined by:

$$\mathbf{div}_s\{\bullet\} = \nabla\{\bullet\} : \mathbf{P} , \quad (2.32)$$

and as the gradient operator, the divergence operator can be decomposed as follow:

$$\mathbf{div}\{\bullet\} = \mathbf{div}_s\{\bullet\} + \mathbf{div}_n\{\bullet\} \quad \text{with} \quad \mathbf{div}_n\{\bullet\} = \nabla\{\bullet\} : \mathbf{P}^\perp . \quad (2.33)$$

Thanks to the surface gradient and divergence operators, the curvature tensor \mathcal{K} can be introduced and defined by

$$\mathcal{K} = -\nabla_s \mathbf{n} . \quad (2.34)$$

This \mathcal{K} tensor is a tangential superficial tensor, from which can be expressed \bar{K} , the total (twice of the mean) curvature:

$$\bar{K} = \text{tr} \mathcal{K} = \mathbf{P} : \mathcal{K} = -\text{div}_s \mathbf{n} , \quad (2.35)$$

and we also have the identity

$$\text{div}_s \mathbf{P} = \bar{K} \mathbf{n} . \quad (2.36)$$

In the following, we will often have to calculate the tangential derivatives of the functions. Let a be a scalar field, \mathbf{v} and \mathbf{w} be two vector fields, and \mathbf{T} be a tensor field defined on a manifold Γ in \mathbb{R}^k . Starting from the previous definitions of tangential derivatives, we can establish (see [Gurtin and Ian Murdoch, 1975] and [Murdoch, 1976] for more details) the following formulas

$$\nabla_s(a\mathbf{v}) = a\nabla_s \mathbf{v} + \mathbf{v} \otimes \nabla_s a , \quad (2.37)$$

$$\text{div}_s(a\mathbf{v}) = a\text{div}_s \mathbf{v} + \mathbf{v} \cdot \nabla_s a , \quad (2.38)$$

$$\text{div}_s(a\mathbf{T}) = a\text{div}_s \mathbf{T} + \mathbf{T} \cdot \nabla_s a , \quad (2.39)$$

$$\text{div}_s(\mathbf{v} \otimes \mathbf{w}) = (\text{div}_s \mathbf{v})\mathbf{w} + (\nabla_s \mathbf{v}) \cdot \mathbf{P} \cdot \mathbf{w} , \quad (2.40)$$

$$\text{div}_s(\mathbf{T}^T \cdot \mathbf{v}) = \mathbf{v} \cdot \text{div}_s \mathbf{T} + \mathbf{T} \cdot \nabla_s \mathbf{v} . \quad (2.41)$$

Denoting by $\mathbf{m}(\mathbf{x})$ the unit vector tangent to Γ but normal to $\partial\Gamma$ at a position $\mathbf{x} \in \partial\Gamma$, then the divergence theorem applied to \mathbf{v} and to \mathbf{T} is written as

$$\int_{\partial\Gamma} \mathbf{v} \cdot \mathbf{m} dl = \int_{\Gamma} \text{div}_s \mathbf{v} dS , \quad (2.42)$$

$$\int_{\partial\Gamma} \mathbf{T} \cdot \mathbf{m} dl = \int_{\Gamma} \text{div}_s \mathbf{T} dS . \quad (2.43)$$

In particular, the left terms of each of the expressions (2.42) and (2.43) is zero when Γ is a closed plane curve or a closed surface.

2.6.2 Problem of composite material with coherent interface

We present here a problem in the framework of the infinitesimal hypothesis. This problem is the basic pattern we consider alone or repeated (periodically or randomly) in the homogenization problems we will solve later by using different numerical strategies. For the sake of simplicity, in this work, the heterogeneous material made of two phases although more phases can be considered.

2.6.2.1 Equilibrium equations and boundary conditions

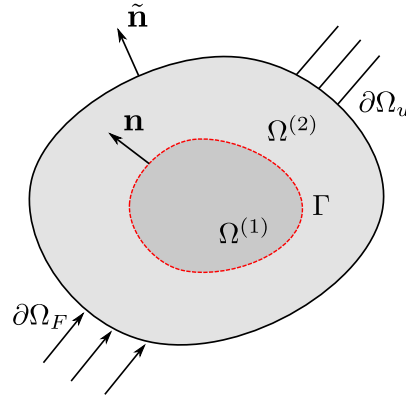


Figure 2.17: Problem of two phases material with an imperfect interface.

We consider here a continuum body described by a bounded domain $\Omega \subset \mathbb{R}^d$ ($d = 2$ or 3), with boundary $\partial\Omega$. This domain consists of two-phases $\Omega^{(1)}$ and $\Omega^{(2)}$ (in the following $\Omega^{(1)}$ and $\Omega^{(2)}$ denote inclusion and matrix, respectively). These two phases are partitioned by an interface Γ (see Figure 2.17) with unit normal vector denoted as \mathbf{n} pointing, conventionally, from $\Omega^{(1)}$ toward $\Omega^{(2)}$. The outward unit normal to $\partial\Omega$ is denoted $\tilde{\mathbf{n}}$. The boundary $\partial\Omega$ is partitioned into $\partial\Omega_u$ where Dirichlet boundary conditions are prescribed and $\partial\Omega_F$ where Neumann boundary conditions hold ($\partial\Omega_F \cup \partial\Omega_u = \partial\Omega$ and $\partial\Omega_F \cap \partial\Omega_u = \emptyset$). The jump of a quantity $\{\bullet\}$ over the interface is defined by $\llbracket \{\bullet\} \rrbracket = \{\bullet\}^{(1)} - \{\bullet\}^{(2)}$.

The bulk equilibrium equations in $\Omega^{(i)}$ ($i = 1, 2$) are given by:

$$\mathbf{div} \boldsymbol{\sigma}^{(i)} + \mathbf{b} = \mathbf{0} \quad \text{in } \Omega^{(i)}, \quad i = 1, 2, \quad (2.44)$$

where $\boldsymbol{\sigma}$ denotes the bulk Cauchy stress tensor and \mathbf{b} denotes a volume force.

The Neumann and Dirichlet boundary conditions on $\partial\Omega$ are defined by:

$$\boldsymbol{\sigma} \cdot \tilde{\mathbf{n}} = \mathbf{F} \quad \text{on } \partial\Omega_F \quad \text{and} \quad \mathbf{u} = \bar{\mathbf{u}} \quad \text{on } \partial\Omega_u. \quad (2.45)$$

As mentioned above, a coherent surface Γ is introduced at the interface between the matrix $\Omega^{(2)}$ and the inclusion $\Omega^{(1)}$. According to the generalized Young-Laplace equation [Povstenko, 1993], [Gurtin et al., 1998] the equilibrium of the interface Γ is given by:

$$\llbracket \boldsymbol{\sigma} \rrbracket \cdot \mathbf{n} + \mathbf{div}_s \boldsymbol{\sigma}_s = \mathbf{0} \quad \text{on } \Gamma, \quad (2.46)$$

where $\boldsymbol{\sigma}_s$ is the surface stress tensor.

Contrary to classical continuum mechanics hypothesis, the generalized Young-Laplace equation allows a jump of the traction across the interface Γ . The traction jump vector can be decomposed into the normal and tangential components. In that case,

Eq. (2.46) becomes:

$$\begin{cases} \mathbf{P}^\perp \cdot \llbracket \boldsymbol{\sigma} \rrbracket \cdot \mathbf{n} = -(\boldsymbol{\sigma}_s : \mathcal{K})\mathbf{n} \\ \mathbf{P} \cdot \llbracket \boldsymbol{\sigma} \rrbracket \cdot \mathbf{n} = -\mathbf{P} \cdot \text{div}_s \boldsymbol{\sigma}_s \end{cases} \quad \text{on } \Gamma. \quad (2.47)$$

The first equation of Eqs. (2.47) relates to the interface equilibrium in the normal direction with the involvement of the curvature tensor \mathcal{K} . In the case of a straight line or plane interface, the right part of this equation vanishes even when the interface stress is non-zero. The second equation of Eqs. (2.47) expresses that the non-uniformity of the interface stress will cause the discontinuity of the bulk shear stress (the non-diagonal components of $\llbracket \boldsymbol{\sigma} \rrbracket$).

Combining the two equations of Eqs. (2.47) allows to rewrite Eq. (2.46) as follow:

$$\llbracket \boldsymbol{\sigma} \rrbracket \cdot \mathbf{n} + (\boldsymbol{\sigma}_s : \mathcal{K})\mathbf{n} + \mathbf{P} \cdot \text{div}_s \boldsymbol{\sigma}_s = \mathbf{0} \quad \text{on } \Gamma. \quad (2.48)$$

In the classical case, the surface terms vanish and Eqs. (2.46), (2.47) and (2.48) reduce to the standard traction continuity equation.

According to the coherent interface model, there is no decohesion at the interface Γ so that, derived from Hadamard's compatibility conditions, we have the following kinematic conditions:

$$\text{across } \Gamma \begin{cases} \llbracket \mathbf{u} \rrbracket = \mathbf{0}, \\ \llbracket \boldsymbol{\epsilon} \rrbracket = (\mathbf{a} \otimes \mathbf{n} + \mathbf{n} \otimes \mathbf{a})^s \quad \mathbf{a} \in \mathbf{R}^d. \end{cases} \quad (2.49)$$

2.6.2.2 Constitutive equations for the bulk and the interface

The bulk constitutive laws in the context of linear elasticity are given by:

$$\boldsymbol{\sigma} = \mathbb{C}^{(i)} : \boldsymbol{\epsilon} \quad \text{in } \Omega^{(i)}, (i = 1, 2), \quad (2.50)$$

where $\mathbb{C}^{(i)}$ is the fourth-order elastic stiffness tensor associated with domain $\Omega^{(i)}$.

On the interface, we introduce a surface/interface elasticity [Gurtin and Ian Murdoch, 1975] given by the following expression:

$$\boldsymbol{\sigma}_s = \tau_o \mathbf{I}_2 + 2(\mu_s - \tau_o) \boldsymbol{\epsilon}_s + (\lambda_s + \tau_o) \text{tr}(\boldsymbol{\epsilon}_s) \mathbf{I}_2, \quad (2.51)$$

where $\boldsymbol{\epsilon}_s$ denotes the surface strain tensor, μ_s and λ_s are surface Lamé's constants characterizing the interface elasticity, \mathbf{I}_2 represents the surface second order identity tensor and τ_o is the surface tension. Eq. (2.51) is considered as the constitutive law of the interface and in the absence of τ_o , as already said in section 2.2, it can be written:

$$\boldsymbol{\sigma}_s = \mathbb{C}^s : \boldsymbol{\epsilon}_s, \quad (2.52)$$

where \mathbb{C}^s is the surface elastic stiffness tensor.

We recall that the interface strain tensor $\boldsymbol{\epsilon}_s$ can be obtained from the bulk strain tensor $\boldsymbol{\epsilon}$ by projection on the tangent plane of the interface through the projection operator \mathbf{P}

$$\boldsymbol{\epsilon}_s = \mathbf{P} \cdot \boldsymbol{\epsilon} \cdot \mathbf{P} . \quad (2.53)$$

All the studied pattern problem can be summed up as follow:

<p>Equilibrium equations</p> $\mathbf{div}(\boldsymbol{\sigma}^{(i)}) + \mathbf{b} = \mathbf{0} \quad \text{in } \Omega^{(i)}$ $\llbracket \boldsymbol{\sigma} \rrbracket \cdot \mathbf{n} + \mathbf{div}_s \boldsymbol{\sigma}_s = \mathbf{0} \quad \text{on } \Gamma$ <p>Constitutive equations</p> $\boldsymbol{\sigma} = \mathbb{C}^{(i)} : \boldsymbol{\epsilon} \quad \text{in } \Omega^{(i)}$ $\boldsymbol{\sigma}_s = \mathbb{C}^s : \boldsymbol{\epsilon}_s \quad \text{on } \Gamma$ <p>Boundary conditions</p> $\boldsymbol{\sigma} \cdot \tilde{\mathbf{n}} = \mathbf{F} \quad \text{on } \partial\Omega_F \quad \text{and} \quad \mathbf{u} = \tilde{\mathbf{u}} \quad \text{on } \partial\Omega_u$ <p>Across the interface</p> $\llbracket \mathbf{u} \rrbracket = \mathbf{0} \quad \text{while} \quad \llbracket \boldsymbol{\sigma} \rrbracket \cdot \mathbf{n} \neq \mathbf{0} \quad \text{and} \quad \llbracket \boldsymbol{\epsilon} \rrbracket \cdot \mathbf{n} \neq \mathbf{0}$	(2.54)
---	--------

It should be noted that the surface stress $\boldsymbol{\sigma}_s$ and surface strain $\boldsymbol{\epsilon}_s$ are tangential superficial tensor fields. Therefore, $\boldsymbol{\sigma}_s$ and $\boldsymbol{\epsilon}_s$ have all the characteristics presented in subsection 2.6.1.

As Eqs. (2.54) are the strong form of the problem, their weak forms depend on the considered numerical strategy. These weak forms will be presented in the next chapters for different numerical approaches.

2.7 Conclusion

In this chapter, we have given a general introduction about nano-reinforced materials, in which, a so-called size effect can be observed on the macroscopic mechanical behavior. This size effect is generally attributed to local phenomena at the atomic scale, and can be interpreted through an increase in the ratio (interface matrix-inclusions) / (volume fraction of inclusions).

First of all, the origin of this size effect has been given from the molecular interaction point of view. The interaction of the atoms located at the interface zone modifies their energy and position leading to different properties of solid in this zone. This phenomenon results in the dependence of the overall behavior on the size of fillers. Due to the very huge interfacial surface of the nano reinforcements, this size dependence is obvious in the case of nanocomposites. This effect has been illustrated

by the experimental results of the mechanical behavior of nanocomposites. For a given volume fraction, an increase of the macroscopic mechanic properties was observed when the size of the nano fillers decreases. Besides, the effect tends to vanish when the reinforcement size is large enough corresponding to the case of classical composites.

Before investigating from the modelization point of view, we presented the notion of interphase and interface which are needed for the vast majority of models. We then investigated the different methods from different scales in the context of nanocomposite. Molecular Dynamics simulations lie at a very fine scale (atom/nano) and mainly aim at providing mechanical information at the interaction zone for approaches at bigger scales. At the continuum mechanical scale, the analytical models with the incorporating in the micromechanical approaches of the imperfect interface models are diverse but limit themselves to simple shapes of reinforcements (spherical or cylindrical).

The two numerical approaches based on FEM (standard FEM with interface element and XFEM/level set) that we found in the literature can overcome the geometry limitation of analytical models. However, from the computational point of view, these two numerical approaches still have certain drawbacks. We also noted, through this bibliographic analysis, the necessity of the development of an efficient numerical strategy for the modeling of nano-reinforced materials not only for elastic behaviors but also for nonlinear behaviors.

We finished the chapter by presenting the mechanical problem with the principal hypothesis and equations we consider in this work for modeling nanocomposite materials.

Chapter 3

FEM with surface/interface element and eXtended-FEM for modeling size effect of nanocomposites: a comparative study.

We present in this chapter a comparative study of the Interface element approaches and XFEM/level set approach. The implementation strategies of these two numerical approaches are built and the result related to the validation, exploitation and performance in various conditions are then reported.

Contents

3.1	Introduction	40
3.2	Governing equations	41
3.3	Finite element implementation	43
3.3.1	Standard FEM with surface/interface element	44
3.3.2	XFEM/level-set approach for modeling size effect	46
3.4	Numerical results	49
3.4.1	Eshelby's problem with coherent interface	50
3.4.1.1	Convergence analysis	50
3.4.1.2	Investigation of local field	51
3.4.1.3	Size effect indicator	53
3.4.2	Size dependence of effective properties of two-phases nanocomposites	54

3.4.3	Effective properties of a nanoporous material and influence of the boundary conditions	56
3.4.4	Spherical void (axisymmetric model)	59
3.4.5	Nanoporous material with random microstructure	60
3.5	Conclusion	65

3.1 Introduction

As mentioned in the previous chapter, whereas a lot of works have been developed from an analytical point of view, only a few contributions are related to numerical description and implementation of surface elasticity effects in Finite Element simulations. To the best of the author's knowledge, standard FEM with surface/interface element (see for instance [Wei et al., 2006]) and XFEM/level set (firstly extended by [Yvonnet et al., 2008] to study nanocomposites) are two of the most considered approaches in the literature to capture the size effect in nanocomposites. We propose in this chapter to compare the efficiency of these two approaches. In order to make the comparison as fair as possible, the numerical implementation of each approach has been performed with the same data: size of finite element mesh, material properties, Representative Volume Element (RVE). The comparison in terms of convergence and performance of the two numerical strategies has been performed and the results in terms of homogenized properties have been compared to the analytical solutions presented in the previous chapter. After validation of the implemented strategies, we investigate, in particular, the influence of the homogenization hypothesis in terms of boundary conditions on the computed effective mechanical properties. To test more realistic configurations, random microstructures are then considered with a comparison not only on the effective behavior but also on the computational cost. The comparison in this chapter gives an evaluation of the two studied approaches and it is expected to be a good basis to elaborate an optimal numerical computation method.

The chapter is organized as follows: in section 3.2, we describe the equations governing the problem of a two-phases medium with a coherent interface. In section 3.3, the fundamentals and the discretization techniques for XFEM approach and Interface element approach are presented. The numerical results obtained for both formulations are compared and analyzed in section 3.4. Finally, in section 3.5, several conclusions of this comparative study are reported.

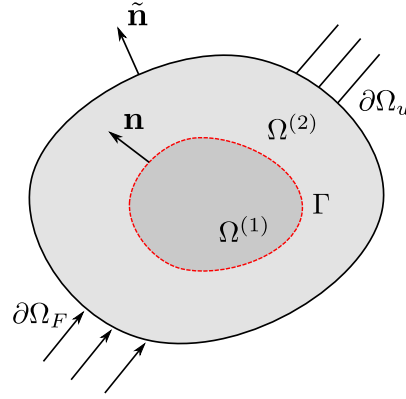


Figure 3.1: Problem of two phases material with coherent interface.

3.2 Governing equations

The problem of a two phase composite material with coherent interface (2.54) proposed in chapter 2 is recalled here (see Figure 3.1). The generalized Young-Laplace equation Eq. (2.46) is considered to describe the equilibrium of the interface while the elastic behavior of this interface is given by the linear expression proposed by Bottomley and Ogino [Bottomley and Ogino, 2001] (2.7). The two equilibrium equations in the bulk and on the interface are given as:

$$\begin{cases} \mathbf{div}(\boldsymbol{\sigma}^{(i)}) + \mathbf{b} = \mathbf{0} & \text{in } \Omega^{(i)} \quad i = 1, 2 \\ \llbracket \boldsymbol{\sigma} \rrbracket \cdot \mathbf{n} + \mathbf{div}_s \boldsymbol{\sigma}_s = \mathbf{0} & \text{on } \Gamma \end{cases} \quad (3.1)$$

where $\boldsymbol{\sigma}_s$ is the surface stress tensor, $\boldsymbol{\sigma}^{(i)}$ denotes the bulk stress tensor in the phase $\Omega^{(i)}$, \mathbf{b} denotes a volume force and \mathbf{n} is the unit normal vector to the interface, oriented, conventional from $\Omega^{(1)}$ to $\Omega^{(2)}$.

The weak form associated with Eq. (3.1) is given by testing with vector valued test functions $\delta \mathbf{u} \in \mathcal{H}^1(\Omega)$ and $\delta \mathbf{u}_s \in \mathcal{H}^1(\Gamma)$ such that:

$$\int_{\Omega \setminus \Gamma} \delta \mathbf{u} \cdot (\mathbf{div} \boldsymbol{\sigma} + \mathbf{b}) \, d\Omega + \int_{\Gamma} \delta \mathbf{u}_s \cdot (\mathbf{div}_s \boldsymbol{\sigma}_s + \llbracket \boldsymbol{\sigma} \rrbracket \cdot \mathbf{n}) \, d\Gamma = \mathbf{0} \quad \forall (\delta \mathbf{u}, \delta \mathbf{u}_s), \quad (3.2)$$

where $\boldsymbol{\sigma}$ and $\boldsymbol{\sigma}_s$ are symmetric second order tensors.

By using the formula (2.41), the terms of the surface integral in Eq. (3.2) can be written as follow:

$$\begin{aligned} \int_{\Gamma} \delta \mathbf{u}_s \cdot (\mathbf{div}_s \boldsymbol{\sigma}_s + \llbracket \boldsymbol{\sigma} \rrbracket \cdot \mathbf{n}) \, d\Gamma &= \int_{\Gamma} \mathbf{div}_s (\delta \mathbf{u}_s \cdot \boldsymbol{\sigma}_s) \, d\Gamma \\ &\quad - \int_{\Gamma} (\nabla_s^s \delta \mathbf{u}_s) : \boldsymbol{\sigma}_s \, d\Gamma + \int_{\Gamma} \delta \mathbf{u}_s \cdot \llbracket \boldsymbol{\sigma} \rrbracket \cdot \mathbf{n} \, d\Gamma \quad \forall (\delta \mathbf{u}_s). \end{aligned} \quad (3.3)$$

Applying the surface divergence theorem (2.43) for the first term on the right hand

of Eq. (3.3) gives:

$$\begin{aligned} \int_{\Gamma} \delta \mathbf{u}_s \cdot (\mathbf{div}_s \boldsymbol{\sigma}_s + \llbracket \boldsymbol{\sigma} \rrbracket \cdot \mathbf{n}) d\Gamma &= \int_{\partial\Gamma} \delta \mathbf{u}_s \cdot \boldsymbol{\sigma}_s \cdot \mathbf{m} dl \\ &\quad - \int_{\Gamma} (\nabla_s^s \delta \mathbf{u}_s) : \boldsymbol{\sigma}_s d\Gamma + \int_{\Gamma} \delta \mathbf{u}_s \cdot \llbracket \boldsymbol{\sigma} \rrbracket \cdot \mathbf{n} d\Gamma \quad \forall (\delta \mathbf{u}_s), \end{aligned} \quad (3.4)$$

where $\partial\Gamma$ is the boundary of Γ and \mathbf{m} is the outward unit normal vector to $\partial\Gamma$.

The bulk integral terms in Eq. (3.2) can be rewritten as:

$$\begin{aligned} \int_{\Omega \setminus \Gamma} \delta \mathbf{u} \cdot (\mathbf{div} \boldsymbol{\sigma} + \mathbf{b}) d\Omega &= \int_{\Omega \setminus \Gamma} \mathbf{div}(\delta \mathbf{u} \cdot \boldsymbol{\sigma}) d\Omega \\ &\quad - \int_{\Omega \setminus \Gamma} (\nabla^s \delta \mathbf{u}) : \boldsymbol{\sigma} d\Omega + \int_{\Omega \setminus \Gamma} \delta \mathbf{u} \cdot \mathbf{b} d\Omega \quad \forall (\delta \mathbf{u}). \end{aligned} \quad (3.5)$$

For the case of a two phase domain that includes an interface ($\Omega = \Omega^{(1)} \cup \Omega^{(2)} \cup \Gamma$), Esmaeili et al [Esmaeili et al., 2017] proposed an extended form of the divergence theorem

$$\int_{\Omega \setminus \Gamma} \mathbf{div}\{\bullet\} d\Omega = \int_{\partial\Omega} \{\bullet\} \cdot \tilde{\mathbf{n}} dS - \int_{\Gamma} \llbracket \bullet \rrbracket \cdot \mathbf{n} d\Gamma. \quad (3.6)$$

Considering this extended divergence theorem, Eq (3.6) becomes:

$$\begin{aligned} \int_{\Omega \setminus \Gamma} \delta \mathbf{u} \cdot (\mathbf{div} \boldsymbol{\sigma} + \mathbf{b}) d\Omega &= \int_{\partial\Omega} \delta \mathbf{u} \cdot \boldsymbol{\sigma} \cdot \tilde{\mathbf{n}} dS \\ &\quad - \int_{\Gamma} \llbracket \delta \mathbf{u} \cdot \boldsymbol{\sigma} \rrbracket \cdot \mathbf{n} d\Gamma - \int_{\Omega \setminus \Gamma} (\nabla^s \delta \mathbf{u}) : \boldsymbol{\sigma} d\Omega + \int_{\Omega \setminus \Gamma} \delta \mathbf{u} \cdot \mathbf{b} d\Omega \quad \forall (\delta \mathbf{u}). \end{aligned} \quad (3.7)$$

Substituting Eq. (3.7) and Eq. (3.4) into Eq. (3.2) leads to: $\forall (\delta \mathbf{u}, \delta \mathbf{u}_s)$

$$\begin{aligned} \int_{\Omega \setminus \Gamma} (\nabla^s \delta \mathbf{u}) : \boldsymbol{\sigma} d\Omega + \int_{\Gamma} \llbracket \delta \mathbf{u} \cdot \boldsymbol{\sigma} \rrbracket \cdot \mathbf{n} d\Gamma &- \int_{\partial\Omega} \delta \mathbf{u} \cdot \boldsymbol{\sigma} \cdot \tilde{\mathbf{n}} dS - \int_{\Omega \setminus \Gamma} \delta \mathbf{u} \cdot \mathbf{b} d\Omega \\ &+ \int_{\Gamma} (\nabla_s^s \delta \mathbf{u}_s) : \boldsymbol{\sigma}_s d\Gamma - \int_{\partial\Gamma} \delta \mathbf{u}_s \cdot (\boldsymbol{\sigma}_s \cdot \mathbf{m}) dl - \int_{\Gamma} \delta \mathbf{u}_s \cdot \llbracket \boldsymbol{\sigma} \rrbracket \cdot \mathbf{n} d\Gamma = 0. \end{aligned} \quad (3.8)$$

In the following, we assume that the interface Γ is closed so that the term $\int_{\partial\Gamma}$ vanishes. Moreover, no decohesion at the interface is considered. It implies that $\llbracket \delta \mathbf{u} \cdot \boldsymbol{\sigma} \rrbracket \cdot \mathbf{n} = \delta \mathbf{u} \cdot \llbracket \boldsymbol{\sigma} \rrbracket \cdot \mathbf{n}$ and $\delta \mathbf{u}_s = \delta \mathbf{u}|_{\Gamma}$, which means that the interface displacement is a restriction of the bulk displacement on the interface. Thus, Eq. (3.8) can be written as: $\forall (\delta \mathbf{u}, \delta \mathbf{u}_s)$

$$\int_{\Omega \setminus \Gamma} \nabla^s \delta \mathbf{u} : \boldsymbol{\sigma} d\Omega + \int_{\Gamma} \nabla_s^s \delta \mathbf{u}_s : \boldsymbol{\sigma}_s d\Gamma - \int_{\Omega \setminus \Gamma} \delta \mathbf{u} \cdot \mathbf{b} d\Omega - \int_{\partial\Omega} \delta \mathbf{u} \cdot \boldsymbol{\sigma} \cdot \tilde{\mathbf{n}} dS = 0. \quad (3.9)$$

Taking into account the constitutive laws of the bulk and the interface presented in problem (2.54)

$$\begin{cases} \boldsymbol{\sigma} = \mathbb{C}^{(i)} : \boldsymbol{\epsilon} & \text{in } \Omega^{(i)} \\ \boldsymbol{\sigma}_s = \mathbb{C}^s : \boldsymbol{\epsilon}_s & \text{on } \Gamma \end{cases} \quad (3.10)$$

and the fact that usually test functions are chosen equal to zero on the Dirichlet

boundary $\partial\Omega_u$, the weak form (3.9) can be expressed as:

$$\begin{aligned} \int_{\Omega \setminus \Gamma} \boldsymbol{\epsilon}(\delta \mathbf{u}) : \mathbb{C}^{(i)} : \boldsymbol{\epsilon}(\mathbf{u}) d\Omega + \int_{\Gamma} \boldsymbol{\epsilon}_s(\delta \mathbf{u}_s) : \mathbb{C}^s : \boldsymbol{\epsilon}_s(\mathbf{u}_s) d\Gamma \\ = \int_{\Omega \setminus \Gamma} \delta \mathbf{u} \cdot \mathbf{b} d\Omega + \int_{\partial\Omega_F} \delta \mathbf{u} \cdot \mathbf{F} d\Gamma \quad \forall (\delta \mathbf{u}, \delta \mathbf{u}_s), \end{aligned} \quad (3.11)$$

where $\boldsymbol{\epsilon}\{\bullet\} = \nabla^s\{\bullet\}$ and $\boldsymbol{\epsilon}_s\{\bullet\} = \nabla_s^s\{\bullet\}$.

Finally, if the relation (2.53) is taken into account, the weak form (3.11) can be written as:

$$\begin{aligned} \int_{\Omega \setminus \Gamma} \boldsymbol{\epsilon}(\delta \mathbf{u}) : \mathbb{C}^{(i)} : \boldsymbol{\epsilon}(\mathbf{u}) d\Omega + \int_{\Gamma} \mathbf{P} \cdot \boldsymbol{\epsilon}(\delta \mathbf{u}) \cdot \mathbf{P} : \mathbb{C}^s : \mathbf{P} \cdot \boldsymbol{\epsilon}(\mathbf{u}) \cdot \mathbf{P} d\Gamma \\ = \int_{\Omega \setminus \Gamma} \delta \mathbf{u} \cdot \mathbf{b} d\Omega + \int_{\partial\Omega_F} \delta \mathbf{u} \cdot \mathbf{F} d\Gamma \quad \forall (\delta \mathbf{u}). \end{aligned} \quad (3.12)$$

The next sections of this chapter aim at comparing two different implementations of an elastic interface namely XFEM [Yvonnet et al., 2008] and an approach based on interface element [Wei et al., 2006]. The two previous equivalent versions of the weak form of the equilibrium equations (3.11) and (3.12) serve, respectively, as basis for interface element discretization and XFEM discretization. Indeed, as shown in the next section, the major difference between the two approaches is the explicit (interface element approach) or implicit (XFEM approach) discretization of the displacement along with the interface Γ . We detail the difference in terms of discretization strategies for the two approaches in the following.

3.3 Finite element implementation

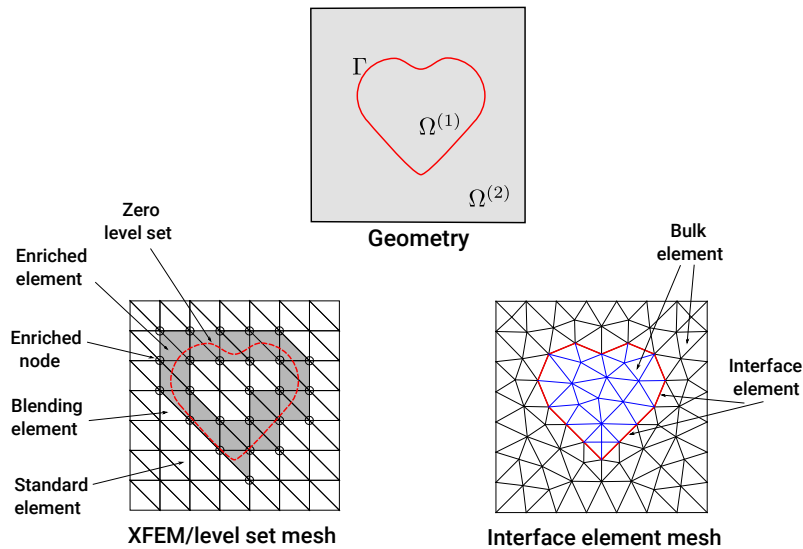


Figure 3.2: An example of XFEM mesh and Interface element mesh.

For the sake of simplicity, in this work, we limit our investigation to three nodes

triangular elements. In the following, we discuss the choices in terms of interpolations and numerical implementation for two different numerical descriptions of the kinematics of the interface, namely XFEM/level set and standard FEM with interface elements. For XFEM/level set approach, the interface is implicitly described by the introduction of a level-set function. Thus, regular meshes can be adopted even if the interface has a complex geometry. On the contrary, for the interface element approach, the interface is explicitly described through a conforming mesh (see Figure 3.2). In both cases, for 2D context, the strain and stress tensor can be expressed in the vector forms:

$$\begin{aligned}\boldsymbol{\epsilon} &= \begin{bmatrix} \epsilon_{11} & \epsilon_{22} & \eta\epsilon_{33} & 2\epsilon_{12} \end{bmatrix}^T, \\ \boldsymbol{\sigma} &= \begin{bmatrix} \sigma_{11} & \sigma_{22} & \eta\sigma_{33} & \sigma_{12} \end{bmatrix}^T,\end{aligned}\tag{3.13}$$

where, for plane strain problems $\eta = 0$ and the indices 1,2,3 are associated with respectively directions e_x , e_y , and e_z while for axisymmetric problems $\eta = 1$ and the indices 1,2,3 are associated with directions e_r , e_z and e_θ .

3.3.1 Standard FEM with surface/interface element

The first strategy explored in the paper of Wei et al [Wei et al., 2006] to account for a coherent interface is based on an explicit discretization of the interface (see Figure 3.2) through the use of interface elements with surface elasticity. This strategy had been detailed in [Esmaeili et al., 2017, Javili et al., 2017, Ottosen et al., 2015] in the framework of finite strains and in the general case of the imperfect interface where both tractions and displacements can be discontinuous across the interface. We develop here a similar strategy in the framework of small strains and focus only on the treatment of the surface elasticity so that no decohesion is, at that stage, taken into account. In that case, we consider the classical interpolation of the displacement in the bulk given as:

$$\mathbf{u}^h(\mathbf{x}) = \sum_{i=1}^n \mathbf{N}_i(\mathbf{x}) \mathbf{u}_i, \tag{3.14}$$

where \mathbf{N}_i is the standard finite element shape function associated with node i , along with a specific interpolation for the displacement on the interface:

$$\mathbf{u}_s^h(\mathbf{x}) = \sum_{i=1}^m \bar{\mathbf{N}}_i(\mathbf{x}) \mathbf{u}_{s,i}, \tag{3.15}$$

where $\bar{\mathbf{N}}_i$ is the shape function of interface element associated to node i and $\mathbf{u}_{s,i}$ corresponds to the displacements of node i along the interface direction obtained by projection of the components of the displacement in the global frame onto the local frame (see Figure 3.3):

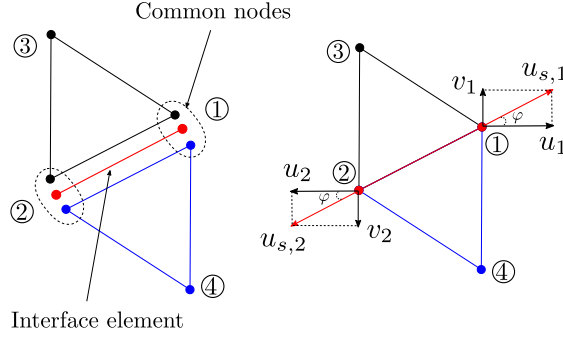


Figure 3.3: Interface element and bulk neighbor elements.

$$\begin{bmatrix} u_{s,1} \\ u_{s,2} \end{bmatrix} = \underbrace{\begin{bmatrix} \cos \varphi & \sin \varphi & 0 & 0 \\ 0 & 0 & \cos \varphi & \sin \varphi \end{bmatrix}}_{\mathbf{T}} \begin{bmatrix} u_1 \\ v_1 \\ u_2 \\ v_2 \end{bmatrix}, \quad (3.16)$$

where φ is the angle between the interface and the horizontal direction.

The surface strain tensor on the interface element e is then built such that:

$$\boldsymbol{\epsilon}_s^{(e)} = \bar{\mathbf{B}}^{(e)} \mathbf{T} \mathbf{u} \quad , \quad (3.17)$$

where $\bar{\mathbf{B}}^{(e)}$ is the matrix of shape function derivatives corresponding to a standard 1D element if 2D problems are considered.

By using the weak form (3.11) and the interpolations (3.14) and (3.15), we obtain the following discrete system of linear equations:

$$(\mathbf{K} + \mathbf{K}^s) \mathbf{u} = \mathbf{f} \quad , \quad (3.18)$$

where

$$\begin{aligned} \mathbf{K} &= \int_{\Omega^{(1)}} \mathbf{B}^T \mathbf{C}^{(1)} \mathbf{B} \tilde{\eta} d\Omega + \int_{\Omega^{(2)}} \mathbf{B}^T \mathbf{C}^{(2)} \mathbf{B} \tilde{\eta} d\Omega \quad , \\ \mathbf{f} &= \int_{\Omega} \mathbf{N}^T \mathbf{b} \tilde{\eta} d\Omega + \int_{\partial\Omega_F} \mathbf{N}^T \mathbf{F} \tilde{\eta} d\Gamma \\ \mathbf{K}^s &= \int_{\Gamma} \mathbf{T}^T \bar{\mathbf{B}}^T \mathbf{C}^s \bar{\mathbf{B}} \mathbf{T} \tilde{\eta} d\Gamma \quad , \end{aligned} \quad (3.19)$$

where \mathbf{B} is strain interpolation matrix for a standard triangular element, $\tilde{\eta} = 1$ for plane strain problems and $\tilde{\eta} = 2\pi r$ for axisymmetric problems and $\mathbf{C}^{(i)}$ is the matrix form of the elastic tensor of the phase (i)

$$\mathbf{C}^{(i)} = \begin{bmatrix} (\lambda^{(i)} + 2\mu^{(i)}) & \lambda^{(i)} & \eta\lambda^{(i)} & 0 \\ \lambda^{(i)} & (\lambda^{(i)} + 2\mu^{(i)}) & \eta\lambda^{(i)} & 0 \\ \eta\lambda^{(i)} & \eta\lambda^{(i)} & \eta(\lambda^{(i)} + 2\mu^{(i)}) & 0 \\ 0 & 0 & 0 & \mu^{(i)} \end{bmatrix} \quad i = 1, 2 \quad . \quad (3.20)$$

The surface elastic tensor \mathbf{C}^s is, when interface elements are considered, defined as:

$$\mathbf{C}^s = \begin{bmatrix} \lambda_s + 2\mu_s & \eta\lambda_s \\ \eta\lambda_s & \eta(\lambda_s + 2\mu_s) \end{bmatrix}. \quad (3.21)$$

With the plane strain hypothesis, $\eta = 0$, \mathbf{C}^s can be expressed with only one scalar $\mathbf{C}^s = \lambda_s + 2\mu_s$. In this case, 1D interface elements behave like springs with a stiffness equal to $\lambda_s + 2\mu_s$.

3.3.2 XFEM/level-set approach for modeling size effect

For the XFEM approach, the specific shape of the interface is defined by means of the introduction of a level set function $\phi(\mathbf{x})$. By denoting \mathbf{x}^c and r^c the center and radius of the inclusion (in the case we consider a circular inclusion), the interface Γ is geometrically defined by:

$$\phi(\mathbf{x}) = \|\mathbf{x} - \mathbf{x}^c\| - r^c = 0, \quad (3.22)$$

Usually, function $\phi(\mathbf{x})$ is chosen as the signed distance to the interface Γ . With such a choice, the sign of function $\phi(\mathbf{x})$ also defines the partition of the domain into two different phases : $\phi(\mathbf{x}) > 0$ in the matrix and $\phi(\mathbf{x}) < 0$ in the inclusion. The implicit interface is not discretized and we can not derive directly the surface strain tensor $\boldsymbol{\epsilon}_s$. In this case, Eq. (2.53) is used to extract the surface strain tensor which implies to form the projection operator $\mathbf{P} = \mathbf{I} - \mathbf{n} \otimes \mathbf{n}$ by numerically evaluating of the unit normal vector \mathbf{n} . This is achieved by considering the discretized form ϕ^h of the level set function $\phi(\mathbf{x})$:

$$\phi^h(\mathbf{x}) = \sum_{i=1}^n \mathbf{N}_i \phi_i. \quad (3.23)$$

where \mathbf{N}_i is the finite element shape function associated with node i and $\phi_i = \phi(\mathbf{x}_i)$ where \mathbf{x}_i corresponds to the position of node i . Therefore, the numerical evaluation of \mathbf{n} is obtained as follows:

$$\mathbf{n}(\mathbf{x}) = \frac{\nabla \phi(\mathbf{x})}{\|\nabla \phi(\mathbf{x})\|}, \quad (3.24)$$

To satisfy the discontinuous conditions (2.49) across the interface within the framework of XFEM, the enriched approximation proposed in [Moës et al., 2003] is used. This approximation is defined at a given point $\mathbf{x} \in \Omega_e$ by:

$$\mathbf{u}^h(\mathbf{x}) = \sum_{i=1}^n \mathbf{N}_i(\mathbf{x}) \mathbf{u}_i + \sum_{j=1}^m \mathbf{N}_j(\mathbf{x}) \psi(\mathbf{x}) \mathbf{a}_j, \quad (3.25)$$

where \mathbf{a}_j the additional degrees of freedom associated to node j and the index j corresponds to the set of nodes pertaining to the elements cut by the interface and

$\psi(\mathbf{x})$ is the enrichment function here defined as:

$$\psi(\mathbf{x}) = \sum_{i=1}^n |\phi_i| \mathbf{N}_i(\mathbf{x}) - \left| \sum_{i=1}^n \phi_i \mathbf{N}_i(\mathbf{x}) \right|. \quad (3.26)$$

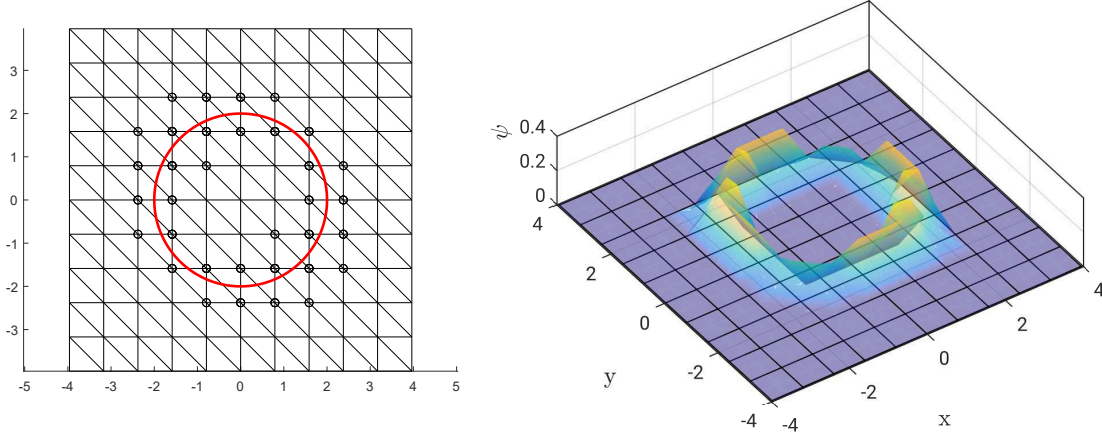


Figure 3.4: Enrichment function ψ for a circle interface in XFEM.

In [Moës et al., 2003], a comparison between an enrichment function defined as the absolute value of the level set function proposed by Sukumar et al [Sukumar et al., 2001] and the enrichment function (3.26) has been performed. The comparison showed that the enrichment function (3.26) gives better convergence. This enrichment function is equal to zero on the nodes of the enriched elements and on the standard (non-enriched) elements (see Figure 3.4). Its values are maximum along the interface and therefore this choice of $\psi(\mathbf{x})$ provides a jump on the strain field across the interface when $\nabla^s \mathbf{u}^h$ is evaluated. The zero value of this enrichment function on the nodes of the enriched elements suggests that a local enrichment could be proposed instead of a global one.

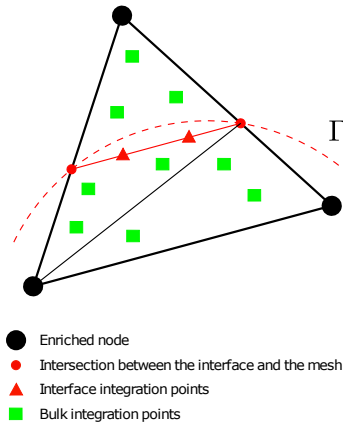


Figure 3.5: Element cut by the interface Γ , approximated interface and integration points in XFEM.

In order to compute the surface integral in the weak form (3.12), a two Gauss points integration is performed along the interface. Note that the geometry of the interface is discretized according to the discretization of the level set function $\phi(\mathbf{x})$ resulting in a piecewise linear approximation of the interface when considering linear finite element interpolation. For the bulk, the elements crossed by the interface are divided into sub-triangles where the numerical integration is carried out considering three integration points (see Figure 3.5). It has to be noticed that, due to the enrichment (see Eq. (3.25)), the interpolations of strains and stresses in the element crossed by the interface are one order higher than for standard elements. Finally, by using the approximation given in Eq. (3.25), the following discrete system of linear equations is obtained:

$$(\mathbf{K} + \mathbf{K}^s)\mathbf{d} = \mathbf{f} , \quad (3.27)$$

where

$$\begin{aligned} \mathbf{K} &= \int_{\Omega^{(1)}} \mathbf{B}^T \mathbf{C}^{(1)} \mathbf{B} \tilde{\eta} d\Omega + \int_{\Omega^{(2)}} \mathbf{B}^T \mathbf{C}^{(2)} \mathbf{B} \tilde{\eta} d\Omega , \\ \mathbf{f} &= \int_{\Omega} \mathbf{N}^T \mathbf{b} \tilde{\eta} d\Omega + \int_{\partial\Omega_F} \mathbf{N}^T \mathbf{F} \tilde{\eta} d\Gamma \\ \mathbf{K}^s &= \int_{\Gamma} \mathbf{B}^T \mathcal{M}^T \mathbf{C}^{(s)} \mathcal{M} \mathbf{B} \tilde{\eta} d\Gamma \end{aligned} \quad (3.28)$$

and \mathbf{d} gathers all the degrees of freedom:

$$\mathbf{d} = [\mathbf{u}_1 \dots \mathbf{u}_n \ \mathbf{a}_1 \dots \mathbf{a}_m]^T . \quad (3.29)$$

$\tilde{\eta} = 1$ for plane strain problems and $\tilde{\eta} = 2\pi r$ for axisymmetric problems.

$\mathbf{C}^{(1)}$, $\mathbf{C}^{(2)}$, $\mathbf{C}^{(s)}$ correspond to the matrix form of the elastic tensor of the phase (1), the phase (2) and the interface Γ , respectively:

$$\mathbf{C}^{(i)} = \begin{bmatrix} (\lambda^{(i)} + 2\mu^{(i)}) & \lambda^{(i)} & \eta\lambda^{(i)} & 0 \\ \lambda^{(i)} & (\lambda^{(i)} + 2\mu^{(i)}) & \eta\lambda^{(i)} & 0 \\ \eta\lambda^{(i)} & \eta\lambda^{(i)} & \eta(\lambda^{(i)} + 2\mu^{(i)}) & 0 \\ 0 & 0 & 0 & \mu^{(i)} \end{bmatrix} \quad i = 1, 2, s . \quad (3.30)$$

The matrix \mathbf{B} is defined as $\mathbf{B} = [\mathbf{B}_1 \dots \mathbf{B}_n \hat{\mathbf{B}}_1 \dots \hat{\mathbf{B}}_m]$ with $\mathbf{B}_i = \mathbf{L}(N_i)$ (\mathbf{L} is the standard matrix form of the symmetric gradient operator) and $\hat{\mathbf{B}}_j = \mathbf{L}(N_j\psi)$. The matrix \mathcal{M} is defined according to

$$\mathcal{M} = \begin{bmatrix} P_{11}^2 & P_{12}^2 & 0 & P_{11}P_{12} \\ P_{12}^2 & P_{22}^2 & 0 & P_{12}P_{22} \\ 0 & 0 & \eta & 0 \\ 2P_{11}P_{12} & 2P_{12}P_{22} & 0 & (P_{12}^2 + P_{11}P_{22}) \end{bmatrix} , \quad (3.31)$$

where P_{11} , P_{12} , P_{22} are the component of the projection tensor \mathbf{P} .

We can note that the introduction of the surface elasticity on the interface Γ results

in the introduction of an added stiffness \mathbf{K}^s in the tangential direction of the interface in the resulting linear system of equations.

In the discrete systems of equations with the Interface element approach Eqs. (3.19) and with the XFEM/level set approach Eqs. (3.28) the stiffness matrix of the bulk \mathbf{K} and the external force \mathbf{f} are similar, while the stiffness matrix of the interface \mathbf{K}^s is different and depends on the surface strain calculation. The surface strain, in the Interface element approach, is a “real” deformation of the 1D (for 2D problems) interface elements, hence the surface elastic tensor \mathbf{C}^s can be expressed with only one scalar value (in the plane strain case). Meanwhile, in XFEM approach, the surface strain is a projection of the strain tensor of the bulk on the piecewise linear approximation of the interface, and the surface elastic stiffness tensor $\mathbf{C}^{(s)}$ is a second order tensor like the elastic stiffness tensor of the bulk.

In the next section, these two approaches are validated and their performance are compared for various numerical examples.

3.4 Numerical results

In this section, we compare the performance and results obtained from the two previously presented approaches for different problems. It’s worth pointing out that with current technologies, there is no possibility of direct measurement of the mechanical properties of the interface. This limitation can be circumvented by appealing to molecular dynamics computations for inverse identification of mechanical properties of the interface [Miller and Shenoy, 2000], [Shenoy, 2005] and [Mi et al., 2008]. The purpose in this section is to compare the performance of two numerical approaches. Therefore the mechanical parameters of the interface, the matrix and the inclusions are not chosen from real materials but to assess the sensibility and robustness of the considered numerical strategies to the problem parameters.

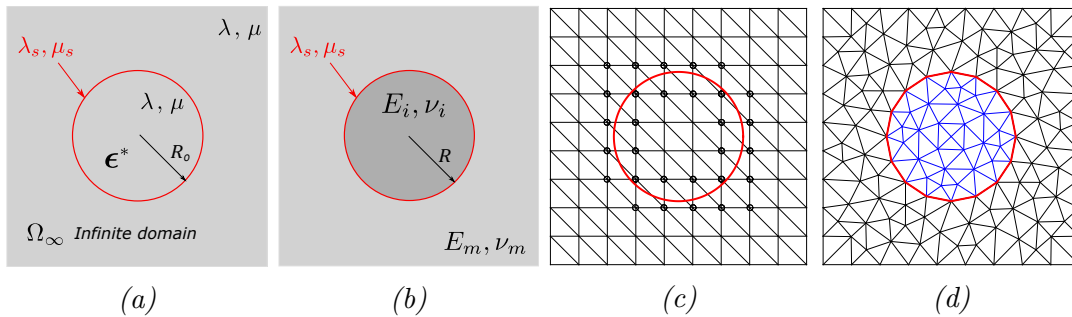


Figure 3.6: Problems with coherent interface are treated in the plane strain context: (a) Eshelby problem ; (b) Two-phases material; (c) XFEM mesh; (d) Interface element mesh.

In order to compare the two considered numerical approaches, we handle the problem of a cell with a cylindrical inclusion by considering plane strain hypothesis.

A representation of the geometry of the considered problem is given in Figure 3.6. To evaluate the performance of the two numerical approaches as regards the problem parameters, we vary the mechanical properties of the interface, the matrix, and the inclusion. To that purpose, we define the two "contrast" coefficients α and β :

$$\alpha = \frac{\hat{\kappa}_s}{\hat{\kappa}_m} \quad \text{and} \quad \beta = \frac{E_i}{E_m}, \quad (3.32)$$

where $\hat{\kappa}_s = \lambda_s + 2\mu_s$ is the plane strain surface modulus of the interface and $\hat{\kappa}_m$ denotes plane strain bulk modulus of the matrix. E_i and E_m denote the Young modulus of the inclusions and the matrix, respectively.

3.4.1 Eshelby's problem with coherent interface

We first consider the problem of an inclusion embedded in an infinite elastic domain and submitted to a dilatational eigenstrain ϵ^* (see Figure 3.6a). Examples of meshes considered for the two approaches are presented in Figures 3.6c and 3.6d. Such a problem corresponds to the so-called Eshelby problem for which analytical solutions including the effect of a coherent interface between the inclusion and the matrix are available in [Sharma and Ganti, 2004, Sharma et al., 2003, Sharma and Ganti, 2005, Sharma et al., 2006]. For the numerical computation, only a bounded domain is considered around the inclusion and the analytical solution in terms of displacements is prescribed on the boundary of the finite domain. In the results presented in this section, the loading conditions correspond to a dilatational eigenstrain ϵ^* prescribed to the inclusion and such that $\epsilon_{xx}^* = \epsilon_{yy}^* = 0.5$, $\epsilon_{zz}^* = 0$.

3.4.1.1 Convergence analysis

For the convergence analysis, we choose the radius of inclusion $R = 1nm$ and the volume fraction of inclusion $f = 0.2$. The performance of the numerical approaches considered in this chapter are evaluated through the evaluation of the error and rate of convergence, computed on the basis of the relative energy norm error defined by:

$$e = \sqrt{\frac{\int_{\Omega} (\epsilon^h(\mathbf{x}) - \epsilon(\mathbf{x})) : \mathbb{C} : (\epsilon^h(\mathbf{x}) - \epsilon(\mathbf{x})) d\Omega}{\int_{\Omega} \epsilon(\mathbf{x}) : \mathbb{C} : \epsilon(\mathbf{x}) d\Omega}}, \quad (3.33)$$

where ϵ^h is the computed strain with the considered numerical strategy and ϵ is the analytical solution.

All the computations are performed considering three-node triangular elements and the error is computed for various element sizes h (from 10x10nodes meshes to 80x80nodes meshes). The results are presented in Figure 3.7. As seen in Figure 3.7a, the introduction of a surface elasticity ($\alpha \neq 0$) degrades the rate of convergence of XFEM. For $\alpha = 0$ (no surface elasticity), the expected rate of convergence

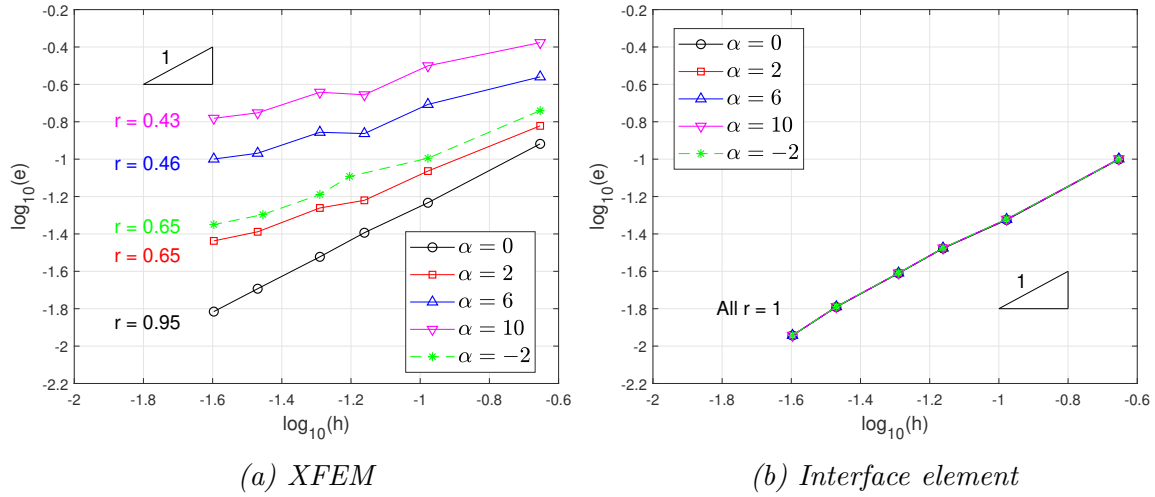


Figure 3.7: Convergence analysis for the extended Eshelby problem ($\beta = 1$) with a coherent interface.

$r \approx 1$ is recovered. On the contrary, when considering interface elements (see Figure 3.7b), the rate of convergence is not affected by the introduction of surface elasticity and we observe, as expected, a rate of convergence close to 1 for all values of α .

It has to be pointed out that for the case $\alpha < 0$ with XFEM, the surface stiffness matrix \mathbf{K}^s in Eqs. (3.28) is negative-definite and it influences the condition number of the total stiffness matrix and therefore causes an ill-conditioned problem leading to inaccurate results. In [Yvonnet et al., 2008], this issue has been handled by using the biconjugate gradient methods ("bicg" function in Matlab). In this test, we simply avoid the meshes leading to ill-conditioning for XFEM.

3.4.1.2 Investigation of local field

In the context of the Eshelby problem with coherent interface presented above, we can also investigate the strain field given by the two numerical approaches. This investigation allows evaluating the accuracy thanks to the comparison with the exact field given by the analytical solution [Sharma and Ganti, 2004].

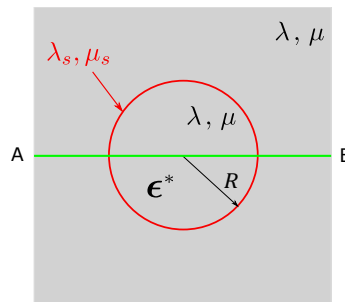


Figure 3.8: Geometry for local strain field investigation

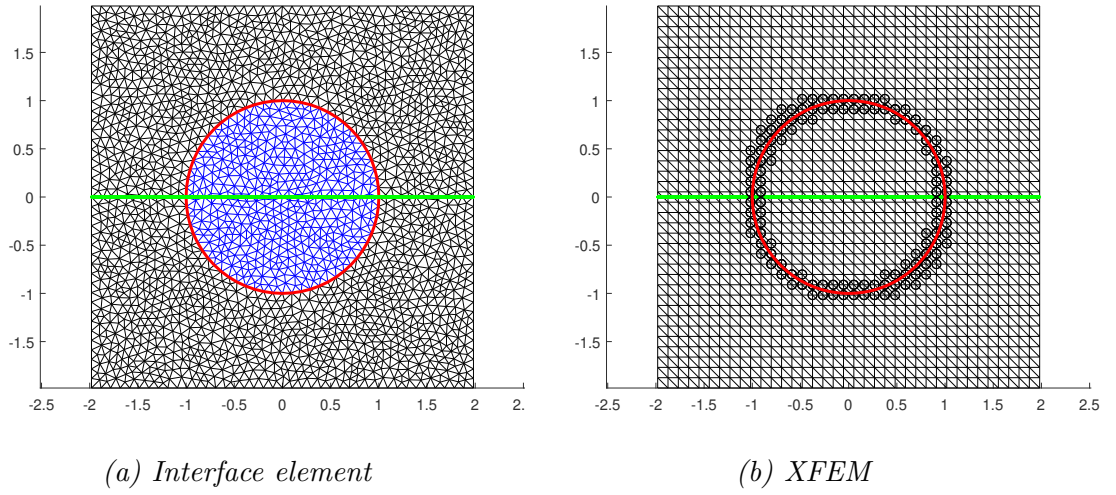


Figure 3.9: Meshes for local strain field investigation.

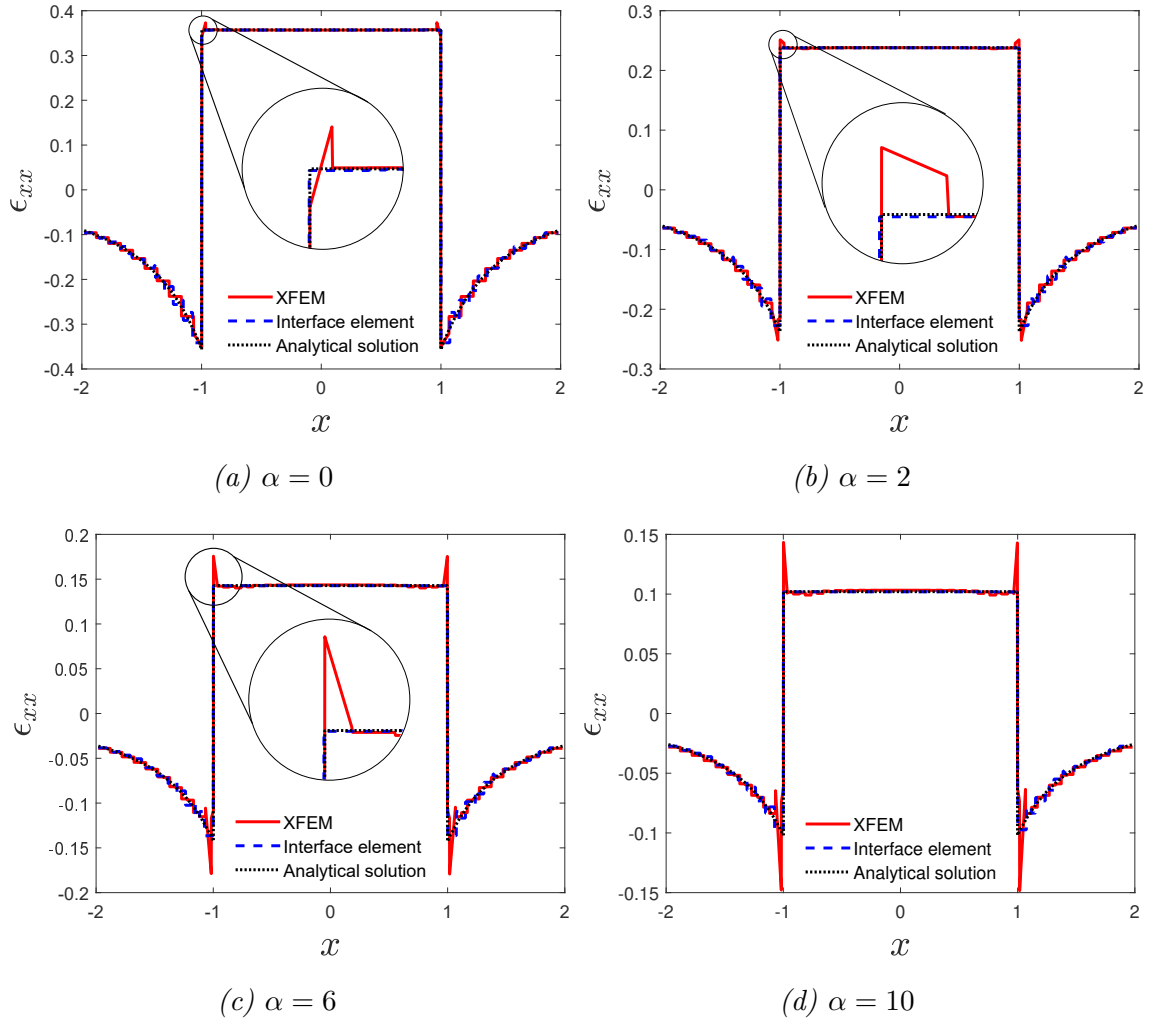


Figure 3.10: ϵ_{xx} along the line A-B for different values of α (XFEM vs Interface element).

By considering the strain component ϵ_{xx} along the line A-B corresponding to the centerline of the RVE (see Figure 3.8), the numerical strain field, as well as the strain jump across the interface, can be observed. 40x40 nodes meshes are used for this test (see Figures 3.9a and 3.9b). The strain component ϵ_{xx} along the line A-B computed by the two numerical approaches for different values of α are presented in Figure 3.10.

As expected, for XFEM approach, in the elements cut by the interface, the strain field is linear because of the displacement field enrichment, while for Interface element approach, in the elements adjacent to the interface, the strain field is constant. We notice that the prediction of XFEM is affected by the change of the value of α or in other words, by the stiffness of the interface. XFEM gives very good results in the classical case without surface elasticity ($\alpha = 0$) while the strain field and the amplitude of strain jump in cut elements (enriched elements) get worse when the value of alpha increases. This trend explains the degradation of convergence on the relative norm of XFEM presented in Figure 3.7. For the Interface element approach, α doesn't affect the results of the strain field.

3.4.1.3 Size effect indicator

In order to validate the efficiency of the two implemented strategies in reproducing the size effect observed when considering surface elasticity, we compute the size effect indicator defined by the ratio between interface energy and total energy proposed

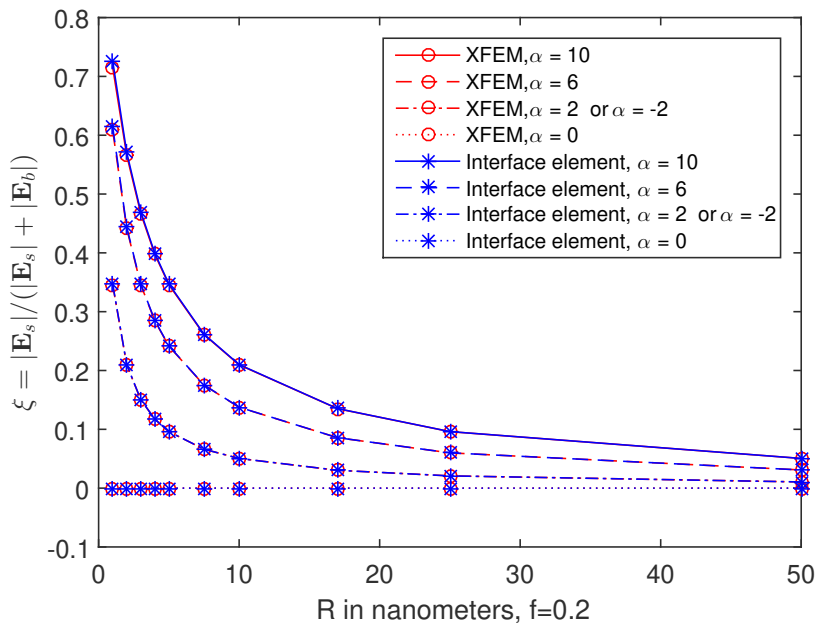


Figure 3.11: Size effect indicator versus inclusion radius for the extended Eshelby problem ($\beta = 1$).

in [Yvonnet et al., 2008]:

$$\xi = \frac{|\mathbf{E}_s|}{|\mathbf{E}_s| + |\mathbf{E}_b|} = \frac{|\int_{\Gamma} \boldsymbol{\sigma}_s : \boldsymbol{\epsilon}_s d\Gamma|}{|\int_{\Gamma} \boldsymbol{\sigma}_s : \boldsymbol{\epsilon}_s d\Gamma| + |\int_{\Omega} \boldsymbol{\sigma} : \boldsymbol{\epsilon} d\Omega|} \quad (3.34)$$

where \mathbf{E}_s and \mathbf{E}_b denote the surface and bulk energy, respectively.

We consider 40×40 nodes mesh for both numerical approaches and compute the size effect indicator ξ for the same volume fraction of inclusion $f = 0.2$ but with various radii of the inclusions and various values of the contrast parameter α . The results are given in Figure 3.11. It can be seen that the results are quite similar, both numerical approaches are capable of reproducing the expected size effect, though, as mentioned above, the convergence of XFEM is slower than the interface element for high values of α . For the inclusion bigger than $40nm$, the interface energy is very small compared to the total energy and the effect is therefore weakened. If we continue to increase the size of inclusion, we approach the case of classical composite where the size effect is too weak and can be ignored.

3.4.2 Size dependence of effective properties of two-phases nanocomposites

The two implemented numerical strategies can be used to estimate, numerically, the homogenized properties of materials presenting nano-inclusions (see Figure 3.6b). The effective bulk and effective shear modulus $(\kappa_{eff}^s, \mu_{eff}^s)$ of the nanocomposites differ from those predicted classically with no effect of the interface $(\kappa_{eff}, \mu_{eff})$. These normalized differences $(\kappa_{eff}^s - \kappa_{eff})/\kappa_{eff}$ and $(\mu_{eff}^s - \mu_{eff})/\mu_{eff}$ depend, for a given volume fraction of inclusion f , on the size of the inclusions.

In this subsection, we vary the value of the contrast parameter β from 0 (porous material) to 10 to assess how the stiffness contrast ratio of the two materials (matrix and inclusion) affects the size effect, the elastic properties of the interface remaining unchanged. The results are reported in Figure 3.12 for the bulk modulus and in Figure 3.13 for the shear modulus. Both strategies provide the same result in terms of size dependence.

For inclusions 10 times stiffer than the matrix ($\beta = 10$), the effective modulus is not much affected by the size of the inclusions while for nanoporous materials ($\beta = 0$) the size effect is more pronounced. The intensity of the size effect depends on the ratio between interface energy and bulk energy (see Figure 3.11). In this example, the stiffness of the matrix and the interface are kept constant. Hence, with the increase of the stiffness of the inclusion, the ratio between interface energy and bulk energy decreases and the effect is weakened. It is worth mentioning that for the purpose of this sensitivity analysis we assumed that the elastic properties of the interface are independent of the elastic properties of the surrounding materials

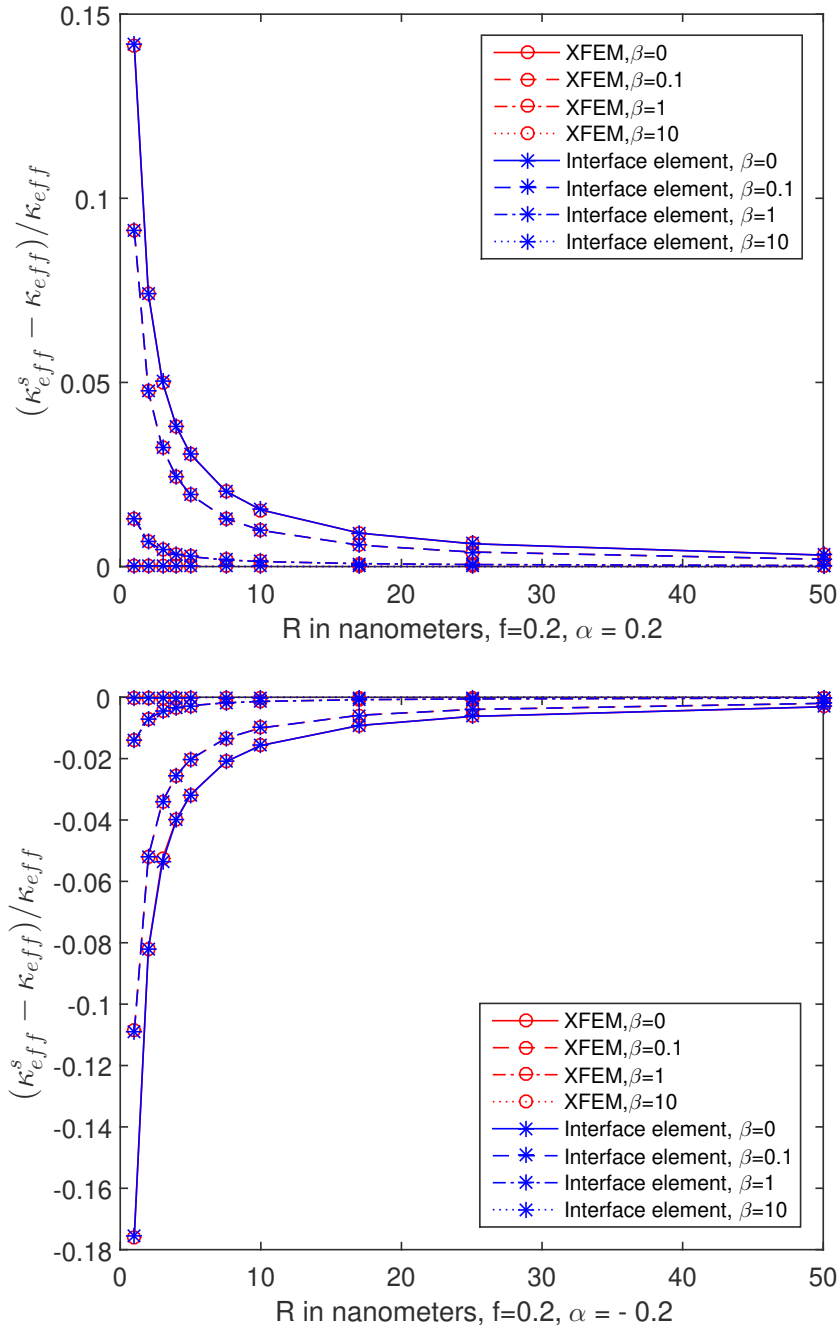


Figure 3.12: Size dependence of effective plane strain bulk modulus of two-phases materials for $\alpha = 0.2$ and $\alpha = -0.2$ for different values of the stiffness contrast β .

(matrix and inclusion).

For sizes of inclusion bigger than $40nm$, the influence of the interface effect on the effective modulus is very small and can be negligible. This result is coherent with the result of size effect indicator plotted in Figure 3.11 for Eshelby problem with the coherent interface model. When the size of inclusion is big enough, the size effect disappear and we then obtain the mechanical behavior of a conventional composite.

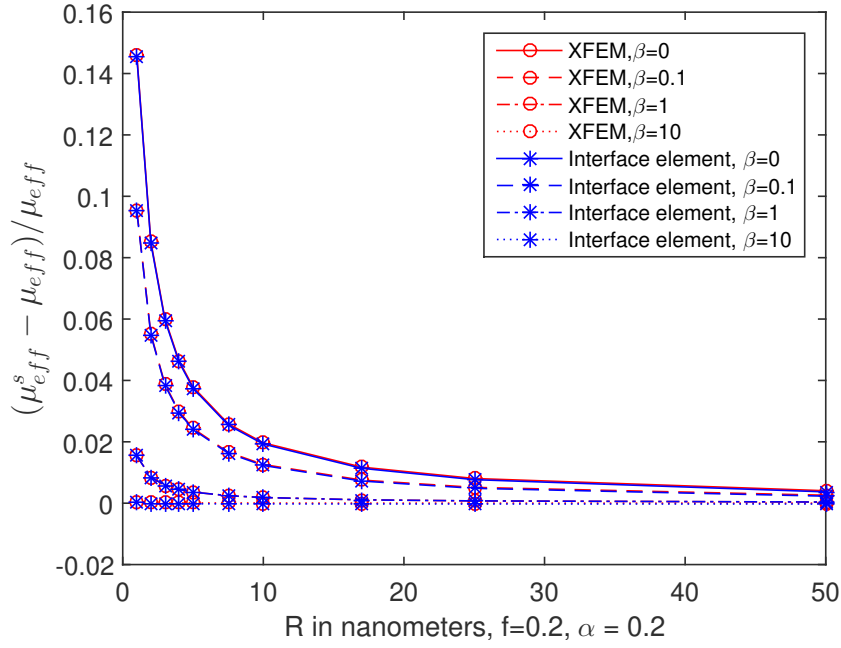


Figure 3.13: Size dependence of effective plane strain shear modulus of two-phases materials for $\alpha = 0.2$.

3.4.3 Effective properties of a nanoporous material and influence of the boundary conditions

In this subsection, we use the interface parameters obtained through molecular dynamics simulations [Miller and Shenoy, 2000] to compute the effective properties of an aluminum based nanoporous material.

- Aluminum matrix : Young modulus $E = 70$ GPa, Poisson ratio $\nu = 0.32$
- Elastic coherent interface: (given in Miller and Shenoy [Miller and Shenoy, 2000])
 - set A: $\lambda_s = 6.842$ N/m, $\mu_s = -0.375$ N/m.
 - set B: $\lambda_s = 3.48912$ N/m, $\mu_s = -6.2178$ N/m.
 - set C: $\lambda_s = 0$ N/m, $\mu_s = 0$ N/m (no interface elasticity).

We report in the following the results obtained considering different types of boundary conditions on the unit cell represented in Figure 3.6b namely: Periodic Boundary Conditions (PBC), Kinematic Uniform Boundary Conditions (KUBC), Stress Uniform Boundary Conditions (SUBC) (see Figure 3.14). The results obtained with both numerical strategies are compared to the ones obtained from the analytical homogenization strategy denoted as GSCM (Generalized Self-Consistent Method) [Chen et al., 2007, Quang and He, 2009]. The results, for the homogenized

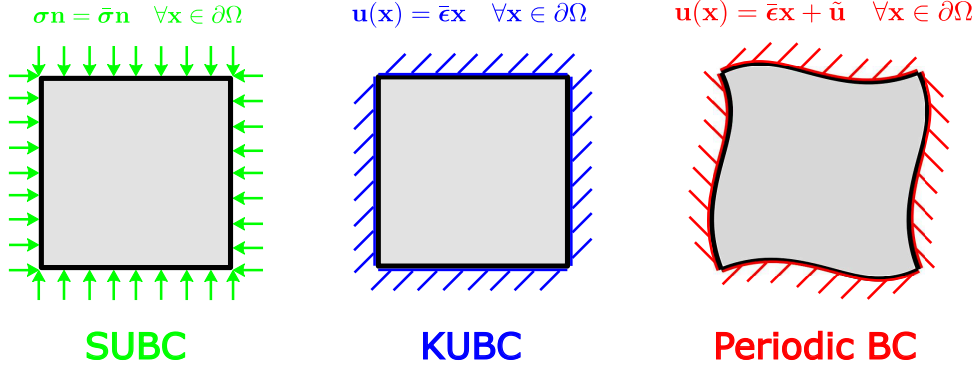


Figure 3.14: Three types of boundary conditions.

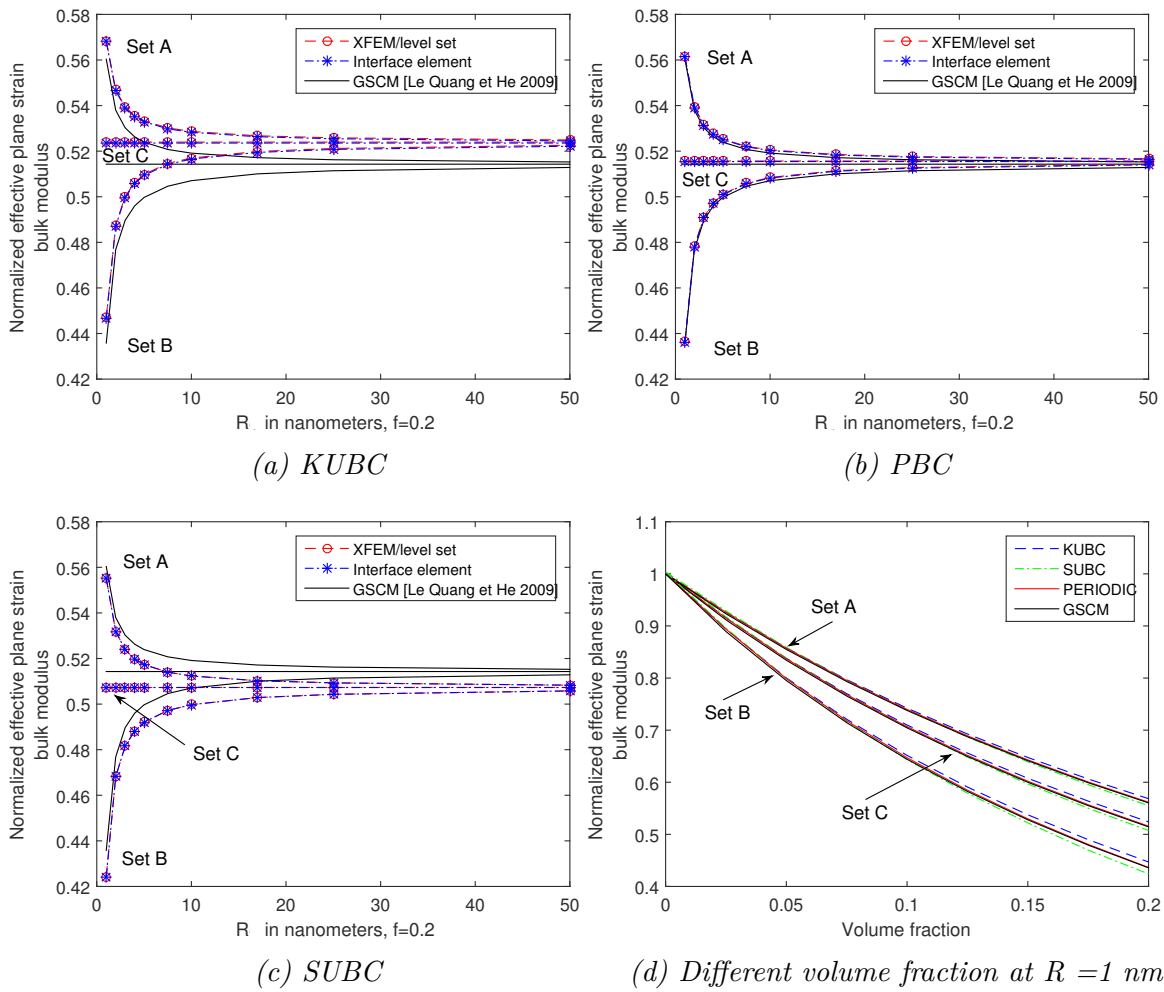


Figure 3.15: Size effect in effective plane-strain bulk modulus for different type of boundary conditions.

bulk moduli, are presented in Figure 3.15 for different values of the radius of void R and different volume fractions f .

We can observe in Figure 3.15 that, for high volume fractions of nano-voids SUBC and KUBC hypothesis lead to results quite different from the analytical predictions. But, in that comparison of the homogenized bulk modulus, for periodic

boundary conditions, the predictions of both numerical strategies are very close to the analytical ones (GSCM model). Note that with the GSCM model used in [Chen et al., 2007, Quang and He, 2009], the cylindrical inclusions in a shell of the matrix with a coherent interface, are surrounded by the effective medium. This result for periodic boundary conditions could be explained because the GSCM model takes into account interactions between inclusions and the Periodic Boundary Conditions are better than Kinematic or Stress Uniform Boundary Conditions to account for the interactions between the considered phases. Indeed, Kinematic and Stress Uniform Boundary Conditions do not take any phase interactions into account. For low volume fraction of nano-voids, numerical and analytical results are very close whatever the boundary conditions.

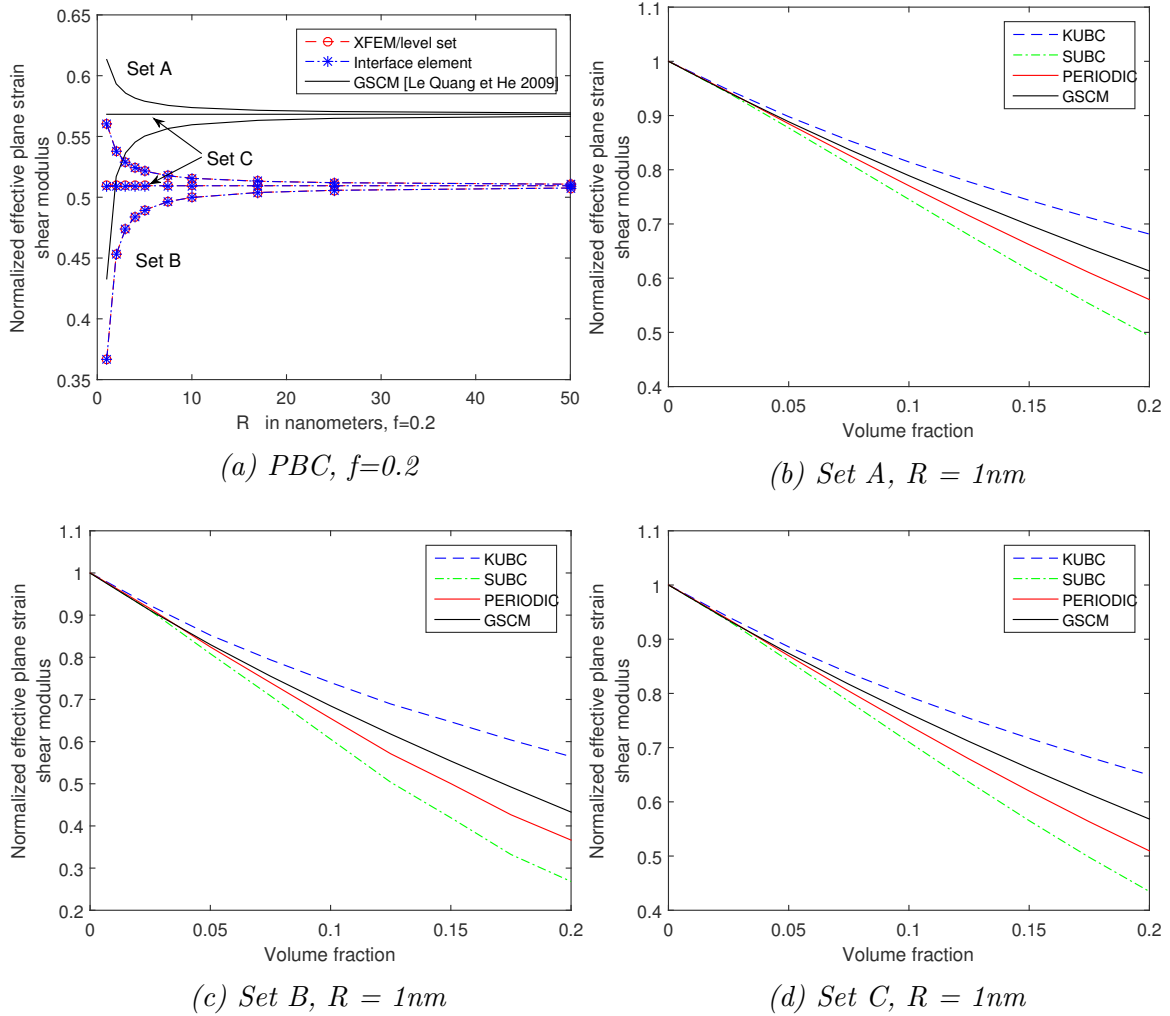


Figure 3.16: Size-dependent effective plane-strain shear modulus for different type of boundary conditions.

The same type of comparisons has been carried out considering the effective shear modulus. The results are presented in Figure 3.16. For the Periodic Boundary Condition, a good agreement between the results given by the two numerical

approaches can be observed in Figure 3.16a, the size dependence of the effective shear modulus is clearly shown up. However, unlike the case of bulk modulus, we found a difference between the results of GSCM and the results of the numerical homogenization, though the periodic boundary conditions still give the closest results (see Figures 3.16b, 3.16c and 3.16d).

3.4.4 Spherical void (axisymmetric model)

The axisymmetric analysis is used here to consider spherical nano-inclusions. This model allows us to work on the 2D meshes but handle symmetric 3D problems. The 2D meshes are represented in Figure 3.17 with $H=2R'$ and R' is chosen to obtain the volume fraction $f = 0.2$.

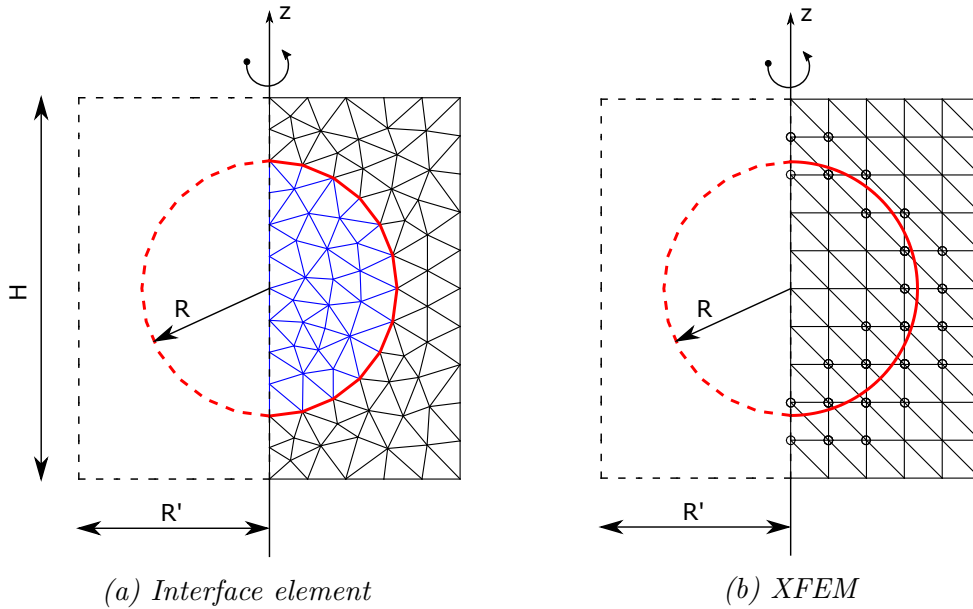


Figure 3.17: Spherical void with coherent interface is treated with axisymmetric model.

To take into account the axisymmetry conditions, the horizontal displacement of the nodes on the left boundary is set to 0 and the factors η in Eqs. (3.13), (3.20), (3.21), (3.30), (3.31) and $\tilde{\eta}$ in Eqs. (3.19), (3.28) are now set to $\eta = 1$ and $\tilde{\eta} = 2\pi r$. It is worth pointing out that the Periodic Boundary Condition can't be applied to the axisymmetric model. Therefore, only the KUBC and SUBC results are presented (see Figure 3.18). The effective properties given by the generalized Mori-Tanaka scheme (see [Duan et al., 2005b]) are, in the following, considered as the reference properties. As shown in Figure 3.18, for the bulk modulus, a good agreement between the two presented approaches and between analytical and numerical solutions is observed.

The results for the effective shear modulus are presented in Figure 3.19. Once again, as in the previous subsection, we obtain a difference between numerical and

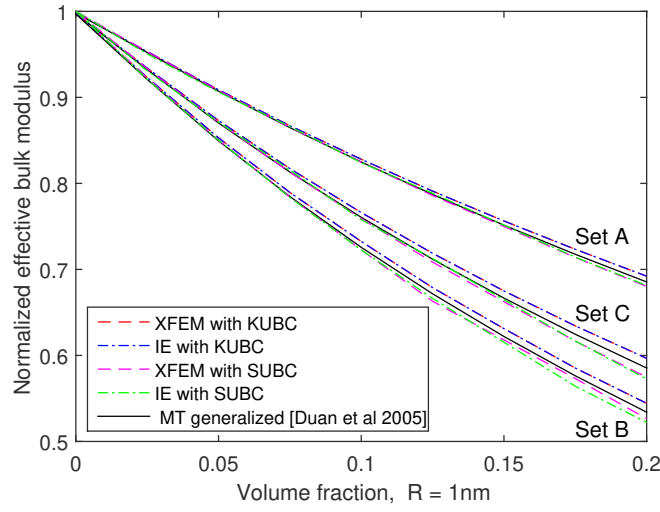


Figure 3.18: Size-dependent effective bulk modulus with a spherical nanovoid for different type of boundary condition (IE: Interface element; MT: Mori-Tanaka).

analytical results. However, the size effect is clearly observed and very good agreement between the two considered numerical approaches is obtained.

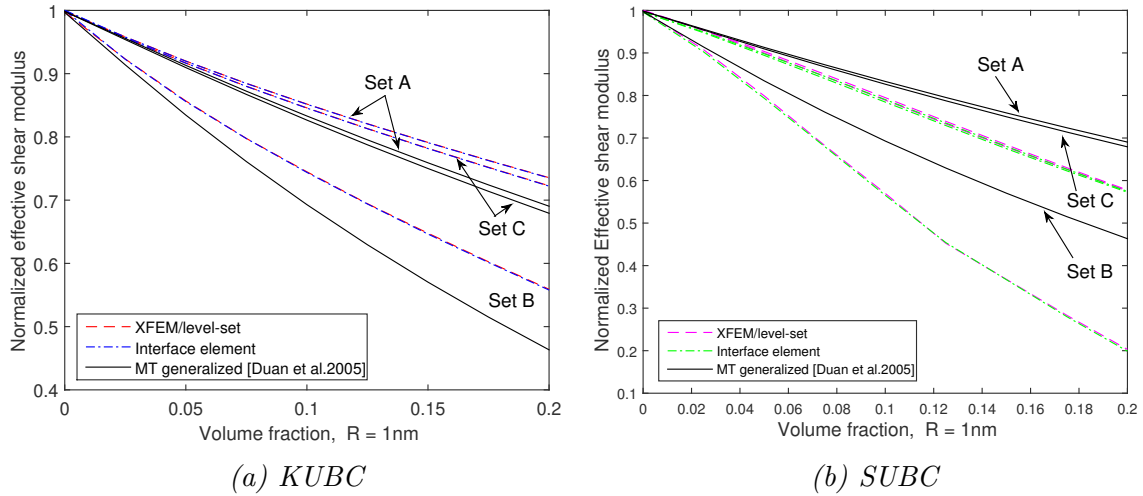


Figure 3.19: Size-dependent effective shear modulus with a spherical nanovoid for different types of boundary condition (MT: Mori-Tanaka).

3.4.5 Nanoporous material with random microstructure

In order to describe more realistic material configurations, we consider a material with randomly distributed nano-voids with coherent interface. We firstly consider the Interface element approach for treating several large RVEs. The elastic coherent interface constants for set A ($\lambda_s = 6.842$ N/m, $\mu_s = -0.375$ N/m) are employed and the radius void is set to 1 nm, while the number of voids is set to 5, 20 and 30. Since the volume fraction is fixed to 0.3, having more voids in the domain leads to

larger size of RVE (see Figure 3.20).

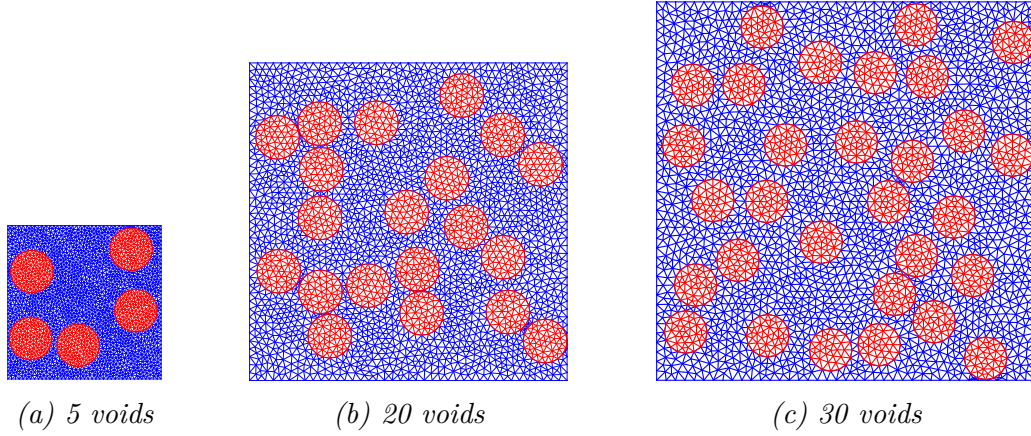


Figure 3.20: Conforming meshes of RVEs with randomly distributed nano-voids.

The computational homogenization is then performed on these RVEs with hydrostatic load. For each size of RVE, the statistical convergence on the mean value of the effective properties is carried out. This statistical convergence is evaluated by

$$A = \frac{1}{N_{iter}} \sum_{i=1}^{N_{iter}} A(i) , \quad (3.35)$$

where N_{iter} the number of realizations and A is the variable that we need to test (in our case k_{eff}/k_M).

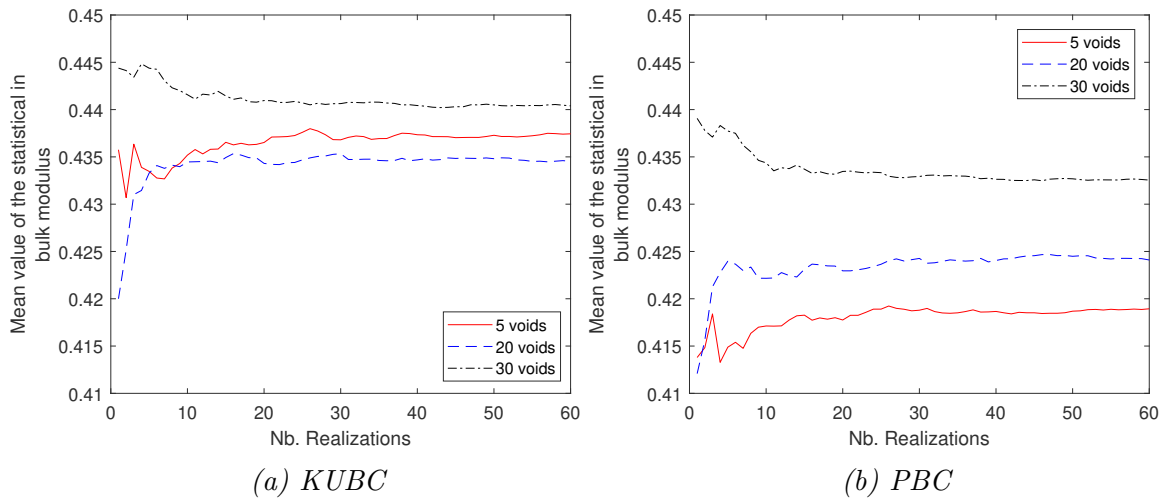


Figure 3.21: Statistical convergence on the normalized effective bulk modulus for different RVEs by the Interface element approach ($f = 0.3$, $E = 70$ GPa, $\nu = 0.32$, $\lambda_s = 6.842$ N/m, $\mu_s = -0.375$ N/m).

As shown in Figure 3.21 and Table 3.1, the mean value of the effective property of the bigger size RVE converge faster. The statistical convergence is reached after 40

realizations for the RVEs containing 5 voids, 30 realizations for RVEs containing 20 voids and only 25 realizations for RVEs with 30 voids.

Number of voids	Number of realizations required to converge	KUBC $\frac{k_{eff}}{k_M}$	PBC $\frac{k_{eff}}{k_M}$	Difference $\frac{k_{KUBC} - k_{PER}}{k_{PER}} \times 100\%$
5	40	0.4374	0.4189	4.42
20	30	0.4345	0.4241	2.46
30	25	0.4404	0.4325	1.81

Table 3.1: Results for different size of RVEs treated by the Interface element approach ($f = 0.3$, $E = 70$ GPa, $\nu = 0.32$, $\lambda_s = 6.842$ N/m, $\mu_s = -0.375$ N/m).

Moreover, when the size of the RVE is big enough, the three type of boundary conditions mentioned in the previous subsection tend to converge. Indeed, as presented in Table 3.1, the difference between the normalized effective bulk modulus obtained with KUBC and with PBC decreases with the increase of the RVE size. The deformation of a samples with 30 voids under hydro-static load with Interface element approach is presented in Figure 3.22.

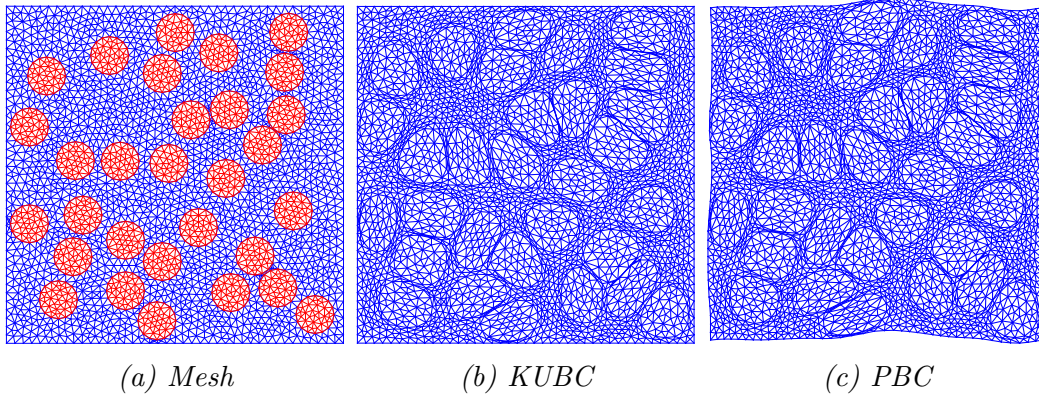
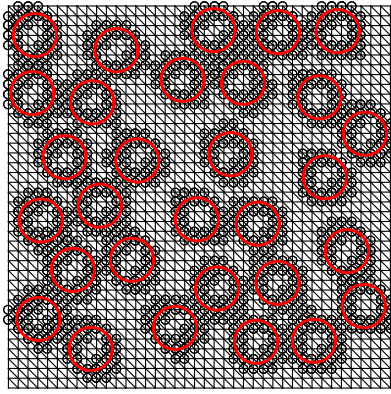


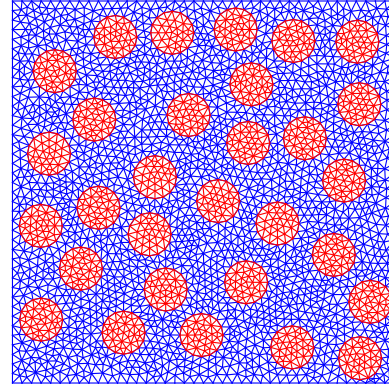
Figure 3.22: Deformation under hydro-static load $\bar{\epsilon}_{11} = \bar{\epsilon}_{22} = 0.5$, ($f = 0.3$, $E = 70$ GPa, $\nu = 0.32$, $\lambda_s = 6.842$ N/m, $\mu_s = -0.375$ N/m)

To complete the comparison between the two considered approaches, the RVE composed of 30 circular nanovoids randomly distributed is now computed with the XFEM approach. Since many voids have to be taken into account in the discretization, the level-set function defined in Eq. (3.22) is now computed to the nearest void.

It should be noticed that, in XFEM approach, an issue occurs when the distance between particles is too small, which leads to the case of an element being cut by many interfaces. This issue can be solved by using the multiple level set approach proposed by Tran et al [Tran et al., 2011] in which each inclusion is associated with its own level set and additional d.o.f are introduced. In this thesis, we simply avoid this issue by setting a constraint on the distance between inclusions/voids.



(a) XFEM non-conform mesh



(b) Interface element conform mesh

Figure 3.23: Two different samples for a 30 randomly distributed nano-voids RVE.

This distance must not be smaller than twice radius plus element size. This constraint will make the voids better distributed (see Figure 3.22a and Figure 3.23b) which leads to an increase of the effective modulus. However, it does not affect the fairness of the comparison since this constraint has been applied to both approaches (XFEM and Interface element). Two different discretizations resulting from two different samples are represented in Figure 3.23.

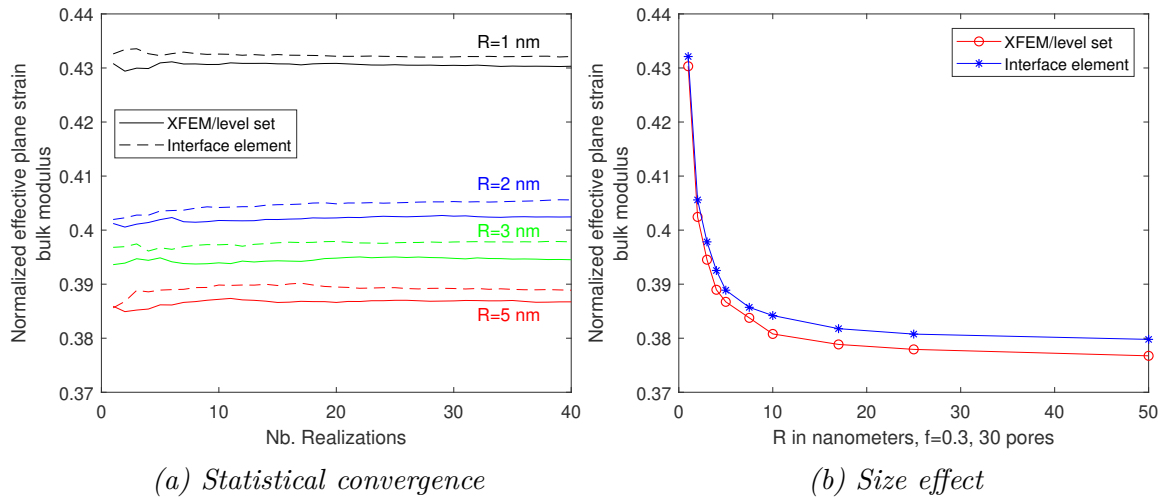


Figure 3.24: Normalized effective plane-strain bulk modulus for nanoporous material with randomly distributed nano-voids ($f = 0.3$, $E = 70$ GPa, $\nu = 0.32$, $\lambda_s = 6.842$ N/m, $\mu_s = -0.375$ N/m).

In order to estimate the size effect of the void on the effective properties, the volume fraction of voids is set to 0.3 while we vary their radius. For each radius, a statistical convergence on the mean value of the effective property is carried out. The meshes of about 20000 standard degrees of freedom have been used for the two approaches. The results in terms of effective bulk modulus with respect to the size

of the nano-voids are presented in Figure 3.24.

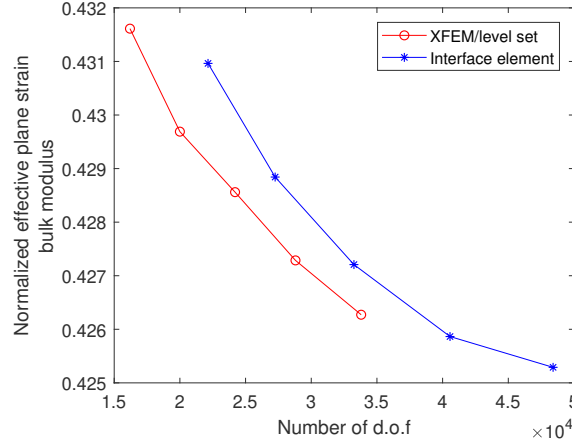


Figure 3.25: Convergence test on number of standard d.o.f.

The influence of the size of nano-voids is clearly observed with both approaches. Note that the comparison here only has a qualitative meaning since the mesh convergence has not been reached for both methods because of the limit of the memory space (see Figure 3.25). Moreover, even if the convergence on mesh size was reached, we couldn't conclude about the accuracy of the approaches in this case without a reference result. The computational cost of the two approaches is compared in Table 3.2. Even if the comparison in terms of computation time shown in Table 3.2 has only a relative meaning since no code optimization process has been done, it can be noticed that XFEM is still much expensive than the Interface element approach, at least for the solution process.

	X-FEM	Interface element
Number of standard d.o.f	20000	21528
Number of additional d.o.f	4560	0
Total unknowns	24560	21528
Size of elemental stiffness matrix	12×12	6×6
Final size of global stiffness matrix	$4.10^4 \times 4.10^4$	21528×21528
Computing time for 1 realization (sec)	106.676	45.223

Table 3.2: Comparison of computational cost (XFEM vs IE).

3.5 Conclusion

In the context of the prediction of the mechanical behavior of nanocomposites, a comparison of two numerical procedures namely XFEM approach and interface element based strategy has been performed. Both approaches are based on the implementation of a coherent interface with surface elasticity to account for size effect in nanocomposites. The results show that whatever the contrasts of "rigidity" of the surface with respect to the matrix (coefficient α in this chapter) the rate of convergence and the prediction of strain field of XFEM are affected by the presence of surface elasticity while for interface element approach, the rate of convergence and the local strain field are not affected. Even so, both of the considered numerical methods are able to reproduce the size effect of the Eshelby problem with coherent interface [Sharma and Ganti, 2004, Sharma et al., 2003, Sharma and Ganti, 2005, Sharma et al., 2006]. Moreover, the performances of the two numerical approaches in reproducing the size effect have also been evaluated for different fictitious materials by varying the contrast of rigidity between the matrix and the inclusions (coefficient β in this chapter). The results obtained by the two studied numerical approaches were also compared to micromechanical schemes proposed in [Quang and He, 2009] and [Duan et al., 2005b] in the context of the evaluation of the effective properties of nanoporous materials. To that purpose, different sets of boundary conditions were considered. As could be expected, due to the underlying hypothesis of the micromechanical model (interactions between inclusions), it emerges that, for the effective bulk moduli, the numerical estimations have a very good agreement with the micromechanical model when considering periodic boundary conditions on the unit cell. However, this is not the case for the estimation of the effective shear modulus although the Periodic Boundary Condition still gives the closest result to the GSCM solution among the three type of boundary conditions.

To test more realistic configurations, a composite material with randomly distributed nano-voids has been considered. The RVEs containing 5, 20 and 30 voids have been firstly treated by the Interface element approach. With the fixed volume fraction and radius, the number of voids is linked to the size of the RVE, an increase of the number of the voids implies an increase in the RVE size. The results confirmed that an increase of RVE reduces the influence of boundary conditions on the effective modulus. Therefore the RVE with 30 voids was chosen to complete the comparison between the two considered numerical approaches not only on the effective modulus but also on the computational cost. Both approaches have shown their ability to reproduce the size effect in this configuration but XFEM is more expensive than the Interface element.

The use of surface/interface elements in standard FEM depends massively on conforming meshes, which are costly for the cases with complex geometries. Meanwhile, the XFEM/level set approach, although it does not require any discretization

effort but the number of degrees of freedom and integration points is raised compared to standard FEM. Moreover, degradation of convergence due to the presence of surface elasticity is another drawback of XFEM. To overcome these disadvantages, a new numerical approach based on the Embedded Finite Element Method is proposed in the next chapter.

Finally, the studies presented in this chapter can serve as a foundation to assess the influence of the nonlinear behavior within the numerical homogenization strategy to get closer to more realistic behaviors than linear elastic behaviors for the constituents. The nonlinear results will be discussed in chapter 5 of this thesis.

Chapter 4

Embedded-FEM approach for modeling the size effect in nanocomposite

A new numerical approach based on the Embedded Finite Element Method (E-FEM) is elaborated in order to model size effect of nanocomposites. For this purpose, a comparison of the performance of the three classically considered formulations of E-FEM is performed for the simple case of a weak discontinuity without surface elasticity. Based on its good performance, the E-FEM standard Statically and Kinematically Optimal Nonsymmetric (SKON) formulation is then chosen to incorporate a surface elasticity at the interface between the matrix and the inclusions. The results obtained with the proposed approach for a couple of problems in the case of nanocomposites (Eshelby problem, two-phase composite, random micro-structures) are confronted with analytical solutions and the Interface Element approach. The developed approach is shown to be an efficient tool for the evaluation and prediction of the mechanical behavior of nanocomposite materials.

Contents

4.1	Introduction	68
4.2	E-FEM formulations to handle weak discontinuities	70
4.2.1	Hu-Washizu three-field variational formulation	70
4.2.2	Enhanced assumed strain method	71
4.2.3	E-FEM discretization	73

4.2.4	Resolution strategy	77
4.3	Performance of the three E-FEM formulations: SOS, KOS and SKON	78
4.4	E-FEM approaches for two phases material with strong contrast of properties	81
4.5	E-FEM with coherent interface model	88
4.5.1	Surface strain enhancement	88
4.5.2	Variational formulation with coherent interface model	89
4.5.3	Enhanced surface strain interpolation	91
4.6	Numerical examples using E-FEM with interface effect	94
4.6.1	Eshelby problem with coherent interface	94
4.6.2	Two phases nanocomposite	96
4.6.3	Nanocomposites with random micro-structures	99
4.7	Conclusion	101

4.1 Introduction

In this chapter, we propose an efficient numerical approach that requires neither a conforming mesh nor additional nodal degrees of freedom. The development is built on the Embedded Finite Element Method (E-FEM). Although E-FEM is usually used to handle strong discontinuities [Dvorkin et al., 1990], [Simo et al., 1993], [Linder and Armero, 2007], [Brancherie and Ibrahimbegovic, 2009], it was originally introduced by Ortiz et al [Ortiz et al., 1987] to capture weak discontinuities to improve the resolution of shear bands. Considering an Assumed Strain Finite Element Method, Ortiz et al enhanced the strain field to embed strain discontinuity in a single element. Based on this idea, two parallel weak discontinuity lines allowing to contain a band of localized strain have been proposed by Belytschko et al [Belytschko et al., 1988]. Several different formulations of E-FEM were developed in the same spirit: the approximation of the displacement or/and strain fields are enriched with additional parameters to capture the jump in the displacement field (strong discontinuity) or strain field (weak discontinuity). The enrichment related to displacement jumps or strain jumps is defined independently for every single element cut by the interface where the jump occurs. Different studies have been derived from various principles, starting from the extended principle of virtual work over Hellinger Reissner [Dujc et al., 2013] to Hu-Washizu variational principle [Roubin et al., 2015], using an enhanced assumed strain (EAS) or B-bar format. For handling strong discontinuities, the E-FEM approaches has been widely applied to many

interesting problems such as piezoelectric materials [Linder and Miehe, 2012], geomaterials [Foster et al., 2007], coupled formulations [Linder et al., 2011], finite strains [Armero and Garikipati, 1996], crack branching [Linder and Armero, 2009], dynamic fracture [Nikolić et al., 2018], etc.

The most interesting advantage of E-FEM (compared to XFEM presented in chapter 3) is that the additional unknowns are solved and condensed at the element level. Hence, the final system of equations to be solved at the global level has the same number of unknowns than a standard Finite Element problem set on the same spatial discretization. In terms of numerical accuracy, Oliver et al [Oliver et al., 2006] compared E-FEM with XFEM for several selected examples and proved that E-FEM can be as accurate as XFEM. However, if a lot of works focus on the use of E-FEM in the context of failure analysis (involving strong discontinuities), very few studies concern the use of E-FEM for numerical homogenization where weak discontinuities have to be taken into account.

Three formulations of E-FEM based on different choices of interpolations have been developed, namely, Statically Optimal Symmetric (SOS), Kinematically Optimal Symmetric (KOS), and Statically and Kinematically Optimal Nonsymmetric (SKON), a detailed comparison of those approaches in strong discontinuities context has been proposed in [Jirásek, 2000] and [Cazes et al., 2016].

In this chapter, we firstly present a comparative study of the performance of the three types of formulations for the case of weak discontinuities which, to the best of our knowledge, has never been presented in the literature. On the basis of this comparison, we then propose an enhanced SKON formulation allowing to incorporate the effect of a coherent interface. In that formulation, the interface mechanical behavior is taken into account and the traction continuity condition at the discontinuity line (interface) is replaced by the generalized Young-Laplace equation (2.48).

This chapter is organized as follows: in section 4.2, the three basic E-FEM formulations are built in the case of standard weak discontinuities. In section 4.3, a comparative study of the performance of the three types of interpolations for handling weak discontinuity problems is presented. Then, we discuss, in section 4.4, an issue of the E-FEM approach in the case of the high contrast of rigidity between the matrix and the inclusion for composite material. On the basis of the comparison presented in section 4.3, we propose in section 4.5 an enhanced SKON formulation allowing, in the context of composite material, to incorporate the effect of surface elasticity at the matrix/inclusion interface. Due to the introduction of surface elasticity on the interface, additional surface terms appear in both global and local equations. In section 4.6, the results obtained from the proposed approach, related to convergence analysis, linear homogenization with periodic microstructure and random microstructure are compared to the analytical solutions as well as to

the Interface element approach results. In section 4.7, several conclusions of the proposed approach are drawn.

4.2 E-FEM formulations to handle weak discontinuities

In this section, the three variants of E-FEM formulation are revisited for problems with weak discontinuities. We consider here a continuum body described by a bounded domain $\Omega \subset \mathbb{R}^d$ ($d = 2$ or 3), with boundary $\partial\Omega$. This domain consists of two-phases $\Omega^{(1)}$ and $\Omega^{(2)}$ (in the following $\Omega^{(1)}$ and $\Omega^{(2)}$ denote inclusion and matrix, respectively). These two phases are partitioned by a **perfect interface** Γ meaning that neither surface elasticity nor debonding are taken into account, (see Figure 4.1). We denote as \mathbf{n} the unit normal vector pointing, conventionally, from $\Omega^{(1)}$ toward $\Omega^{(2)}$.

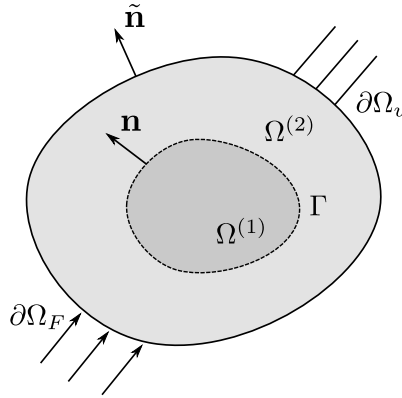


Figure 4.1: Problem of two phases material with a perfect interface (classical composite).

The outward unit normal to $\partial\Omega$ is denoted $\tilde{\mathbf{n}}$. The boundary $\partial\Omega$ is partitioned into $\partial\Omega_u$ where Dirichlet boundary conditions are prescribed and $\partial\Omega_F$ where Neumann boundary conditions hold ($\partial\Omega_F \cup \partial\Omega_u = \partial\Omega$ and $\partial\Omega_F \cap \partial\Omega_u = \emptyset$).

4.2.1 Hu-Washizu three-field variational formulation

A unified mathematical framework to enrich the kinematics of a finite element by the Embedded Finite Element Method can be obtained from the three-field variational formulation of Hu-Washizu [Washizu, 1975]. The Hu-Washizu functional has the form:

$$\begin{aligned} \Pi^{HW}(\mathbf{u}, \boldsymbol{\epsilon}, \boldsymbol{\sigma}) = & \int_{\Omega} (\nabla^s \mathbf{u} : \boldsymbol{\sigma} - \boldsymbol{\epsilon} : \boldsymbol{\sigma} + \frac{1}{2} \boldsymbol{\epsilon} : \mathbb{C} : \boldsymbol{\epsilon}) d\Omega \\ & - \int_{\Omega} \mathbf{u} \cdot \mathbf{b} d\Omega - \int_{\partial\Omega_F} \mathbf{u} \cdot \mathbf{F} dS. \end{aligned} \quad (4.1)$$

where, \mathbf{b} and \mathbf{F} are volume force and external loads, respectively.

The real fields $(\mathbf{u}, \boldsymbol{\epsilon}, \boldsymbol{\sigma})$ corresponding to the displacements field, strain field and stress field, respectively, are considered as independent. We denote $(\delta\mathbf{u}, \delta\boldsymbol{\epsilon}, \delta\boldsymbol{\sigma})$ the virtual displacement, virtual strain and virtual stress field, respectively. Note that these three virtual fields are also independent. With all these notations, the three-field variational principle derived from Eq. (4.1) can be written as:

$$\forall(\delta\mathbf{u}, \delta\boldsymbol{\epsilon}, \delta\boldsymbol{\sigma}) \left\{ \begin{array}{l} \int_{\Omega} \nabla^s \delta\mathbf{u} : \boldsymbol{\sigma} d\Omega - \int_{\Omega} \delta\mathbf{u} \cdot \mathbf{b} d\Omega - \int_{\partial\Omega_F} \delta\mathbf{u} \cdot \mathbf{F} dS = 0 \\ \int_{\Omega} \delta\boldsymbol{\sigma} : (\nabla^s \mathbf{u} - \boldsymbol{\epsilon}) d\Omega = 0 \\ \int_{\Omega} \delta\boldsymbol{\epsilon} : (\hat{\boldsymbol{\sigma}}(\boldsymbol{\epsilon}) - \boldsymbol{\sigma}) d\Omega = 0 \end{array} \right. \quad (4.2)$$

where $\hat{\boldsymbol{\sigma}}(\boldsymbol{\epsilon})$ denotes the stress field derived from the behavior law.

The three equations in the system (4.2) correspond to the weak form of the equilibrium equation, kinematic compatibility equation and behavior law, respectively. If the kinematic equation and behavior equation are imposed in strong form ($\nabla^s \mathbf{u} = \boldsymbol{\epsilon}$ and $\hat{\boldsymbol{\sigma}}(\boldsymbol{\epsilon}) = \boldsymbol{\sigma}$), the system (4.2) returns to the classical variational formulation written in displacement.

4.2.2 Enhanced assumed strain method

The Embedded Finite Element formulation is based on a mixed-type formulation with independent strains and displacements. Based on the Enhanced Assumed Strain [Simo and Rifai, 1990] or equivalently on the so-called incompatible mode method [Wilson and Ibrahimbegovic, 1990], the infinitesimal real strain field $\boldsymbol{\epsilon}$ is decomposed into the compatible part $\nabla^s \mathbf{u}$ and an added enhanced field denoted here as $\boldsymbol{\gamma}$:

$$\boldsymbol{\epsilon} = \nabla^s \mathbf{u} + \boldsymbol{\gamma} . \quad (4.3)$$

Following the idea of the Enhanced Assumed strain method, not only the real but also the virtual strain field is enhanced in the same way.

$$\delta\boldsymbol{\epsilon} = \nabla^s \delta\mathbf{u} + \delta\boldsymbol{\gamma} . \quad (4.4)$$

With these notations, the system (4.2) becomes:

$$\forall(\delta\mathbf{u}, \delta\boldsymbol{\gamma}, \delta\boldsymbol{\sigma}) \left\{ \begin{array}{l} \int_{\Omega} \nabla^s \delta\mathbf{u} : \boldsymbol{\sigma} d\Omega - \int_{\Omega} \delta\mathbf{u} \cdot \mathbf{b} d\Omega - \int_{\partial\Omega_F} \delta\mathbf{u} \cdot \mathbf{F} dS = 0 \quad (4.5a) \\ \int_{\Omega} \delta\boldsymbol{\sigma} : \boldsymbol{\gamma} d\Omega = 0 \quad (4.5b) \\ \int_{\Omega} \nabla^s \delta\mathbf{u} : (\hat{\boldsymbol{\sigma}}(\boldsymbol{\epsilon}) - \boldsymbol{\sigma}) d\Omega + \int_{\Omega} \delta\boldsymbol{\gamma} : (\hat{\boldsymbol{\sigma}}(\boldsymbol{\epsilon}) - \boldsymbol{\sigma}) d\Omega = 0 \quad (4.5c) \end{array} \right.$$

Taking into account that $\delta \mathbf{u}$ and $\delta \boldsymbol{\gamma}$ are independent, the system (4.5) can be rewritten as

$$\forall(\delta \mathbf{u}, \delta \boldsymbol{\gamma}, \delta \boldsymbol{\sigma}) \left\{ \begin{array}{l} \int_{\Omega} \nabla^s \delta \mathbf{u} : \boldsymbol{\sigma} d\Omega - \int_{\Omega} \delta \mathbf{u} \cdot \mathbf{b} d\Omega - \int_{\partial\Omega_F} \delta \mathbf{u} \cdot \mathbf{F} dS = \mathbf{0} \quad (4.6a) \\ \int_{\Omega} \delta \boldsymbol{\sigma} : \boldsymbol{\gamma} d\Omega = \mathbf{0} \quad (4.6b) \\ \int_{\Omega} \nabla^s \delta \mathbf{u} : (\hat{\boldsymbol{\sigma}}(\boldsymbol{\epsilon}) - \boldsymbol{\sigma}) d\Omega = \mathbf{0} \quad (4.6c) \\ \int_{\Omega} \delta \boldsymbol{\gamma} : (\hat{\boldsymbol{\sigma}}(\boldsymbol{\epsilon}) - \boldsymbol{\sigma}) d\Omega = \mathbf{0} \quad (4.6d) \end{array} \right.$$

Combining Eq. (4.6a) and Eq. (4.6c) gives

$$\forall(\delta \mathbf{u}, \delta \boldsymbol{\gamma}, \delta \boldsymbol{\sigma}) \left\{ \begin{array}{l} \int_{\Omega} \nabla^s \delta \mathbf{u} : \hat{\boldsymbol{\sigma}}(\boldsymbol{\epsilon}) d\Omega - \int_{\Omega} \delta \mathbf{u} \cdot \mathbf{b} d\Omega - \int_{\partial\Omega_F} \delta \mathbf{u} \cdot \mathbf{F} dS = \mathbf{0} \quad (4.7a) \\ \int_{\Omega} \delta \boldsymbol{\sigma} : \boldsymbol{\gamma} d\Omega = \mathbf{0} \quad (4.7b) \\ \int_{\Omega} \nabla^s \delta \mathbf{u} : (\hat{\boldsymbol{\sigma}}(\boldsymbol{\epsilon}) - \boldsymbol{\sigma}) d\Omega = \mathbf{0} \quad (4.7c) \\ \int_{\Omega} \delta \boldsymbol{\gamma} : (\hat{\boldsymbol{\sigma}}(\boldsymbol{\epsilon}) - \boldsymbol{\sigma}) d\Omega = \mathbf{0} \quad (4.7d) \end{array} \right.$$

The second key point of the Enhanced Assumed Strain is to build the space of the stress fields $(\boldsymbol{\sigma}, \delta \boldsymbol{\sigma})$ and the enhanced strain fields $(\boldsymbol{\gamma}, \delta \boldsymbol{\gamma})$ as orthogonal which makes it possible to avoid the presence of the stress fields in the discretized formulation:

$$\int_{\Omega} \delta \boldsymbol{\sigma} : \boldsymbol{\gamma} d\Omega = \mathbf{0} \quad \text{and} \quad \int_{\Omega} \delta \boldsymbol{\gamma} : \boldsymbol{\sigma} d\Omega = \mathbf{0} \quad (4.8)$$

By integrating Eq. (4.8) into Eqs. (4.7), we have a two-fields variational formulation:

$$\forall(\delta \mathbf{u}, \delta \boldsymbol{\gamma}) \left\{ \begin{array}{l} \int_{\Omega} \nabla^s \delta \mathbf{u} : \hat{\boldsymbol{\sigma}}(\boldsymbol{\epsilon}) d\Omega - \int_{\Omega} \delta \mathbf{u} \cdot \mathbf{b} d\Omega - \int_{\partial\Omega_F} \delta \mathbf{u} \cdot \mathbf{F} dS = \mathbf{0} \quad (4.9a) \\ \int_{\Omega} \nabla^s \delta \mathbf{u} : (\hat{\boldsymbol{\sigma}}(\boldsymbol{\epsilon}) - \boldsymbol{\sigma}) d\Omega = \mathbf{0} \quad (4.9b) \\ \int_{\Omega} \delta \boldsymbol{\gamma} : \hat{\boldsymbol{\sigma}}(\boldsymbol{\epsilon}) d\Omega = \mathbf{0} \quad (4.9c) \end{array} \right.$$

The last point of the EAS method is to assume that the stress field verifies the constitutive equation in the strong form $\hat{\boldsymbol{\sigma}}(\boldsymbol{\epsilon}) = \boldsymbol{\sigma}$. In that case, the system (4.9) becomes:

$$\forall(\delta \mathbf{u}, \delta \boldsymbol{\gamma}) \left\{ \begin{array}{l} \int_{\Omega} \nabla^s \delta \mathbf{u} : \hat{\boldsymbol{\sigma}}(\boldsymbol{\epsilon}) d\Omega - \int_{\Omega} \delta \mathbf{u} \cdot \mathbf{b} d\Omega - \int_{\partial\Omega_F} \delta \mathbf{u} \cdot \mathbf{F} dS = \mathbf{0} \quad (4.10a) \\ \int_{\Omega} \delta \boldsymbol{\gamma} : \hat{\boldsymbol{\sigma}}(\boldsymbol{\epsilon}) d\Omega = \mathbf{0} \quad (4.10b) \end{array} \right.$$

Note that the interpolations of the enhanced strains are not necessarily continuous

from one element to another. Therefore no inter-element continuity on enhanced strains needs to be enforced when constructing finite element approximations and Eq. (4.10b) is evaluated at the element level

$$\forall(\delta \mathbf{u}, \delta \boldsymbol{\gamma}) \left\{ \begin{array}{l} \int_{\Omega} \nabla^s \delta \mathbf{u} : \hat{\boldsymbol{\sigma}}(\boldsymbol{\epsilon}) d\Omega - \int_{\Omega} \delta \mathbf{u} \cdot \mathbf{b} d\Omega - \int_{\partial\Omega_F} \delta \mathbf{u} \cdot \mathbf{F} dS = \mathbf{0} \quad (4.11a) \\ \int_{\Omega_e} \delta \boldsymbol{\gamma} : \hat{\boldsymbol{\sigma}}(\boldsymbol{\epsilon}) d\Omega = \mathbf{0} \quad \forall e \quad \text{with enhanced strain} \quad (4.11b) \end{array} \right.$$

To ensure the convergence of this method, the enhanced element must verify the patch-test [Zienkiewicz and Taylor, 2005], in other words, it must be able to represent a constant stress field, with $\hat{\boldsymbol{\sigma}}(\boldsymbol{\epsilon}) = \hat{\boldsymbol{\sigma}}_c$. To verify this patch-test, Eq. (4.11b) leads to $\forall \hat{\boldsymbol{\sigma}}_c$ constant per element:

$$\int_{\Omega_e} \delta \boldsymbol{\gamma} : \hat{\boldsymbol{\sigma}}_c d\Omega = \mathbf{0} \quad \Rightarrow \quad \hat{\boldsymbol{\sigma}}_c \int_{\Omega_e} \delta \boldsymbol{\gamma} d\Omega = \mathbf{0} \quad \Rightarrow \quad \int_{\Omega_e} \delta \boldsymbol{\gamma} d\Omega = \mathbf{0}, \quad (4.12)$$

which means that the enhanced part of the virtual strain must satisfies the zero mean condition over the element.

4.2.3 E-FEM discretization

As mentioned in the introduction, E-FEM is usually formulated for strong discontinuities using three different formulations based on different choices of interpolations, namely, Statically Optimal Symmetric (SOS), Kinematically Optimal Symmetric (KOS), and Statically and Kinematically Optimal Nonsymmetric (SKON). We present here some basic features of the three formulations:

- Statically Optimal Symmetric (SOS)

Using the study of Belytschko et al [Belytschko et al., 1988], SOS formulation has been developed and used over the next decades in many works like [Larsson et al., 1996], [Armero and Garikipati, 1996], [Sluys and Berends, 1998]. This method only enhances the strain field, without any enrichment of the displacement field. The shape of the enhanced parts (both virtual and real strain) can be determined thanks to the zero mean condition (4.12). Once this condition is satisfied, the stress field is continuous over the element and the traction continuity condition across the interface is verified. Due to the fact that the enhanced part of virtual and real strain is interpolated in the same way, the matrix of the system to be solved is symmetric. Nevertheless, the main drawback of this formulation is the lack of kinematic compatibility since the displacement field is not enhanced.

- Kinematically Optimal Symmetric (KOS)

Contrary to the SOS formulation, the KOS formulation of Lotfi and Shing [Lotfi and Shing, 1995] only considers the kinematic aspect of the discontinuity. The enhanced strain is derived from the enriched part of the displacement field by using the symmetrical kinematics gradient operator ∇^s , similar to the regular part. By choosing a suitable interpolation matrix, the stress field is deleted from the equations and the final form of the system becomes identical to the one obtained by using SOS formulation. The difference lies on the interpolation of the enhanced strain which does not respect the zero mean condition. Hence, the traction continuity condition, as well as the patch test, are not satisfied.

- Statically and Kinematically Optimal Nonsymmetric (SKON)

The SKON formulation of embedded elements proposed in [Simo and Oliver, 1994] and [Oliver, 1996] combines the two above formulations to have the advantages of both. The interpolation of the enhanced part of the real strain is built from the enrichment of the displacement field and suitably represents the discontinuity kinematics. Meanwhile, the interpolation of the enhanced part of the virtual strain respects the zero mean condition and guarantees traction continuity. Due to the different interpolations of the real and virtual enhanced strain, the matrix of the final system to resolve becomes nonsymmetric.

Whereas these formulations have been elaborated in the framework of strong discontinuity, we adapt them here for the case of weak discontinuity. Due to the fact that SKON is a combination of SOS and KOS, in the following we only present the SKON formulation. nevertheless, the KOS and SOS formulations can be then obtained by choosing one of two interpolations in SKON formulation.

To build proper kinematics discontinuity, we first consider the displacement field and derive, from this displacement, the strain enhancement. In the case of a weak discontinuity problem like the one on hand, the displacement field is continuous across the interface Γ separating the two phases $\Omega^{(1)}$ and $\Omega^{(2)}$. For elements cut by the interface, the displacement field can be written in the form:

$$\mathbf{u}^h(\mathbf{x}) = \sum_{i=1}^n \mathbf{N}_i(\mathbf{x}) \mathbf{u}_i + \mathbf{M}(\mathbf{x}) \mathbf{a} , \quad (4.13)$$

where $\mathbf{M}(\mathbf{x})$ is an added shape function, continuous at Γ and \mathbf{a} are additional local degrees of freedom.

Function $\mathbf{M}(\mathbf{x})$ is chosen consistent with a weak kinematic discontinuity in the form:

$$\mathbf{M}(\mathbf{x}) = \varphi(\mathbf{x}) \mathcal{H}_{\Gamma}(\mathbf{x}) - \sum_{i \in \Omega^{(1)}} \mathbf{N}_i(\mathbf{x}) \varphi(\mathbf{x}_i) , \quad (4.14)$$

where \mathcal{H}_Γ denotes the Heaviside function defined as:

$$\mathcal{H}_\Gamma(\mathbf{x}) = \begin{cases} 0 & \text{if } \mathbf{x} \in \Omega^{(2)} \\ 1 & \text{if } \mathbf{x} \in \Omega^{(1)} \end{cases} \quad (4.15)$$

$\varphi(\mathbf{x})$ is here chosen to ensure that $\mathbf{M}(\mathbf{x})$ equals 0 on all nodes of the element and $\varphi(\mathbf{x}_i)$ corresponds to the evaluation of $\varphi(\mathbf{x})$ on node i .

To allow a strain discontinuity, the function $\varphi(\mathbf{x})$ is here chosen as the restriction to the element of the signed distance to the interface Γ . The unit normal vector to the interface Γ is thus given as:

$$\mathbf{n}(\mathbf{x}_\Gamma) = \frac{\nabla \varphi}{\|\nabla \varphi\|}(\mathbf{x}_\Gamma), \quad (4.16)$$

where \mathbf{x}_Γ is the position vector of the considered point on Γ .

In the present work, the linear approximated interface is considered in the element.

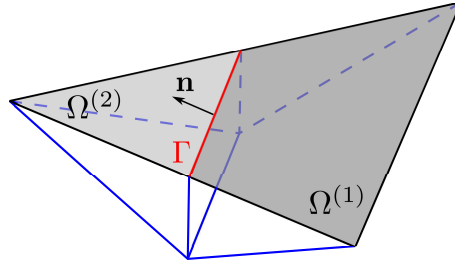


Figure 4.2: Shape function $\mathbf{M}(\mathbf{x})$ in a discontinuous element

The normal vector to the interface is therefore constant in the element considered (see Figure 4.2). The signed distance function $\varphi(\mathbf{x})$ takes the zero value on the interface, it corresponds to the level set function used in the XFEM approach presented in the previous chapter. Hence, as presented in Eqs. (3.23) and (3.24), the components of the normal vector $\mathbf{n}(\mathbf{x})$ can be evaluated at every \mathbf{x} position in the element considered by:

$$\mathbf{n}(\mathbf{x}) = \frac{\nabla \varphi^h(\mathbf{x})}{\|\nabla \varphi^h(\mathbf{x})\|} \quad \text{with} \quad \varphi^h(\mathbf{x}) = \sum_{i=1}^n \mathbf{N}_i(\mathbf{x}) \varphi(\mathbf{x}_i). \quad (4.17)$$

Considering (4.13) and the chosen expression of \mathbf{M} , the real strain field is written in the form:

$$\boldsymbol{\epsilon}(\mathbf{x}) = \underbrace{\mathbf{B}(\mathbf{x})\mathbf{u}}_{\nabla^s \mathbf{u}} + \underbrace{\mathbf{G}_r(\mathbf{x})\mathbf{a}}_{\gamma}, \quad (4.18)$$

with

$$\mathbf{G}_r(\mathbf{x}) = \mathbf{L}\mathbf{M}(\mathbf{x}) = \mathcal{N}\mathcal{H}_\Gamma(\mathbf{x}) - \sum_{i \in \Omega^{(1)}} \mathbf{B}_i(\mathbf{x}) \varphi(\mathbf{x}_i), \quad (4.19)$$

where \mathbf{L} is the matrix operator associated with the symmetric gradient ∇^s .

Following the Voigt notation, \mathcal{N} is defined as (for 2D plane strain problems):

$$\mathcal{N} = \begin{bmatrix} n_x & 0 \\ 0 & n_y \\ n_y & n_x \end{bmatrix}. \quad (4.20)$$

As seen from its definition, the enhanced part of the real strain tensor is a derivation from an enhanced part of the displacement field. Hence, it respects the kinematic compatibility.

The interpolation of the virtual strain field is defined as:

$$\delta\epsilon(\mathbf{x}) = \underbrace{\mathbf{B}(\mathbf{x})\delta\mathbf{u}}_{\nabla^s \delta\mathbf{u}} + \underbrace{\mathbf{G}_v(\mathbf{x})\delta\mathbf{a}}_{\delta\gamma}, \quad (4.21)$$

where \mathbf{G}_v is built as a modified version of \mathbf{G}_r in order to satisfy the zero mean condition (4.12).

This \mathbf{G}_v ensures the satisfaction of the patch-test and can be obtained by following the procedure proposed for the method of incompatible modes proposed by Ibrahimbegovic and Wilson [Ibrahimbegovic and Wilson, 1991] leading to:

$$\mathbf{G}_v(\mathbf{x}) = \mathbf{G}_r(\mathbf{x}) - \frac{1}{V} \int_{\Omega^e} \mathbf{G}_r(\mathbf{x}) d\Omega. \quad (4.22)$$

We then obtain, for three nodes triangular elements:

$$\begin{aligned} \mathbf{G}_v^{(1)}(\mathbf{x}) &= \frac{V^{(2)}}{V} \mathcal{N} \quad \text{on } \Omega^{(1)} \\ \mathbf{G}_v^{(2)}(\mathbf{x}) &= -\frac{V^{(1)}}{V} \mathcal{N} \quad \text{on } \Omega^{(2)}, \end{aligned} \quad (4.23)$$

where $V^{(1)}$ and $V^{(2)}$ denotes the volume (for 3D problems or area for 2D problems) of $\Omega^{(1)}$ and $\Omega^{(2)}$, respectively.

Using the definitions (4.21) in Eq. (4.10b) gives:

$$\int_{\Omega_e} \delta\gamma : \hat{\boldsymbol{\sigma}}(\epsilon) d\Omega = \delta\mathbf{a} \left(\int_{\Omega^{(1)}} (\mathbf{G}_v^{(1)})^T \hat{\boldsymbol{\sigma}}^{(1)} d\Omega + \int_{\Omega^{(2)}} (\mathbf{G}_v^{(2)})^T \hat{\boldsymbol{\sigma}}^{(2)} d\Omega \right) = 0. \quad (4.24)$$

By using Eqs. (4.23) and by considering that, in a three nodes triangular elements, the stress field is constant in each sub-domain $\Omega^{(1)}$ and $\Omega^{(2)}$, Eq. (4.24) can be written as:

$$\int_{\Omega_e} \delta\gamma : \hat{\boldsymbol{\sigma}}(\epsilon) d\Omega = \delta\mathbf{a} \left(\frac{V^{(1)}V^{(2)}}{V} \mathcal{N}^T \hat{\boldsymbol{\sigma}}^{(1)} - \frac{V^{(1)}V^{(2)}}{V} \mathcal{N}^T \hat{\boldsymbol{\sigma}}^{(2)} \right) = 0. \quad (4.25)$$

As $\mathcal{N}^T \hat{\boldsymbol{\sigma}}$ is the Voigt notation for $\hat{\boldsymbol{\sigma}}\mathbf{n}$, Eq. (4.25) can be interpreted as the traction

continuity condition:

$$\int_{\Omega_e} \delta \boldsymbol{\gamma} : \hat{\boldsymbol{\sigma}}(\boldsymbol{\epsilon}) d\Omega = \frac{V^{(1)}V^{(2)}}{V} \llbracket \hat{\boldsymbol{\sigma}} \rrbracket \mathbf{n} = \mathbf{0} . \quad (4.26)$$

It can be seen from Eq. (4.26) that with the use of \mathbf{G}_v the traction continuity condition is satisfied.

The system of SKON formulation is obtained by injecting Eq. (4.18) and Eq. (4.21) in Eqs. (4.11):

$$\begin{cases} \int_{\Omega} \mathbf{B}^T \hat{\boldsymbol{\sigma}}(\mathbf{B}\mathbf{u} + \mathbf{G}_r \mathbf{a}) d\Omega = \mathbf{f}_{ext} & (4.27a) \\ \int_{\Omega_e} \mathbf{G}_v^T \hat{\boldsymbol{\sigma}}(\mathbf{B}\mathbf{u} + \mathbf{G}_r \mathbf{a}) d\Omega = \mathbf{0} & (4.27b) \end{cases}$$

If we replace \mathbf{G}_r in the real strain interpolation (4.18) by \mathbf{G}_v , we then obtain the SOS formulation in which the traction continuity is verified in Eq. (4.26) and the system (4.27) becomes symmetric. However, without \mathbf{G}_r , the compatibility between the strain field and the displacement field is not ensured since $\boldsymbol{\gamma}$ is not derived directly from a displacement field. On the contrary, if \mathbf{G}_v in the virtual strain interpolation (4.21) is changed to \mathbf{G}_r , we obtain the KOS formulation, which is also symmetric with a reliable kinematic expression but the traction continuity is no longer satisfied. Although the system (4.27) of SKON formulation is not symmetric, it satisfies both the condition of traction continuity and the kinematic compatibility.

4.2.4 Resolution strategy

In the case of linear elastic behavior, the system (4.27) can be rewritten in matrix form as:

$$\begin{cases} \sum_{e=1}^{N_{elem}} (\mathbf{K}_{uu}^e \mathbf{u} + \mathbf{K}_{ua}^e \mathbf{a}) = \sum_{e=1}^{N_{elem}} \mathbf{f}_{ext}^e & (4.28a) \\ \mathbf{K}_{au}^e \mathbf{u} + \mathbf{K}_{aa}^e \mathbf{a} = \mathbf{0} \quad \forall e \text{ cut by } \Gamma & (4.28b) \end{cases}$$

where

$$\begin{aligned} \mathbf{K}_{uu}^e &= \int_{\Omega_e^{(1)}} \mathbf{B}^T \mathbf{C}^{(1)} \mathbf{B} d\Omega + \int_{\Omega_e^{(2)}} \mathbf{B}^T \mathbf{C}^{(2)} \mathbf{B} d\Omega \\ \mathbf{K}_{ua}^e &= \int_{\Omega_e^{(1)}} \mathbf{B}^T \mathbf{C}^{(1)} \mathbf{G}_r^{(1)} d\Omega + \int_{\Omega_e^{(2)}} \mathbf{B}^T \mathbf{C}^{(2)} \mathbf{G}_r^{(2)} d\Omega \\ \mathbf{K}_{au}^e &= \int_{\Omega_e^{(1)}} (\mathbf{G}_v^{(1)})^T \mathbf{C}^{(1)} \mathbf{B} d\Omega + \int_{\Omega_e^{(2)}} (\mathbf{G}_v^{(2)})^T \mathbf{C}^{(2)} \mathbf{B} d\Omega \\ \mathbf{K}_{aa}^e &= \int_{\Omega_e^{(1)}} (\mathbf{G}_v^{(1)})^T \mathbf{C}^{(1)} \mathbf{G}_r^{(1)} d\Omega + \int_{\Omega_e^{(2)}} (\mathbf{G}_v^{(2)})^T \mathbf{C}^{(2)} \mathbf{G}_r^{(2)} d\Omega \end{aligned} \quad (4.29)$$

with $\mathbf{C}^{(i)}$ is the matrix form of the elastic tensor for phase (i) :

$$\mathbf{C}^{(i)} = \begin{bmatrix} (\lambda^{(i)} + 2\mu^{(i)}) & \lambda^{(i)} & 0 \\ \lambda^{(i)} & (\lambda^{(i)} + 2\mu^{(i)}) & 0 \\ 0 & 0 & \mu^{(i)} \end{bmatrix} \quad i = 1, 2 . \quad (4.30)$$

The system (4.28) is solved by taking advantage of the fact that Eq. (4.28b) are written at the element level. An "operator split" method is then considered for the resolution: Eq. (4.28b) is solved at the element level in order to obtain the variables \mathbf{a} for each element crossed by the interface, then, after a static condensation procedure [Wilson, 1974] at the element level, nodal displacements \mathbf{u} are obtained as solution of:

$$\sum_{e=1}^{N_{\text{elem}}} \widetilde{\mathbf{K}}^e \mathbf{u} = \sum_{e=1}^{N_{\text{elem}}} \mathbf{f}_{ext}^e \quad (4.31)$$

with

$$\widetilde{\mathbf{K}}^e = \mathbf{K}_{uu}^e - \mathbf{K}_{ua}^e (\mathbf{K}_{aa}^e)^{-1} \mathbf{K}_{au}^e. \quad (4.32)$$

Due to static condensation, the size of the final global system (4.31) to be solved is not modified. Hence, no matter how many inclusions and interfaces exist in the RVE, the size of the problem is preserved and only depends on the number of nodes of the mesh.

4.3 Performance of the three E-FEM formulations: SOS, KOS and SKON

In this section, we aim at comparing the numerical performance of the three E-FEM formulations presented in the previous section. Such comparisons have already been conducted in the case of strong discontinuities, leading to the conclusion that, for linear elements, the SKON formulation gives the best results regarding convergence and alleviates all the difficulties due to stress locking [Jirásek, 2000, Cazes et al., 2016]. Since this PhD work deals with weak discontinuities, the classical first Eshelby problem and two-phase material problem are chosen to test the efficiency of the three formulations. The results of conforming FEM is also added to the comparison as a reference result.

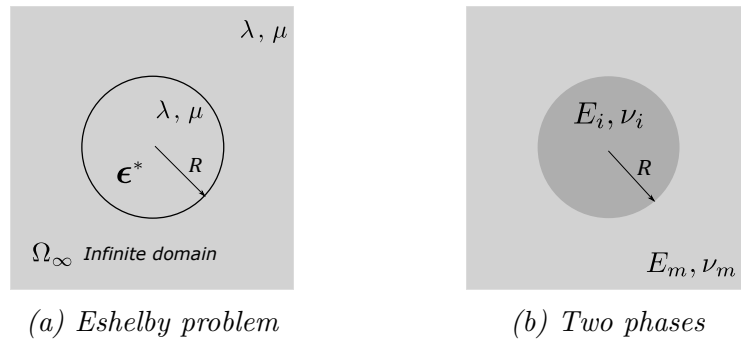


Figure 4.3: Classical first Eshelby problem and two-phase material problem ($R = 1\text{nm}$, $f = 0.2$).

For the first Eshelby problem, we consider a bounded domain surrounding an inclusion (see Figure 4.3a) and we conduct the computations by prescribing the an-

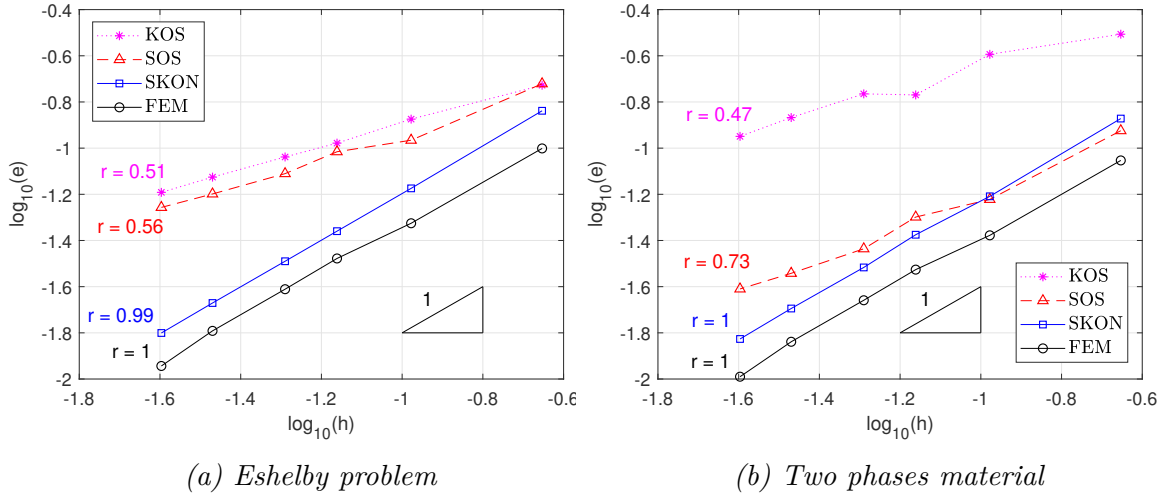


Figure 4.4: Convergence analysis of the three formulations of E-FEM in treating the First Eshelby problem and the two phase material problem.

analytical solution in terms of displacements on the boundary of the finite domain. In the results presented in this section, the loading conditions correspond to a dilational eigenstrain ϵ^* prescribed to the inclusion and such that $\epsilon^* = \epsilon_{xx}^* = \epsilon_{yy}^* = 0.5, \epsilon_{zz}^* = 0$. For the two phases material problem, the considered RVE represented in Figure 4.3b is considered and submitted to an hydrostatic stress by prescribing the exact solution of the displacement field given in [Sukumar et al., 2001] on the boundary of the domain. The material constants are chosen as: $E_m = 70$ GPa, $E_i = 0.1E_m$, $\nu_m = 0.3$ and $\nu_i = 0.25$.

The performances of KOS, SOS, and SKON formulations are evaluated through the relative energy norm error defined in Eq. (3.33) and convergence rate. As shown in Figures 4.4a and 4.4b, the convergence of SKON is the best among the three formulations of E-FEM in both problems. The expected conforming FEM rate of convergence $r = 1$ is recovered for SKON.

We also investigate the efficiency of the three formulations in representing the local fields. A 40x40 nodes mesh is used for this test (see Figure 4.5a). The strain component ϵ_{xx} along the line A-B (see Figure 4.5a) corresponding to the center line of the RVE is represented for the three formulations in Figure 4.5. For the KOS formulation (Figure 4.5b), the strain field in the matrix, as well as the strain jump, are overestimated compared to the exact solution. Regarding SOS (Figure 4.5c), a good estimation of the strain jump is obtained but the level of strain in the element cut by the interface is not correctly captured. Finally, for the SKON formulation (Figure 4.5d) the strain field, as well as the strain jump, are correctly computed.

The same investigation has been performed for the two-phase material problem. The strain component ϵ_{xx} along the line A-B are presented in Figure 4.6. It can be seen in Figure 4.6b that the stress field given by KOS formulation is discontinuous across the interface at $x = -1$ and $x = 1$. Meanwhile, the stress fields obtained from

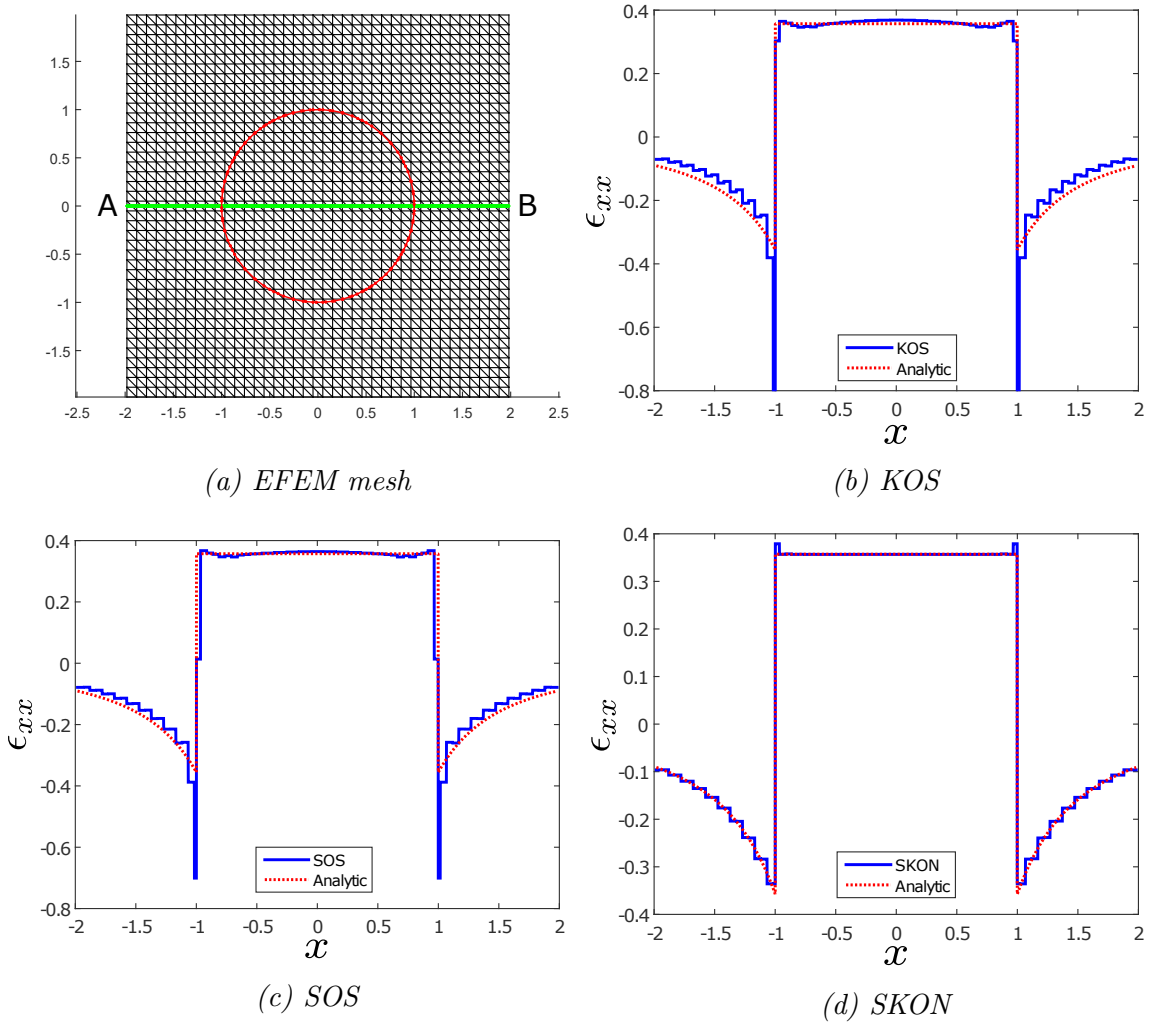


Figure 4.5: ϵ_{xx} along the line A-B for the classical first Eshelby problem.

SOS and SKON formulations (see Figures 4.6d and 4.6f) are continuous across the interface because the traction continuity condition is verified in these formulations.

Among the three formulations, SKON gives the results closest to the analytical solution. Its convergence is, therefore, better than the other ones as shown in Figure 4.4b. However, in the enhanced elements, the strain field in the inclusion part, as well as the strain jump, are overestimated. Meanwhile, the strain field in the standard elements of the inclusion is slightly smaller than the exact one. Therefore, the total strain energy in the inclusion needed for the numerical homogenization is still correct. Nonetheless, for the future works when decohesion or damage of the interface is considered, this issue may cause inaccurate results. The issue related to the strong variation of the stiffness coefficients between the two domains has also been reported in [Idelsohn et al., 2017]. We open a discussion in the next section for several efforts to solve the issue with a strong contrast of the stiffness of the two phases.

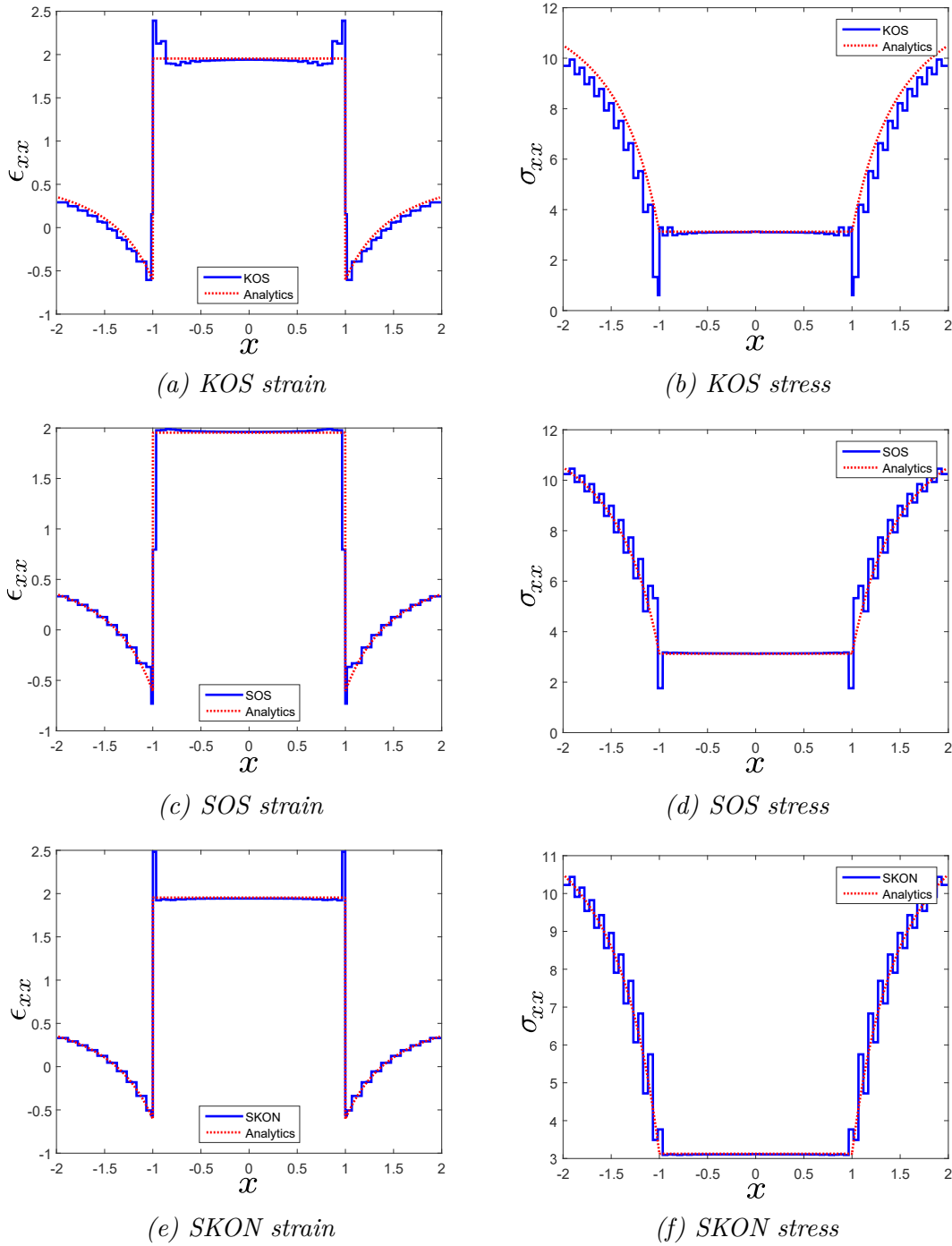


Figure 4.6: ϵ_{xx} and σ_{xx} along the line A-B for the classical two phases problem.

4.4 E-FEM approaches for two phases material with strong contrast of properties

In this subsection, we investigate the overestimation of the strain field as well as strain jump in the E-FEM element when a high contrast of rigidity $\beta = \frac{E_{matrix}}{E_{inclusion}}$ of the composite material is considered. Considering the two-phase problem presented in the previous section (see Figure 4.3b), the strain component ϵ_{xx} along the line A-B

obtained from the three E-FEM formulations for the case of $\beta = 100$ and $\beta = 1000$ are presented in Figure 4.7. We notice that the results of KOS formulation are almost not affected by the high value of β whereas those given by SOS formulation and especially SKON formulation are affected by β .

In this section, we try to find the cause of this issue by few simple tests on SKON formulation.

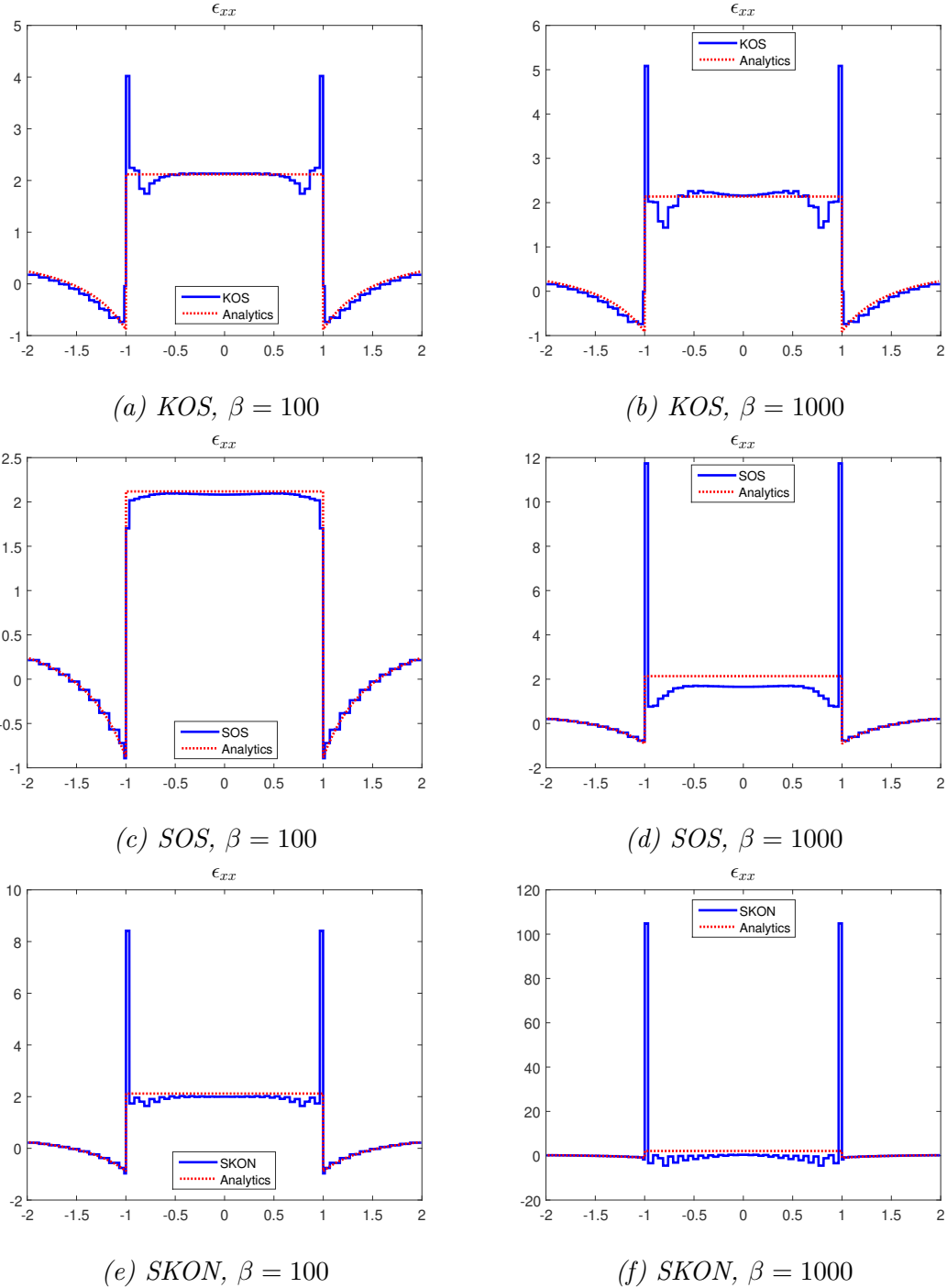


Figure 4.7: ϵ_{xx} along the line A-B for different E-FEM formulations with $\beta = 100$ and $\beta = 1000$.

First of all, from the mathematical point of view, the strong contrast of stiffness between the phases may result in a conditioning problem of the global stiffness matrix. To verify it, we perform a test on a heterogeneous bar where a very high stiffness coefficient ($\beta = 10^6$) is considered. The boundary conditions are $u(x) = 0$ on left edge and $u(x) = 1$ on the right edge, $u(y) = 0$ on the top and bottom edges. This two phases bar is shown in Figure 4.8a. The strain component ϵ_{xx} obtained from SKON formulation are presented in Figure 4.8b for $\beta = 10$ and in Figure 4.8c for $\beta = 10^6$.

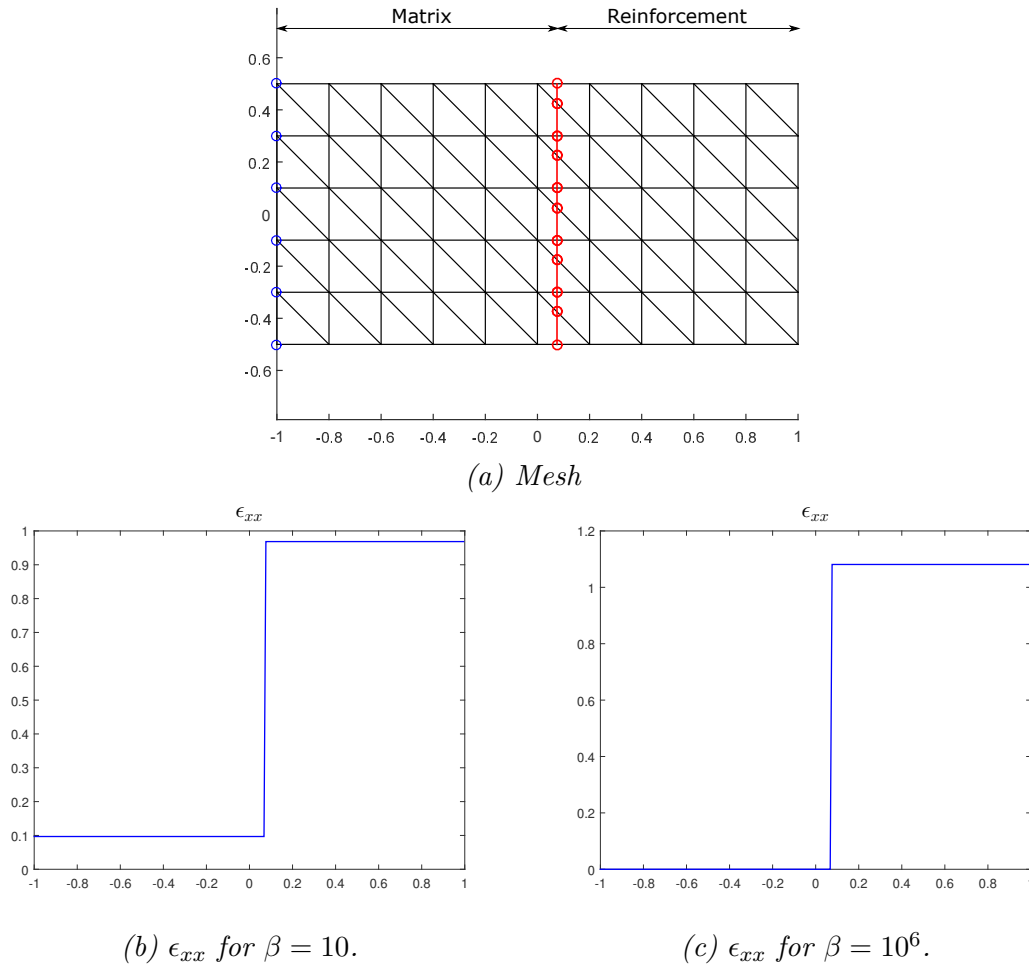


Figure 4.8: Traction test of a two phases bar using SKON formulation in the case of stiffness coefficients $\beta = 10$ and $\beta = 10^6$ ($E_{matrix} = 70$ GPa, $\nu_{matrix} = \nu_{inclusion} = 0$).

It can be seen that SKON provides correct results even with the very high value of the stiffness coefficient β . Therefore, the conditioning of the stiffness matrix is not the cause of the overestimation observed. As shown in Figure 4.9, the same conclusion can be drawn in the case of a three phases bar (matrix-reinforcement-matrix).

The second possibility can be the cause of the issue related to the alignment and position of the interface relatively to the element edge. This geometric problem has

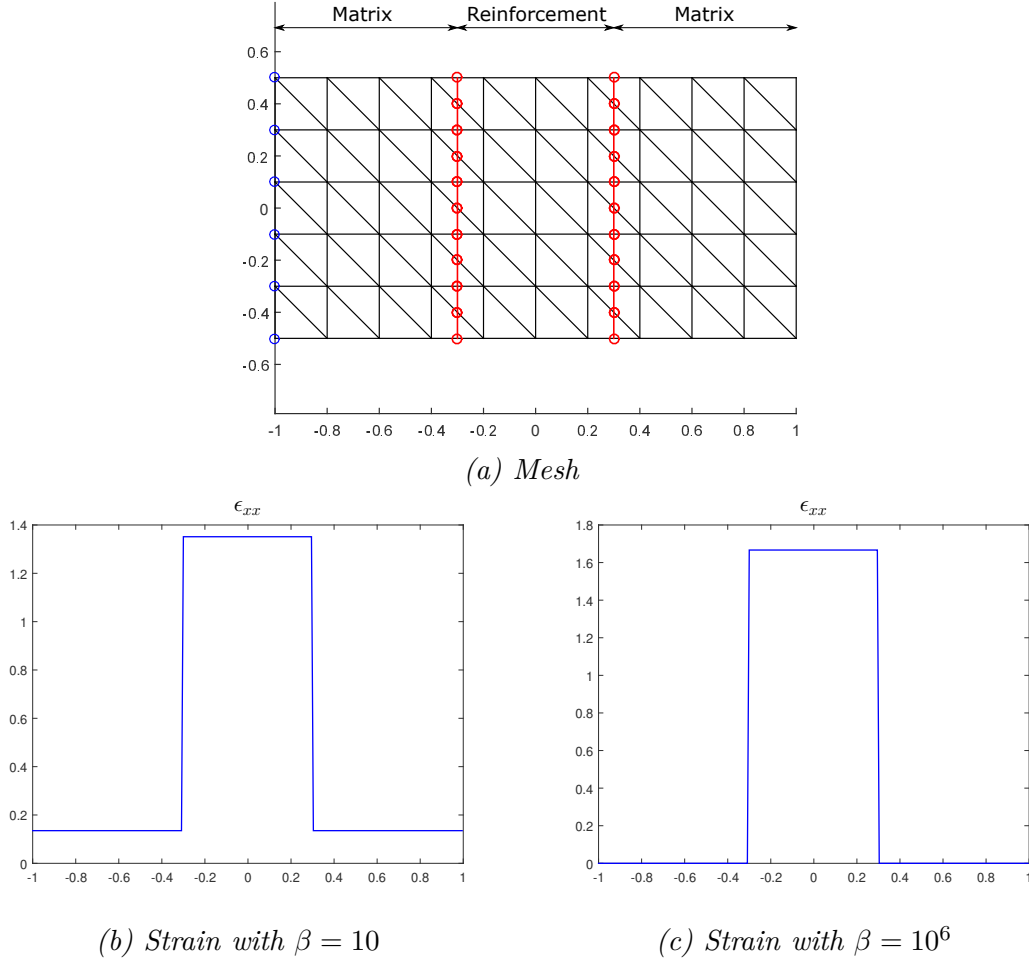


Figure 4.9: Traction test of a three phases bar using SKON formulation in the case of stiffness coefficients $\beta = 10$ and $\beta = 10^6$.

been reported in the framework of E-FEM in [Juárez-Luna and Ayala, 2014] for the case of strong discontinuity. In this study, the authors pointed out that the different positions and directions of the interface in the enhanced element can lead to different results. They also showed that for the constant triangle element, the case with an interface located at mid-height of the element and parallel to the border (element edge) gave the best result. These two conditions have been enforced in several studies of strong discontinuities as [Sancho et al., 2006, Reyes et al., 2009, Gálvez et al., 2013, Alberti et al., 2017, Suárez et al., 2019]. Moreover, in [Idelsohn et al., 2017], a singular case when the interface is very close to a node has been mentioned. All these geometrical reasons can affect the results given by the E-FEM method.

In order to verify this possibility, we consider here a "special" mesh in which the interfaces are always placed at mid-height and parallel to an edge of the corresponding enhanced element (see Figure 4.10a). The two phases material problem of a square domain surrounding a circular inclusion presented in Figure 4.3b is reconsidered.

As shown in Figure 4.10b on the convergence analysis for different values of β ,

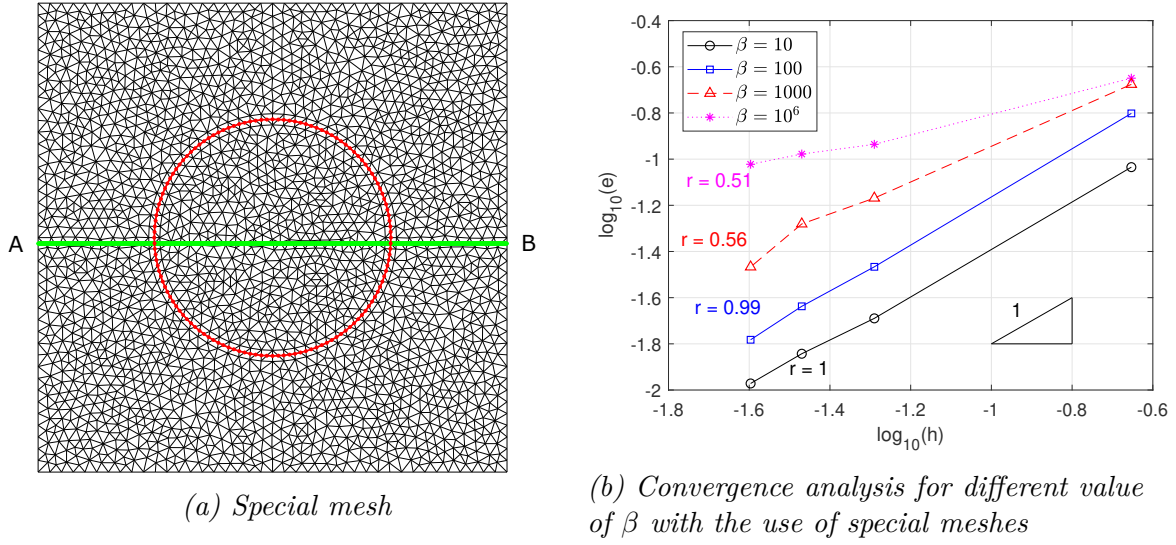


Figure 4.10: Two phases composite problem is treated by SKON with special mesh

the SKON resolution still converges although its rate of convergence is degraded for high values of β . The deformed mesh and the strain component ϵ_{xx} along the line AB for different values of β are presented in Figures 4.11, 4.12, 4.13 and 4.14. It can be seen that although we have better results compared to those of regular meshes in Figures 4.7e and 4.7f, the issue related to the high value of β still happens even when the geometric conditions are satisfied.

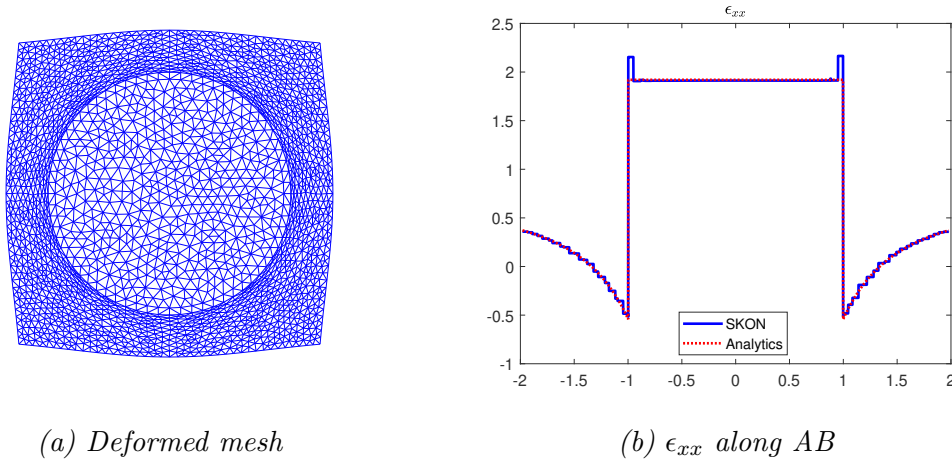
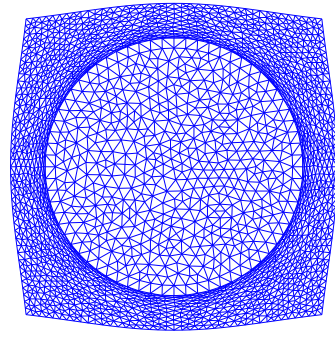
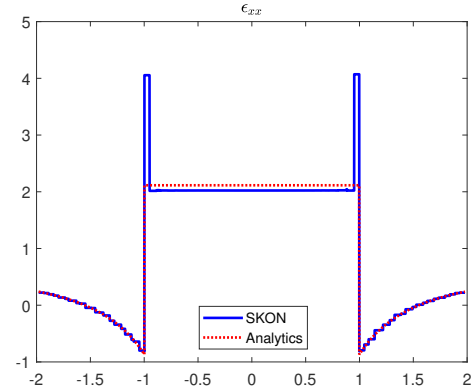
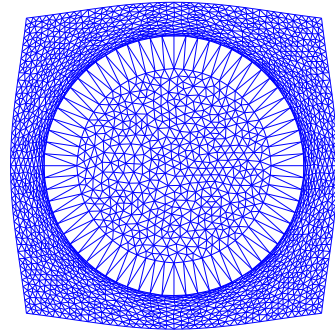


Figure 4.11: $\beta = 10$ with special mesh.

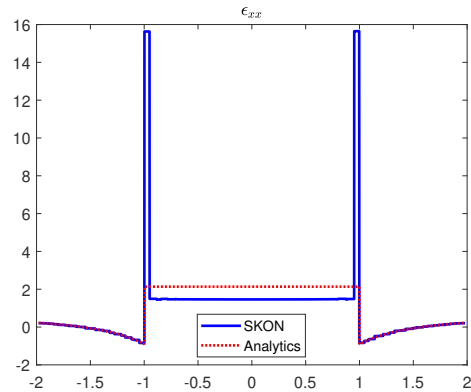
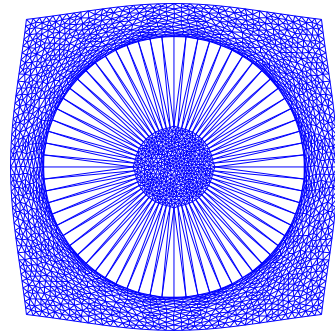
By observing the deformed meshes for the values of the stiffness coefficient β ranging from 10 to 10^6 , we notice that the displacement field, as well as regular part of strain field in the enhanced elements, is also affected (overestimated) leading to the underestimation of the displacement and strain field in the standard elements in the inclusion (see Figures 4.13 and 4.14 for the clearest observation). These results show that the FEM resolution at the global level seems to be working well, whereas the local enhancement at the elementary level needs to be improved.



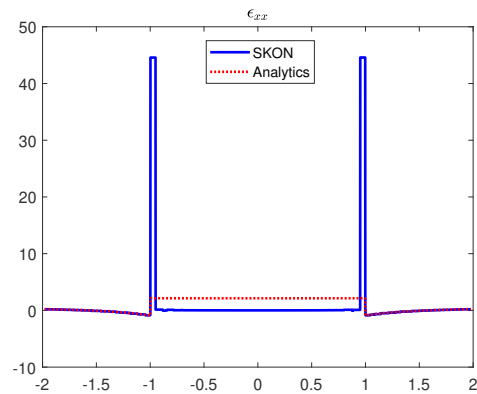
(a) Deformed mesh

(b) ϵ_{xx} along ABFigure 4.12: $\beta = 100$ with special mesh.

(a) Deformed mesh

(b) ϵ_{xx} along ABFigure 4.13: $\beta = 1000$ with special mesh.

(a) Deformed mesh

(b) ϵ_{xx} along ABFigure 4.14: $\beta = 10^6$ with special mesh.

Due to the fact that KOS formulation is almost not affected by the high value of β while SOS and SKON formulations are affected (see Figure 4.7). We can conclude that the problem lies at the evaluation of the traction continuity condition at the

elementary level (see equations from Eq. (4.24) to Eq. (4.26)). This condition is imposed at the elementary level without "looking" what happens in the neighboring elements. In the traction test on the heterogeneous bars presented above, the interfaces are straight and open lines, leading to the fact that the continuity condition in a single enhanced element and at the global level are exactly the same. In this case, even with very high contrasts of rigidity of the phases, SKON still gives the correct results.

The local equilibrium at the elementary level of SOS and SKON formulations is evaluated with the linear approximation of the interface. The approximated interface in these elements is considered as a straight line and the normal vector is constant over each element. Moreover, there is no assembly procedure to connect these linear approximated interfaces at the local level. Therefore, when the interface is a curve, the local equilibrium "forget" the fact that the interface is a curve and treat it like a straight line.

To solve this issue, the local equilibrium evaluation has to take into account the global geometry of the interface (curvature, open or close interface). Although the assembly procedure can not be performed at the local level, the interaction between the enhanced elements can be proceeded by using the inter-element force presented in [Idelsohn et al., 2017]. Another promising possibility is to perform the computation of the local equilibrium with the curvilinear coordinates systems. For example, in 2D context as in this work, for the circular base cylindrical inclusion, the cylindrical coordinate system can be used, or in 3D context, if the inclusion is a sphere, the spherical coordinate system can be used in the equations at the elementary level so that the curvature of the interface is accounted for.

With the restrictions in terms of the time of this Ph.D. work, we limit ourselves to the determination of the cause of this issue. Nevertheless, some promising solutions have been suggested for future works. One of them is still underway and gives some very first positive results though more detail develops need to be done for a complete solution that works well for every case.

Although this issue has not been solved, at low contrast of rigidity of the phases, E-FEM formulations still give pretty good results with a much smaller computational cost compared to the global kinematic enrichment of XFEM. They are used to deal with the weak discontinuity and heterogeneous material in studies of [Hautefeuille et al., 2009, Benkemoun et al., 2010, Roubin et al., 2015].

In the following of this thesis, numerical tests using the E-FEM approach consider a contrast coefficient $\beta = 10$. From the numerical evaluations with weak discontinuity problems presented in the previous section, SKON shows that it's the best one among the three E-FEM formulations. Based on its very good performance, we chose this formulation to deal with the case of nanocomposites.

4.5 E-FEM with coherent interface model

The problem considered now is the one already presented in chapter 2 (see Eqs. (2.54)) of a two phases material with a coherent interface. The contribution of the interface will be added into the system (4.11). The generalized Young-Laplace equation (2.48) will replace the traction continuity condition to describe the equilibrium of the interface.

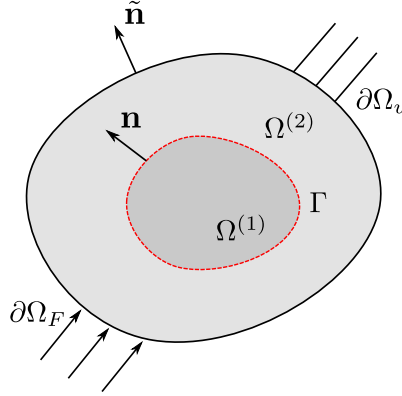


Figure 4.15: Problem definition: two phases material with imperfect interface.

4.5.1 Surface strain enhancement

As presented in the previous section in Eqs. (4.18) and (4.21) for E-FEM formulation, the real and virtual strain fields in the bulk are defined as:

$$\text{in } \Omega^{(i)} \quad i = 1, 2 \quad \begin{cases} \boldsymbol{\epsilon} = \nabla^s \mathbf{u} + \boldsymbol{\gamma} = \mathbf{B}\mathbf{u} + \mathbf{G}_r \mathbf{a} \\ \delta \boldsymbol{\epsilon} = \nabla^s \delta \mathbf{u} + \delta \boldsymbol{\gamma} = \mathbf{B} \delta \mathbf{u} + \mathbf{G}_v \delta \mathbf{a} \end{cases} \quad (4.33)$$

It has to be noticed that $\boldsymbol{\gamma}$ allows a discontinuity of the strain field across the interface Γ . According to the Hadamard's compatibility conditions (2.49) mentioned in chapter 2, there is no strain jump in the tangential direction of the interface. The strain enhancement in this direction is therefore unnecessary. The construction of \mathbf{G}_r and \mathbf{G}_v presented in subsection 4.2.3 leads to $\gamma_{mm}^{(i)} = \delta \gamma_{mm}^{(i)} = 0$, in other words, the projection of $\boldsymbol{\gamma}$ and $\delta \boldsymbol{\gamma}$ on the tangential direction (see Figure 4.16) of the interface is equal to zero $\mathbf{P} \cdot \boldsymbol{\gamma} \cdot \mathbf{P} = \mathbf{P} \cdot \delta \boldsymbol{\gamma} \cdot \mathbf{P} = 0$.

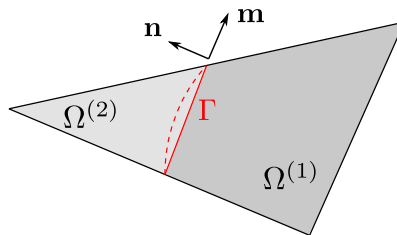


Figure 4.16: Discontinuous element

Since the surface strain is a tangential superficial tensor field, only the regular part of the strain field in the bulk can be projected on the tangential direction of the interface. In order to take into account the influence of the interface at the local level, an enhanced part of surface strain $\gamma_s \neq \mathbf{P} \cdot \boldsymbol{\gamma} \cdot \mathbf{P}$ is proposed:

$$\boldsymbol{\epsilon}_s = \mathbf{P} \cdot (\nabla^s \mathbf{u}) \cdot \mathbf{P} + \boldsymbol{\gamma}_s = \mathcal{M}\mathbf{B}\mathbf{u} + \mathbf{G}_{rs}\mathbf{a} \quad \text{on } \Gamma, \quad (4.34)$$

Note that $\boldsymbol{\gamma}_s$ is defined on Γ , as a tangential superficial tensor field ($\boldsymbol{\gamma}_s = \mathbf{P}\boldsymbol{\gamma}_s\mathbf{P}$). $\boldsymbol{\gamma}_s$ corresponds to the incompatible part of the surface strain on Γ . Following the idea of the Enhanced Assumed strain method the virtual surface strain field is also enhanced in the form:

$$\delta\boldsymbol{\epsilon}_s = \mathbf{P}(\nabla^s \delta\mathbf{u})\mathbf{P} + \delta\boldsymbol{\gamma}_s = \mathcal{M}\mathbf{B}\mathbf{u} + \mathbf{G}_{vs}\delta\mathbf{a} \quad \text{on } \Gamma. \quad (4.35)$$

It has to be pointed out that the enhanced surface strain $\boldsymbol{\gamma}_s$ and $\delta\boldsymbol{\gamma}_s$ share the same additional degrees of freedom (\mathbf{a} and $\delta\mathbf{a}$) with $\boldsymbol{\gamma}$ and $\delta\boldsymbol{\gamma}$. Hence, $\boldsymbol{\gamma}_s$ and $\delta\boldsymbol{\gamma}_s$ are not independent to $\boldsymbol{\gamma}$ and $\delta\boldsymbol{\gamma}$.

4.5.2 Variational formulation with coherent interface model

As we consider a coherent interface model, the surface elasticity energy has to enter the total energy of the whole system $\Omega^{(1)} \cup \Omega^{(2)} \cup \Gamma$. For sake of simplicity, we omit the body force in the equations. We start from the Hu-Washizu functional for $\Omega^{(1)}$, $\Omega^{(2)}$, respectively:

$$\begin{aligned} \Pi^{(1)} = \int_{\Omega^{(1)}} (\nabla^s \mathbf{u} : \boldsymbol{\sigma}^{(1)} - \boldsymbol{\epsilon} : \boldsymbol{\sigma}^{(1)} + \frac{1}{2} \boldsymbol{\epsilon} : \mathbb{C}^{(1)} : \boldsymbol{\epsilon}) d\Omega \\ - \int_{\Gamma} \mathbf{u} \cdot (\boldsymbol{\sigma}^{(1)} \cdot \mathbf{n}) d\Gamma - \int_{\partial\Omega_F^{(1)} \setminus \Gamma} \mathbf{u} \cdot \mathbf{F} dS \end{aligned} \quad (4.36)$$

$$\begin{aligned} \Pi^{(2)} = \int_{\Omega^{(2)}} (\nabla^s \mathbf{u} : \boldsymbol{\sigma}^{(2)} - \boldsymbol{\epsilon} : \boldsymbol{\sigma}^{(2)} + \frac{1}{2} \boldsymbol{\epsilon} : \mathbb{C}^{(2)} : \boldsymbol{\epsilon}) d\Omega \\ + \int_{\Gamma} \mathbf{u} \cdot (\boldsymbol{\sigma}^{(2)} \cdot \mathbf{n}) d\Gamma - \int_{\partial\Omega_F^{(2)} \setminus \Gamma} \mathbf{u} \cdot \mathbf{F} dS \end{aligned} \quad (4.37)$$

Similarly, the interface contribution $\Pi^{(s)}$ can be built as:

$$\Pi^{(s)} = \int_{\Gamma} (\mathbf{P} \cdot \nabla^s \mathbf{u} \cdot \mathbf{P} : \boldsymbol{\sigma}_s - \boldsymbol{\epsilon}_s : \boldsymbol{\sigma}_s + \frac{1}{2} \boldsymbol{\epsilon}_s : \mathbb{C}^s : \boldsymbol{\epsilon}_s) d\Gamma + \int_{\Gamma} \mathbf{u} \cdot \llbracket \boldsymbol{\sigma} \rrbracket \cdot \mathbf{n} d\Gamma \quad (4.38)$$

where $\llbracket \boldsymbol{\sigma} \rrbracket \cdot \mathbf{n} = (\boldsymbol{\sigma}^{(1)} - \boldsymbol{\sigma}^{(2)}) \cdot \mathbf{n}$ acts like a body force along the interface.

By combining Eq. (4.36), Eq. (4.37) and Eq. (4.38), the total functional written on

$\Omega^{(1)} \cup \Omega^{(2)} \cup \Gamma$ takes the form:

$$\begin{aligned} \Pi^{tot} = & \int_{\Omega \setminus \Gamma} (\nabla^s \mathbf{u} : \boldsymbol{\sigma} - \boldsymbol{\epsilon} : \boldsymbol{\sigma} + \frac{1}{2} \boldsymbol{\epsilon} : \mathbb{C} : \boldsymbol{\epsilon}) d\Omega \\ & + \int_{\Gamma} (\mathbf{P} \cdot \nabla^s \mathbf{u} \cdot \mathbf{P} : \boldsymbol{\sigma}_s - \boldsymbol{\epsilon}_s : \boldsymbol{\sigma}_s + \frac{1}{2} \boldsymbol{\epsilon}_s : \mathbb{C}^s : \boldsymbol{\epsilon}_s) d\Gamma - \int_{\partial\Omega_F} \mathbf{u} \cdot \mathbf{F} dS . \end{aligned} \quad (4.39)$$

By using the same process processed in the case with perfect interface in section 4.2, the stationarity of $\Pi^{tot} \forall (\delta \mathbf{u}, \delta \boldsymbol{\sigma}, \delta \boldsymbol{\sigma}_s, \delta \boldsymbol{\gamma})$ provides the following system of equations:

$$\int_{\Omega \setminus \Gamma} \nabla^s \delta \mathbf{u} : \hat{\boldsymbol{\sigma}}(\boldsymbol{\epsilon}) d\Omega + \int_{\Gamma} (\mathbf{P} \cdot \nabla^s \delta \mathbf{u} \cdot \mathbf{P}) : \hat{\boldsymbol{\sigma}}_s(\boldsymbol{\epsilon}_s) d\Gamma - \int_{\partial\Omega_F} \delta \mathbf{u} \cdot \mathbf{F} dS = \mathbf{0} \quad (4.40a)$$

$$\int_{\Omega \setminus \Gamma} \delta \boldsymbol{\sigma} : \boldsymbol{\gamma} d\Omega = \mathbf{0} \quad (4.40b)$$

$$\int_{\Gamma} \delta \boldsymbol{\sigma}_s : \boldsymbol{\gamma}_s d\Gamma = \mathbf{0} \quad (4.40c)$$

$$\int_{\Omega \setminus \Gamma} \delta \boldsymbol{\gamma} : (\hat{\boldsymbol{\sigma}}(\boldsymbol{\epsilon}) - \boldsymbol{\sigma}) d\Omega + \int_{\Gamma} \delta \boldsymbol{\gamma}_s : (\hat{\boldsymbol{\sigma}}_s(\boldsymbol{\epsilon}_s) - \boldsymbol{\sigma}_s) d\Gamma = \mathbf{0} \quad (4.40d)$$

where $\hat{\boldsymbol{\sigma}}_s(\boldsymbol{\epsilon}_s)$ denotes the surface stress field obtained from the constitutive law of the interface (elasticity in our case).

Note that Eq. (4.40d) is written on the whole system and not on the bulks and interface independently because $\delta \boldsymbol{\gamma}$ and $\delta \boldsymbol{\gamma}_s$ have been chosen to be not independent (see subsection 4.5.1). This choice aims to be able to latter introduce the interface equilibrium (generalized Young-Laplace equation (2.48)).

By following the process presented in section 4.2 with the perfect interface, the L_2 -orthogonality between the stress fields and the enhanced strain fields is enforced for the bulk (see Eq. (4.8)) as well as for the interface leading to the additional conditions:

$$\int_{\Gamma} \delta \boldsymbol{\sigma}_s : \boldsymbol{\gamma}_s d\Gamma = \mathbf{0} \quad \text{and} \quad \int_{\Gamma} \delta \boldsymbol{\gamma}_s : \boldsymbol{\sigma}_s d\Gamma = \mathbf{0} , \quad (4.41)$$

We finally end up with the following system $\forall (\delta \mathbf{u}, \delta \boldsymbol{\gamma})$

$$\left\{ \begin{aligned} & \int_{\Omega \setminus \Gamma} \nabla^s \delta \mathbf{u} : \hat{\boldsymbol{\sigma}}(\boldsymbol{\epsilon}) d\Omega + \int_{\Gamma} (\mathbf{P} \cdot \nabla^s \delta \mathbf{u} \cdot \mathbf{P}) : \hat{\boldsymbol{\sigma}}_s(\boldsymbol{\epsilon}_s) d\Gamma \\ & \qquad \qquad \qquad - \int_{\partial\Omega_F} \delta \mathbf{u} \cdot \mathbf{F} dS = \mathbf{0} \end{aligned} \right. \quad (4.42a)$$

$$\left\{ \begin{aligned} & \int_{\Omega_e \setminus \Gamma_e} \delta \boldsymbol{\gamma} : \hat{\boldsymbol{\sigma}}(\boldsymbol{\epsilon}) d\Omega + \int_{\Gamma_e} \delta \boldsymbol{\gamma}_s : \hat{\boldsymbol{\sigma}}_s(\boldsymbol{\epsilon}_s) d\Gamma = \mathbf{0} \end{aligned} \right. \quad (4.42b)$$

4.5.3 Enhanced surface strain interpolation

By injecting Eq. (4.33), Eq. (4.34) and Eq. (4.35) into the system (4.42), the discretized problem reads as follows:

$$\bigwedge_{e=1}^{N_{\text{elem}}} [\mathbf{f}_{int}^{\Omega_e \setminus \Gamma_e} + \mathbf{f}_{int}^{\Gamma_e} - \mathbf{f}_{ext}^e] = \mathbf{0} , \quad (4.43)$$

$$\mathbf{h}_e = \int_{\Omega_e^{(1)}} (\mathbf{G}_v^{(1)})^T \hat{\boldsymbol{\sigma}}^{(1)} d\Omega + \int_{\Omega_e^{(2)}} (\mathbf{G}_v^{(2)})^T \hat{\boldsymbol{\sigma}}^{(2)} d\Omega + \int_{\Gamma_e} \mathbf{G}_{vs}^T \hat{\boldsymbol{\sigma}}_s d\Gamma = \mathbf{0} \quad \forall e \text{ cut by } \Gamma , \quad (4.44)$$

where $\bigwedge_{e=1}^{N_{\text{elem}}}$ denotes the assembly process and with

$$\begin{aligned} \mathbf{f}_{int}^{\Omega_e \setminus \Gamma_e} &= \int_{\Omega_e^{(1)}} \mathbf{B}^T \mathbf{C}^{(1)} (\mathbf{B}\mathbf{u} + \mathbf{G}_r^{(1)} \mathbf{a}) d\Omega + \int_{\Omega_e^{(2)}} \mathbf{B}^T \mathbf{C}^{(2)} (\mathbf{B}\mathbf{u} + \mathbf{G}_r^{(2)} \mathbf{a}) d\Omega , \\ \mathbf{f}_{int}^{\Gamma_e} &= \int_{\Gamma_e} \mathbf{B}^T \mathcal{M}^T \mathbf{C}^{(s)} (\mathcal{M}\mathbf{B}\mathbf{u} + \mathbf{G}_{rs} \mathbf{a}) d\Gamma , \\ \mathbf{f}_{ext}^e &= \int_{\Omega_e} \mathbf{N}^T \mathbf{b} d\Omega + \int_{\partial\Omega_F} \mathbf{N}^T \mathbf{F} dS , \end{aligned} \quad (4.45)$$

In the bulk, the compatibility condition between the enhanced strain and the displacement field is ensured by using \mathbf{G}_r and the traction continuity condition is verified by using \mathbf{G}_v . On the interface these conditions are not required, only one interpolation, that will be later defined, for both virtual and real strain of the interface is considered: $\mathbf{G}_s = \mathbf{G}_{rs} = \mathbf{G}_{vs}$.

Due to the form of the interpolation of the enhanced strain fields, similar to the system (4.28) of the perfect interface case, Eq. (4.44) is solved independently on each element crossed by the interface Γ . Taking into account the expression (4.23) of \mathbf{G}_v in Eq. (4.44), we obtain the following local equation:

$$\mathbf{h}_e = \left(\frac{V^{(2)}}{V} \int_{\Omega_e^{(1)}} \mathcal{N}^T \hat{\boldsymbol{\sigma}}^{(1)} d\Omega - \frac{V^{(1)}}{V} \int_{\Omega_e^{(2)}} \mathcal{N}^T \hat{\boldsymbol{\sigma}}^{(2)} d\Omega + \int_{\Gamma_e} \mathbf{G}_s^T \hat{\boldsymbol{\sigma}}_s d\Gamma \right) = \mathbf{0} . \quad (4.46)$$

With the fact that we consider here 3 nodes triangular elements, where the stress fields are constant in $\Omega_e^{(1)}$ and $\Omega_e^{(2)}$ and also on Γ , Eq. (4.46) can be rewritten as:

$$\frac{V^{(2)}V^{(1)}}{V} \mathcal{N}^T \llbracket \hat{\boldsymbol{\sigma}} \rrbracket + A \mathbf{G}_s^T \hat{\boldsymbol{\sigma}}_s = \mathbf{0} , \quad (4.47)$$

where A is the length (surface in 3D case) of the portion of Γ crossing the considered element.

It remains at this stage to choose the function \mathbf{G}_s used for the interpolation of the enhanced surface strain. This choice is made in such a way that the local equation (4.46) corresponds to the equilibrium equation of the coherent interface, namely the generalized Young Laplace equation (2.48). We can notice that $\mathcal{N}^T \llbracket \hat{\boldsymbol{\sigma}} \rrbracket$ is the Voigt's notation of $\llbracket \hat{\boldsymbol{\sigma}} \rrbracket \mathbf{n}$. Hence, combining Eq. (2.48) and Eq. (4.47) leads

to:

$$\frac{V^{(2)}V^{(1)}}{V} [(\hat{\boldsymbol{\sigma}}_s : \mathcal{K})\mathbf{n} + \mathbf{P}\mathbf{div}_s(\hat{\boldsymbol{\sigma}}_s)] = A\mathbf{G}_s^T \hat{\boldsymbol{\sigma}}_s. \quad (4.48)$$

Note that Eq. (4.48) is solved at the element level and that for three nodes triangle element, the surface stress is constant on each element. Therefore, the surface divergence of the interface stress $\mathbf{div}_s \hat{\boldsymbol{\sigma}}_s$ vanishes. It should be pointed out here that the non-uniform distribution of the interface stress (related to $\mathbf{div}_s \hat{\boldsymbol{\sigma}}_s$) has been taken into account at the global level via the global equilibrium equation (where the integral is done for the whole length of the interface Γ). The local curvature tensor \mathcal{K} is a tangential superficial tensor that can be written in the 2D context as:

$$\mathcal{K} = \frac{1}{R}\mathbf{P}, \quad (4.49)$$

where R is the local radius of curvature of the interface on the considered element. Eq. (4.48) now becomes

$$\frac{V^{(2)}V^{(1)}}{VA} \frac{1}{R} \mathbf{n}(\hat{\boldsymbol{\sigma}}_s : \mathbf{P}) = \mathbf{G}_s^T \hat{\boldsymbol{\sigma}}_s. \quad (4.50)$$

Since $\hat{\boldsymbol{\sigma}}_s$ and \mathbf{P} are symmetric tensors, Eq. (4.50) can be written as:

$$\frac{V^{(2)}V^{(1)}}{VA} \frac{1}{R} \mathbf{n}\mathcal{P}^T \hat{\boldsymbol{\sigma}}_s = \mathbf{G}_s^T \hat{\boldsymbol{\sigma}}_s. \quad (4.51)$$

where \mathcal{P} is the Voigt's notation of \mathbf{P} .

From Eq. (4.51), we finally obtain the expression of \mathbf{G}_s in the form

$$\mathbf{G}_s = \frac{V^{(2)}V^{(1)}}{VA} \frac{1}{R} \mathcal{P} \mathbf{n}^T. \quad (4.52)$$

The computation of \mathbf{G}_s requires the value of the radius of curvature R of the interface. In the general case where the radius of curvature is not available or when the interface shape changes with respect to time as in fluid mechanics, the value of the radius of curvature can be numerically estimated through the nodal values of signed distance to the interface (level set). The computational process and the influence of the numerical curvature on results are presented in Appendix A.

By using the interpolations of \mathbf{G}_v , \mathbf{G}_r and \mathbf{G}_s given in Eqs. (4.19), (4.23) and (4.52), Eqs (4.43) and Eq. (4.44) can be rewritten in the matrix form as:

$$\begin{cases} \sum_{e=1}^{N_{\text{elem}}} (\mathbf{K}_{uu}^e \mathbf{u} + \mathbf{K}_{ua}^e \mathbf{a}) = \sum_{e=1}^{N_{\text{elem}}} \mathbf{f}_{ext}^e & (4.53a) \\ \mathbf{K}_{au}^e \mathbf{u} + \mathbf{K}_{aa}^e \mathbf{a} = \mathbf{0} \quad \forall e \text{ cut by } \Gamma & (4.53b) \end{cases}$$

where

$$\begin{aligned}
\mathbf{K}_{uu}^e &= \int_{\Omega_e^{(1)}} \mathbf{B}^T \mathbf{C}^{(1)} \mathbf{B} d\Omega + \int_{\Omega_e^{(2)}} \mathbf{B}^T \mathbf{C}^{(2)} \mathbf{B} d\Omega + \int_{\Gamma_e} \mathbf{B}^T \mathcal{M}^T \mathbf{C}^{(s)} \mathcal{M} \mathbf{B} d\Gamma \\
\mathbf{K}_{ua}^e &= \int_{\Omega_e^{(1)}} \mathbf{B}^T \mathbf{C}^{(1)} \mathbf{G}_r^{(1)} d\Omega + \int_{\Omega_e^{(2)}} \mathbf{B}^T \mathbf{C}^{(2)} \mathbf{G}_r^{(2)} d\Omega + \int_{\Gamma_e} \mathbf{B}^T \mathcal{M}^T \mathbf{C}^{(s)} \mathbf{G}_s d\Gamma \\
\mathbf{K}_{au}^e &= \int_{\Omega_e^{(1)}} (\mathbf{G}_v^{(1)})^T \mathbf{C}^{(1)} \mathbf{B} d\Omega + \int_{\Omega_e^{(2)}} (\mathbf{G}_v^{(2)})^T \mathbf{C}^{(2)} \mathbf{B} d\Omega + \int_{\Gamma_e} \mathbf{G}_s^T \mathbf{C}^{(s)} \mathcal{M} \mathbf{B} d\Gamma \\
\mathbf{K}_{aa}^e &= \int_{\Omega_e^{(1)}} (\mathbf{G}_v^{(1)})^T \mathbf{C}^{(1)} \mathbf{G}_r^{(1)} d\Omega + \int_{\Omega_e^{(2)}} (\mathbf{G}_v^{(2)})^T \mathbf{C}^{(2)} \mathbf{G}_r^{(2)} d\Omega + \int_{\Gamma_e} \mathbf{G}_s^T \mathbf{C}^{(s)} \mathbf{G}_s d\Gamma
\end{aligned} \tag{4.54}$$

where $\mathbf{C}^{(1)}$, $\mathbf{C}^{(2)}$, $\mathbf{C}^{(s)}$ correspond to the matrix form of the elastic tensor of the phase (1), (2) and of the interface Γ , respectively, their expression being:

$$\mathbf{C}^{(i)} = \begin{bmatrix} (\lambda^{(i)} + 2\mu^{(i)}) & \lambda^{(i)} & 0 \\ \lambda^{(i)} & (\lambda^{(i)} + 2\mu^{(i)}) & 0 \\ 0 & 0 & \mu^{(i)} \end{bmatrix} \quad i = 1, 2, s. \tag{4.55}$$

The system (4.53) is solved by the same strategy used to solve the system (4.28). The final global system is written as:

$$\bigwedge_{e=1}^{N_{\text{elem}}} \widetilde{\mathbf{K}}^e \mathbf{u} = \bigwedge_{e=1}^{N_{\text{elem}}} \mathbf{f}_{ext}^e \tag{4.56}$$

with

$$\widetilde{\mathbf{K}}^e = \mathbf{K}_{uu}^e - \mathbf{K}_{ua}^e (\mathbf{K}_{aa}^e)^{-1} \mathbf{K}_{au}^e. \tag{4.57}$$

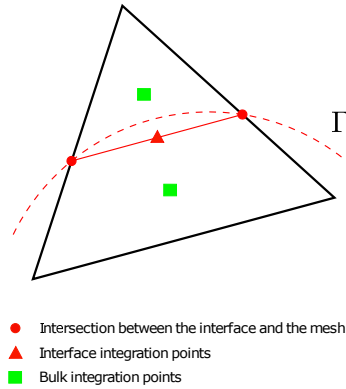


Figure 4.17: Element cut by the interface Γ , approximated interface and integration points in E-FEM.

As the enrichment does not affect the degree of interpolation of the fields in the element (contrary to XFEM enrichment), the numerical integration procedure only needs one integration point for each subdomain in the considered element (see Figure 4.17).

4.6 Numerical examples using E-FEM with interface effect

Based on the performance test presented in section 4.3, we consider here the SKON formulation for different the next numerical examples incorporating a surface elasticity: Eshelby problem, two phases composite and nanocomposite with random microstructures.

4.6.1 Eshelby problem with coherent interface

The first example aims to validate the proposed numerical approach for the Eshelby problem incorporating surface elasticity at the matrix/inclusion interface. This problem has already been presented in subsection 3.4.1 (see Figure 3.6a). As consider the linear plane strain hypothesis, the problem corresponds to a cylindrical inclusion immersed in an infinite elastic domain. An elastic interface is introduced between the infinite domain and the inclusion. As for the classical Eshelby problem, a uniform dilational eigenstrain ϵ^* is prescribed in the inclusion. We consider here that $\epsilon^* = \epsilon_{xx}^* = \epsilon_{yy}^* = 0.5, \epsilon_{zz}^* = 0$, and the material parameters of the bulk are $E = 3GPa$ and $\mu = 0.3$. The convergence analysis obtained from the proposed approach is compared to those of the XFEM and Interface element approach which have already presented in subsection 3.4.1.

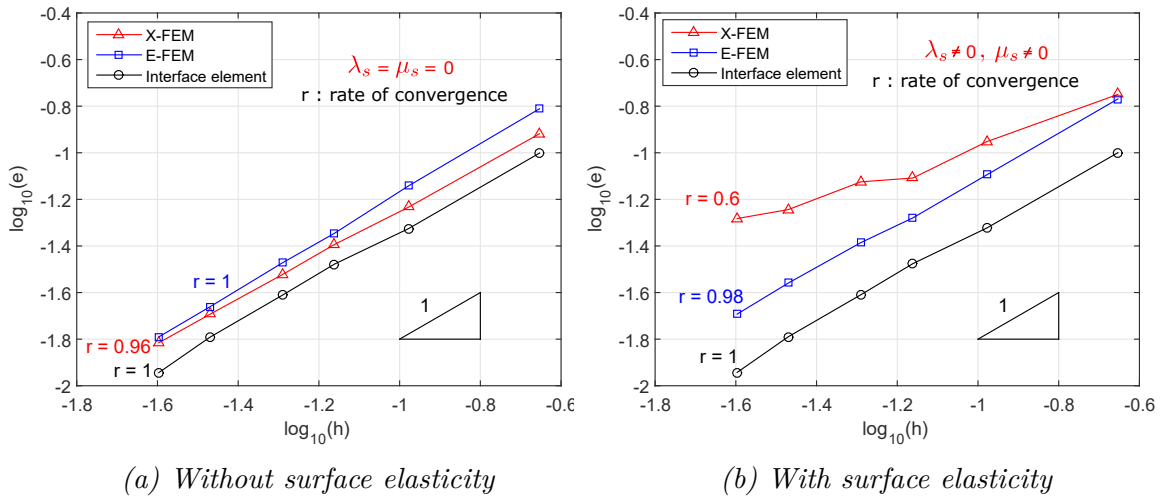


Figure 4.18: Convergence analysis for the Eshelby problem with and without surface elasticity for the three methods: E-FEM, XFEM and Interface element.

Figure 4.18 presents the comparison in terms of convergence rate and efficiency of the three numerical approaches for the case without ($k_s = 0$ N/m) and with surface elasticity ($k_s = 6.092$ N/m corresponding to $\lambda_s = 6.842$ N/m, $\mu_s = -0.375$ N/m [Miller and Shenoy, 2000]). It can be seen that the convergence of E-FEM

is slightly affected by the presence of surface elasticity but the expected rate of convergence $r \approx 1$ is recovered in both cases. The accuracy of the three compared strategies shows that the E-FEM solution is slightly less accurate than the "Interface element" solution but better than XFEM solution for the case with surface elasticity.

In the previous chapter, we tested the performance of the XFEM and Interface element approaches for various mechanical properties of the interface. To that end, we introduced the contrast coefficient $\alpha = \frac{\hat{k}_s}{\hat{k}_m}$. We showed in the previous chapter that the performance of the XFEM is affected by the contrast parameter α . We perform here the same test for the E-FEM approach and the results are reported in Figure 4.19a. To facilitate comparison, the results of XFEM presented in Figure 3.7a are plotted again here in Figure 4.19b.

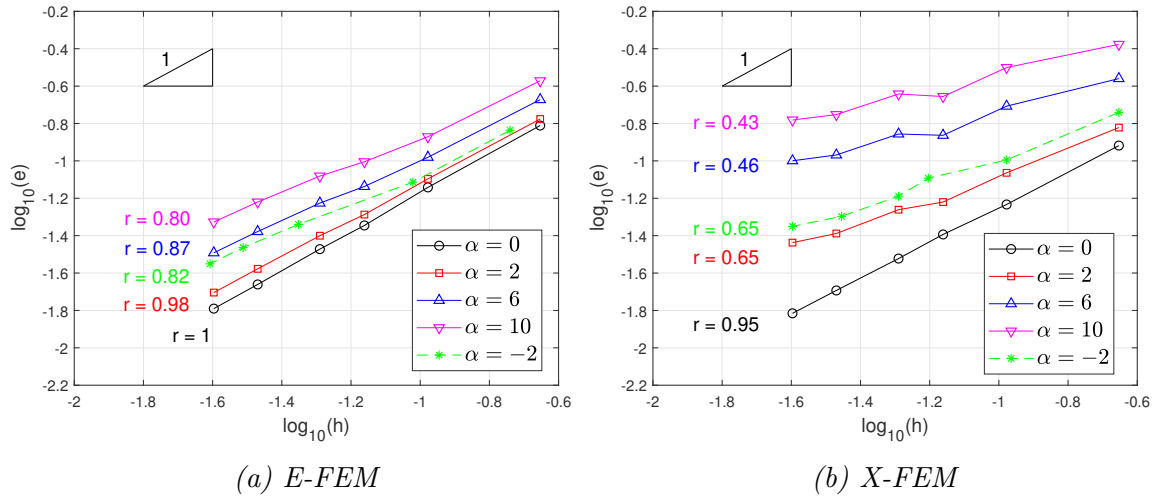


Figure 4.19: Convergence analysis of E-FEM for the extended Eshelby problem with different values of α , compared to XFEM results ($\beta = 1$).

Compared to XFEM, we can note that the convergence of E-FEM is less affected by the introduction of surface elasticity. The rate of convergence remains higher than for XFEM ($r = 0.80$ compared to $r = 0.43$ for XFEM for $\alpha = 10$). For the case $\alpha < 0$, to avoid the ill-condition problem caused by the negative-definite interface stiffness matrices, the following meshes are chosen: 12x12 nodes, 22x22 nodes, 46x46 nodes, 66x66 nodes, and 82x82 nodes.

The local field investigation that have been done with the XFEM and Interface element approaches in the previous chapter is now performed with the proposed approach. The component ϵ_{xx} of the strain along the line AB is plotted in Figure 4.20. The 40x40 nodes meshes are used for this test (see Figures 4.5a). The results of the XFEM approach are added in the figures for comparison. We notice that the strain jump across the interface is better estimated by E-FEM than by XFEM for high values of α . The accurate estimation of strain jump of E-FEM leads to better convergence as reported in Figure 4.19a.

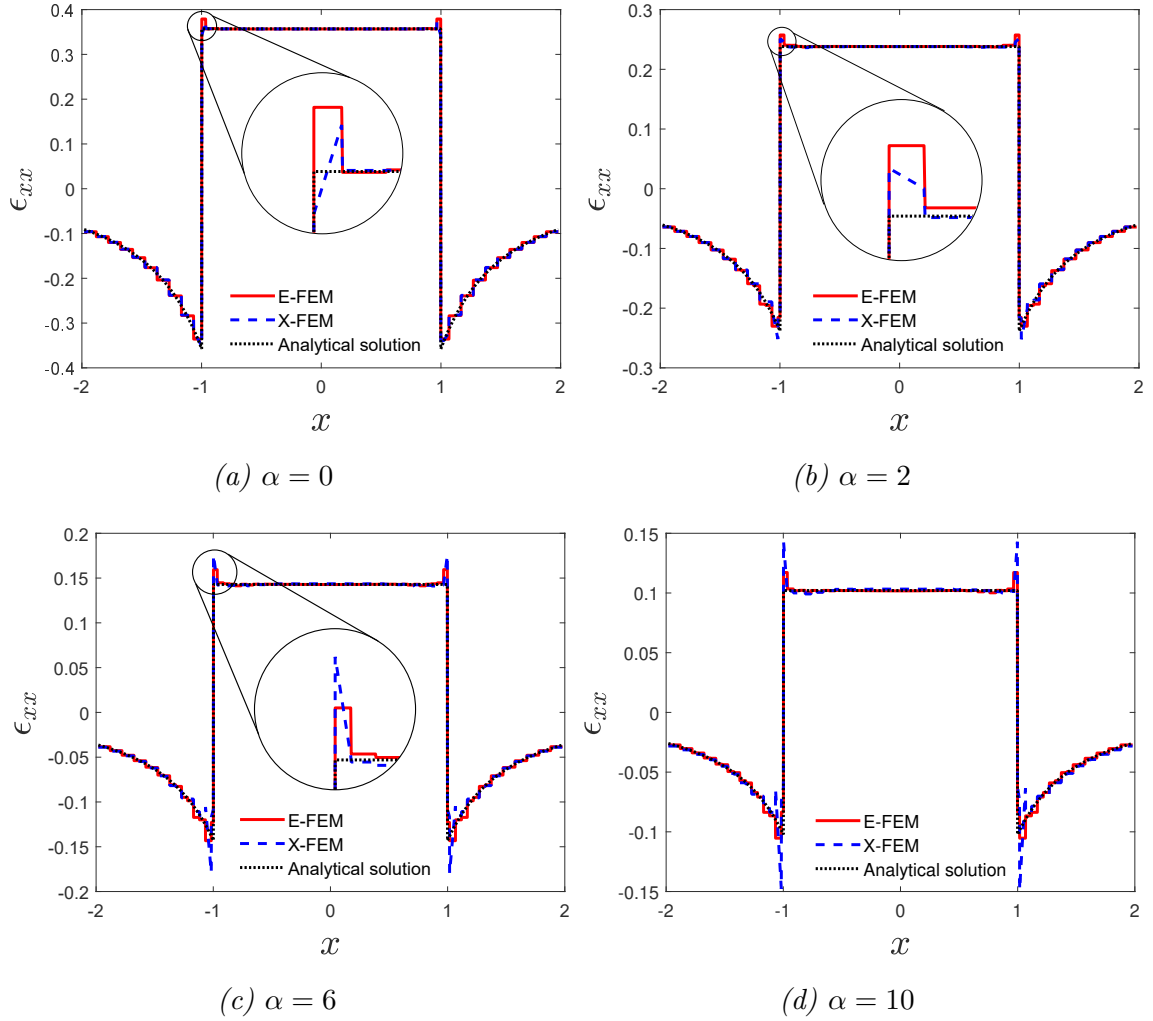


Figure 4.20: ϵ_{xx} along the line A-B for different values of α (E-FEM vs XFEM).

4.6.2 Two phases nanocomposite

In this subsection, we consider the problem of the linear homogenization of a two-phase material with coherent interfaces at the matrix/inclusion interface. The homogenization is performed assuming a periodic microstructure, the considered RVE corresponding to a unit-cell is represented in Figure 4.21. The chosen material properties are as follows: $\nu_m = \nu_i = 0.32$, $E_m = 70$ GPa, $E_i = 7$ GPa and $\lambda_s = 6.842$ N/m, $\mu_s = -0.375$ N/m [Miller and Shenoy, 2000] (corresponding to $k_s = 6.092$ N/m). The computation is carried out on a 40x40 nodes mesh for both approaches: E-FEM and Interface element. The normalized effective bulk modulus obtained for the cases with and without surface elasticity versus the radius of inclusion for a fixed volume fraction $f = 0.2$ is plotted in Figure 4.21. We can observe a very good agreement between the results obtained from both approaches but also with the analytical results given in [Quang and He, 2009], in which, cylindrical inclusions in a shell of the matrix with a coherent interface, are surrounded by the effective

medium. It may be noticed that the size effect observed for the case accounting for surface elasticity is more pronounced for small radius of the nano-inclusions. As expected, no size effect is observed for the case without surface elasticity.

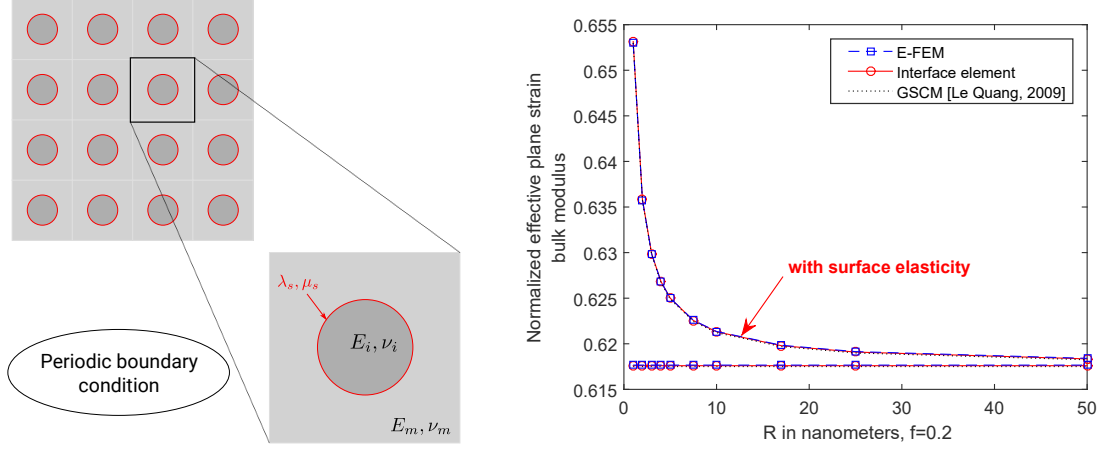


Figure 4.21: Size effect in effective plane-strain bulk modulus for circular inclusion ($f = 0.2$, $E_m = 70$ GPa, $E_i = 0.1E_m$, $\nu_m = \nu_i = 0.32$).

As already mentioned in chapter 2, the limitation of the analytical solutions remains in the fact that only the circular cylindrical or spherical shape of inclusions can be considered. In order to show the ability of the numerical approach in dealing with more complex geometries, the case of an ellipse with $a = 2b$ (where a is the main axis and b is the minor one) is treated (see Figure 4.22). The radius of curvature R_C at any point $C(x, y)$ on the ellipse is calculated by:

$$R_C = \frac{a^2}{b} \left(1 - \frac{(a^2 - b^2)x^2}{a^4} \right)^{3/2}. \quad (4.58)$$

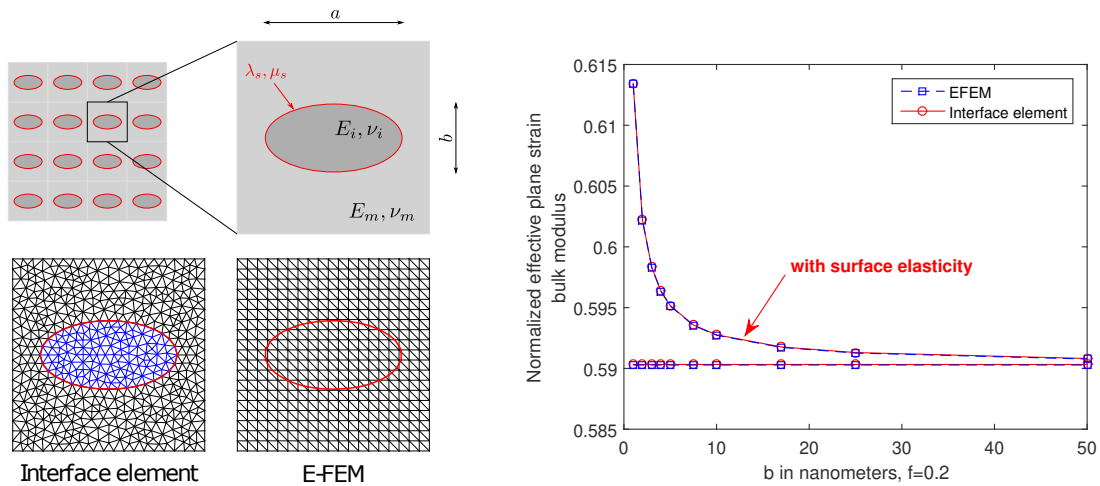


Figure 4.22: Size effect in effective plane-strain bulk modulus for ellipse inclusion ($f = 0.2$, $E_m = 70$ GPa, $E_i = 0.1E_m$, $\nu_m = \nu_i = 0.32$).

Since no analytical result for the case of the elliptical cylinder with surface elasticity is available in the literature, we compare the results obtained from the E-FEM proposed approach with the Interface element results, consider here as the reference results. The normalized effective bulk modulus versus the minor axis b of the elliptic inclusion is shown in Figure 4.22. The size effect is here again clearly reproduced by the proposed approach and a good agreement with the Interface element approach is observed.

In order to evaluate the ability of the proposed strategy in reproducing the size effect for complex geometries, we consider non-convex "arbitrary" shapes of inclusion. To that end, we consider the radius function proposed in [Yvonnet et al., 2008]:

$$R(\alpha) = R_o + A \sin(B\alpha), \quad \alpha \in [0, 2\pi], \quad (4.59)$$

where R_o is the reference radius, A, B are deterministic constants which define the amplitude and the period of oscillations of the shape "around" the perfect circle. With such a function, the associated area of inclusion can be derived as:

$$V = \frac{4A^2B\pi + 8AR_o + 8B\pi R_o^2 - 8AR_o \cos(2B\pi)}{8B} + \frac{A^2 \sin(4B\pi)}{8B}, \quad (4.60)$$

We choose here $A = 0.25R_o$ and $B = \{3, 5, 7\}$.

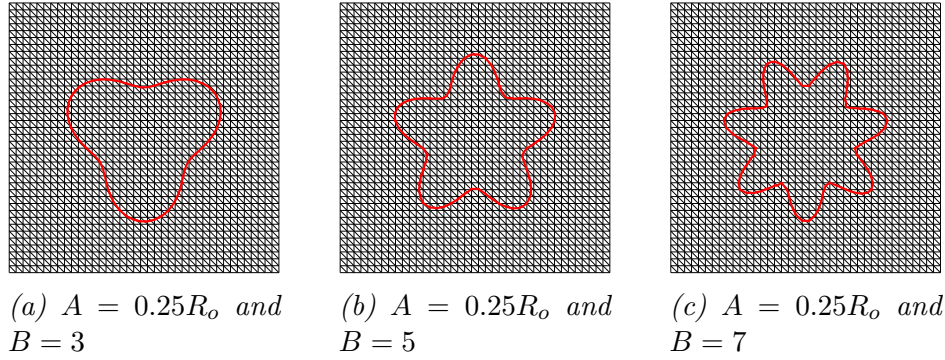


Figure 4.23: Arbitrary shapes

The shapes corresponding to those choices are presented in Figure 4.23. Due to the complexity of geometry, the generation of the conforming meshes needed for the Interface element approach is costly and the analytical solutions, of course, are not available for these cases.

We observe in Figure 4.24, a big influence of the inclusion shape on the effective bulk modulus. For a fixed volume fraction, a decrease of the module according to the increasing number of oscillations can be reported. This tendency has also been shown with the XFEM/level set approach in [Yvonnet et al., 2008]. In addition, the size effect for different shapes of inclusion is clearly presented.

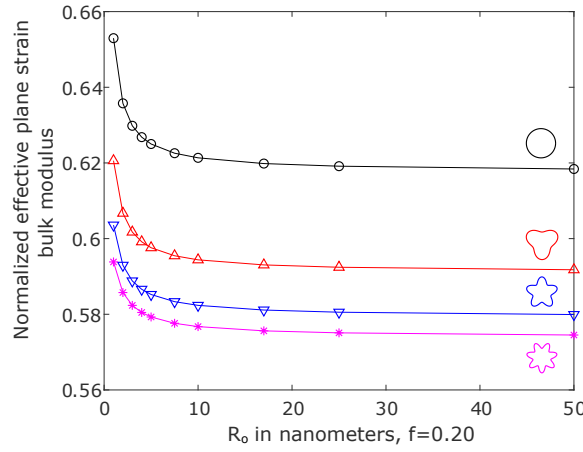


Figure 4.24: Size effect and shape dependence in normalized effective bulk modulus. $E_m = 10E_i$, $\nu_m = \nu_i = 0.32$, $f = 0.2$

4.6.3 Nanocomposites with random micro-structures

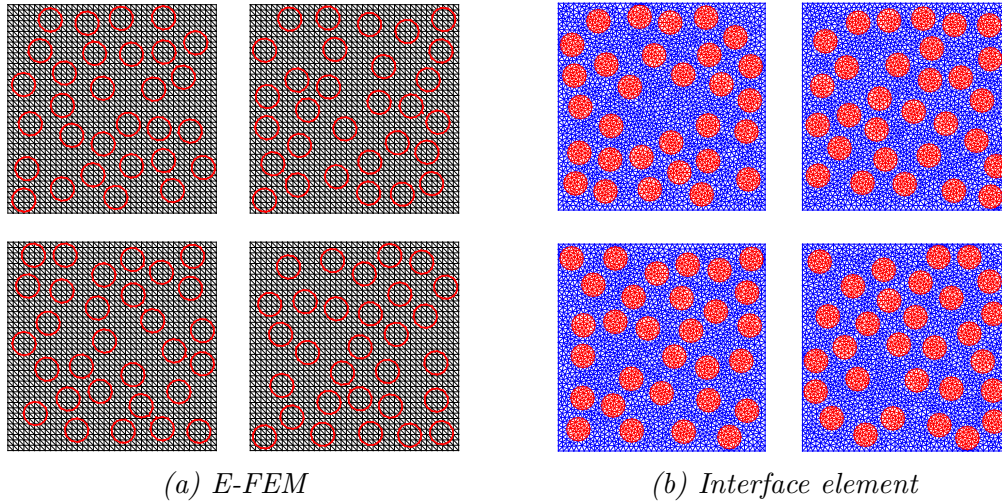


Figure 4.25: Several samples for 30 randomly distributed nano-inclusions.

To consider more realistic micro-structures, different RVEs consisting of randomly distributed nano-inclusions are analyzed. We investigate here a domain with 30 monodisperse inclusions (see Figure 4.25). The radius of the inclusions is chosen in a range from 1 nm to 50 nm while the volume fraction is fixed to $f = 0.3$. For each size of inclusion, we generate a random microstructure and calculate the homogenized bulk modulus until we reach the statistical convergence of the average value of the effective modulus (see Figure 4.26a). The results obtained from the proposed approach in comparison with those of the XFEM and Interface element approaches are shown in Figure 4.26b. As mentioned in chapter 3 the comparison only has a qualitative meaning since the mesh convergence has not been reached, but expected size effect is well observed for the three approaches.

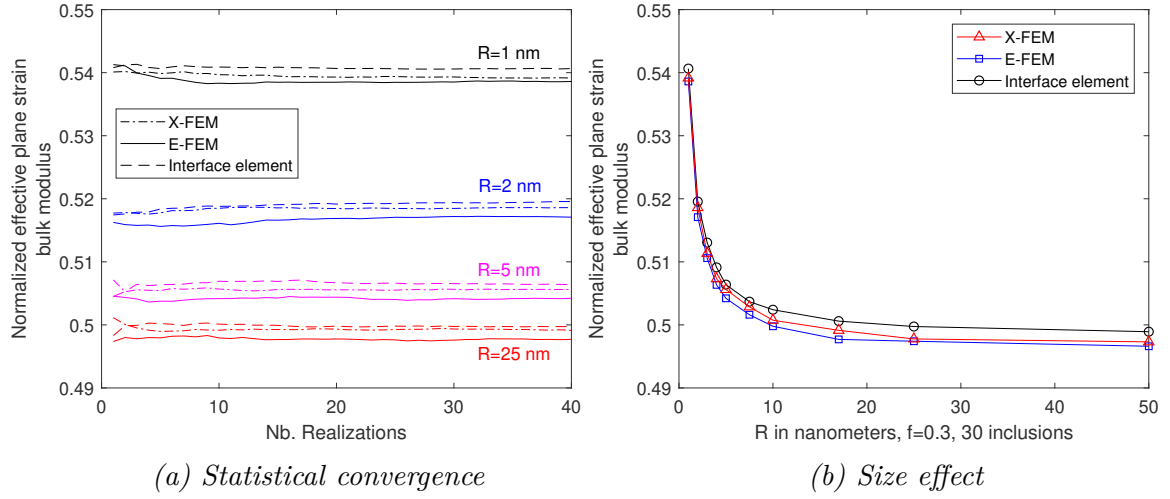


Figure 4.26: Size effect for effective plane-strain bulk modulus with randomly distributed nano-inclusions ($f = 0.3$, $E_m = 70$ GPa, $E_i = 0.1E_m$, $\nu_m = \nu_i = 0.32$; $\lambda_s = 6.842$ N/m, $\mu_s = -0.375$ N/m, corresponding to $k_s = 6.092$ N/m).

	X-FEM	E-FEM	Interface element
Number of standard d.o.f	20000	20000	21528
Number of additional d.o.f	4560	4560	0
Total unknowns	24560	24560	21528
Number of integration points on each enriched element	9 (2 on Γ)	2 (1 on Γ)	\emptyset
Size of elemental stiffness matrix	12×12	6×6	6×6
Final size of global stiffness matrix	$4.10^4 \times 4.10^4$	$2.10^4 \times 2.10^4$	21528×21528
Computing time for 1 realization (sec)	106.676	46.206	45.223

Table 4.1: Comparison of computational cost (XFEM vs E-FEM vs IE).

The computational costs of the three approaches are compared in Table 4.1. Note that the calculation time presented in Table 4.1 has to be compared only qualitatively and has a relative meaning since no code optimization process has been done. We notice that XFEM and E-FEM have the same number of additional degrees of freedom over the whole domain. However, due to the nodal enrichment strategy of XFEM, the elemental and global stiffness matrix has double size compared to standard FEM. Although the global matrix of XFEM is hollow with a lot of zeros, the assembly process takes much more time than the two other approaches. Moreover,

this enrichment makes the interpolations of the fields in the enriched element are one order higher than for standard FEM. Therefore, XFEM strategy requires more integration points in the bulk and on the interface of the enriched element. On the contrary, the local enhancement of E-FEM allows condensing the additional degrees of freedom at the element level leading to the final size of the global stiffness matrix that is identical to that of standard FEM. The memory space needed and the computational time of the E-FEM and Interface element approach are almost equal. For the approaches performed on the regular mesh which does not require any discretization effort, the results given by E-FEM and XFEM are very close but the proposed approach is less costly than XFEM.

4.7 Conclusion

In this chapter, we have proposed a numerical approach based on the Embedded Finite Element Method for predicting the effective modulus of nanocomposites, taking into account size effect.

Before adding the surface elasticity, the classical first Eshelby problem and the classical two-phases material problem have been treated by the three formulations of E-FEM. By applying the ideas of the Enhanced Assumed Strain method and the method of Incompatible Modes into the Hu-Washizu three-field variational formulation, the three formulations of E-FEM, namely SOS, KOS, SKON have been presented and compared. The comparison in terms of performance and accuracy for dealing with weak discontinuities, which is missing in the literature, showed that SKON formulation gave the best results among the three formulations. We also reported an issue relating to the evaluation of the local equilibrium at the elementary level. This issue makes E-FEM formulations only work well at low contrast of rigidity of the different phases. Several promising solutions for this issue have been suggested for future works. Based on its good performance, the SKON formulation has been chosen to handle the case of nanocomposites with a coherent interface.

The coherent interface model with a surface elasticity has been added in the framework of three-fields variational formulation, leading to the introduction of interface terms in both global and local equilibrium equations. Instead of the traction continuity condition, the generalized Young-Laplace equation is introduced at the element level by choosing an appropriate interpolation of the virtual enhanced surface strain. Due to the use of the "operator split method" and the "static condensation" at the element level, the global size of the problem does not depend on the number of inclusions and interfaces. In terms of numerical resources, the memory space needed only depends on the mesh size.

The validation of the E-FEM developed approach has been done by comparing the results obtained to the analytical solutions and to the results given by the In-

terface element approach. We noticed that the convergence and the accuracy of the strain jump obtained from the proposed approach are less affected by the introduction of surface elasticity than those of XFEM. We then performed the numerical homogenization with periodic and random microstructure in which the size dependence of the nanocomposite has been reproduced with high accuracy. Moreover, the proposed approach allows for handling complex shapes of inclusion.

The capacity of working with the nonlinear behavior of the E-FEM based approach will be shown in the next chapter.

Chapter 5

Modeling nonlinear behavior with surface elasticity by numerical approaches

In this chapter, the numerical models presented in the previous chapters are used in the context of nonlinear behaviors. A von Mises type elastoplastic law with linear isotropic hardening is considered for the bulk while the interface is considered as linear elastic. Results on the homogeneous behavior obtained from the three different numerical approaches (Interface element, XFEM and E-FEM) are then presented and compared.

Contents

5.1	Introduction	104
5.2	Plasticity model	104
5.2.1	Plasticity model with von Mises plasticity criterion . . .	105
5.2.2	Numerical integration	108
5.3	Finite element implementation	113
5.3.1	Interface element approach	113
5.3.2	XFEM approach	114
5.3.3	E-FEM approach	115
5.4	Nonlinear results	117
5.4.1	Interface element approach	117
5.4.2	XFEM and E-FEM	120
5.5	Conclusion	123

5.1 Introduction

Despite the increase in the use of nanocomposites in the industry, researches on the nonlinear behaviors of this kind of material are still limited. As well as many other composite materials, nano-reinforced materials can exhibit nonlinear behavior, particularly because the matrix may exhibit nonlinear behavior. On one hand, analytical homogenization approaches integrating nonlinear aspects are complex to implement [Brach et al., 2017a, Brach et al., 2017b], on the other hand, numerical methods are robust tools in handling nonlinear laws.

We present in this chapter the first step into the nonlinear domain by using the three numerical approaches presented in the previous chapters. In a very first example here, a von Mises type elastoplastic law with linear isotropic hardening is considered for the bulk while the interface mechanical behavior is considered linear elastic. In that nonlinear context, a standard Newton-Raphson procedure is used to solve the global nonlinear set of equations. While at the local level, a return mapping algorithm [Simo and Hughes, 2006] is used to determine the evolution of the internal and state variables associated with the elastoplasticity model. In the following, due to the use of the von Mises criterion, the deviatoric part of the stress and strain tensors are used for the computation. Therefore, although as consider the 2D plane strain hypothesis, the strain and stress tensor are now expressed in the vector forms as:

$$\begin{aligned}\boldsymbol{\epsilon} &= \begin{bmatrix} \epsilon_{11} & \epsilon_{22} & \epsilon_{33} & 2\epsilon_{12} \end{bmatrix}^T, \\ \boldsymbol{\sigma} &= \begin{bmatrix} \sigma_{11} & \sigma_{22} & \sigma_{33} & \sigma_{12} \end{bmatrix}^T,\end{aligned}\tag{5.1}$$

In section 5.2 we will recall the main ingredients of the plasticity model based on a von Mises criterion as well as its numerical integration. For the seek of comparison, the introduction of the surface elasticity is performed considering the three different approaches presented in the previous chapters (Interface element, XFEM, and E-FEM). In section 5.3, linearized forms corresponding to the three different approaches considered in this work will be given. Then, the results obtained from the three considered approaches for a simple traction test on a unit cell composed of an elastoplastic matrix and a circular nano-inclusion will be compared in section 5.4. Finally, the conclusions of these nonlinear developments are reported in section 5.5.

5.2 Plasticity model

In the following, as an opportunity to define our notations, we recall the main ingredients of the standard elastoplastic model that we used in this work.

5.2.1 Plasticity model with von Mises plasticity criterion

To describe an inelastic behavior and the corresponding irreversible processes, internal variables, capable of representing the different phenomena that characterize a particular inelastic behavior, have to be introduced to define the local state of the material. The choice of internal variables can be made according to various criteria. We limit ourselves in this work to elastoplasticity with linear isotropic hardening behavior. Therefore, the elastoplastic strain $\boldsymbol{\epsilon}^p$ and hardening variable ξ are introduced in the set of the internal variables (see Table 5.1).

State variables	Associated variables
$\boldsymbol{\epsilon}$	$\boldsymbol{\sigma}$
$\boldsymbol{\epsilon}^p$	$\boldsymbol{\sigma}$
ξ	q

Table 5.1: State and associated variables.

With the infinitesimal strain hypothesis, we consider an additive decomposition of the strain. In which, the total strain is composed by the elastic part $\boldsymbol{\epsilon}^e$ and plastic part $\boldsymbol{\epsilon}^p$

$$\boldsymbol{\epsilon} = \boldsymbol{\epsilon}^e + \boldsymbol{\epsilon}^p . \quad (5.2)$$

The free energy potential can be written in terms of the state variables $(\boldsymbol{\epsilon}, \boldsymbol{\epsilon}^p, \xi)$ in the case of linear isotropic hardening and isothermal conditions:

$$\Psi(\boldsymbol{\epsilon}, \boldsymbol{\epsilon}^p, \xi) = \Psi^e(\boldsymbol{\epsilon}, \boldsymbol{\epsilon}^p) + \Psi^p(\xi) = \frac{1}{2}(\boldsymbol{\epsilon} - \boldsymbol{\epsilon}^p) : \mathbb{C} : (\boldsymbol{\epsilon} - \boldsymbol{\epsilon}^p) + \frac{1}{2}\xi K \xi , \quad (5.3)$$

where K is the hardening modulus and ξ is the hardening variable (or accumulated plastic strain).

We consider in this work, as a first step, an associated model. Therefore, the last ingredient needed to elaborate the plastic constitutive model is the yield function, also corresponding in this context to the dissipation function. We chose here the classical von Mises criterion given as:

$$f(\boldsymbol{\sigma}, q) = \|\mathbf{dev} \boldsymbol{\sigma}\| - \sqrt{\frac{2}{3}}(\sigma_y - q) \leq 0 , \quad (5.4)$$

where

$$\|\mathbf{dev} \boldsymbol{\sigma}\| = \sqrt{\mathbf{dev} \boldsymbol{\sigma} : \mathbf{dev} \boldsymbol{\sigma}} \quad \text{with} \quad \mathbf{dev} \boldsymbol{\sigma} = \boldsymbol{\sigma} - \frac{1}{3}(\text{tr}(\boldsymbol{\sigma}))\mathbf{I} , \quad (5.5)$$

σ_y denotes the elastic limit stress and q is the stress-like variable associated to the hardening variable ξ (see Table 5.1).

The stress and stress-like variable can be derived through the state equations as

$$\boldsymbol{\sigma} = \frac{\partial \Psi}{\partial \boldsymbol{\epsilon}} = -\frac{\partial \Psi}{\partial \boldsymbol{\epsilon}^p} = \mathbb{C} : (\boldsymbol{\epsilon} - \boldsymbol{\epsilon}^p) , \quad (5.6a)$$

$$q = -\frac{\partial \Psi}{\partial \xi} = -\frac{\partial \Psi^p}{\partial \xi} = -K\xi . \quad (5.6b)$$

The plastic dissipation is then obtained thanks to the second principle of thermodynamics [Maugin, 1992] in the form:

$$0 \leq \mathcal{D} = \boldsymbol{\sigma} : \dot{\boldsymbol{\epsilon}} - \frac{\partial \Psi}{\partial t} \quad (5.7a)$$

$$= \boldsymbol{\sigma} : \dot{\boldsymbol{\epsilon}} - \frac{\partial \Psi}{\partial \boldsymbol{\epsilon}} : \dot{\boldsymbol{\epsilon}} - \frac{\partial \Psi}{\partial \boldsymbol{\epsilon}^p} : \dot{\boldsymbol{\epsilon}}^p - \frac{\partial \Psi}{\partial \xi} \dot{\xi} \quad (5.7b)$$

$$= \left(\boldsymbol{\sigma} - \frac{\partial \Psi}{\partial \boldsymbol{\epsilon}} \right) : \dot{\boldsymbol{\epsilon}} - \frac{\partial \Psi}{\partial \boldsymbol{\epsilon}^p} : \dot{\boldsymbol{\epsilon}}^p - \frac{\partial \Psi}{\partial \xi} \dot{\xi} \quad (5.7c)$$

Substituting Eqs. (5.6) into Eq. (5.7c) gives the evaluation of the plastic dissipation in terms of the evolution of internal variables

$$0 \leq \mathcal{D} = \boldsymbol{\sigma} : \dot{\boldsymbol{\epsilon}}^p + q\dot{\xi} . \quad (5.8)$$

As we consider an associated model, the evolution of the internal variables is obtained by invoking the principle of maximum dissipation [Lubliner, 1990]. Among all the admissible stresses ($f(\boldsymbol{\sigma}, q) \leq 0$), the system "chooses" the one maximizing the dissipation. This maximization process under constraints is recast into a stationarity problem of Lagrangian:

$$\mathcal{L}(\boldsymbol{\sigma}, q, \gamma) = -\mathcal{D} + \gamma f(\boldsymbol{\sigma}, q) , \quad (5.9)$$

where γ is the Lagrange multiplier.

Thereby the evolution equations are obtained through the Kuhn-Tucker optimality conditions:

$$\frac{\partial \mathcal{L}}{\partial \boldsymbol{\sigma}} = 0 \quad \Rightarrow \quad \dot{\boldsymbol{\epsilon}}^p = \gamma \frac{\partial f}{\partial \boldsymbol{\sigma}} , \quad (5.10a)$$

$$\frac{\partial \mathcal{L}}{\partial q} = 0 \quad \Rightarrow \quad \dot{\xi} = \gamma \frac{\partial f}{\partial q} , \quad (5.10b)$$

along with the loading/unloading conditions

$$\gamma f(\boldsymbol{\sigma}, q) = 0 \quad , \quad \gamma \geq 0 \quad , \quad f(\boldsymbol{\sigma}, q) \leq 0 . \quad (5.11)$$

Moreover, for a plastic loading, the consistency condition gives:

$$\dot{f}(\boldsymbol{\sigma}, q) = 0 \quad \Rightarrow \quad \frac{\partial f}{\partial \boldsymbol{\sigma}} : \dot{\boldsymbol{\sigma}} + \frac{\partial f}{\partial q} \dot{q} = 0. \quad (5.12)$$

Accounting for the choose of the von Mises criterion for the yield function f (see Eq. (5.4)), we obtain

$$\dot{\boldsymbol{\epsilon}}^p = \gamma \frac{\text{dev } \boldsymbol{\sigma}}{\|\text{dev } \boldsymbol{\sigma}\|} = \gamma \boldsymbol{\zeta}, \quad (5.13a)$$

$$\dot{\xi} = \sqrt{\frac{2}{3}} \gamma, \quad (5.13b)$$

where we denote $\boldsymbol{\zeta} = \frac{\text{dev } \boldsymbol{\sigma}}{\|\text{dev } \boldsymbol{\sigma}\|}$.

In Eq. (5.13), the multiplier γ describes the magnitude of plastic flow and $\boldsymbol{\zeta}$ defines the flow direction. Combining Eqs (5.6), (5.13) and (5.12), the expression of the multiplier γ can be obtained:

$$\gamma \boldsymbol{\zeta} : \mathbb{C} : (\dot{\boldsymbol{\epsilon}} - \gamma \boldsymbol{\zeta}) - \sqrt{\frac{2}{3}} \gamma K \sqrt{\frac{2}{3}} \gamma = 0 \quad \Rightarrow \quad \gamma = \frac{\boldsymbol{\zeta} : \mathbb{C} : \dot{\boldsymbol{\epsilon}}}{\boldsymbol{\zeta} : \mathbb{C} : \boldsymbol{\zeta} + \frac{2}{3} K}. \quad (5.14)$$

Note that $\boldsymbol{\zeta} = \frac{\text{dev } \boldsymbol{\sigma}}{\|\text{dev } \boldsymbol{\sigma}\|}$ is a deviatoric tensor, hence $\text{tr}(\boldsymbol{\zeta}) = 0$ which leads to:

$$\boldsymbol{\zeta} : \mathbb{C} = \lambda(\text{tr}(\boldsymbol{\zeta})) \mathbf{I} + 2\mu \boldsymbol{\zeta} = 2\mu \boldsymbol{\zeta}, \quad (5.15a)$$

$$\boldsymbol{\zeta} : \mathbb{C} : \boldsymbol{\zeta} = 2\mu(\boldsymbol{\zeta} : \boldsymbol{\zeta}) = 2\mu \left(\frac{\text{dev } \boldsymbol{\sigma}}{\|\text{dev } \boldsymbol{\sigma}\|} : \frac{\text{dev } \boldsymbol{\sigma}}{\|\text{dev } \boldsymbol{\sigma}\|} \right) = 2\mu. \quad (5.15b)$$

Thereby, the final expression of the Lagrange multiplier is:

$$\gamma = \frac{2\mu \boldsymbol{\zeta} : \dot{\boldsymbol{\epsilon}}}{2\mu + \frac{2}{3} K} = \frac{1}{1 + \frac{K}{3\mu}} \boldsymbol{\zeta} : \dot{\boldsymbol{\epsilon}}. \quad (5.16)$$

The combination of Eqs. (5.13) and (5.16) provides the relation between the stress rate and the strain rate:

$$\dot{\boldsymbol{\epsilon}}^p = \gamma \boldsymbol{\zeta} = \frac{(\boldsymbol{\zeta} : \dot{\boldsymbol{\epsilon}}) \boldsymbol{\zeta}}{1 + \frac{K}{3\mu}}, \quad (5.17a)$$

$$\dot{\boldsymbol{\sigma}} = \mathbb{C} : (\dot{\boldsymbol{\epsilon}} - \dot{\boldsymbol{\epsilon}}^p) = \mathbb{C} : \dot{\boldsymbol{\epsilon}} - \frac{2\mu}{1 + \frac{K}{3\mu}} \boldsymbol{\zeta} (\boldsymbol{\zeta} : \dot{\boldsymbol{\epsilon}}) = \left(\mathbb{C} - \frac{2\mu}{1 + \frac{K}{3\mu}} \boldsymbol{\zeta} \otimes \boldsymbol{\zeta} \right) : \dot{\boldsymbol{\epsilon}}. \quad (5.17b)$$

So the constitutive relation can then be written as:

$$\dot{\boldsymbol{\sigma}} = \mathbb{C}^{ep} : \dot{\boldsymbol{\epsilon}}, \quad (5.18)$$

with

$$\mathbb{C}^{ep} = \begin{cases} \mathbb{C} & \text{if } \gamma = 0 \\ \left(\mathbb{C} - \frac{2\mu}{1+\frac{K}{3\mu}} \boldsymbol{\zeta} \otimes \boldsymbol{\zeta} \right) & \text{if } \gamma > 0 \end{cases} \quad (5.19)$$

In the next section, we will see how this plasticity model can be numerically implemented.

5.2.2 Numerical integration

The solution of the nonlinear problem induced by the use of a nonlinear irreversible behavior is provided by an incremental strategy combined with an operator split technique. Therefore, the problem to be solved is written as:

$$\begin{array}{l} \textbf{Given : } \boldsymbol{\epsilon}_n = \boldsymbol{\epsilon}(t_n), \boldsymbol{\epsilon}_n^p = \boldsymbol{\epsilon}^p(t_n), \boldsymbol{\xi}_n = \boldsymbol{\xi}(t_n) \\ \quad \text{for all integration points of } \Omega^h \\ \textbf{Find : } \boldsymbol{\epsilon}_{n+1} = \boldsymbol{\epsilon}(t_n + \Delta t_n) = \boldsymbol{\epsilon}(t_{n+1}), \boldsymbol{\epsilon}_{n+1}^p, \boldsymbol{\xi}_{n+1} \\ \quad \text{for all integration points} \\ \text{such that } \begin{cases} \gamma_{n+1} \geq 0; f_{n+1} \leq 0; \gamma_{n+1} f_{n+1} = 0 \\ \quad \text{for all integration points} \\ \bigwedge_{e=1}^{N_{\text{elem}}} [\mathbf{f}_{n+1}^{e,int} - \mathbf{f}_{n+1}^{e,ext}] = 0 \end{cases} \end{array} \quad (5.20)$$

where $\mathbf{f}_{n+1}^{e,int}$ and $\mathbf{f}_{n+1}^{e,ext}$ denote the internal and external forces at time step t_{n+1} , respectively.

The use of the operator split technique allows separating the determination of the internal variables at the local level (integration points) to the determination of the nodal unknowns at the global level.

It has to be noticed that the stresses-involved in the evaluation of $\mathbf{f}_{n+1}^{e,int}$ are modified either through the modifications of internal variables at the local level or through modifications of the nodal displacements (inducing modifications of total strain). The resolution algorithm is summarized in Figure 5.1.

In order to better understand the resolution process, let's start at the local level, where we compute the internal variables producing the admissible stresses in agreement with the given (best) iterative value of the total strain $\boldsymbol{\epsilon}_{n+1}^{(i)}$. This can be written as follows:

- **Computation of plastic flow at the local level**

$$\begin{array}{l} \textbf{Given : } \boldsymbol{\epsilon}_{n+1}^{(i)}, \boldsymbol{\epsilon}_n^p, \boldsymbol{\xi}_n \\ \textbf{Find : } \boldsymbol{\epsilon}_{n+1}^p, \boldsymbol{\xi}_{n+1} \\ \text{such that } \gamma_{n+1} \geq 0; f_{n+1} \leq 0; \gamma_{n+1} f_{n+1} = 0 \end{array} \quad (5.21)$$

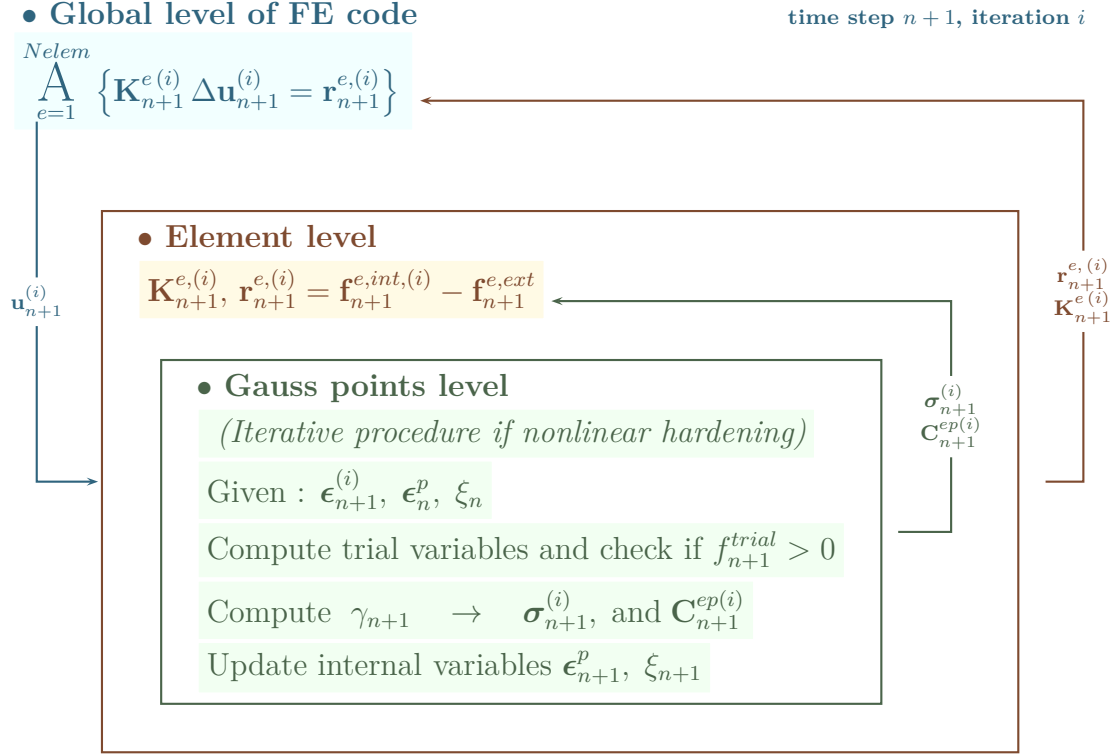


Figure 5.1: Resolution algorithm for standard plasticity model

To facilitate reading the document, as we are at the local level in a global iteration i , the superscript (i) is omitted. As a classical return mapping algorithm [Simo and Hughes, 2006] to compute the evolution of the internal variables at the local level is considered, the first step is to assume no evolution of internal variables ϵ^p , ξ and their associated variables σ , q :

$$\epsilon_{n+1}^{p,trial} = \epsilon_{n+1}^p \quad \text{and} \quad \xi_{n+1}^{trial} = \xi_n \quad (5.22a)$$

$$\sigma_{n+1}^{trial} = \mathbb{C} : (\epsilon_{n+1} - \epsilon_n^p) \quad \text{and} \quad q_{n+1}^{trial} = -K\xi_n \quad (5.22b)$$

$$f_{n+1}^{trial} = \|\text{dev } \sigma_{n+1}^{trial}\| - \sqrt{\frac{2}{3}} (\sigma_y - q_{n+1}^{trial}) . \quad (5.22c)$$

If $f_{n+1}^{trial} < 0$, the trial state is admissible, the internal variables do not evolve:

$$\epsilon_{n+1}^p = \epsilon_n^p \quad ; \quad \xi_{n+1} = \xi_n . \quad (5.23)$$

If $f_{n+1}^{trial} > 0$, the trial elastic state is not admissible and internal variables have to be updated. In that case, we have to find the positive value of the plastic multiplier $\gamma_{n+1} > 0$, which guarantees plastic admissibility of stress with $f_{n+1}(\sigma_{n+1}, q_{n+1}) = f_{n+1}(\gamma_{n+1}) = 0$ (see Figure 5.2). As this plastic multiplier is positive ($\gamma_{n+1} > 0$) the

plastic strain and hardening variable have to be updated:

$$\boldsymbol{\epsilon}_{n+1}^p = \boldsymbol{\epsilon}_n^p + \gamma_{n+1} \boldsymbol{\zeta}_{n+1} \quad \text{with} \quad \boldsymbol{\zeta}_{n+1} = \frac{\text{dev } \boldsymbol{\sigma}_{n+1}}{\|\text{dev } \boldsymbol{\sigma}_{n+1}\|} \quad (5.24)$$

$$\xi_{n+1} = \xi_n + \sqrt{\frac{2}{3}} \gamma_{n+1} \quad (5.25)$$

The final value of the stress tensor is computed as:

$$\begin{aligned} \boldsymbol{\sigma}_{n+1} &= \mathbb{C} : (\boldsymbol{\epsilon}_{n+1} - \boldsymbol{\epsilon}_{n+1}^p) \\ &= \mathbb{C} : (\boldsymbol{\epsilon}_{n+1} - \boldsymbol{\epsilon}_n^p) - \gamma_{n+1} \mathbb{C} : \boldsymbol{\zeta}_{n+1} \\ &= \boldsymbol{\sigma}_{n+1}^{trial} - \gamma_{n+1} 2\mu \boldsymbol{\zeta}_{n+1} . \end{aligned} \quad (5.26)$$

The deviatoric part of the final stress can also be written as the appropriate modification of the trial stress:

$$\text{dev } \boldsymbol{\sigma}_{n+1} = \text{dev } \boldsymbol{\sigma}_{n+1}^{trial} - \gamma_{n+1} 2\mu \boldsymbol{\zeta}_{n+1} . \quad (5.27)$$

From Eq. (5.27), we can have some important results related to plastic flow:

$$\text{dev } \boldsymbol{\sigma}_{n+1}^{trial} = \text{dev } \boldsymbol{\sigma}_{n+1} + \gamma_{n+1} 2\mu \frac{\text{dev } \boldsymbol{\sigma}_{n+1}}{\|\text{dev } \boldsymbol{\sigma}_{n+1}\|} \quad (5.28)$$

$$= \text{dev } \boldsymbol{\sigma}_{n+1} \underbrace{\left(1 + \frac{\gamma_{n+1} 2\mu}{\|\text{dev } \boldsymbol{\sigma}_{n+1}\|} \right)}_{\text{scalar}} \Rightarrow \quad (5.29)$$

$$\begin{cases} \boldsymbol{\zeta}_{n+1}^{trial} = \frac{\text{dev } \boldsymbol{\sigma}_{n+1}^{trial}}{\|\text{dev } \boldsymbol{\sigma}_{n+1}^{trial}\|} = \frac{\text{dev } \boldsymbol{\sigma}_{n+1}}{\|\text{dev } \boldsymbol{\sigma}_{n+1}\|} = \boldsymbol{\zeta}_{n+1} \\ \|\text{dev } \boldsymbol{\sigma}_{n+1}^{trial}\| = \|\text{dev } \boldsymbol{\sigma}_{n+1}\| + \gamma_{n+1} 2\mu \end{cases} \quad (5.30)$$

The first equation of Eqs. (5.30) expresses that the normal to the yield surface is kept the same for the trial and the final state. By combining Eq. (5.22c), Eq. (5.25) and the second equation of Eqs. (5.30), we have the expression of the yield function in terms of its trial value:

$$\begin{aligned} 0 = f_{n+1} &= \|\text{dev } \boldsymbol{\sigma}_{n+1}\| - \sqrt{\frac{2}{3}} (\sigma_y + K \xi_{n+1}) \\ &= \|\text{dev } \boldsymbol{\sigma}_{n+1}^{trial}\| - \gamma_{n+1} 2\mu - \sqrt{\frac{2}{3}} \left[\sigma_y + K \left(\xi_n + \sqrt{\frac{2}{3}} \gamma_{n+1} \right) \right] \\ &= \|\text{dev } \boldsymbol{\sigma}_{n+1}^{trial}\| - \sqrt{\frac{2}{3}} (\sigma_y + K \xi_n) - \gamma_{n+1} \left(2\mu + \frac{2}{3} K \right) \\ &= f_{n+1}^{trial} - \gamma_{n+1} \left(2\mu + \frac{2}{3} K \right) . \end{aligned} \quad (5.31)$$

We then obtain the value of the plastic multiplier ensuring plastic admissibility

($f_{n+1} = 0$):

$$\gamma_{n+1} = \frac{f_{n+1}^{trial}}{2\mu + \frac{2}{3}K} . \quad (5.32)$$

With the expression of γ_{n+1} above, the final stress can be computed from the trial values in Eq. (5.26).

The corresponding graphic illustration of the return mapping algorithm computation is given in Figure 5.2.

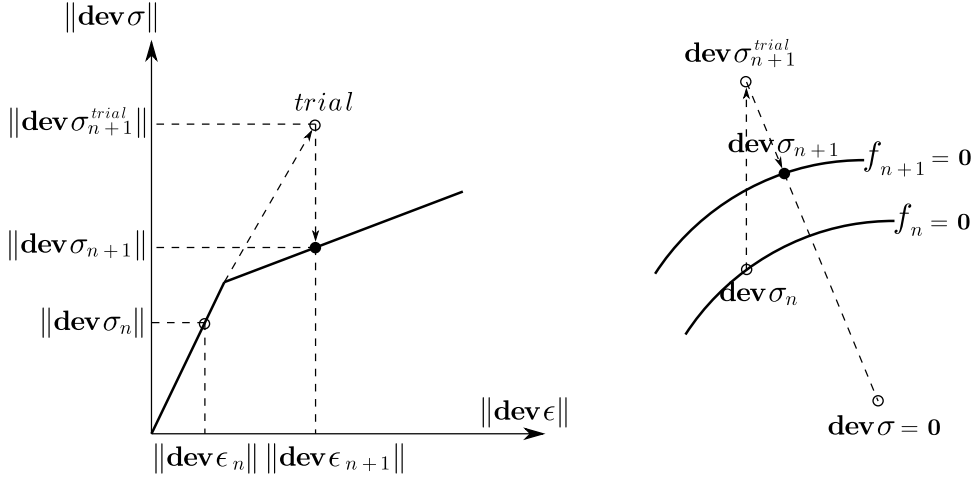


Figure 5.2: Computation of final stress from the elastic trial state by radial return mapping algorithm, where total deformation is kept fixed [Ibrahimbegovic, 2009].

For an elastic step, $\gamma_{n+1} = 0$, therefore $\sigma_{n+1} = \sigma_{n+1}^{trial}$ and the consistent elastoplastic tangent modulus remains the same as the elastic tensor

$$\mathbb{C}_{n+1}^{ep} = \frac{\partial \sigma_{n+1}}{\partial \epsilon_{n+1}} = \frac{\partial \sigma_{n+1}^{trial}}{\partial \epsilon_{n+1}} = \frac{\partial (\mathbb{C} : (\epsilon_{n+1} + \epsilon_n^p))}{\partial \epsilon_{n+1}} = \mathbb{C} . \quad (5.33)$$

For a plastic step, $\gamma_{n+1} > 0$, therefore σ_{n+1} is computed from Eq. (5.26) and the consistent elastoplastic tangent modulus is computed as the corresponding modification of the elasticity tensor

$$\begin{aligned} \mathbb{C}_{n+1}^{ep} &= \frac{\partial \sigma_{n+1}}{\partial \epsilon_{n+1}} \\ &= \frac{\partial \sigma_{n+1}^{trial}}{\partial \epsilon_{n+1}} - \frac{\partial (\gamma_{n+1} 2\mu \zeta_{n+1})}{\partial \epsilon_{n+1}} \\ &= \mathbb{C} - 2\mu \zeta_{n+1}^{trial} \otimes \frac{\partial \gamma_{n+1}}{\partial \epsilon_{n+1}} - 2\mu \gamma_{n+1} \frac{\partial \zeta_{n+1}^{trial}}{\partial \epsilon_{n+1}} \\ &= \mathbb{C} - \frac{2\mu}{1 + \frac{K}{3\mu}} \zeta_{n+1}^{trial} \otimes \zeta_{n+1}^{trial} - \gamma_{n+1} \frac{4\mu^2 \left(\mathbb{I} - \frac{1}{3} \mathbb{I} \otimes \mathbb{I} - \zeta_{n+1}^{trial} \otimes \zeta_{n+1}^{trial} \right)}{\| \text{dev } \sigma_{n+1}^{trial} \|} . \end{aligned} \quad (5.34)$$

We notice that the elastoplastic tangent modulus in Eq. (5.34) for the discrete problem, which is consistent with respect to the implicit Euler scheme computation

of stress, is not the same as the one in Eq. (5.19) defined for the continuum problem. However, for a large time, it is very important to employ the consistent (rather than continuum) elastoplastic tangent modulus in order to ensure the quadratic convergence rate of Newton's method (at the global level).

The internal variables ϵ_{n+1}^p and ξ_{n+1} are updated by using Eq. (5.24) and Eq. (5.25) with γ_{n+1} from Eq. (5.32) and ζ_{n+1} from Eq. (5.30). These information are needed to compute σ_{n+1} and C_{n+1}^{ep} for each integration points of the considered element. These two terms are then used to compute the residual and the stiffness matrix of the considered element before assembly for the computation at the global level (see Figure 5.1).

• **Solving equilibrium equations at the global level**

After computing the internal variables for each integration point which ensures the plastic admissibility of stress for a given iterative value of total deformation $\epsilon_{n+1}^{(i)}$, the global equilibrium equations can be solved:

<p>Given : $\epsilon_{n+1}^{p,(i)}, \xi_{n+1}^{(i)}$, with</p> <p style="text-align: center;">$\sigma_{n+1} = \mathbf{C} : (\epsilon_{n+1}^{(i)} - \epsilon_{n+1}^{p,(i)})$ and $q_{n+1} = -K\xi_{n+1}^{(i)}$</p> <p style="text-align: center;">plastically admissible for all integration points</p> <p>Test : $\mathbf{r}(\epsilon_{n+1}^{(i)}, \epsilon_{n+1}^p, \xi_{n+1}) = \sum_{e=1}^{Nelem} [\mathbf{f}_{n+1}^{e,int} - \mathbf{f}_{n+1}^{e,ext}] \stackrel{?}{=} \mathbf{0}$</p> <p style="text-align: center;">IF : $\ \mathbf{r}_{n+1}^{(i)}\ \leq tol \Rightarrow \text{next time step } n \leftarrow n + 1$</p> <p style="text-align: center;">ELSE : next iteration $i \leftarrow i + 1$</p>	(5.35)
--	--------

At this global level, the computation is performed with the Newton-Raphson iterative method, the linearization form of the equilibrium equations is given as

$$\begin{aligned}
 0 &= Lin \left[\sum_{e=1}^{Nelem} (\mathbf{f}_{n+1}^{e,int}(\mathbf{u}_{n+1}) - \mathbf{f}_{n+1}^{e,ext}) \right] \\
 &= \sum_{e=1}^{Nelem} (\mathbf{f}_{n+1}^{e,int}(\mathbf{u}_{n+1}) - \mathbf{f}_{n+1}^{e,ext}) + \sum_{e=1}^{Nelem} \frac{\partial \mathbf{f}_{n+1}^{e,int}}{\partial \mathbf{u}}(\mathbf{u}_{n+1}) \Delta \mathbf{u}_{n+1}^{(i)} \\
 &= \sum_{e=1}^{Nelem} \mathbf{r}_{n+1}^{e,(i)} + \sum_{e=1}^{Nelem} \mathbf{K}_{n+1}^{e,(i)} \Delta \mathbf{u}_{n+1}^{(i)}
 \end{aligned} \tag{5.36}$$

where $\mathbf{K}_{n+1}^{e,(i)}$ is the tangent stiffness matrix of element e at iteration i and time step $n + 1$. $\Delta \mathbf{u}_{n+1}^{(i)}$ computed by Eq. (5.36) is the incremental displacement of the iteration i . The displacement and strain field are then updated to the iteration $i + 1$ as:

$$\mathbf{u}_{n+1}^{(i+1)} = \mathbf{u}_{n+1}^{(i)} + \Delta \mathbf{u}_{n+1}^{(i)}, \tag{5.37}$$

$$\epsilon_{n+1}^{(i+1)} = \mathbf{B} \mathbf{u}_{n+1}^{e,(i+1)}. \tag{5.38}$$

In Eq. (5.36), the expression of $\mathbf{K}_{n+1}^{e,(i)}$, $\mathbf{f}_{n+1}^{e,int}$ are given by

$$\mathbf{K}_{n+1}^{e,(i)} = \int_{\Omega_e} \mathbf{B}^T \mathbf{C}_{n+1}^{ep,(i)} \mathbf{B} d\Omega, \quad (5.39a)$$

$$\mathbf{f}_{n+1}^{e,int} = \int_{\Omega_e} \mathbf{B}^T \boldsymbol{\sigma}_{n+1}(\boldsymbol{\epsilon}_{n+1}^{(i)}, \boldsymbol{\epsilon}_{n+1}^{p,(i)}, \gamma_{n+1}^{(i)}) d\Omega \quad (5.39b)$$

Note that all the expressions presented in this section are only for the bulk in which the nonlinear behavior is applied. The contribution of the linear elastic interface to the global system depends on the numerical approach and will be discussed in the next section.

5.3 Finite element implementation

5.3.1 Interface element approach

Since we consider plane strain hypothesis, the strain–displacement matrix \mathbf{B} and the elastic tensor \mathbf{C} for the bulk element are given as

$$\mathbf{B} = [\mathbf{B}_I, \mathbf{B}_{II}, \dots, \mathbf{B}_n] \quad \text{with} \quad \mathbf{B}_I = \begin{bmatrix} \frac{\partial N_I}{\partial x_1} & 0 \\ 0 & \frac{\partial N_I}{\partial x_2} \\ 0 & 0 \\ \frac{\partial N_I}{\partial x_2} & \frac{\partial N_I}{\partial x_1} \end{bmatrix}, \quad (5.40)$$

$$\mathbf{C} = \begin{bmatrix} \lambda + 2\mu & \lambda & \lambda & 0 \\ \lambda & \lambda + 2\mu & \lambda & 0 \\ \lambda & \lambda & \lambda + 2\mu & 0 \\ 0 & 0 & 0 & \mu \end{bmatrix}. \quad (5.41)$$

The strain–displacement matrix $\bar{\mathbf{B}}$ and the surface elastic tensor \mathbf{C}^s for the interface element are the same as in the case of linear behavior of nanocomposites Eq. (3.21) already discussed in subsection 3.3.1. Therefore, the problem to be solved with interface terms can be written in an incremental form as:

$$\sum_{e=1}^{N_{\text{elem}}} \left(\mathbf{f}_{n+1}^{int, \Omega_e, (i)} + \mathbf{f}_{n+1}^{int, \Gamma_e, (i)} - \mathbf{f}_{n+1}^{ext} \right) + \sum_{e=1}^{N_{\text{elem}}} \left(\mathbf{K}_{n+1}^{\Omega_e, (i)} + \mathbf{K}_{n+1}^{\Gamma_e, (i)} \right) \Delta \mathbf{u}_{n+1}^{(i)} = \mathbf{0} \quad (5.42)$$

where, for a discretization with interface elements, we have:

$$\mathbf{f}_{n+1}^{int, \Gamma_e, (i)} = \int_{\Gamma_e} \mathbf{T}^T \bar{\mathbf{B}}^T \boldsymbol{\sigma}_{s, n+1}^{(i)} d\Gamma, \quad (5.43a)$$

$$\boldsymbol{\sigma}_{s, n+1}^{(i)} = \mathbf{C}^s : \boldsymbol{\epsilon}_{s, n+1}^{(i)} \quad \text{and} \quad \boldsymbol{\epsilon}_{s, n+1}^{(i)} = \bar{\mathbf{B}} \mathbf{T} \mathbf{u}_{n+1}^{(i)}, \quad (5.43b)$$

$$\mathbf{K}_{n+1}^{\Gamma_e, (i)} = \int_{\Gamma_e} \mathbf{T}^T \bar{\mathbf{B}}^T \mathbf{C}^s \bar{\mathbf{B}} \mathbf{T} d\Gamma. \quad (5.43c)$$

For each iteration of the iterative procedure, we need, at each integration point, to update all the internal variables (for the considered model, we count 5 internal variables: the plastic strain tensor components and the cumulated plastic strain ξ).

5.3.2 XFEM approach

With the global enrichment strategy of XFEM, the displacement vector (\mathbf{d}) contains both standard d.o.f (\mathbf{u}) and additional d.o.f (\mathbf{a}) (see Eq. (3.29)). After linearization, the set of equations to be solved becomes:

$$\sum_{e=1}^{N_{\text{elem}}} \mathbf{r}_{n+1}^{e,(i)} + \sum_{e=1}^{N_{\text{elem}}} \mathbf{K}_{n+1}^{e,(i)} \Delta \mathbf{d}_{n+1}^{(i)} = \mathbf{0} . \quad (5.44)$$

The displacement and strain field are then updated to the iteration $i + 1$ as:

$$\mathbf{u}_{n+1}^{(i+1)} = \mathbf{d}_{n+1}^{(i)} + \Delta \mathbf{d}_{n+1}^{(i)} , \quad (5.45)$$

$$\boldsymbol{\epsilon}_{n+1}^{(i+1)} = \mathbf{B} \mathbf{d}_{n+1}^{e,(i+1)} , \quad (5.46)$$

where matrix \mathbf{B} is defined as $\mathbf{B} = [\mathbf{B}_I \dots \mathbf{B}_n \hat{\mathbf{B}}_I \dots \hat{\mathbf{B}}_m]$ with \mathbf{B}_I as defined in Eq. (5.40) and with $\hat{\mathbf{B}}_I$ defined as follow:

$$\hat{\mathbf{B}}_I = \begin{bmatrix} \frac{\partial(N_I \psi)}{\partial x_1} & 0 \\ 0 & \frac{\partial(N_I \psi)}{\partial x_2} \\ 0 & 0 \\ \frac{\partial(N_I \psi)}{\partial x_2} & \frac{\partial(N_I \psi)}{\partial x_1} \end{bmatrix} , \quad (5.47)$$

where ψ is the enrichment function defined by Eq. (3.26).

For the XFEM approach, the interface is implicitly modeled via the level-set function and the interface integration is performed through the approximated interface of the enriched element. The contribution of the interface into the tangent stiffness matrix and internal force vector of the enriched elements being now considered, the expressions (5.39) become (for enriched elements):

$$\mathbf{K}_{n+1}^{e,(i)} = \int_{\Omega_e \setminus \Gamma_e} \mathbf{B}^T \mathbf{C}_{n+1}^{ep,(i)} \mathbf{B} d\Omega + \int_{\Gamma_e} \mathbf{B}^T \mathcal{M}^T \mathbf{C}^{(s)} \mathcal{M} \mathbf{B} d\Gamma , \quad (5.48a)$$

$$\mathbf{f}_{n+1}^{e,int} = \int_{\Omega_e \setminus \Gamma_e} \mathbf{B}^T \boldsymbol{\sigma}_{n+1}(\boldsymbol{\epsilon}_{n+1}^{(i)}, \boldsymbol{\epsilon}_{n+1}^p, \gamma_{n+1}) d\Omega + \int_{\Gamma_e} \mathbf{B}^T \mathcal{M}^T \boldsymbol{\sigma}_{s,n+1}(\boldsymbol{\epsilon}_{s,n+1}^{(i)}) d\Gamma \quad (5.48b)$$

$$\text{with } \boldsymbol{\epsilon}_{s,n+1}^{(i)} = \mathcal{M} \mathbf{B} \mathbf{d}_{n+1}^{e,(i)} \quad (5.48c)$$

Since we used a total of 9 Gauss points on an enriched element (see Figure 3.5), the iterative procedure for enriched elements requires to compute and update 45 variables per enriched element. In that sense, for complex nonlinear irreversible behaviors, XFEM requires a huge amount of local updatings, each of them resulting

from the resolution of local nonlinear equations.

5.3.3 E-FEM approach

For the E-FEM approach, on the enhanced elements, besides the internal variables computed at the Gauss point level, we need to determine the additional d.o.f (\mathbf{a}) at the element level. The equilibrium equation at the element level (Eq. (4.44)) needs to be verified on the enhanced element before updating the information to the global level. In addition, as in the case of linear elasticity, the interface terms appear at both the elemental level and global level. The problem to be solved after computing the plastic flow, on these elements, is modified into

$$\begin{aligned}
 &\textbf{Given} : \boldsymbol{\epsilon}_{n+1}^p, \xi_{n+1}, \quad \text{with} \\
 &\quad \boldsymbol{\sigma}_{n+1} = \mathbf{C} : (\boldsymbol{\epsilon}_{n+1}^{(i)} - \boldsymbol{\epsilon}_{n+1}^p) \quad \text{and} \quad q_{n+1} = -K\xi_{n+1} \\
 &\quad \text{plastically admissible} \\
 &\textbf{Test} : \underset{\text{element level}}{\mathbf{h}_{e,n+1}^{(i),(k)}} = \int_{\Omega_e \setminus \Gamma_e} \mathbf{G}_v \boldsymbol{\sigma}_{n+1}^{(i),(k)} d\Omega + \int_{\Gamma_e} \mathbf{G}_s \boldsymbol{\sigma}_{s,n+1}^{(i),(k)} d\Gamma \stackrel{?}{=} \mathbf{0} \\
 &\quad \textbf{IF} : \|\mathbf{h}_{e,n+1}^{(i),(k)}\| \leq \text{tol} \Rightarrow \text{break to global level} \\
 &\quad \textbf{ELSE} : \text{next iteration } k \leftarrow k + 1 \\
 &\textbf{Test} : \underset{\text{global level}}{\mathbf{r}(\boldsymbol{\epsilon}_{n+1}^{(i)}, \boldsymbol{\epsilon}_{n+1}^p, \xi_{n+1})} = \sum_{e=1}^{N_{\text{elem}}} [\mathbf{f}_{n+1}^{e,int} - \mathbf{f}_{n+1}^{e,ext}] \stackrel{?}{=} \mathbf{0} \\
 &\quad \textbf{IF} : \|\mathbf{r}_{n+1}^{(i)}\| \leq \text{tol} \Rightarrow \text{next time step } n \leftarrow n + 1 \\
 &\quad \textbf{ELSE} : \text{next iteration } i \leftarrow i + 1
 \end{aligned} \tag{5.49}$$

The linearization form of the local equilibrium equation is given as:

$$\begin{aligned}
 0 &= \text{Lin} \left[\mathbf{h}_e \left(\mathbf{u}_{n+1}^{(i)}, \mathbf{a}_{n+1}^{(i),(k)} \right) \right] \\
 &= -\mathbf{h}_e \left(\mathbf{u}_{n+1}^{(i)}, \mathbf{a}_{n+1}^{(i),(k)} \right) + \frac{\partial \mathbf{h}_e \left(\mathbf{u}_{n+1}^{(i)}, \mathbf{a}_{n+1}^{(i),(k)} \right)}{\partial \mathbf{a}} \Delta \mathbf{a}_{n+1}^{(i),(k)} \\
 &= -\mathbf{h}_e \left(\mathbf{u}_{n+1}^{(i)}, \mathbf{a}_{n+1}^{(i),(k)} \right) + \left([\mathbf{K}_{aa}^e]_{n+1}^{(i),(k)} \right) \Delta \mathbf{a}_{n+1}^{(i),(k)}
 \end{aligned} \tag{5.50}$$

where \mathbf{K}_{aa}^e is now computed by changing \mathbf{C} to \mathbf{C}^{ep} in Eq. (4.54).

The displacement and strain field are then updated to the local iteration $k + 1$ as

$$\mathbf{a}_{n+1}^{(i),(k+1)} = \mathbf{a}_{n+1}^{(i),(k)} + \Delta \mathbf{a}_{n+1}^{(i),(k)} \tag{5.51}$$

$$\boldsymbol{\epsilon}_{n+1}^{(i),(k+1)} = \mathbf{B} \mathbf{u}_{n+1}^{(i)} + \mathbf{G}_r \mathbf{a}_{n+1}^{(i),(k+1)} \tag{5.52}$$

After we found the value of \mathbf{a} that verifies the local equilibrium, the static condensation given in Eq. (4.57) is executed and the classical form of FEM is retrieved. Note that all stiffness matrices $\mathbf{K}_{uu}^e, \mathbf{K}_{ua}^e, \mathbf{K}_{au}^e$ in Eq. (4.54) are now also computed

with the coherent tangent stiffness \mathbf{C}^{ep} . After performing the linearization for the global equilibrium equation, we end up with the form

$$\sum_{e=1}^{Nelem} (\mathbf{f}_{n+1}^{e,int} - \mathbf{f}_{n+1}^{e,ext}) + \sum_{e=1}^{Nelem} \widetilde{\mathbf{K}}_{n+1}^{e,(i)} \Delta \mathbf{u}_{n+1}^{(i)} = \mathbf{0} \quad (5.53)$$

where $\widetilde{\mathbf{K}}_{n+1}^{e,(i)}$ is computed by Eq. (4.57) and

$$\mathbf{f}_{n+1}^{e,int} = \int_{\Omega_e \setminus \Gamma_e} \mathbf{B}^T \boldsymbol{\sigma}_{n+1}(\boldsymbol{\epsilon}_{n+1}^{(i)}, \boldsymbol{\epsilon}_{n+1}^p, \gamma_{n+1}) d\Omega + \int_{\Gamma_e} \mathbf{B}^T \mathcal{M}^T \boldsymbol{\sigma}_{s,n+1}(\boldsymbol{\epsilon}_{s,n+1}^{(i)}) d\Gamma \quad (5.54)$$

$$\text{with } \boldsymbol{\epsilon}_{s,n+1}^{(i)} = \mathcal{M} \mathbf{B} \mathbf{u}_{n+1}^{e,(i)} + \mathbf{G}_s \mathbf{a}_{n+1}^{e,(i)}. \quad (5.55)$$

The resolution algorithm for the case of E-FEM approach is summed up in Figure 5.3.

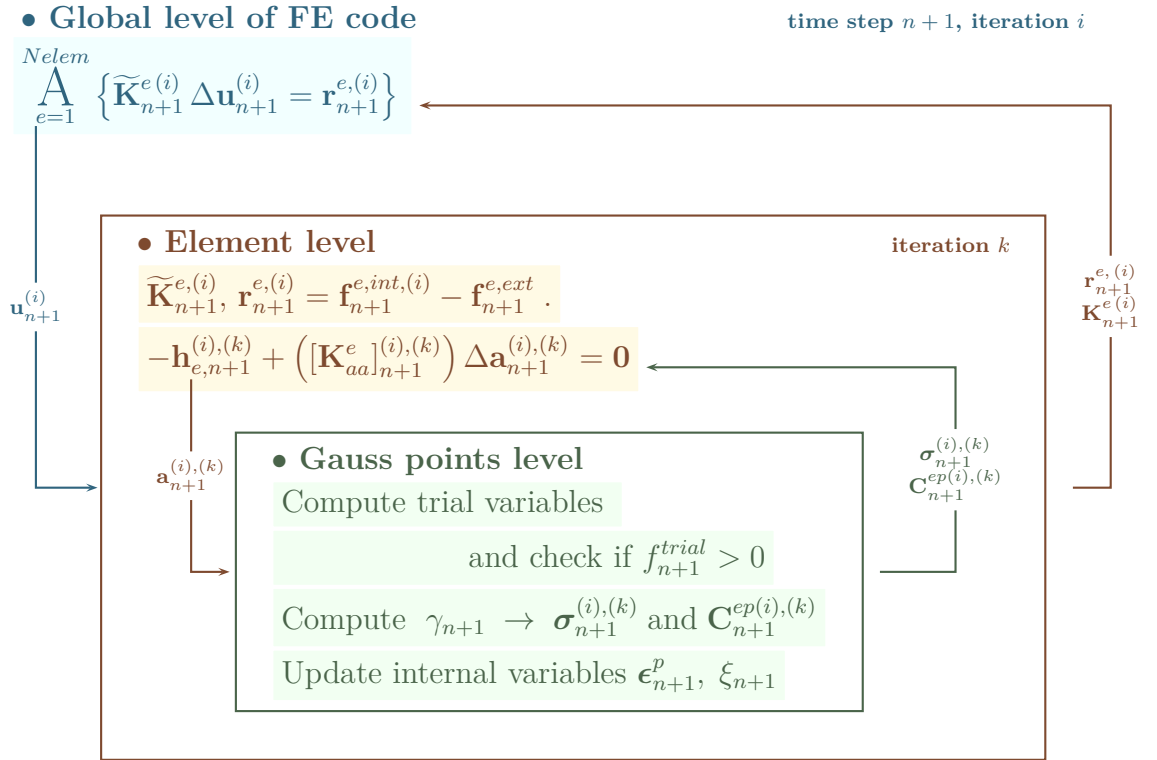


Figure 5.3: Resolution algorithm with E-FEM approach

The number of internal variables to be updated on each enhanced element totally depends on the number of Gauss points we use on these elements. In our work, we used 2 integration points per enhanced element (see Figure 4.17) resulting in 10 internal variables in addition to the 2 additional parameters \mathbf{a} related to the strain jump.

In the next section, the numerical results obtained from the three considered approaches for nonlinear behavior are presented and compared.

5.4 Nonlinear results

In chapter 3 and chapter 4, by using the considered numerical approaches, we performed a homogenization process to determine the macroscopic mechanical behavior of several materials made of nanoinclusions with an elastic behavior for the bulk and the interface. In this section, the von Mises type elastoplastic law with linear isotropic hardening presented above is considered for the bulk. The interface remains linear elastic. We study the homogeneous behavior of a nanocomposite material in terms of the evolution of the mean deviatoric stress with respect to the mean deviatoric strain. Such analysis aims at obtaining the nonlinear homogenized behavior of the composite including interface effect. A simple traction test (prescribed macroscopic strain $\epsilon_{11}^M = 0.3, \epsilon_{22}^M = \epsilon_{33}^M = \epsilon_{12}^M = 0$) is performed on the RVE presented in Figure 3.6b. The radius of inclusion and the volume fraction are set to $R = 1nm$ and $f = 0.2$. The material parameters are chosen as:

- Bulk material : Young modulus $E_m = 70$ GPa, $E_i = 0.1E_m$, Poisson ratio $\nu_m = \nu_i = 0.32$, elastic limit stress $\sigma_y = 7$ GPa, hardening modulus $K = 20$ GPa.
- Elastic coherent interface: (given in Miller and Shenoy [Miller and Shenoy, 2000])
 - set A: $\lambda_s = 6.842$ N/m, $\mu_s = -0.375$ N/m $\Rightarrow k_s = 6.092$ N/m.
 - set B: $\lambda_s = 3.48912$ N/m, $\mu_s = -6.2178$ N/m $\Rightarrow k_s = -8.9465$ N/m.
 - set C: $\lambda_s = 0$ N/m, $\mu_s = 0$ N/m $\Rightarrow k_s = 0$ N/m (no interface elasticity).

5.4.1 Interface element approach

We first present the results obtained from the Interface element approach. We plot in Figure 5.4 the component xx of the deviatoric stress on the deformed mesh for different set of parameters for the interface. We notice that the deformation of the inclusion is the biggest for the case of set B and the smallest for the case of set A. This is a reasonable result since set A with $k_s > 0$ increases the global stiffness of the resulting composite and vice versa in the case of interface set B when $k_s < 0$.

In the same manner, the value of hardening variable (accumulated plastic strain) is presented in Figure 5.5. Due to the stress concentration, the bulk elements in the matrix that are near the interface turn soon into the plastic phase resulting in higher accumulated plastic strain ξ on these elements. It clearly shows that the interface influences the value of ξ of these elements. As the stress concentration is stronger with interface set B, the values of ξ are higher and vice versa in the case with the interface set A.

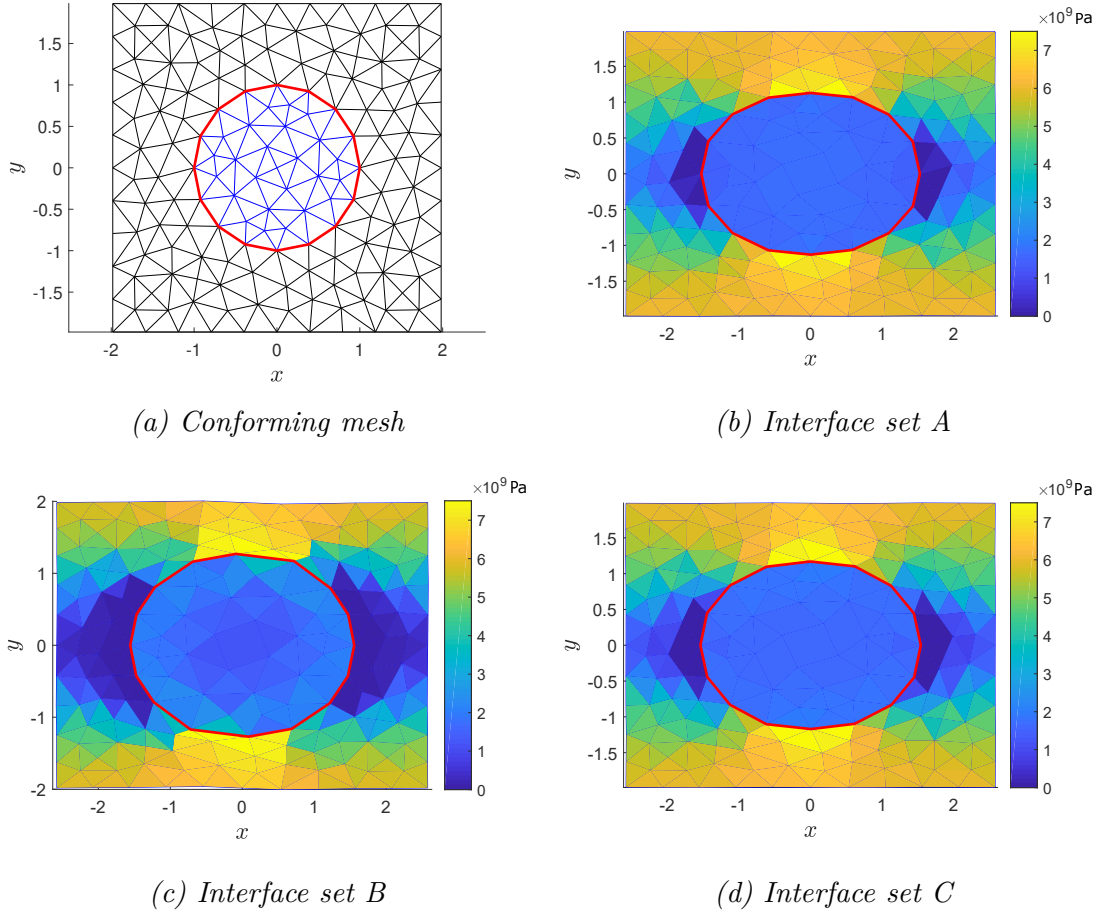
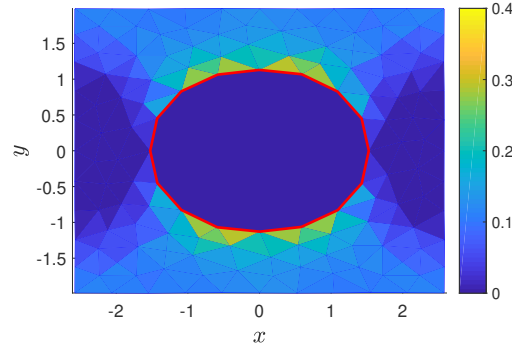


Figure 5.4: Deviatoric stress $(\mathbf{dev} \boldsymbol{\sigma})_{11}$ on deformed mesh for different interface parameters under a simple traction test.

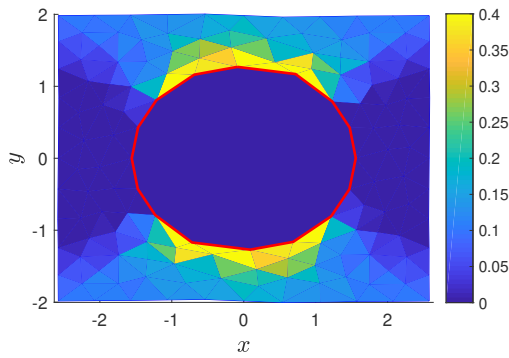
The difference caused by the interface on the local stress and strain fields results in different overall elastoplastic behavior. To evaluate the influence of the interface on the homogenized behavior, the mean value of stress and strain are considered.

The homogenized behaviors in terms of the deviatoric part of the stress with respect to the deviatoric part of the strain for different interface sets are presented in Figure 5.6a. We can notice the influence of the interface on the homogenized behavior of the composite material. While the interface set A increases the global rigidity of the composite, the interface set B decreases the rigidity.

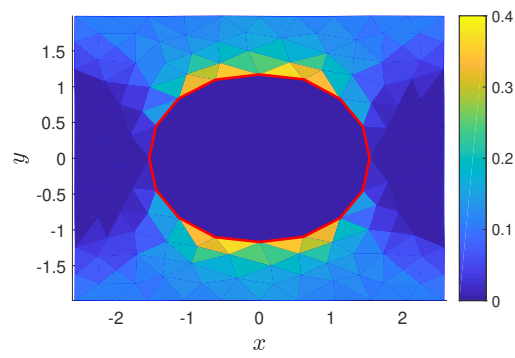
To highlight the size effect, we vary the radius of inclusion while keeping the volume fraction unchanged $f = 0.2$. The size dependence of the homogenized behavior is reported in Figure 5.6b. We can observe that the homogenized behavior of the composite is influenced by the size of the inclusion both in the elastic part (as already shown previously in chapter 3 and chapter 4) and in the plastic part of the behavior leading to different apparent elastic limit of the composite.



(a) with Interface set A

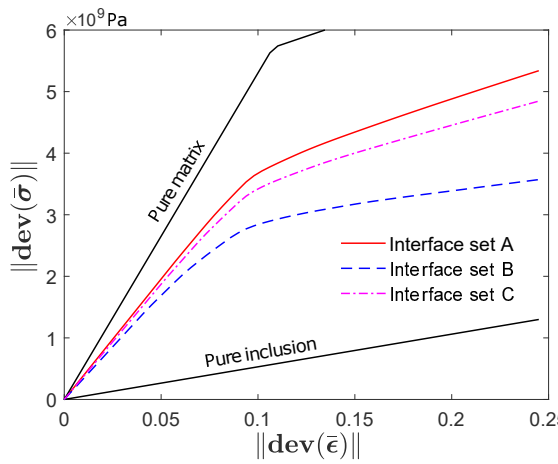


(b) Interface set B

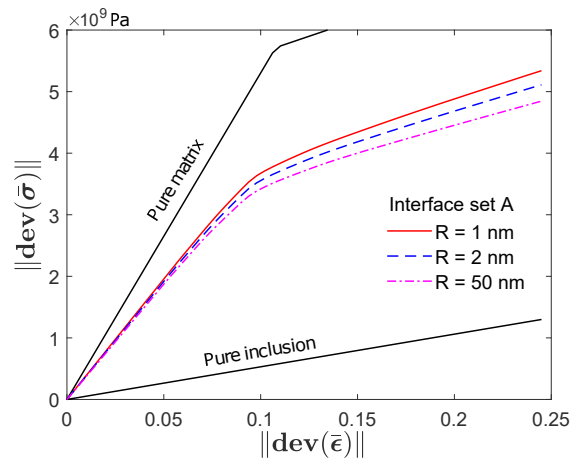


(c) Interface set C

Figure 5.5: Hardening variable ξ for different interface parameters under a simple traction test.



(a) Different interface parameters



(b) Different radius of inclusion

Figure 5.6: Homogenized elastoplastic effective behavior under a simple traction test.

5.4.2 XFEM and E-FEM

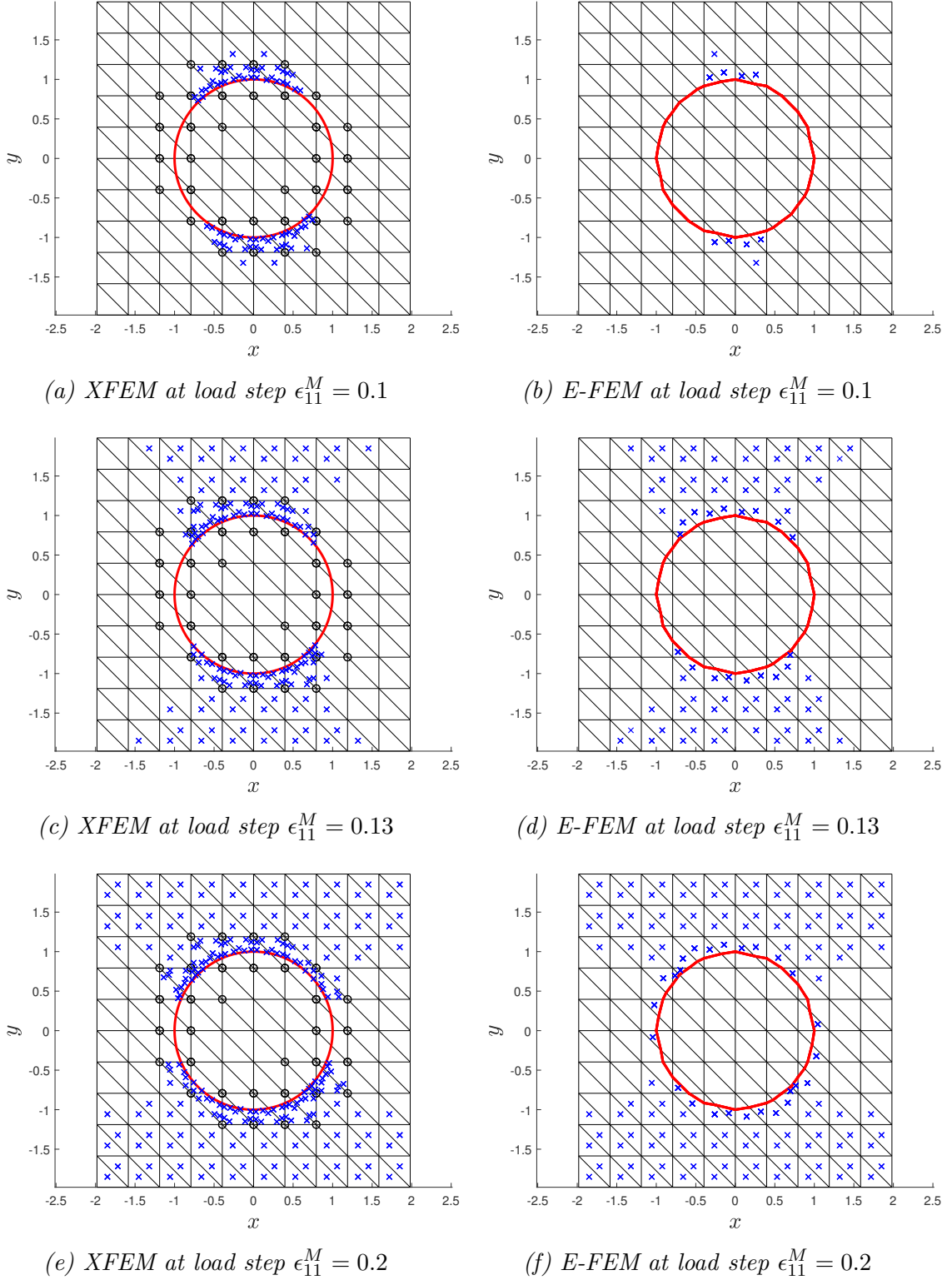


Figure 5.7: Integration points turned into plastic phase for different time steps with XFEM and E-FEM for interface set A.

The same simple tensile test has been also carried out with the XFEM and E-FEM approaches. On the enriched elements, due to the different stiffness and the stress concentration, the integration points that lie in the matrix have much higher stress than those in the inclusion. The Gauss points in the matrix, therefore, turn into the plastic phase while those in the inclusion remain elastic. For the E-FEM approach, we have only one integration point in the matrix part of the enriched element (see Figure 4.17). Meanwhile, for the XFEM approach, the number of integration points in the matrix on the enriched element is 3 or 6 points (see Figure 3.5). In Figure 5.7, the integration points that have already been in the plastic phase are marked on the mesh at load (time) steps of $\epsilon_{11}^M = 0.1$, $\epsilon_{11}^M = 0.13$ and $\epsilon_{11}^M = 0.15$. It can be seen that the plastic behavior spreads from Gauss points near the interface to points on the standard elements of the bulk.

It is worth pointing out that due to the ill-conditioned problem causing by the negative-definite interface stiffness matrix, the resolutions of XFEM and E-FEM are no convergence for the case of interface set B (negative value of k_s).

The homogenized behavior obtained from XFEM and E-FEM for the interface set A is then compared to those obtained from the Interface element approach. Figure 5.8 shows the homogeneous behavior of the mean deviatoric stress with respect to the mean deviatoric strain. The notable size dependence is shown not only for the elastic limit but also in terms of stiffness both in the elastic and plastic behavior phases of the behavior of the material. In addition, an excellent agreement between the three numerical approaches is obtained whereas the amount of local nonlinear updating is not the same order for each method.

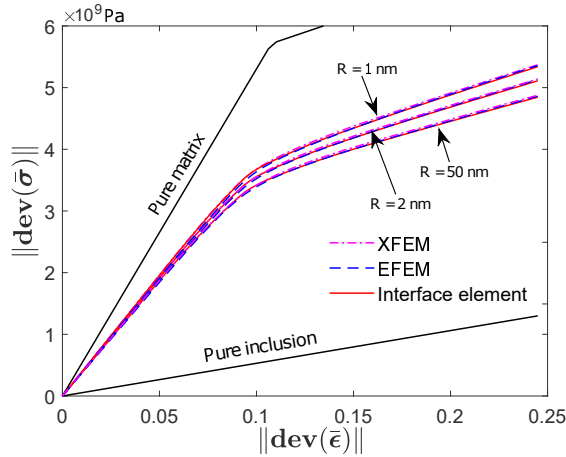


Figure 5.8: Homogenized elastoplastic behavior for three different radius of nano-inclusion using XFEM, E-FEM or Interface element approach.

At this stage, we can proceed with a comparison in terms of computational cost in handling the nonlinear behavior of the three considered approaches. For the case of circular nano-inclusion presented above, we compare the three considered approaches in Table 5.2. It can be seen that XFEM is the most expensive approach

among the three ones and the Interface element approach is the cheapest one. The reason lies in the number of the integration points in which the internal variables need to be updated at each iteration. The enriched FEM approaches require more than one integration point on the enriched elements resulting in larger computational cost. Compared to XFEM, E-FEM requires less integration points on each enriched elements (see Figures 3.5 and 4.17). Moreover, the additional d.o.f of E-FEM can be also technically considered as internal variables of the enriched element since they are determined and condensed at the local level by the use of the operator split technique. Therefore, among the two enriched FEM approaches, E-FEM is cheaper than XFEM in terms of computational cost.

	X-FEM	E-FEM	Interface element
Number of standard d.o.f	242	242	338
Number of enriched elements	34	34	0
Number of additional d.o.f	68	68	0
Total unknowns at the global level	310	242	338
Number of integration points for each standard element	1	1	1
Number of internal variables for each standard element	5	5	5
Number of integration points for each enriched element	9	2	\emptyset
Number of internal variables for each enriched element	45	10	\emptyset
Final size of global stiffness matrix	484×484	242×242	338×338
Computing time (sec)	27.679	15.292	5.767

Table 5.2: Comparison of computational cost in the case of elastoplastic behavior (XFEM vs E-FEM vs IE).

With the enriched E-FEM approaches, the test can be performed on more complex geometries of the RVE such as inclusions with non-convex shapes as presented in Figure 4.24. For a fixed volume fraction $f = 0.2$, the shape dependence on nonlinear behavior is presented in Figure 5.9. The same conclusion as reported in subsection 4.6.2 is observed. For a fixed volume fraction, we notice a descending tendency of the rigidity according to the increasing number of oscillations in both elastic and plastic phases.

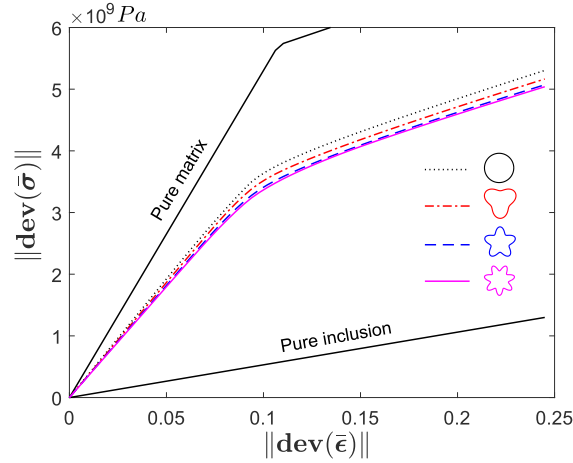


Figure 5.9: Homogenized elastoplastic behavior for different shapes of inclusion.

Note that the studies presented above are only the first step, for future works, more complex behaviors could be taken into account and sensitivity analysis of the model parameters could be carried out.

5.5 Conclusion

In order to assess the influence of the nonlinear behavior of the bulk, a nanocomposite unit cell composed of an elastoplastic bulk with linear isotropic hardening and coherent interface has been studied. The von Mises plasticity criterion and the implicit backward Euler integration scheme with the return mapping algorithm have been used.

Because of the nonlinearity of the problem, the linearization process of Newton-Raphson was employed and adapted to the finite element implementation form of the three studied approaches. For XFEM and the Interface element approach, the linearization and interface terms only need to be handled at the global level with the global equilibrium equation. For the E-FEM approach, both global and local equilibrium equations are nonlinear, the linearization was then performed at both levels.

We illustrated the homogenized nonlinear behavior on the deviatoric part of stresses and strains in the case of a simple traction test with the three numerical approaches. The results obtained showed a very good agreement between them. Moreover, the notable influence of the interface is clearly shown. The size effect is observed both in the elastic part and in the plastic part as well as on the apparent elastic limit of the nanocomposite.

A comparison in terms of computational cost showed that the Interface element approach is the cheapest among the three numerical strategies. Due to the use of fewer internal variables in the enriched elements plus the condensation of additional d.o.f, E-FEM is less expensive than XFEM.

Those first results allow envisaging to consider more complex nonlinear behaviors by numerical homogenization strategy in order to determine the behavior of more realistic materials than nanocomposites made of linear elastic components. The nonlinearities being here limited to the behavior of the bulk. For future works, we could also consider the nonlinear behavior of the interface.

Chapter 6

General conclusion and perspectives

Contents

6.1	General conclusion	125
6.2	Perspectives	128

6.1 General conclusion

In the present thesis work, by using the coherent interface model, we have proposed several contributions to the numerical modeling of the mechanical behavior of nano-reinforced material, summarized as follows (see Figure 6.1).

Firstly, a comparative study that provides the evaluation of the two numerical approaches namely XFEM/ level set and interface elements based strategy has been performed. These two approaches have been tested for many cases in which we have varied the different parameters influencing the effective behavior, namely the stiffness of the different phases, the parameters of the interface, the radius of inclusion, the volume fraction of the inclusions, the boundary conditions. The results showed that the convergence and the prediction of the strain field of XFEM are affected by the introduction of the surface elasticity whereas those of the interface element approach is not. Even so, both of the considered approaches were able to reproduce the size dependence of the effective behavior of nanocomposites in the case of plane strain hypothesis as well as axisymmetric model. The numerical estimations have a very good agreement with the analytical solutions when considering periodic boundary conditions on the unit cell. To test more realistic configurations, the random microstructure with the coherent interface has also been considered. Both approaches have shown their ability to reproduce the size effect in this configuration but XFEM is more expensive than the Interface element. The use of surface/interface elements

in standard FEM depends massively on conforming meshes, which are costly for the cases with complex geometries. Meanwhile, the XFEM/level set approach, although does not requires any discretization effort but the number of degrees of freedom and integration points are raised compared to standard FEM.

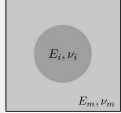
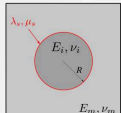
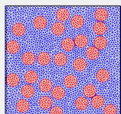
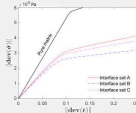
	XFEM	Interface element	EFEM
 Homogenization	<i>[Sukumar et al., 2001]</i> ...	<i>Classical FEM (conforming mesh)</i>	<i>[Roubin et al., 2015]</i> ... Chapter 4
 Homogenization + Surface elasticity	<i>[Yvonnet et al., 2008]</i> <i>[Farsad et al., 2010]</i> ...	<i>[Wei et al., 2006]</i> <i>[Javili et al., 2017]</i> ...	Chapter 4
 Homogenization + Surface elasticity + Random microstructure	<i>[Yvonnet et al., 2008]</i> ...	Chapter 3	Chapter 4
 Homogenization + Surface elasticity + Nonlinear behavior	Chapter 5	Chapter 5	Chapter 5

Figure 6.1: Contributions of this PhD work

In chapter 4, we provide the second and main contribution of this PhD work is the proposition of an E-FEM type formulation to take into account the surface elasticity. To this purpose, an evaluation of the three standard formulations of the E-FEM approach for numerical homogenization without surface elasticity has been carried out. A limitation of this approach for the high contrast of rigidity of phases has been reported. For low contrast of rigidity, the SKON formulation has given the best results in terms of convergence among the 3 available formulations. Based on this result, we have proposed an enhanced SKON formulation allowing us to incorporate the effect of the coherent interface model. The proposed approach is original as it is the first time to our best knowledge that the size effect is modeled in the

framework of embedded finite elements method. The results related to convergence analysis, linear homogenization with periodic microstructure have been provided and validated to the analytical approaches. In addition, the ability to handle random microstructure of the proposed approach has been shown up.

At this point, after studying the three numerical approaches namely Interface Element, XFEM and E-FEM in the homogenization context with or without the imperfect interface, we can indicate their effective domain of application in handling the different characteristics of the material. If the geometry of RVE is simple enough to create easily a conforming mesh, the Interface element is the best choice due to its accuracy. On the contrary, if the shape of the inhomogeneity is complex, the enriched methods (XFEM, E-FEM) can be employed. In these two approaches, E-FEM has some advantages relate to computational cost but the improvements are necessary to handle the high contrast of rigidity of phases. Our efforts to improve the approach for such cases have been carried out and will be reported in the near future. Before that, E-FEM can be used for low contrast of rigidity of components while XFEM for high contrast.

In chapter 5, the extension of the numerical approaches to assess the nonlinear behavior of nanocomposite has been performed. A nanocomposite unit cell composed of an elastoplastic matrix with linear isotropic hardening and a linear coherent interface has been studied. The von Mises plasticity criterion and the implicit backward Euler integration scheme for the nonlinear model were used. The differences in terms of linearization and updating of the internal variables for the considered approaches have been reported. We then illustrated the homogenized nonlinear behavior on the deviatoric part of stress and strain by performing a simple traction test. The results obtained from the three numerical approaches show a very good agreement between them. Moreover, the notable influence of the interface is clearly shown. The size effect is observed both on the elastic part and on the plastic part as well as the elastic limit of the nanocomposites. This is the first step into the nonlinear behavior modeling of this kind of material within the numerical homogenization strategy. Some prospects on this point are proposed here after.

Note that the numerical developments presented in this Ph.D. works are essentially used to deal with the interface between two solid materials, whereas it can be applied for many other cases such as a solid-fluid interface or fluid-fluid interface... The applications can be related to thermal problems or other multiphysics problems where the interface between two domains causing a discontinuity of the interest fields. In some problems, the movement of the interface needs to be envisaged and the numerical strategies based on the fixed mesh as XFEM and E-FEM bring a big advantage.

6.2 Perspectives

There are many potential extensions and perspectives to this work, and necessary studies should be realized to improve these numerical approaches, and answer the remaining questions (raised in this work).

• Short-term prospects

First of all, as reported in chapter 4, we encountered a problem related to the evaluation of the local equilibrium at the elementary level. This problem restricts E-FEM to the low contrast of rigidity of phases in performing numerical homogenization. Since the cause of the problem has been determined and some promising routes have been pointed out, we can immediately start on the improvement of the method.

For the XFEM approach, although the actual convergence is adequate for most purposes, the degradation of the convergence in the presence of surface elasticity (reported in chapter 3) still need to be overcome. With its global enrichment strategy, a good convergence will help to avoid using very fine mesh and therefore, reduce the high computational cost of XFEM, especially in treating the complex nonlinear behavior. From the good convergences of the E-FEM method including coherent interface, we can propose a similar surface strain field tensor in the framework of XFEM as:

$$\epsilon^h = \mathcal{M}\mathbf{B}\mathbf{u} + \frac{1}{R}\mathcal{P}\mathbf{n}^T(\mathbf{N}\psi)\mathbf{a}, \quad (6.1)$$

The convergence obtained by using Eq. (6.1) in the Eshelby problem with coherent interface (see subsections 3.4.1 and 4.6.1) for different values of the contrast coefficient α are presented in Figure 6.2a. Compared to the those with standard XFEM

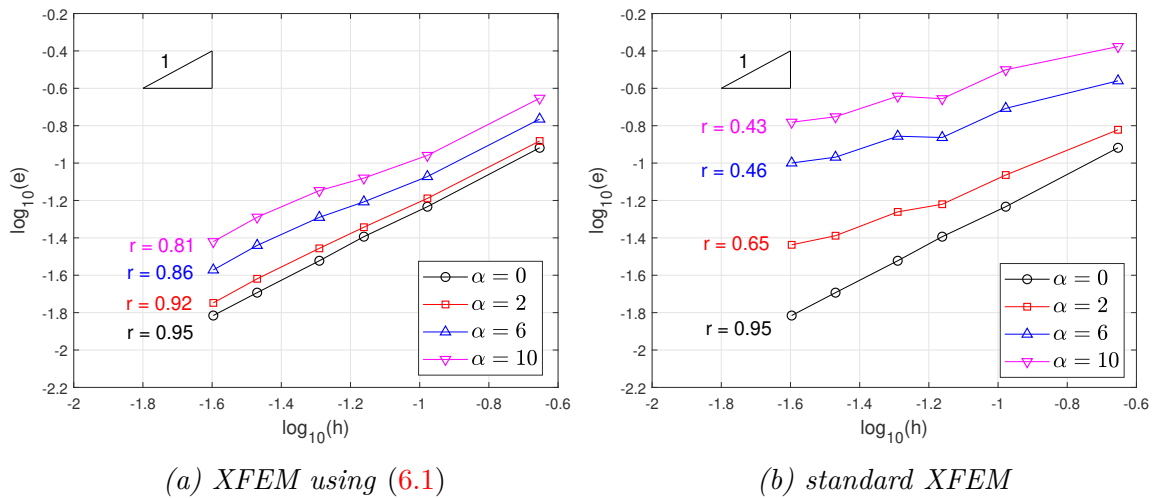


Figure 6.2: Convergence analysis for the Eshelby problem with a coherent interface and different values of α (XFEM using Eq. (6.1) vs standard XFEM).

presented in Figure 6.2b, the convergence of XFEM using Eq. (6.1) are clearly improved. These are only the preliminary results, we still need to develop the theoretical framework of the enriched surface strain field tensor given in Eq. (6.1) in order to build an extension of the XFEM in the context of the coherent interface.

In the present work, the von Mises plasticity has been used whereas many other nonlinear behaviors can be applied to the bulk in the framework of these numerical approaches. The von Mises plasticity is a simple model that is certainly not suitable for the targeted materials. With the presented procedure in this Ph.D. work, it is easy to introduce other more complex nonlinear behaviors including more complex phenomena (damage, hardening, ...). The validation of numerical models accounting for these plasticity criteria and the imperfect interface could then be performed by comparing to the results obtained with the analytical works of Brach et al [Brach et al., 2017a] and [Brach et al., 2017b] in which a nanoporous material with a spherical inclusion has been used. In this case, the Interface element approach is therefore convenient to be extended firstly.

Besides the nonlinear law for the bulk, we can also consider the nonlinear behavior for the interface, even if it will require many other parameters of the interfaces that have never been measured or estimated by MD simulation. However, a fictive interface material can be used for the numerical work before these parameters are really determined in the future. The bases for taking into account a nonlinear behavior of the interface could be proposed. This will make it possible later to enrich the models used and could, moreover, make it possible to see the influence of the assumptions concerning the behavior of the interface on the homogenized properties. In addition to the nonlinear mechanical laws on the tangential direction of the interface, the question of partial or total decohesion at the matrix/inclusion interface may arise. In this case, non-linear interface models are also to be considered. E-FEM, used essentially, to represent strong discontinuities, offers a privileged framework for this. In the short-term, the elasto-plastic or viscoelastic behavior can be considered for the interface.

• Long-term prospects

The 3D model is still a necessary prospect. In the 3D context, the interface element becomes a membrane-type element and the approximated interfaces in the enriched methods (XFEM, E-FEM) could have different shapes. An example of the 3D model can be found in the study of Zhu et al [Zhu et al., 2011] in the framework of XFEM and the spring-layer model. The 3D development will open the possibility to perform a confrontation between numerical results and experimental results like those obtained by Blivi et al [Blivi, 2018]. To this purpose, the parameters of the interface between the silica inclusions and PMMA matrix are required and can be determined thanks to MD simulations.

The coherent interface model used in the present work specified that the displacement field is continuous across the interface. For the other interface models, the discontinuity of displacement field across the interface has to be considered and the spring-layer model in the work of Zhu et al [Zhu et al., 2011] or the general interface model in [Javili et al., 2017] can be employed to the proposed development. In the context of enriched FEM approaches such as XFEM or E-FEM, the coupling between weak and strong discontinuity to take into account the general interface model is absolutely possible.

Appendix A

E-FEM with numerical evaluation of curvature

A.1 Numerical evaluation of curvature

With 2D plane strain hypothesis, the value of curvature is defined as:

$$\kappa_c = \frac{1}{R}, \quad (\text{A.1})$$

where R is the local radius of curvature of the interface within the considered element. In the general case where the radius of curvature is not available or when the interface shape changes with respect to time as in fluid mechanics, the value of the radius of curvature can be numerically estimated through the nodal values of signed distance to the interface (level set). In chapter 4, (see Eq. (4.17)) we presented the numerical evaluation of the normal vector of the interface as:

$$\mathbf{n} = \frac{\nabla\varphi}{\|\nabla\varphi\|}. \quad (\text{A.2})$$

The curvature can be computed in terms of the discretized signed distance function as:

$$\kappa_c = \nabla \cdot \mathbf{n} = \nabla \cdot \left(\frac{\nabla\varphi}{\|\nabla\varphi\|} \right). \quad (\text{A.3})$$

It has to be noted that the interface is approximated by a linear interpolation based on the finite element shape function, the normal \mathbf{n} is therefore constant in each element and $\nabla^2\varphi$ vanish in element interior. We cannot rely directly on the interpolation of \mathbf{n} to calculate curvature. We, therefore, use the strategy proposed by Chessa and Belytschko [Chessa and Belytschko, 2003] for problems of axisymmetric two-phase flow with surface tension. We thus introduce two auxiliary fields related to the interface:

- The vector gradient of the level set \mathbf{g}

- The value of curvature κ_c

These fields need only to be determined on the elements cut by the interface. The procedure to compute these fields has been presented in [Chessa and Belytschko, 2003] based on minimizing the following functional for \mathbf{g} and κ_c

$$I_g = \int_{\Omega} \frac{1}{2} (\mathbf{g} - \nabla \varphi)^2 d\Omega , \quad (\text{A.4})$$

$$I_{\kappa_c} = \int_{\Omega} \frac{1}{2} \left[\kappa_c - \nabla \cdot \left(\frac{\mathbf{g}}{\|\mathbf{g}\|} \right) \right]^2 d\Omega . \quad (\text{A.5})$$

By using the C^0 finite element approximation for \mathbf{g}^h and κ_c^h we obtain the discrete finite element equations:

$$\tilde{\mathbf{Q}}\mathbf{g} = \mathbf{f}^g \varphi , \quad (\text{A.6})$$

$$\mathbf{Q}\kappa_c = \mathbf{f}^{\kappa}(\mathbf{g}^h) , \quad (\text{A.7})$$

where

$$\tilde{\mathbf{Q}} = \int_{\Omega} \mathbf{N}^T \mathbf{N} d\Omega \quad \text{with} \quad \mathbf{N} = \begin{bmatrix} N_1 & 0 & N_2 & 0 & N_3 & 0 \\ 0 & N_1 & 0 & N_2 & 0 & N_3 \end{bmatrix} \quad (\text{A.8})$$

$$\mathbf{f}^g = \int_{\Omega} \mathbf{N}^T (\nabla \mathbf{N}) d\Omega \quad (\text{A.9})$$

$$\mathbf{Q} = \int_{\Omega} \tilde{\mathbf{N}}^T \tilde{\mathbf{N}} d\Omega \quad \text{with} \quad \tilde{\mathbf{N}} = [N_1 \quad N_2 \quad N_3] \quad (\text{A.10})$$

$$\mathbf{f}^{\kappa_c} = \int_{\Omega} \tilde{\mathbf{N}}^T \nabla \cdot \left(\frac{\mathbf{g}}{\|\mathbf{g}\|} \right) d\Omega . \quad (\text{A.11})$$

After evaluation of nodal value of κ_c^i thanks to Eq. (A.5), the curvature in the element is determined as:

$$\kappa_c^h(\mathbf{x}) = \sum_{i=1}^n \tilde{\mathbf{N}}_i(\mathbf{x}) \kappa_c^i \quad (\text{A.12})$$

The radius of curvature R is then computed by using Eq. (A.1).

A.2 Influence of the numerical evaluation of the curvature on the results

The numerical evaluation of the curvature is used in the case of the Eshelby problem with coherent interface presented in subsection 4.6.1 of chapter 4. The convergence analysis is presented in Figure A.1. We observe a small degradation of convergence of E-FEM due to the error which comes from the numerical evaluation of the curvature. However, the convergence using E-FEM is still better than that using XFEM.

We then consider the case of an ellipsoidal inclusion as presented in subsection

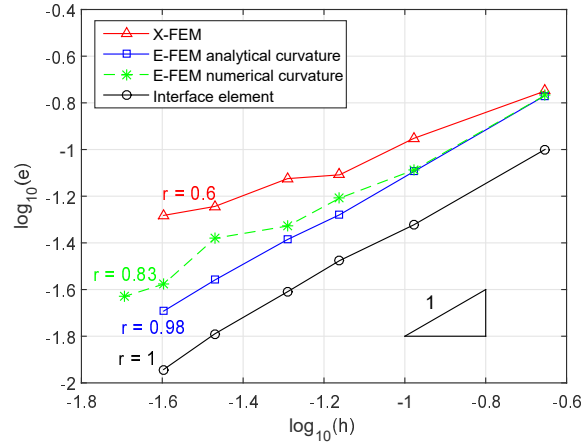


Figure A.1: Convergence analysis for the Eshelby problem with a circular inclusion

4.6.2. In Figure A.2, the results obtained with the numerical estimation of the curvature are compared to those obtained with the analytical calculation of the curvature using Eq. (4.58). The 40x40 nodes and 80x80 nodes meshes have been used for this test. We notice that the numerical curvature almost doesn't affect the effective bulk modulus.

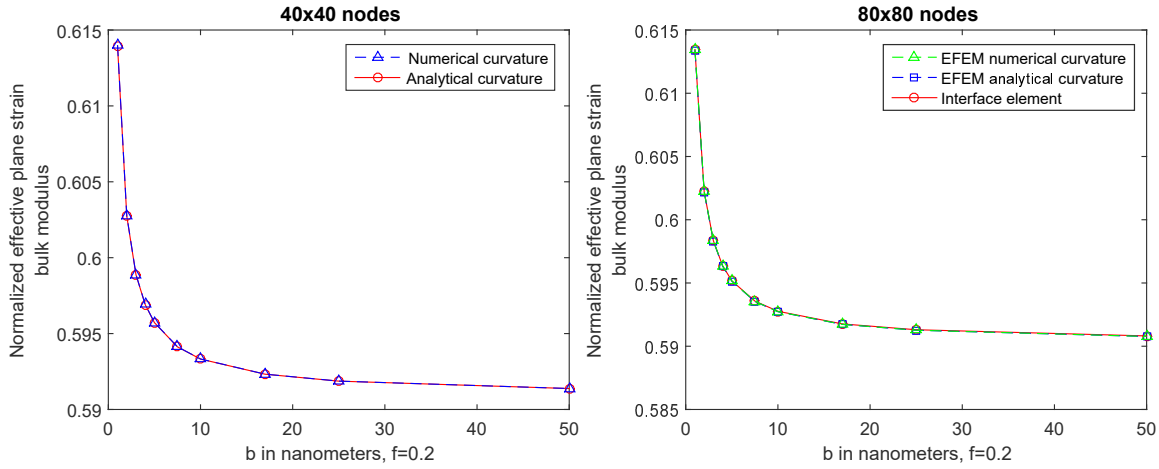


Figure A.2: Size effect in effective plane-strain bulk modulus for ellipsoidal inclusion ($a = 2b$, $f = 0,2$, $E_m = 70 \text{ GPa}$, $E_i = 0,1E_m$, $\nu_m = \nu_i = 0,32$, $\lambda_s = 6.842 \text{ N/m}$, $\mu_s = -0.375 \text{ N/m}$).

Bibliography

- [Adnan et al., 2007] Adnan, A., Sun, C., and Mahfuz, H. (2007). A molecular dynamics simulation study to investigate the effect of filler size on elastic properties of polymer nanocomposites. *Composites Science and Technology*, 67(3-4):348–356.
- [Alberti et al., 2017] Alberti, M., Enfedaque, A., Gálvez, J., and Reyes, E. (2017). Numerical modelling of the fracture of polyolefin fibre reinforced concrete by using a cohesive fracture approach. *Composites Part B: Engineering*, 111:200–210.
- [Armero and Garikipati, 1996] Armero, F. and Garikipati, K. (1996). An analysis of strong discontinuities in multiplicative finite strain plasticity and their relation with the numerical simulation of strain localization in solids. *International Journal of Solids and Structures*, 33(20-22):2863–2885.
- [Belytschko et al., 1988] Belytschko, T., Fish, J., and Engelmann, B. E. (1988). A finite element with embedded localization zones. *Computer methods in applied mechanics and engineering*, 70(1):59–89.
- [Benkemoun et al., 2010] Benkemoun, N., Hautefeuille, M., Colliat, J.-B., and Ibrahimbegovic, A. (2010). Failure of heterogeneous materials: 3d meso-scale fe models with embedded discontinuities. *International Journal for Numerical Methods in Engineering*, 82(13):1671–1688.
- [Benveniste, 2006] Benveniste, Y. (2006). A general interface model for a three-dimensional curved thin anisotropic interphase between two anisotropic media. *Journal of the Mechanics and Physics of Solids*, 54(4):708–734.
- [Benveniste, 2013] Benveniste, Y. (2013). Models of thin interphases and the effective medium approximation in composite media with curvilinearly anisotropic coated inclusions. *International Journal of Engineering Science*, 72:140–154.
- [Blivi et al., 2016] Blivi, A., Benhui, F., Bai, J., Kondo, D., and Bédoui, F. (2016). Experimental evidence of size effect in nano-reinforced polymers: Case of silica reinforced pmma. *Polymer Testing*, 56:337–343.
- [Blivi, 2018] Blivi, A. S. (2018). *Effet de taille dans les polymères nano-renforcés: caractérisation multi-échelles et modélisation*. PhD thesis.

- [Bogue, 2011] Bogue, R. (2011). Nanocomposites: a review of technology and applications. *Assembly Automation*, 31(2):106–112.
- [Bottomley and Ogino, 2001] Bottomley, D. and Ogino, T. (2001). Alternative to the shuttleworth formulation of solid surface stress. *Physical Review B*, 63(16):165412.
- [Boutaleb et al., 2009] Boutaleb, S., Zaïri, F., Mesbah, A., Naït-Abdelaziz, M., Gloaguen, J.-M., Boukharouba, T., and Lefebvre, J.-M. (2009). Micromechanics-based modelling of stiffness and yield stress for silica/polymer nanocomposites. *International Journal of Solids and Structures*, 46(7-8):1716–1726.
- [Bövik, 1994] Bövik, P. (1994). On the modelling of thin interface layers in elastic and acoustic scattering problems. *The Quarterly Journal of Mechanics and Applied Mathematics*, 47(1):17–42.
- [Brach et al., 2017a] Brach, S., Dormieux, L., Kondo, D., and Vairo, G. (2017a). Nanoporous materials with a general isotropic plastic matrix: Exact limit state under isotropic loadings. *International Journal of Plasticity*, 89:1–28.
- [Brach et al., 2017b] Brach, S., Dormieux, L., Kondo, D., and Vairo, G. (2017b). Strength properties of nanoporous materials: A 3-layered based non-linear homogenization approach with interface effects. *International Journal of Engineering Science*, 115:28–42.
- [Brancherie and Ibrahimbegovic, 2009] Brancherie, D. and Ibrahimbegovic, A. (2009). Novel anisotropic continuum-discrete damage model capable of representing localized failure of massive structures: Part i: theoretical formulation and numerical implementation. *Engineering Computations*, 26(1/2):100–127.
- [Brisard et al., 2010a] Brisard, S., Dormieux, L., and Kondo, D. (2010a). Hashinshtrikman bounds on the bulk modulus of a nanocomposite with spherical inclusions and interface effects. *Computational Materials Science*, 48(3):589–596.
- [Brisard et al., 2010b] Brisard, S., Dormieux, L., and Kondo, D. (2010b). Hashinshtrikman bounds on the shear modulus of a nanocomposite with spherical inclusions and interface effects. *Computational Materials Science*, 50(2):403–410.
- [Brown et al., 2008] Brown, D., Marcadon, V., Mele, P., and Alberola, N. (2008). Effect of filler particle size on the properties of model nanocomposites. *Macromolecules*, 41(4):1499–1511.
- [Brown et al., 2003] Brown, D., Mele, P., Marceau, S., and Alberola, N. (2003). A molecular dynamics study of a model nanoparticle embedded in a polymer matrix. *Macromolecules*, 36(4):1395–1406.

- [Burman et al., 2015] Burman, E., Claus, S., Hansbo, P., Larson, M. G., and Massing, A. (2015). Cutfem: discretizing geometry and partial differential equations. *International Journal for Numerical Methods in Engineering*, 104(7):472–501.
- [Burman and Hansbo, 2010] Burman, E. and Hansbo, P. (2010). Fictitious domain finite element methods using cut elements: I. a stabilized lagrange multiplier method. *Computer Methods in Applied Mechanics and Engineering*, 199(41–44):2680–2686.
- [Burman et al., 2016] Burman, E., Hansbo, P., Larson, M. G., and Zahedi, S. (2016). Cut finite element methods for coupled bulk–surface problems. *Numerische Mathematik*, 133(2):203–231.
- [Cammarata, 1994] Cammarata, R. C. (1994). Surface and interface stress effects in thin films. *Progress in surface science*, 46(1):1–38.
- [Cauvin et al., 2010] Cauvin, L., Kondo, D., Brieu, M., and Bhatnagar, N. (2010). Mechanical properties of polypropylene layered silicate nanocomposites: Characterization and micro-macro modelling. *Polymer Testing*, 29(2):245–250.
- [Cazes et al., 2016] Cazes, F., Meschke, G., and Zhou, M.-M. (2016). Strong discontinuity approaches: An algorithm for robust performance and comparative assessment of accuracy. *International Journal of Solids and Structures*, 96:355–379.
- [Cenanovic et al., 2016] Cenanovic, M., Hansbo, P., and Larson, M. G. (2016). Cut finite element modeling of linear membranes. *Computer Methods in Applied Mechanics and Engineering*, 310:98–111.
- [Chen et al., 2006] Chen, T., Chiu, M.-S., and Weng, C.-N. (2006). Derivation of the generalized young-laplace equation of curved interfaces in nanoscaled solids. *Journal of Applied Physics*, 100(7):074308.
- [Chen et al., 2007] Chen, T., Dvorak, G. J., and Yu, C. (2007). Size-dependent elastic properties of unidirectional nano-composites with interface stresses. *Acta Mechanica*, 188(1-2):39–54.
- [Chessa and Belytschko, 2003] Chessa, J. and Belytschko, T. (2003). An enriched finite element method and level sets for axisymmetric two-phase flow with surface tension. *International Journal for Numerical Methods in Engineering*, 58(13):2041–2064.
- [Cho et al., 2006] Cho, J., Joshi, M., and Sun, C. (2006). Effect of inclusion size on mechanical properties of polymeric composites with micro and nano particles. *Composites Science and Technology*, 66(13):1941–1952.

- [Christensen and Lo, 1979] Christensen, R. and Lo, K. (1979). Solutions for effective shear properties in three phase sphere and cylinder models. *Journal of the Mechanics and Physics of Solids*, 27(4):315–330.
- [Dormieux and Kondo, 2013] Dormieux, L. and Kondo, D. (2013). Non linear homogenization approach of strength of nanoporous materials with interface effects. *International Journal of Engineering Science*, 71:102–110.
- [Douce et al., 2004] Douce, J., Boilot, J.-P., Biteau, J., Scodellaro, L., and Jimenez, A. (2004). Effect of filler size and surface condition of nano-sized silica particles in polysiloxane coatings. *Thin Solid Films*, 466(1-2):114–122.
- [Drzal et al., 1983] Drzal, L. T., Rich, M. J., Koenig, M. F., and Lloyd, P. F. (1983). Adhesion of graphite fibers to epoxy matrices: Ii. the effect of fiber finish. *The Journal of Adhesion*, 16(2):133–152.
- [Duan et al., 2005a] Duan, H., Wang, J., Huang, Z., and Karihaloo, B. L. (2005a). Eshelby formalism for nano-inhomogeneities. *Proceedings of the Royal Society A: Mathematical, Physical and Engineering Sciences*, 461(2062):3335–3353.
- [Duan et al., 2005b] Duan, H., Wang, J.-x., Huang, Z., and Karihaloo, B. L. (2005b). Size-dependent effective elastic constants of solids containing nano-inhomogeneities with interface stress. *Journal of the Mechanics and Physics of Solids*, 53(7):1574–1596.
- [Dujc et al., 2013] Dujc, J., Brank, B., and Ibrahimbegovic, A. (2013). Stress-hybrid quadrilateral finite element with embedded strong discontinuity for failure analysis of plane stress solids. *International journal for numerical methods in engineering*, 94(12):1075–1098.
- [Dvorkin et al., 1990] Dvorkin, E. N., Cuitiño, A. M., and Gioia, G. (1990). Finite elements with displacement interpolated embedded localization lines insensitive to mesh size and distortions. *International journal for numerical methods in engineering*, 30(3):541–564.
- [Eshelby, 1957] Eshelby, J. D. (1957). The determination of the elastic field of an ellipsoidal inclusion, and related problems. In *Proceedings of the Royal Society of London A: Mathematical, Physical and Engineering Sciences*, volume 241, pages 376–396. The Royal Society.
- [Esmaeili et al., 2017] Esmaeili, A., Steinmann, P., and Javili, A. (2017). Non-coherent energetic interfaces accounting for degradation. *Computational Mechanics*, 59(3):361–383.
- [Eyring, 1954] Eyring, H. (1954). Structure and properties of solid surfaces.

- [Farsad et al., 2010] Farsad, M., Vernerey, F. J., and Park, H. S. (2010). An extended finite element/level set method to study surface effects on the mechanical behavior and properties of nanomaterials. *International Journal for Numerical Methods in Engineering*, 84(12):1466–1489.
- [Foster et al., 2007] Foster, C., Borja, R., and Regueiro, R. (2007). Embedded strong discontinuity finite elements for fractured geomaterials with variable friction. *International Journal for Numerical Methods in Engineering*, 72(5):549–581.
- [Fried and Gurtin, 2007] Fried, E. and Gurtin, M. E. (2007). Thermomechanics of the interface between a body and its environment. *Continuum Mechanics and Thermodynamics*, 19(5):253–271.
- [Fu et al., 2019] Fu, S., Sun, Z., Huang, P., Li, Y., and Hu, N. (2019). Some basic aspects of polymer nanocomposites: A critical review. *Nano Materials Science*, 1(1):2–30.
- [Gálvez et al., 2013] Gálvez, J., Planas, J., Sancho, J., Reyes, E., Cendón, D., and Casati, M. (2013). An embedded cohesive crack model for finite element analysis of quasi-brittle materials. *Engineering Fracture Mechanics*, 109:369–386.
- [Gates et al., 2005] Gates, T., Odegard, G., Frankland, S., and Clancy, T. (2005). Computational materials: multi-scale modeling and simulation of nanostructured materials. *Composites Science and Technology*, 65(15-16):2416–2434.
- [Gibbs, 1906] Gibbs, J. W. (1906). *The scientific papers of J. Willard Gibbs*, volume 1. Longmans, Green and Company.
- [Gu et al., 2016] Gu, H., Ma, C., Gu, J., Guo, J., Yan, X., Huang, J., Zhang, Q., and Guo, Z. (2016). An overview of multifunctional epoxy nanocomposites. *Journal of Materials Chemistry C*, 4(25):5890–5906.
- [Gu, 2008] Gu, S.-T. (2008). *Contributions à la modélisation des interfaces imparfaites et à l’homogénéisation des matériaux hétérogènes*. PhD thesis.
- [Gurtin et al., 1998] Gurtin, M., Weissmüller, J., and Larche, F. (1998). A general theory of curved deformable interfaces in solids at equilibrium. *Philosophical Magazine A*, 78(5):1093–1109.
- [Gurtin and Ian Murdoch, 1975] Gurtin, M. E. and Ian Murdoch, A. (1975). A continuum theory of elastic material surfaces. *Archive for Rational Mechanics and Analysis*, 57(4):291–323.
- [Hamilton and Wolfer, 2009] Hamilton, J. and Wolfer, W. (2009). Theories of surface elasticity for nanoscale objects. *Surface Science*, 603(9):1284–1291.

- [Hashin, 1962] Hashin, Z. (1962). The elastic moduli of heterogeneous materials. *Journal of Applied Mechanics*, 29(1):143–150.
- [Hashin, 1992] Hashin, Z. (1992). Extremum principles for elastic heterogeneous media with imperfect interfaces and their application to bounding of effective moduli. *Journal of the Mechanics and Physics of Solids*, 40(4):767–781.
- [Hashin and Rosen, 1964] Hashin, Z. and Rosen, B. W. (1964). The elastic moduli of fiber-reinforced materials. *Journal of applied mechanics*, 31(2):223–232.
- [Hautefeuille et al., 2009] Hautefeuille, M., Melnyk, S., Colliat, J.-B., and Ibrahimbegovic, A. (2009). Failure model for heterogeneous structures using structured meshes and accounting for probability aspects. *Engineering Computations*, 26(1/2):166–184.
- [Hill, 1961] Hill, R. (1961). Discontinuity relations in mechanics of solids. *Progress in solid mechanics*, 2(72):245–276.
- [Hill, 1964] Hill, R. (1964). Theory of mechanical properties of fibre-strengthened materials: I. elastic behaviour. *Journal of the Mechanics and Physics of Solids*, 12(4):199–212.
- [Ibrahimbegovic, 2009] Ibrahimbegovic, A. (2009). *Nonlinear solid mechanics: theoretical formulations and finite element solution methods*, volume 160. Springer Science & Business Media.
- [Ibrahimbegovic and Wilson, 1991] Ibrahimbegovic, A. and Wilson, E. (1991). A modified method of incompatible modes. *Communications in Applied Numerical Methods*, 7(3):187–194.
- [Idelsohn et al., 2017] Idelsohn, S. R., Gimenez, J. M., Marti, J., and Nigro, N. M. (2017). Elemental enriched spaces for the treatment of weak and strong discontinuous fields. *Computer Methods in Applied Mechanics and Engineering*, 313:535–559.
- [Javili et al., 2015] Javili, A., Chatzigeorgiou, G., McBride, A. T., Steinmann, P., and Linder, C. (2015). Computational homogenization of nano-materials accounting for size effects via surface elasticity. *GAMM-Mitteilungen*, 38(2):285–312.
- [Javili et al., 2017] Javili, A., Steinmann, P., and Mosler, J. (2017). Micro-to-macro transition accounting for general imperfect interfaces. *Computer Methods in Applied Mechanics and Engineering*, 317(Supplement C):274 – 317.
- [Jesson and Watts, 2012] Jesson, D. A. and Watts, J. F. (2012). The interface and interphase in polymer matrix composites: effect on mechanical properties and methods for identification. *Polymer Reviews*, 52(3):321–354.

- [Jirásek, 2000] Jirásek, M. (2000). Comparative study on finite elements with embedded discontinuities. *Computer methods in applied mechanics and engineering*, 188(1-3):307–330.
- [Juárez-Luna and Ayala, 2014] Juárez-Luna, G. and Ayala, G. (2014). Improvement of some features of finite elements with embedded discontinuities. *Engineering Fracture Mechanics*, 118:31–48.
- [Kausar et al., 2017] Kausar, A., Rafique, I., and Muhammad, B. (2017). Aerospace application of polymer nanocomposite with carbon nanotube, graphite, graphene oxide, and nanoclay. *Polymer-Plastics Technology and Engineering*, 56(13):1438–1456.
- [Larsson et al., 1996] Larsson, R., Runesson, K., and Sture, S. (1996). Embedded localization band in undrained soil based on regularized strong discontinuity—theory and fe-analysis. *International Journal of Solids and Structures*, 33(20-22):3081–3101.
- [Le et al., 2016] Le, T.-T., Guillemot, J., and Soize, C. (2016). Stochastic continuum modeling of random interphases from atomistic simulations. application to a polymer nanocomposite. *Computer Methods in Applied Mechanics and Engineering*, 303:430–449.
- [Le Quang and He, 2007] Le Quang, H. and He, Q.-C. (2007). Thermoelastic composites with columnar microstructure and cylindrically anisotropic phases. part i: Exact results. *International journal of engineering science*, 45(2-8):402–423.
- [Le Quang and He, 2008] Le Quang, H. and He, Q.-C. (2008). Variational principles and bounds for elastic inhomogeneous materials with coherent imperfect interfaces. *Mechanics of materials*, 40(10):865–884.
- [Linder and Armero, 2007] Linder, C. and Armero, F. (2007). Finite elements with embedded strong discontinuities for the modeling of failure in solids. *International Journal for Numerical Methods in Engineering*, 72(12):1391–1433.
- [Linder and Armero, 2009] Linder, C. and Armero, F. (2009). Finite elements with embedded branching. *Finite Elements in Analysis and Design*, 45(4):280–293.
- [Linder and Miehe, 2012] Linder, C. and Miehe, C. (2012). Effect of electric displacement saturation on the hysteretic behavior of ferroelectric ceramics and the initiation and propagation of cracks in piezoelectric ceramics. *Journal of the Mechanics and Physics of Solids*, 60(5):882–903.

- [Linder et al., 2011] Linder, C., Rosato, D., and Miehe, C. (2011). New finite elements with embedded strong discontinuities for the modeling of failure in electromechanical coupled solids. *Computer Methods in Applied Mechanics and Engineering*, 200(1-4):141–161.
- [Lotfi and Shing, 1995] Lotfi, H. R. and Shing, P. B. (1995). Embedded representation of fracture in concrete with mixed finite elements. *International journal for numerical methods in engineering*, 38(8):1307–1325.
- [Lubliner, 1990] Lubliner, J. (1990). The theory of plasticity.
- [Marcadon, 2005] Marcadon, V. (2005). *Effets de taille et d’interphase sur le comportement mécanique de nanocomposites particuliers*. PhD thesis, Ecole Polytechnique X.
- [Marcadon et al., 2013] Marcadon, V., Brown, D., Hervé, E., Mélé, P., Albérola, N., and Zaoui, A. (2013). Confrontation between molecular dynamics and micromechanical approaches to investigate particle size effects on the mechanical behaviour of polymer nanocomposites. *Computational Materials Science*, 79:495–505.
- [Marcadon et al., 2007] Marcadon, V., Herve, E., and Zaoui, A. (2007). Micromechanical modeling of packing and size effects in particulate composites. *International Journal of Solids and Structures*, 44(25-26):8213–8228.
- [Marceau, 2003] Marceau, S. (2003). *Architecture Multiéchelle et propriétés mécaniques de nanocomposites*. Theses, Université de Savoie.
- [Maugin, 1992] Maugin, G. A. (1992). *The thermomechanics of plasticity and fracture*, volume 7. Cambridge University Press.
- [Mi et al., 2008] Mi, C., Jun, S., Kouris, D. A., and Kim, S. Y. (2008). Atomistic calculations of interface elastic properties in noncoherent metallic bilayers. *Phys. Rev. B*, 77:075425.
- [Miller and Shenoy, 2000] Miller, R. E. and Shenoy, V. B. (2000). Size-dependent elastic properties of nanosized structural elements. *Nanotechnology*, 11(3):139.
- [Mishra et al., 2005] Mishra, S., Sonawane, S., and Singh, R. (2005). Studies on characterization of nano caco3 prepared by the in situ deposition technique and its application in pp-nano caco3 composites. *Journal of Polymer Science Part B: Polymer Physics*, 43(1):107–113.
- [Moës and Belytschko, 2002] Moës, N. and Belytschko, T. (2002). Extended finite element method for cohesive crack growth. *Engineering fracture mechanics*, 69(7):813–833.

- [Moës et al., 2003] Moës, N., Cloirec, M., Cartraud, P., and Remacle, J.-F. (2003). A computational approach to handle complex microstructure geometries. *Computer Methods in Applied Mechanics and Engineering*, 192(28):3163 – 3177. Multiscale Computational Mechanics for Materials and Structures.
- [Moës et al., 1999] Moës, N., Dolbow, J., and Belytschko, T. (1999). A finite element method for crack growth without remeshing. *International journal for numerical methods in engineering*, 46(1):131–150.
- [Monchiet and Kondo, 2013] Monchiet, V. and Kondo, D. (2013). Combined voids size and shape effects on the macroscopic criterion of ductile nanoporous materials. *International Journal of Plasticity*, 43:20–41.
- [Mori and Tanaka, 1973] Mori, T. and Tanaka, K. (1973). Average stress in matrix and average elastic energy of materials with misfitting inclusions. *Acta metallurgica*, 21(5):571–574.
- [Murdoch, 1976] Murdoch, A. I. (1976). A thermodynamical theory of elastic material interfaces. *The Quarterly Journal of Mechanics and Applied Mathematics*, 29(3):245–275.
- [Naskar et al., 2016] Naskar, A. K., Keum, J. K., and Boeman, R. G. (2016). Polymer matrix nanocomposites for automotive structural components. *Nature nanotechnology*, 11(12):1026.
- [Nazarenko et al., 2017] Nazarenko, L., Bargmann, S., and Stolarski, H. (2017). Closed-form formulas for the effective properties of random particulate nanocomposites with complete gurtin–murdoch model of material surfaces. *Continuum Mechanics and Thermodynamics*, 29(1):77–96.
- [Nikolić et al., 2018] Nikolić, M., Do, X. N., Ibrahimbegovic, A., and Nikolić, Ž. (2018). Crack propagation in dynamics by embedded strong discontinuity approach: Enhanced solid versus discrete lattice model. *Computer Methods in Applied Mechanics and Engineering*, 340:480–499.
- [Odegard et al., 2005] Odegard, G., Clancy, T., and Gates, T. (2005). Modeling of the mechanical properties of nanoparticle/polymer composites. *Polymer*, 46(2):553–562.
- [Oliver, 1996] Oliver, J. (1996). Modelling strong discontinuities in solid mechanics via strain softening constitutive equations. part 1: Fundamentals. *International journal for numerical methods in engineering*, 39(21):3575–3600.
- [Oliver et al., 2006] Oliver, J., Huespe, A. E., and Sánchez, P. J. (2006). A comparative study on finite elements for capturing strong discontinuities: E-fem vs x-fem. *Computer methods in applied mechanics and engineering*, 195(37-40):4732–4752.

- [Olshanskii et al., 2009] Olshanskii, M. A., Reusken, A., and Grande, J. (2009). A finite element method for elliptic equations on surfaces. *SIAM journal on numerical analysis*, 47(5):3339–3358.
- [Orowan, 1970] Orowan, E. (1970). Surface energy and surface tension in solids and liquids. *Proceedings of the Royal Society of London. A. Mathematical and Physical Sciences*, 316(1527):473–491.
- [Ortiz et al., 1987] Ortiz, M., Leroy, Y., and Needleman, A. (1987). A finite element method for localized failure analysis. *Computer methods in applied mechanics and engineering*, 61(2):189–214.
- [Osher and Fedkiw, 2001] Osher, S. and Fedkiw, R. P. (2001). Level set methods: an overview and some recent results. *Journal of Computational physics*, 169(2):463–502.
- [Ottosen et al., 2015] Ottosen, N. S., Ristinmaa, M., and Mosler, J. (2015). Fundamental physical principles and cohesive zone models at finite displacements—limitations and possibilities. *International Journal of Solids and Structures*, 53:70–79.
- [Paliwal et al., 2012] Paliwal, B., Cherkaoui, M., and Fassi-Fehri, O. (2012). Effective elastic properties of nanocomposites using a novel atomistic–continuum interphase model. *Comptes Rendus Mecanique*, 340(4-5):296–306.
- [Povstenko, 1993] Povstenko, Y. Z. (1993). Theoretical investigation of phenomena caused by heterogeneous surface tension in solids. *Journal of the Mechanics and Physics of Solids*, 41(9):1499–1514.
- [Quang and He, 2009] Quang, H. L. and He, Q. C. (2009). Estimation of the effective thermoelastic moduli of fibrous nanocomposites with cylindrically anisotropic phases. *Archive of Applied Mechanics*, 79(3):225–248.
- [Reyes et al., 2009] Reyes, E., Gálvez, J., Casati, M., Cendón, D., Sancho, J., and Planas, J. (2009). An embedded cohesive crack model for finite element analysis of brickwork masonry fracture. *Engineering Fracture Mechanics*, 76(12):1930–1944.
- [Reynaud et al., 2001] Reynaud, E., Jouen, T., Gauthier, C., Vigier, G., and Varlet, J. (2001). Nanofillers in polymeric matrix: a study on silica reinforced pa6. *Polymer*, 42(21):8759–8768.
- [Roubin et al., 2015] Roubin, E., Vallade, A., Benkemoun, N., and Colliat, J.-B. (2015). Multi-scale failure of heterogeneous materials: A double kinematics enhancement for embedded finite element method. *International Journal of Solids and Structures*, 52:180–196.

- [Sancho et al., 2006] Sancho, J., Planas, J., Gálvez, J., Reyes, E., and Cendón, D. (2006). An embedded cohesive crack model for finite element analysis of mixed mode fracture of concrete. *Fatigue & Fracture of Engineering Materials & Structures*, 29(12):1056–1065.
- [Sharma and Ganti, 2004] Sharma, P. and Ganti, S. (2004). Size-dependent eshelby’s tensor for embedded nano-inclusions incorporating surface/interface energies. *Transactions-American society of mechanical engineers journal of applied mechanics*, 71(5):663–671.
- [Sharma and Ganti, 2005] Sharma, P. and Ganti, S. (2005). Erratum: ”Size-Dependent Eshelby’s Tensor for Embedded Nano-Inclusions Incorporating Surface/Interface Energies” [Journal of Applied Mechanics, 2004, 71 (5), pp. 663–671]. *Journal of Applied Mechanics*, 72(4):628–628.
- [Sharma et al., 2003] Sharma, P., Ganti, S., and Bhate, N. (2003). Effect of surfaces on the size-dependent elastic state of nano-inhomogeneities. *Applied Physics Letters*, 82(4):535–537.
- [Sharma et al., 2006] Sharma, P., Ganti, S., and Bhate, N. (2006). Erratum: “effect of surfaces on the size-dependent elastic state of nano-inhomogeneities” [appl. phys. lett. 82, 535 (2003)]. *Applied Physics Letters*, 89(4):535.
- [Shenoy, 2005] Shenoy, V. B. (2005). Atomistic calculations of elastic properties of metallic fcc crystal surfaces. *Phys. Rev. B*, 71:094104.
- [Shuttleworth, 1950] Shuttleworth, R. (1950). The surface tension of solids. *Proceedings of the physical society. Section A*, 63(5):444.
- [Simo and Oliver, 1994] Simo, J. and Oliver, J. (1994). A new approach to the analysis and simulation of strain softening in solids. *Fracture and damage in quasibrittle structures*, pages 25–39.
- [Simo and Hughes, 2006] Simo, J. C. and Hughes, T. J. (2006). *Computational inelasticity*, volume 7. Springer Science & Business Media.
- [Simo et al., 1993] Simo, J. C., Oliver, J., and Armero, F. (1993). An analysis of strong discontinuities induced by strain-softening in rate-independent inelastic solids. *Computational mechanics*, 12(5):277–296.
- [Simo and Rifai, 1990] Simo, J. C. and Rifai, M. (1990). A class of mixed assumed strain methods and the method of incompatible modes. *International journal for numerical methods in engineering*, 29(8):1595–1638.

- [Sluys and Berends, 1998] Sluys, L. and Berends, A. (1998). Discontinuous failure analysis for mode-i and mode-ii localization problems. *International Journal of Solids and Structures*, 35(31-32):4257–4274.
- [Streitz et al., 1994] Streitz, F., Cammarata, R., and Sieradzki, K. (1994). Surface-stress effects on elastic properties. i. thin metal films. *Physical Review B*, 49(15):10699.
- [Suárez et al., 2019] Suárez, F., Gálvez, J., Enfedaque, A., and Alberti, M. (2019). Modelling fracture on polyolefin fibre reinforced concrete specimens subjected to mixed-mode loading. *Engineering Fracture Mechanics*, 211:244–253.
- [Sukumar et al., 2001] Sukumar, N., Chopp, D. L., Moës, N., and Belytschko, T. (2001). Modeling holes and inclusions by level sets in the extended finite-element method. *Computer methods in applied mechanics and engineering*, 190(46-47):6183–6200.
- [Tran et al., 2011] Tran, A., Yvonnet, J., He, Q.-C., Toulemonde, C., and Sanahuja, J. (2011). A multiple level set approach to prevent numerical artefacts in complex microstructures with nearby inclusions within xfem. *International Journal for Numerical Methods in Engineering*, 85(11):1436–1459.
- [Vu-Bac et al., 2014] Vu-Bac, N., Lahmer, T., Zhang, Y., Zhuang, X., and Rabczuk, T. (2014). Stochastic predictions of interfacial characteristic of polymeric nanocomposites (pnacs). *Composites Part B: Engineering*, 59:80–95.
- [Washizu, 1975] Washizu, K. (1975). *Variational methods in elasticity and plasticity*, volume 3. Pergamon press Oxford.
- [Wei et al., 2006] Wei, G., Shouwen, Y., and Ganyun, H. (2006). Finite element characterization of the size-dependent mechanical behaviour in nanosystems. *Nanotechnology*, 17(4):1118.
- [Wilson, 1974] Wilson, E. L. (1974). The static condensation algorithm. *International Journal for Numerical Methods in Engineering*, 8(1):198–203.
- [Wilson and Ibrahimbegovic, 1990] Wilson, E. L. and Ibrahimbegovic, A. (1990). Use of incompatible displacement modes for the calculation of element stiffnesses or stresses. *Finite Elements in Analysis and Design*, 7(3):229–241.
- [Yu et al., 2009] Yu, S., Yang, S., and Cho, M. (2009). Multi-scale modeling of cross-linked epoxy nanocomposites. *Polymer*, 50(3):945–952.

- [Yvonnet et al., 2008] Yvonnet, J., Quang, H. L., and He, Q.-C. (2008). An xfem/level set approach to modelling surface/interface effects and to computing the size-dependent effective properties of nanocomposites. *Computational Mechanics*, 42(1):119–131.
- [Zhu et al., 2011] Zhu, Q.-Z., Gu, S.-T., Yvonnet, J., Shao, J.-F., and He, Q.-C. (2011). Three-dimensional numerical modelling by xfem of spring-layer imperfect curved interfaces with applications to linearly elastic composite materials. *International Journal for Numerical Methods in Engineering*, 88(4):307–328.
- [Zienkiewicz and Taylor, 2005] Zienkiewicz, O. C. and Taylor, R. L. (2005). *The finite element method for solid and structural mechanics*. Elsevier.